A Cumulant LBM approach for Large Eddy Simulation of Dispersion Microsystems

Von der
Fakultät Architektur, Bauingenieurwesen und Umweltwissenschaften
der Technischen Universität Carolo-Wilhelmina
zu Braunschweig

zur Erlangung des Grades eines
Doktoringenieurs (Dr.-Ing.)
genehmigte

Dissertation

von
Ehsan Goraki Fard
geboren am 16. September 1984
aus Booshehr im Iran

Eingereicht am	6. Juni 2014
Mündliche Prüfung am	17. März 2015
Berichterstatter	Prof. Dr.-Ing. habil. Manfred Krafczyk
	Prof. Dr.-Ing. Arno Kwade

2015

I dedicate this thesis to my lovely grandmother, khadijeh Bolvardi
and to cancer patients

Was mich

nicht umbringt,

macht mich

Stärker.

Friedrich Nietzsche

Acknowledgment

All of my work at the institute of IRMB from 2011 to 2014 resulted in this thesis. Since this time was very noteworthy in my life, I would like to thank those who marked my path with their views, comments, or even just presence.

First of all, I would thank Prof. Manfred Krafczyk, for the marvelous opportunity to work on the the Lattice Boltzmann method, for always bringing up plenty of comments, for answering my confusing questions and for being able to constantly motivate me to broaden my limited horizon, enabling me to grow. I am so grateful to Prof. Arno Kwade for examining this thesis. I want to say thank you to Martin Geier for being even more than an adviser, for being helpful with any questions, for his effective comments when I got stuck in the project, for editing this thesis and for the close and effective cooperation. Furthermore, I have a deep gratitude to Sebastian Geller for being supportive and for editing this thesis. I am thankful to all my colleagues, especially Maik Stiebler and Jannis Linxweiler. In addition, I acknowledge Kostyantyn Kucher for answering my programming questions. Certainly, I do express my gratitude towards all my friends understanding and encouraging me by making me laugh in the most serious situations.

I thank the Deutsche Forschungsgemeinschaft for financial support of the research training group FOR 856. I also thank Mr. Stefan Beinart for preparation of aggregate geometries used in our simulations. Mr. Thomas Gothsch provided the flow rate measurement and Mr. Rodrigo Segura prepared the PIV measurements.

Yet more importantly, I thank my parent and my brothers, Mohsen and Mojtaba for supporting me in terrible situations, standing up for me, respecting my decisions. I first learned the meaning of love and freedom important in my life from them. Thank you for all moments we have spent together. Moreover, I want to thank Shima Golmohammdi which was strongly affected during the writing of this thesis, for her patience.

Zussammenfassung

Die Erzeugung von Nanopartikeln aus größeren Aggregaten ist ein wichtiger industrieller Prozess insbesondere in den Lebenswissenschaften. In dieser Dissertation wird ein von der DFG-Forschergruppe FOR 856 mikroPART entwickelter Dispergierkanal mit Hilfe der Kumulanten-Lattice-Boltzmann-Methode numerisch untersucht. Die Aggregate werden als Partikel mit Masse und Strömungswiderstandsbeiwert modelliert. Sie zeichnen den Verlauf der Spannungen und den der Relativgeschwindigkeit zwischen Partikel und Fluid über die Zeit auf. Die Geschwindigkeiten und Spannungen werden mit Hilfe eines kompakten Interpolationsschemas zweiter Ordnung berechnet. Die Partikelsimulation wird in ein massiv-paralleles Mehrskalen-Lattice-Boltzmann-Framework eingebettet. Zur Validierung wird die Simulation des Dispergierkanals mit PIV- und Flussratenmessungen verglichen, die von Projektpartnern innerhalb der mikroPART-Forschergruppe durchgeführt wurden. Die Strömungswiderstandsbeiwerte der Aggregate werden durch umfangreiche Simulationen synthetischer Aggregate in einfachen Scherströmungen, Dehnströmungen und Rotationsströmungen ermittelt. Es wird ein empirischer Zusammenhang zwischen dem Strömungswiderstandsbeiwert und der Anzahl der Partikel im Aggregat sowie dessen fraktaler Dimension aufgestellt. Dieser wird in der Partikelsimulation des Dispergierkanals verwendet.

Die Simulation liefert verschiedene Masse für die Belastung der Aggregate, unter anderem die maximale Dehnung, die Einwirkzeit einer gegebenen Mindestdehnung und die Relativgeschwindigkeit der Partikel zu dem umgebenden Fluid. Es wird angenommen, dass keramische Aggregate brechen, wenn eine bestimmte Schwellendehnungsrate überschritten wird. Die Verteilung der maximalen von einem Aggregat erfahrene Dehnungsrate kann durch eine einfache exponentielle kumulative Wahrscheinlichkeitsverteilung ausgedrückt werden. In Verbindung mit dem Schwellenwert kann dieses reduzierte Modell zur Abschätzung der Wahrscheinlichkeit des Aggregatbruches nach n Durchquerungen des Dispergierkanals verwendet werden.

Es wird festgestellt, dass bei realistischen Aggregatsgeometrien (fraktale Dimension 1.85) typischerweise Stokeszahlen kleiner als eins auftreten, so dass der dominierende Lastmechanismus die Dehnung durch das umgebende Fluid ist. Im Gegensatz dazu treten bei kugelförmigen Partikeln (fraktale Dimension 3) Stokeszahlen größer als eins auf. Daher ist die Last aus der Relativgeschwindigkeit zu dem umgebenden Fluid nicht vernachlässigbar.

Abstract

The production of nano-particles from larger aggregates is an important industrial process, especially for life-science products. In this thesis a micro-machined disperser developed by the DFG Research Group FOR 856 mikroPART is studied numerically by the cumulant lattice Boltzmann method. The aggregates are modeled as tracer particles with mass and drag coefficient. They record the history of the stresses and the relative velocity of the aggregates with respect to the fluid. For the evaluation of the velocities and stresses a compact second-order interpolation scheme is utilized. The tracer particles are implemented in a massively parallel multi-resolution lattice Boltzmann framework. The simulation of the disperser is validated against PIV and flow rate measurements from collaborators in the mikroPART Research Group. The drag coefficients of the aggregates are obtained by detailed simulations of synthetic aggregates in simple shear flow, elongational flow, and rotational flow. An empirical relation between the drag coefficient and the number of primary particles in the aggregate and its fractal dimensions is found and used in the tracer simulation of the disperser.

Different measures of load on the aggregates are obtained by the simulation, for example maximal strain, exposure time to a certain strain, and relative velocity of the particles with respect to the surrounding fluid. It is assumed that ceramic aggregates break-up when they suffer a threshold strain rate. The distribution of the maximum strain rate seen by an aggregate can be condensed into a simple exponential cumulative probability distribution. Combined with a given threshold for the particle break-up this condensed model can also be used to determine the probability for aggregate breakage after n passages of the device.

It is found that aggregates with realistic geometry (fractal number 1.85) usually have Stokes numbers smaller than one such that the load on these aggregates is dominated by the strain in the surrounding fluid. This is in contrast to spherical particles (fractal number 3) that have Stokes numbers in excess of one such that the load from their relative velocity with respect to the surrounding fluid is not negligible.

Contents

List of Figures

List of Tables

Nomenclature

Abbreviations

ASD	Accelerated Stokesian dynamics
BGK model	Bhatnagar, Gross and Krook model
CDF	Cumulantive distribution function
CFD	Computational fluid dynamics
CGF	Cumulant generating function
CLBM	Cascade lattice Boltzmann method
DLA	Diffusion-limited aggregation
FCLBM	Factorized central lattice Boltzmann method
IBM	Immersed boundary method
LBM	Lattice Boltzmann method
LES	Large eddy simulation
MGF	Moment generating function
MRT model	multi-relaxation times model
PDF	Probability density function
PMF	Probability mass function
RLA	Reaction-limited aggregation
RNAS	Reynolds-averaged Navier Stokes
VirtualFluids	Lattice Boltzmann research code of IRMB

Greek symbols

ϵ	Turbulent dissipation rate	$m^2 \times s^{-3}$
γ	strain rate	s^{-1}
λ	Relaxation time	s^{-1}
μ	Dynamic viscosity	$kg \times s^{-1} \times m^{-2}$
Ω	Collision operator	
τ	Shear stress	$kg \times m^{-1} \times s^{-2}$
τ_l	Laminar shear stress	$kg \times m^{-1} \times s^{-2}$
τ_t	Turbulence shear stress	$kg \times m^{-1} \times s^{-2}$
${\tau_{ij}}^R$	Reynolds stress tensor	-
δ	Dirac delta	
μ_n	$k-th$ moment	
ν	Kinematic viscosity	$m^2 \times s^{-1}$
ν_t	Turbulent eddy viscosity	$m^2 \times s^{-1}$

Roman symbols

Δp	Pressure difference between inlet and out let of disperser	$kg \times m^{-1} \times s^{-2}$
ρ	Density	$kg \times m^{-3}$
c	Cumulant of distribution function	
D_f	Fractal dimension	-
e_n	Normal coefficient of restitution	-
e_{tz}	tangential coefficients of restitution	-
F_{prim}	Force on a primary particle of an aggregate	$kg \times m \times s^{-2}$
k	Central moment of distribution function	
N	Number of primary particles	-
R_e	Reynolds number	-

r_{CM}	Center of mass of the aggregate	m
r_{CM}	Radius of gyration	m
R_{gyr}	Radius of gyration	m
R_v	Volume equivalence radius	m
S	Magnitude strain rate	s^{-1}
S_t	Stokes number	-
s_{ij}	Strain rate component	s^{-1}
Δt	Lattice Boltzmann time step	s
Δx	Lattice Boltzmann grid spacing	s
C	Non-dimensional strain rate	-
c_s	Lattice Boltzmann speed of sound	$m \times s^{-1}$
f	Distribution function	
f^{eq}	Equilibrium distribution function	
$y+$	Non-dimensional wall-unit	-

1. Motivation and outline

1.1. Motivation

Recently, applications of micro-systems became a fundamental element of researches [2–4]. Micro-systems minimize required quantities and make processes economically efficient and environmentally friendly. Branches of process engineering, pharmaceutical industry and biotechnology, especially in the field of life-science products are some examples of implementations of micro-systems [5]. Drugs composed of aggregates consisting of a hundred nanometers or more in size are potential key factors in life-science products. An inappropriate size of the colloidal aggregates causes a reduction of the drugs effectiveness for patients. Therefore, having a desirable size of each drug component can help physicians to improve the patient's health effectively. An efficient way to achieve this is to use a micro-machined disperser to break-up large aggregates into suitable small-sized ones. This motivates to analyze a complex micro-system used for dispersion. The disperser has to be able to generate defined stresses (shear, elongational, turbulent flow) inside micro channel geometries designed to break-up nanoparticle aggregates [6].

Moreover, the use of high pressure in micro-systems is a vital factor in chemical, pharmaceutical, food and paint industry. Dispersion and emulsification processes related to agglomeration and aggregation are acquired by high pressure processes in nanoparticle production. The final diameter of aggregates is in the nanometer range. The reunion of primary particles is primarily due to Van der Waals forces leading to aggregations by sintering bridges or chemical bonds and forming clusters of a few hundred nanometers. These clusters need to be broken up in a dispersion process. Although many researchers have analyzed details of the mechanism of high pressure drop dispersion, some aspects such as small channel dimensions and high velocities as a result of high pressure drops imply extraordinary challenges for the modeling of the experimental setups hampering a complete analysis [7].

Besides, contrary to low pressure micro-systems with laminar flow, turbulent flow generated in high pressure micro-systems make the numerical simulations more challenging. Due to the concurrent presence of shear, elongational and turbulent stresses, identifying the primary dispersion mechanism and the actual place of aggregate's break-up is very demanding. There are various ways including experiments, analytical methods, and computational fluid dynamics (CFD) to explore the flow fields. However, the exact mechanism of the particle breakage is still unclear.

The process of manufacturing life-science products is often modeled by numerical methods to estimate results and assess the final product quality. In classical CFD methods, Navier-Stokes equations are usually solved to simulate the fluid dynamics in the disperser because other methods are either inaccurate or limited to specific ranges of fluid flow [8]. However, the lattice Boltzmann method (LBM) as an alternative method to solve fluid dynamic equations has recently been significantly improved [9] with respect to its capability of modeling weakly compressible turbulent flows. Its suitability for parallel hardware allows researchers to obtain solutions relatively fast. The cumulant LBM [10] used throughout this thesis as a new method reduces Galilean invariance problems as compared to previous LBM variants. This method is thus used to simulate fluid flow with high Reynolds numbers created in the disperser by high pressure gradients.

1.2. Outline

The main goal of this thesis is to quantify and model the break-up process of aggregates in a disperser. The obtained information is expected to be helpful to design a sophisticated disperser for increasing fragmentation rate of fragments and reducing the average aggregate's sizes.

The dispersion process of ceramic aggregates modeled as solid particles with mass and drag coefficient in a micro-machined disperser is simulated with the cumulant LBM. This thesis is organized into four parts. In the first part, an introduction is presented and previous related works in this field are listed. The cumulant LBM as the main solver is described in detail. In the second part, a parallel pathline algorithm is introduced and explained. In the third part, aggregates suspended in the flow are simulated and useful correlations between the hydrodynamic drag force and the number of primary particles are extracted. In addition, the hydrodynamic behavior of particles forming aggregates of a predefined structure is investigated in detail. In the fourth part, the complete dispenser is simulated. Moreover, different relations of break-up of aggregate mechanisms are proposed and the flow field for various pressure differences is analyzed in detail.

2. Introduction

The separation of aggregated particles in a fluid medium containing suspended particles of sizes smaller than ten microns plays a critical role in many industrial applications. Water treatment, crystallization (where aggregates are used as catalysts), food processing, biomechanics, and pharmaceutical process are prominent examples of the various fields in which breaking-up of aggregates and a tunable size of aggregates are important [11–13]. Properties of dispersed particles mainly depend on their size, shape and the carrier fluid media [8].

There are many definitions of an aggregate break-up. For example, break-up can be considered as the separation of pieces or fragments from a whole [14]. In addition, the destruction of the integrity of a system caused by forces is defined as a break-up [14]. Abrasion, cleavage and shattering are three main mechanisms for breaking-up aggregates [14]. These mechanisms depend on the input energy and the balance of the applied forces. If the energy intensity is not too large, small particles from the surface of the cluster are removed. This mechanism is known as abrasion. If energy increases such that a large aggregate is cleaved into smaller ones, being of comparable size as the whole, the cleavage break-up mechanism dominates. When many regions of an aggregate suffer much higher intensity than its breaking-up point, a shattering mechanism is observed. Then, the fragments have much smaller sizes than their parents [13].

Moreover, the system variables influence the break-up process [15]. For instance, the particle impact velocity on a surface which has been widely investigated by Brown [14] and Thornton [16] has significant effects on the break-up. The breakage of an aggregate in a single collision process has been modeled by Austin [17]. In this model, the impact energy and particle size are correlated to each other.

Numerous studies have been carried out to analyze the process of the break-up. However, most of them are limited to laminar flow conditions [14, 16, 18–20]. Specific flow geometries such as the so-called "elbows" lead to highly turbulent flows which are unique characteristics of these geometries, resulting in significant aggregate break-up rates [12, 21, 22].

The break-up of aggregates suspended in turbulent flows is assumed to occur due to shear effects [2]. Experimental work on breaking-up of aggregates into small particles under simple transversal shear and pure longitudinal shear in turbulent flow was conducted by Kao et al. [23]. After him, many experimental researches have been conducted to study break-up effects in detail [24–29]. Elongational flows are more effective for the break-up of aggregates than pure shear flow at the same energy dissipation rate [2, 30–32]. Therefore, more breakage of aggregates are observed in extensional flows. Fife et al. [33], Gregoriades et al. [2] and Ma et al. [34] investigated the break-up of nematodes and cells traveling through a nozzle. Parker et al. [35] developed floc break-up theories for complex sludge flocs. Yuan et al. [36] studied flocs under turbulent shear condition with a questionable particle geometry. In their study a relationship between the turbulent shear rate and the frequency of particle break-ups was proposed. Sonntag et al. [37] considered particles composed of deformable spheres in their research. Ellipsoidal particles were used by Blaser [25]. Parker et al. [35] used two-bead particles to propose a multi-body model. Higashitani [38] considered van der Waals forces between clusters of spherical particles adhered together to obtain improved results compatible with experimental data.

Break-up mechanisms have been widely investigated in experimental and numerical studies. For example micro-mechanical stretching was proposed by Yeung [39] and ultrasound and hydrodynamic methods were used by Gibson [3, 40] whereas large-scale fragmentation due to hydrodynamic forces was studied by Fernandes [41]. Generally, if the tension or force acting on the particle is larger than the yield strength of this particle or the internal bonding forces of the aggregate, breaking-up will occur. Nevertheless, this critical threshold shows a high degree of variability. Higashitani [42] showed that small aggregates have relatively more resistance than large aggregates. Yeung [39] and Gibson [3] also proved large aggregates to have more potential to break-up than small particles and that the rupture strength can decrease up to 10-fold with size.

Numerous researches were conducted with elbow, flanged elbow and pump leading to disruptive flow fields which have the potential to break-up aggregates and further influence aggregate's properties. In fact, forces created usually by the pressure drop [43] are driving the flow through a constriction or hole. The experimental analysis of turbulent micro-scale flows is difficult because of the limitation on the space available, the high velocities created inside the disperser, centrifuging entrance regions, installing cameras or other apparatus to measure particle size evolution are significantly difficult. The flow field inside the orifice and the main reasons of aggregates break-up can be simulated accurately at turbulent flow regimes by computational fluid dynamics (CFD). See e.g. Sonntag [37], Nguyen [44], Higashitani [38], and Zumaeta et al. [8]. Kobayashi [11], Zumaeta et al. [8], and Higashitani [38] showed permanent deformation on polymeric substances in the orifice flow. Some subsequent processes such as the separation of aggregates in sedimentation and filtration operations are influenced by various aggregate properties. Sedimentation is strongly increased by enlarging aggregate's size. Smaller aggregates produced by breaking-up large aggregates are more difficult to recover in sedimentation process and filter centrifuges as the settling rate is reduced for smaller aggregates.

All of the above references utilized the flow field intensity as the break-up criterion. They calculated the dissipation energy derived from strain rates of the fluid flow and proposed correlations to evaluate the aggregate breakage. The elongation of a droplet in orifice flow based on the experienced strain over a distance was studied by Galinat et al. [27]. A challenging question for investigators is whether the breaking-up occurs before, inside, or past the orifice. Sonntag, Russel [37] and Higashitani [42] identified the entrance of the orifice as the dominant location for break-up.

The correlation between the size reduction of the aggregates and various parameters such as pressure drop, kinetic energy, etc. has been widely investigated by many researchers. Flow intensity inside a given geometry strongly influences these parameters. Variation of pressure drop and kinetic energy versus drop breakage of aggregates studied by Galinat et al. [45], Scott et al. [29]. Moreover, flow pattern and the flow rate inside a variety of channel shapes were analyzed by James and Saringer [46]. They concluded that the pressure drop and the fluid pattern were strongly influenced by the geometry of the dispersers. Higashitani and Iimura [47] proposed a correlation between the number of primary particles of an aggregate and shear strain rates. Kobayashi [11] extended his method and correlated flow rate and break-up aggregate. They showed that with increasing shear strain rate or volumetric flow rate, large aggregates were broken up with a higher rate more often than small aggregates. Davies [48], Sonntag and Russel [37] and Zumaeta et al. [8, 49, 50] extended previous results with a new correlation between energy dissipation and floc breakage.

The CFD investigations outlined above were carried out by the direct discretization of the Navier-Stokes equations or turbulence models. Complementarily, the LBM was developed and used to simulate fluid flow in various fields such as; porous media [51, 52], fluid structure interaction [53], multi-phase flows [54, 55], turbulent flows [56, 57]. For the first time breaking-up of aggregates into the smaller fractions by shear stress created in turbulent flow is simulated by the cumulant LBM in this thesis.

A specific micro-machined disperser [58] is investigated in this thesis which is depicted in Fig. 2.1. Large aggregates are released in the left hand side in the flow and are passing through this disperser. The large aggregates are broken-up into smaller aggregates observed in the right hand side of this picture. The sudden decrease in the channel cross section in the orifice is intended to enlarge the shear rate experienced by the aggregates and thereby causing their break-up. The tracer simulation of the particles through the complete disperser is performed in addition to the flow simulations by the cumulant LBM.

Cavitation occurs when the pressure in the devices drops below the vapor pressure. Cavitation can damage the device due to the water hammer effect [59] when the vapor bubbles collapse. The water hammer effect may also help in breaking down aggregates. However, in the case of a continuously driven device, as in our case, where the big bubbles collapse

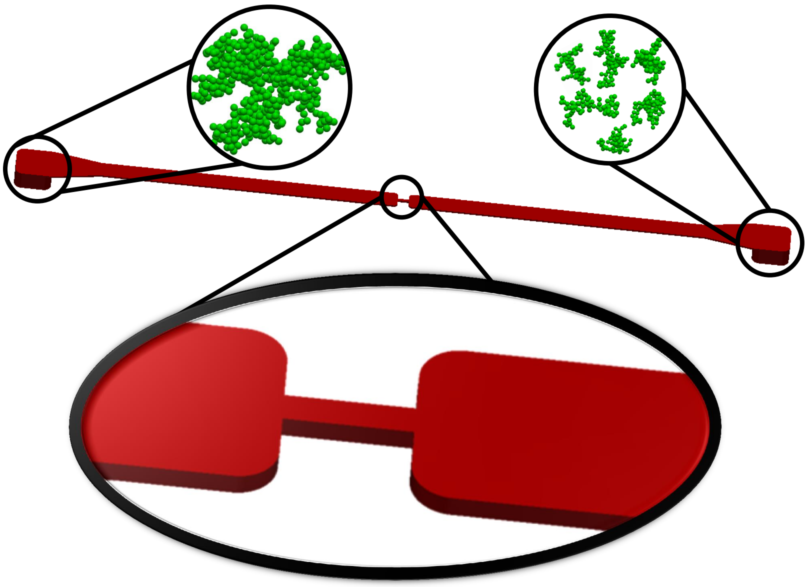

Figure 2.1.: Breaking-up of a big aggregate into smaller fractions by turbulent flow inside the micro-machined disperser (schematic).

only when the device is turned off, such a positive effect of cavitation cannot be expected. Cavitation can be avoided through a sufficiently high back pressure at the exit of the device. Here we assume that no cavitation occurs.

Although it appears as a widely accepted approximation to consider small aggregates as mass-less objects in a turbulent flow, this assumption will not hold for larger aggregates and thus their dynamics has to be studied including their inertia. With the advent of new computational methods such as the LBM and using parallel programming techniques, the simulation of the behavior of aggregates moving through the disperser is possible.

The effect of aggregates characteristics such as mass, fractal dimension on the aggregate breakage mechanism was not considered up until now. It was usually assumed that spherical-shaped aggregates following the flow are used. The aggregates can be broken-up by forces generated by the relative velocities between the aggregate and the surrounding fluid. The fractal dimension and the number of primary particles of aggregates cause the relative velocity to change. The use of the spherical-shaped aggregate assumption leads an overestimation of the relative velocity.

It is not possible to calculate exposure time to a certain load as an important parameter in the breakage process without considering the behavior of aggregates in CFD methods. Up to now, the relationship between the exposure time and the breakage was only proposed by researchers using experimental methods. Since in this thesis not only the flow intensity but also the behavior of aggregates is studied, we calculate the exposure time for the aggregates. Consequently, we propose both quantitative as well as simple model for exposure time versus breakage of aggregates.

All the aggregates in this thesis are considered to have mass, which introduces a drag force during their motion through the surrounding fluid. The drag coefficients are obtained by additional LBM-simulations on the aggregate scale. In fact, many simulations have been conducted for the aggregates suspended in a computational flow domain by the cumulant LBM to compute their drag properties. A body fitting grid refinement is used to reduce the cost of computation and increase computational performance. The Reynolds number is assumed to be small on this case.

To the best of the author's knowledge, in this thesis the effects of the fractal dimension and the number of primary particles related to the mass on the breakage of aggregates are investigated for the first time. Different groups of aggregates experiencing various drag forces are released into the turbulent flow and pass through the disperser. The particles record the complete history of tensorial stress experienced on their passage through the disperser. These simulations allow us to determine the relationships in the break-up process between the fractal dimension and the number of primary particles and the breakage of aggregates.

Finally, the data are condensed into a compact model predicting the probability that aggregates have experienced a certain amount of mechanical load. Compact second order interpolation is used for the integration of the particle pathlines and their recording of the local shear rate [60]. All new algorithms have been implemented within a massively parallel framework, VirtualFluids [61].

3. Fractal aggregates

The study of aggregate properties allows us to analyze and predict their behavior in different situations especially when hydrodynamic forces acting on the aggregates by the surrounding fluid are considered. Complex aggregates are characterized by a few specific parameters such as the fractal dimension and the gyration radius. In this chapter, they are briefly defined and their relationships are given. It is noted that usually the terms aggregate and agglomerate are widely interchanged in the literature although each term has a specific meaning. An aggregate is defined in the Oxford English Dictionary as "a mass formed by the union of individual particles; an assemblage, a collection" [62]. However, other references use different definitions for the word "aggregate" which are not compatible with the Oxford definition [63–66]. The Chamber Science and Technology Dictionary defines [63] an aggregate as an assemblage of particles which are loosely coherent. Gerstner [64] defines an aggregate as a combination of particles attached at their surfaces. In this thesis, an aggregate is defined as a cluster in which primary particles are connected to each other by strong chemical bonds due to sintering while in an agglomerate, primary particles are held together by weaker van der Waal forces.

One of the main characteristics of aggregates is the radius of gyration. The radius of gyration, basically, is the distance from the axis that all mass can be concentrated to obtain the same mass moment of inertia. Thus, the radius of gyration is the equivalent distance of the mass from the axis of rotation [67, 68].

$$R_{gyr}^2 = \frac{1}{N}\sum_i (r_i - r_{CM})^2 \tag{3.1}$$

where r_{CM} is the center of mass of the aggregate. The volume equivalence radius, R_v is another useful variable to characterize the aggregate and it is defined as the radius of a sphere with the same material volume as the aggregate. The radius of gyration, the volume equivalence radius, and the radius of a random aggregate are depicted in Fig. 3.1.

Mandelbrot [69] introduced the word "fractal" to characterize wrinkled objects like aggregates which are in a large range of length scales. Self-similarity is one of the important properties of the fractal aggregate and it means that a structure remains geometrically

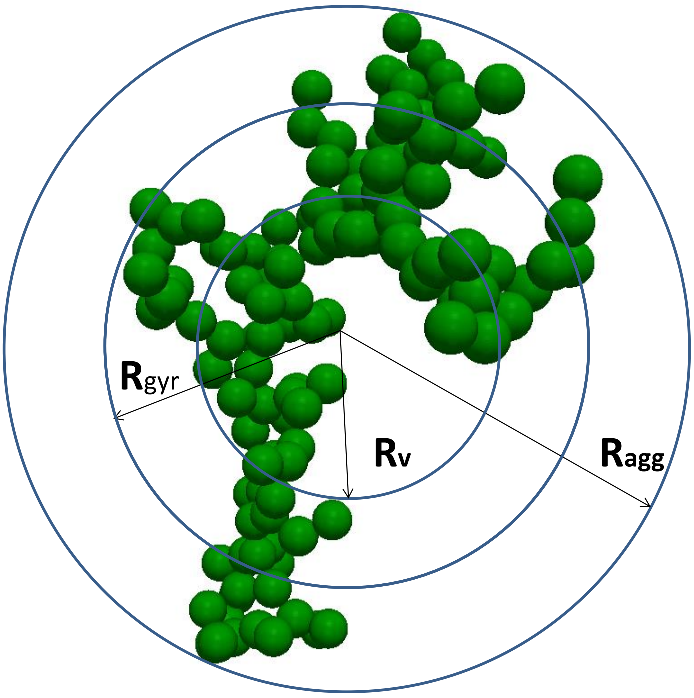

Figure 3.1.: Different types of radius for a random aggregate. The radius of gyration, the volume equivalence radius and radius of a random aggregate are shown as R_{gyr}, R_v and, R_{agg} respectively. The sizes of these radii are arbitrary demonstrated.

similar on different scales [70, 71]. In fact, there is a continuum of levels from a large structure down to individual primary particles in the self-similar aggregates. A distinguished property of self-similar fractal objects appears in the fractal dimension or the fractal exponent [69]. The degree of occupation of the embedding space is measured by the fractal dimension. If the particles are aligned in one dimension, the fractal dimension is one (D=1) and in a regular two dimensional array, the fractal dimension is two (D=2). In general, the fractal dimension is similar to the space dimension. However, a fractal aggregate has the lower fractal dimension than space dimension and may not be an integer. The formation mechanism and environment where aggregates are formed has a big effect on the fractal dimension of aggregates. For example, the fractal dimension is varied between 1 up to almost 3 in the astronomical environment.

The mechanism of growth determines the fractal dimension. Diffusion-limited aggregation (DLA) and reaction-limited aggregation (RLA) are two main categories of this mechanism. DLA happens when all collisions lead to a permanent bond while RLA occurs when a fraction of collisions results in irreversible adhesion. The collision mechanism can be divided into two main types; particle-cluster and cluster-cluster mechanism. In the following we try to briefly explain these mechanisms.

The fractal geometry was associated with particle clusters by Forrest and Witten [72]. A few years later, Witten and Sander proposed a simple model to simulate a diffusion-limited aggregation with a fractal structure [73, 74]. This is called particle-cluster diffusion limited aggregation. The procedure of building this aggregation model can be summarized in the following way [75]. The first particle of aggregate is located at the origin of the simulation domain. Then, a large circle in comparison to the resulted aggregate is drawn at the center. A second particle is released randomly in the circle and starts going on a random walk. The probability of adhesion is considered to be one, therefore, when the moving particle collides to the first particle, it stops its random walk and sticks permanently to the first particle. Now, the aggregate has two particles. In the same way, another particle is released in the circle to move randomly. When it reaches the aggregate, it stays there and so on.

Meakin [75] proposed an extension of the Witten-sander model which is called the cluster-cluster model. The collision between diffusing clusters is the basis of this model. A collection of equal sized particles located in a square box is considered at first. These particles undergo a diffusional random walk in the domain of simulation. When two particles collide to each other, they stick together to form a small cluster. Unlike the previous model, this cluster can move in the domain. Then, this cluster is able to stick to other clusters or a single particle. Larger clusters are created after each collision and this mechanism is pursued until a single large cluster remains in the domain [70, 76]. The information of the reaction-limited aggregation mechanism can be be found in [77].

A way for calculating the fractal dimension of aggregates formed by primary particles is to determine the slope of the log-log plot of the number of primary particles against the ratio of the radius of gyration to the radius of primary particle. This slope gives us the fractal dimension of aggregates. In other words, the number of primary particles N of aggregates with different sizes is related to its gyration radius R_g by the following equation [76]:

$$N = k_g \left(\frac{R_g}{R_p} \right)^{D_f} \tag{3.2}$$

where D_f is the fractal dimension of the aggregate, k_g is the coefficient that have been found empirically to be of order unity [78], and R_p is the radius of the primary particles. Fig. 3.2 shows aggregates with 160 primary particles with four different fractal numbers.

The aggregates used in the current study are produced by the particle-cluster diffusion limited aggregation mechanism such that the fractal dimension is kept constant while a

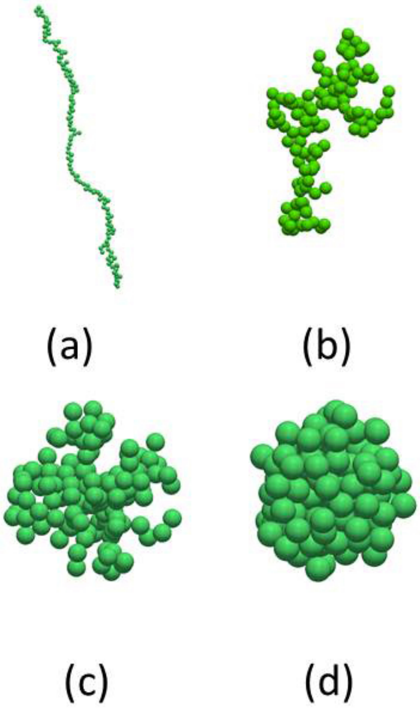

Figure 3.2.: Aggregates with 160 primary particles and 4 different fractal dimensions. (a) fractal dimension 1.2 (b) fractal dimension 1.85.(c) fractal dimension 2.3 (d) fractal dimension 2.8.

primary particle is added to the cluster. At first, a primary particle is placed in the center of the computational domain. Then, the second particle is added to the first particle so that its fractal number is equal to the given fractal number. This algorithm is repeated until the desired aggregate is governed. The fractal dimension of 1.85 with k_g 1.6 as depicted in Fig. 3.2,(b) is used in this thesis. All aggregates used in this thesis have been prepared by Beinart [4, 7].

4. The lattice Boltzmann method

In this chapter the main aspects of the LBM and more specifically the cumulant LBM are explained. The mathematical concept of the moment, the central moment and the cumulant are addressed in Appendix A. At the end of the chapter, the boundary conditions used are briefly introduced.

4.1. Lattice Boltzmann methods

The lattice Boltzmann method is an explicit time marching scheme for for a general class of advection-diffusion models, the most prominent one being the weakly compressible Navier-Stokes equations. This method is an alternative way for simulating fluid dynamics [79–82] and it is a mesoscopic method since it potentially includes finite Knudsen number effects. Therefore, probability density functions are used for the modeling of the momentum distribution in discrete space. Depending on how many directions or velocities in the momentum space for the moving particle are defined, different lattices are chosen. For example, for a 2D lattice, nine different directions can be chosen (Fig. 4.1). The stencil for this 2D lattice is D2Q9 [83]. In general, a stencil for a lattice can be defined as DdQq where d is the number of dimension and q is the number of the discrete velocity vectors. The isotropy of the second rank tensor [84] is a condition for a lattice to be valid for the Navier-Stokes equations. There are lots of velocity sets that satisfy this condition. They are chosen as a a compromising between efficiency and accuracy. In two dimensions, the most popular velocity set is D2Q9. In three dimensions, the stencils D3Q15, D3Q19 and D3Q27 are most popular. In this thesis, the stencil D3Q27 (Fig. 4.2) which can satisfy solutions in axis-symmetry problems especially in high Reynolds numbers is used for all simulations [61, 85, 86].

The lattice Boltzmann equation after discretization of a time-dependent Boltzmann equation without an external force can be written as [84]

$$f_i(x + e_{xi}c\Delta t, y + e_{yi}c\Delta t, z + e_{zi}c\Delta t, t + \Delta t) - f_i(x, y, z, t) = \Omega_i \tag{4.1}$$

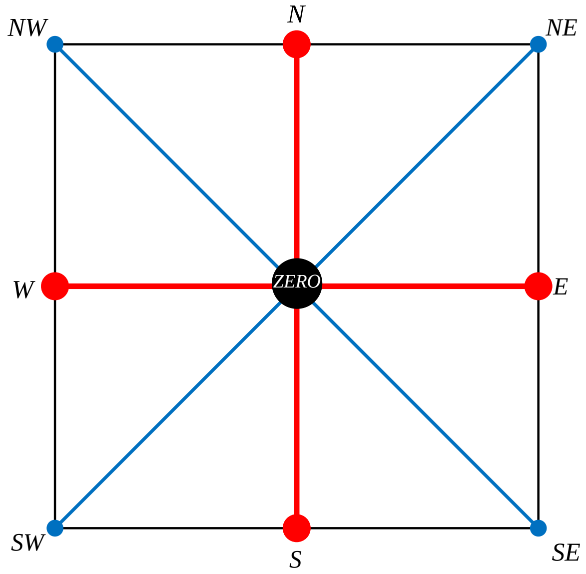

Figure 4.1.: Discrete velocities for the D2Q9 stencil.

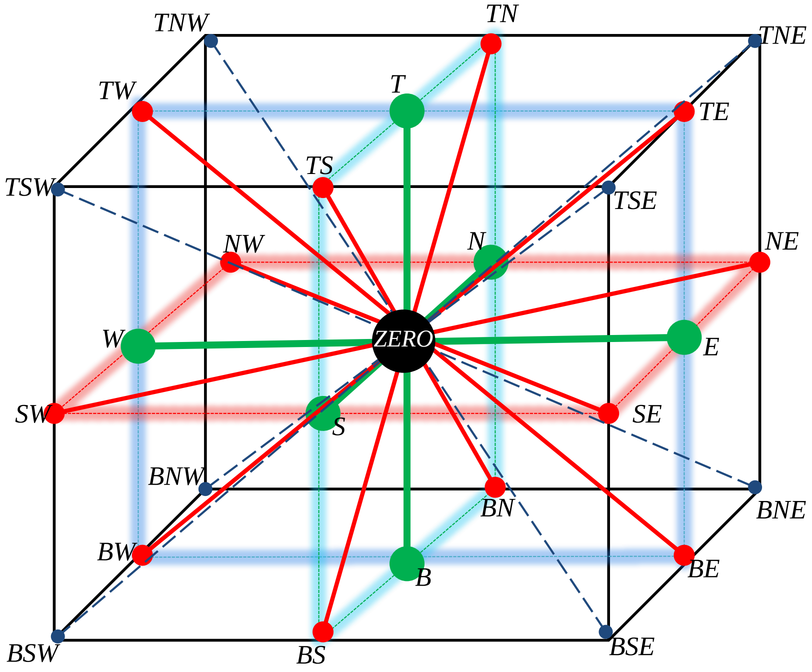

Figure 4.2.: Discrete velocities for the D3Q27 stencil.

where f_i and Ω_i are the discrete momentum distribution function and the collision operator, respectively. Here x, y and z are positions of the lattice node. The lattice speed $c = \frac{\Delta x}{\Delta t}$ is defined as the ratio of the lattice spacing to the time step such that the distributions are shifted by $e_{xi} c \Delta t$ from one lattice node to another one on a Cartesian grid during one time step. For example, the discretized microscopic velocities for the D3Q27 stencil are:

$$
\begin{aligned}
&e_i = \\
&i = 0, 1, ..., 15 = \left\{ \begin{array}{cccccccccccccccc} 0 & 1 & -1 & 0 & 0 & 0 & 0 & 1 & -1 & -1 & 1 & 1 & -1 & 1 & -1 & 0 \\ 0 & 0 & 0 & 1 & -1 & 0 & 0 & 1 & -1 & -1 & 1 & 0 & 0 & 0 & 0 & 1 \\ 0 & 0 & 0 & 0 & 0 & 1 & -1 & 0 & 0 & 0 & 0 & 1 & -1 & -1 & 1 & 1 \end{array} \right\} \\
&i = 16, ..., 26 = \left\{ \begin{array}{ccccccccccc} 0 & 0 & 0 & 1 & -1 & 1 & -1 & -1 & -1 & 1 & -1 \\ -1 & 1 & -1 & 1 & 1 & -1 & 1 & -1 & 1 & -1 & -1 \\ -1 & -1 & 1 & 1 & 1 & 1 & -1 & 1 & -1 & -1 & -1 \end{array} \right\}
\end{aligned}
\tag{4.2}
$$

The LBM consist of two steps [84]: collision and streaming. In the collision step, the local distribution function relaxes towards a quasi-equilibrium. In the streaming step, the distributions move to the neighboring nodes. The collision operator plays a key role for the accuracy and the stability of the method. With the proper collision operator, flow even with large Reynolds numbers can be simulated accurately. The local distribution function and the local equilibrium distribution function are acted on a collision operator set of functions to obtain a new local distribution. Bhatnagar, Gross and Krook (BGK) proposed a simplified model for the collision operator as [87]

$$
\Omega = -\frac{\Delta t}{\tau}(f_i(x, y, z, t) - f_i^{eq}(x, y, z, t)) \tag{4.3}
$$

where f^{eq} is the local equilibrium distribution function playing the role of an attractor during collision and τ is the LBM relaxation time [87].

The post-collision distributions are obtained with relaxing the pre-collision distributions towards the equilibrium distributions. This relaxation time approximation is used in almost all Lattices Boltzmann models. The BGK model using only one relaxation rate is not stable at high Reynolds numbers. The LBM is not completely incompressible and has a finite bulk viscosity which is a function of relaxation rate [9]. This bulk viscosity is responsible for damping pressure waves. Higher bulk viscosity leads to faster decay of pressure waves in the system. One relaxation rate is used for both the bulk and shear viscosity in the BGK model. Therefore, it is not possible to reduce the effects of pressure waves at high Reynolds numbers. This defect motivated researchers to use a LBM model with different relaxation rates called the multi-relaxation times (MRT) model [88]. The goal of using the MRT model is to maximize the number of adjustable parameters to increase both stability and accuracy. The MRT method is based on a linear transformation of the state of each node into equivalent moment space. Physical quantities are associated with moments. For example, the velocity is related to the first moment. In the MRT model, some relaxation parameters are chosen such that they satisfy the physical parameters of the fluid and some are selected to make the system more stable. The second group of parameters can increase or decrease the stability of the system by choosing different values. After the collision step, the moments are transformed back into the distribution space. Therefore, in the MRT model, the pressure waves can be effectively eliminated with selecting the bulk viscosity of the fluid much higher than its shear viscosity. The collision operator for the MRT model is given by [56, 88]:

$$\Omega = -M^{-1}S(Mf(x,y,z,t) - m^{eq}(x,y,z,t)) \tag{4.4}$$

where M is the transformation matrix, S is a diagonal matrix containing the relaxation rates s_i and m_{eq} are the equilibrium moments [88]. In the MRT model, the local distribution functions, f, are transformed to raw moments by multiplying them by the transformation matrix M. Then, they are relaxed by a diagonal matrix, S. In the end, they are transformed back by the inversion matrix of M. The MRT model is considerably more stable than the BGK model but still only partially suitable for turbulent flows [89].

Moments are taken in the rest frame of reference in the MRT method (Appendix A). Each unconsecrated moment is an observable quantity with a separated relaxation rate such that it is relaxed with its own rate. Thus, a violation of Galilean invariance generated for this method which is not observed in the BKG model with the same conditions [10].

The cascade lattice Boltzmann model (CLBM) as new a LBM scheme solves this problem. This model was developed by Geier [9, 90] to overcome previous LBM instability problems and modeling artifacts for simulation of fluid flow. Geier proposed that instead of performing the collision process in the rest frame of reference (such as in the MRT model), a frame of reference shifted by the macroscopic velocity should be used. This removes the insufficient degree of the Galilian invariant which is the main reason of the instability problems. In fact, Geier used a non-linear transformation of the distribution function into the frame of the moving fluid in the CLBM instead of the linear one used in MRT model to solve Galilean invariant problems. The moments calculated in the rest frame of reference are called raw moments and moments in the moving frame of reference are named central moments. Using central moments instead of row moments is the basis of the CLBM [91].

It is demonstrated in Appendix A that central moments of a given order are polynomial combinations of raw moments with lower or equal order. In fact, there is a one way influence of lower order raw moments on higher-order central moments and changing the central moments has no effect on the raw moments. It is also seen that in higher orders, central moments are dependent on the lower central moments. Thus, there is a structured sequential computation of relaxation in the CLBM [9].

4.1.1. The cumulant method for LB

The cascade LBM can be significantly improved with removing the effects of lower order moments on the higher order moments. This goal is achieved by using the cumulant method [10]. A transformation to a set of functions in which higher order moments are independent of lower order moments is defined. An efficient way to calculate cumulants is by utilizing central moments. It has been mentioned (Appendix A) that central moments are equal to cumulants up to third order and the first deviation is seen in the fourth-order. Seeger proposed a cumulant method for solving the Boltzmann equation [92, 93]. In the following part, the cumulant method for solving the LBM is described in detail.

The local momentum distribution function f_i in the LBM is assumed to be a probability mass function (PMF) consisting of three discrete random variables ξ, υ and ζ with following ranges corresponding to the normalized microscopic velocities in x, y, and z direction.

$$R_\xi = \{\xi_1, \xi_2, \xi_3...\} = \{e_{\xi 1}, e_{\xi 2}, e_{\xi 3}...\} \tag{4.5}$$

$$R_\upsilon = \{\upsilon_1, \upsilon_2, \upsilon_3...\} = \{e_{\upsilon 1}, e_{\upsilon 2}, e_{\upsilon 3}...\} \tag{4.6}$$

$$R_\zeta = \{\zeta_1, \zeta_2, \zeta_3...\} = \{e_{\zeta 1}, e_{\zeta 2}, e_{\zeta 3}...\} \tag{4.7}$$

thus, a probability density function (PDF) is defined as (Appendix A):

$$f(\xi, \upsilon, \zeta) = \sum_{ijk} f(\xi_i, \upsilon_j, \zeta_k)\delta(\xi - \xi_i)\delta(\upsilon - \upsilon_i)\delta(\zeta - \zeta_i) \tag{4.8}$$

The moments for this PDF can be calculated as:

$$\mu_{\xi^m \upsilon^n \zeta^l} = \int_{-\infty}^{\infty}\int_{-\infty}^{\infty}\int_{-\infty}^{\infty} f(\xi, \upsilon, \zeta)\xi^m \upsilon^n \zeta^l d\xi d\upsilon d\zeta \tag{4.9}$$

$$\begin{aligned}
\mu_{\xi^m \upsilon^n \zeta^l} &= \textstyle\int_{-\infty}^{\infty}\int_{-\infty}^{\infty}\int_{-\infty}^{\infty} \sum\limits_{ijk} f(\xi_i, \upsilon_j, \zeta_k)\delta(\xi - \xi_i)\delta(\upsilon - \upsilon_j)\delta(\zeta - \zeta_k)\xi^m \upsilon^n \zeta^l d\xi d\upsilon d\zeta \\
&= \textstyle\sum\limits_{ijk} f(\xi_i, \upsilon_j, \zeta_k) \int_{-\infty}^{\infty}\int_{-\infty}^{\infty}\int_{-\infty}^{\infty} \delta(\xi - \xi_i)\delta(\upsilon - \upsilon_j)\delta(\zeta - \zeta_k)\xi^m \upsilon^n \zeta^l d\xi d\upsilon d\zeta \\
&= \textstyle\sum\limits_{ijk} f(\xi_i, \upsilon_j, \zeta_k)(\xi_i)^m (\upsilon_j)^n (\zeta_k)^l
\end{aligned} \tag{4.10}$$

or

$$\mu_{\xi^m \upsilon^n \zeta^l} = \sum_{ijk} f(\xi_i, \upsilon_j, \zeta_k)(e_{\xi_i})^m (e_{\upsilon_j})^n (e_{\zeta_k})^l \tag{4.11}$$

The moment generating function allows to make distribution functions in the LBM independent of the frame of reference. The moment generating function for the LBM of $f(\xi, \upsilon, \zeta)$ can be calculated as:

$$M(\Xi, \Upsilon, \mathrm{Z}) = \int_{-\infty}^{\infty} \int_{-\infty}^{\infty} \int_{-\infty}^{\infty} f(\xi, \upsilon, \zeta) e^{\Xi\xi} e^{\Upsilon\upsilon} e^{\mathrm{Z}\zeta} d\xi d\upsilon d\zeta \tag{4.12}$$

$$\begin{aligned} M(\Xi, \Upsilon, \mathrm{Z}) &= \textstyle\int_{-\infty}^{\infty} \int_{-\infty}^{\infty} \int_{-\infty}^{\infty} \sum\limits_{ijk} f(\xi_i, \upsilon_j, \zeta_k) \delta(\xi - \xi_i) \delta(\upsilon - \upsilon_i) \delta(\zeta - \zeta_i) e^{\Xi\xi} e^{\Upsilon\upsilon} e^{\mathrm{Z}\zeta} d\xi d\upsilon d\zeta \\ &= \sum_{ijk} f(\xi_i, \upsilon_j, \zeta_k) \textstyle\int_{-\infty}^{\infty} \int_{-\infty}^{\infty} \int_{-\infty}^{\infty} \delta(\xi - \xi_i) \delta(\upsilon - \upsilon_i) \delta(\zeta - \zeta_i) e^{\Xi\xi} e^{\Upsilon\upsilon} e^{\mathrm{Z}\zeta} d\xi d\upsilon d\zeta \\ &= \sum_{ijk} f(\xi_i, \upsilon_j, \zeta_k) e^{\Xi\xi_i} e^{\Upsilon\upsilon_j} e^{\mathrm{Z}\zeta_k} \end{aligned} \tag{4.13}$$

or

$$M(\Xi, \Upsilon, \mathrm{Z}) = \sum_{ijk} f(\xi_i, \upsilon_j, \zeta_k) e^{\Xi e_{\xi i}} e^{\Upsilon e_{\upsilon i}} e^{\mathrm{Z} e_{\zeta i}} \tag{4.14}$$

where Ξ, Υ, and Z are the normalized wave numbers. The power of the exponential function has a non-dimension values. The moment generating function which is a two-sided Laplace transform of the distribution is a continuous function in the momentum wave numbers. Therefore, moments are obtained without any discontinuity problems. The moments can also be calculated by the moment generating function as:

$$\mu_{\xi^m \upsilon^n \zeta^l} = \frac{\partial^m \partial^n \partial^l}{\partial \Xi^m \partial \Upsilon^n \partial \mathrm{Z}^l} M(\Xi, \Upsilon, \mathrm{Z}) \bigg|_{\Xi = \Upsilon = \mathrm{Z} = 0} \tag{4.15}$$

The moments are relaxed toward their equilibrium states with their relaxation rates. For a model with stencil D3Q27, the moment distribution function can be matched with the Maxwellien equilibrium moments with twenty seven independent degrees of freedom. These collision operators are given by:

$$\mu^*_{\xi^m \upsilon^n \zeta^l} = \mu_{\xi^m \upsilon^n \zeta^l} + \omega_{\xi^m \upsilon^n \zeta^l} (\mu^{eq}_{\xi^m \upsilon^n \zeta^l} - \mu_{\xi^m \upsilon^n \zeta^l}) \tag{4.16}$$

The asterik here shows the post-collision state.

Each observable quantity is related to one moment in the LBM methods using more than one relaxation rate. Then, the relaxation rates can be chosen independently. This approach makes the LBM flexible and stable. However, including as many independent relaxation rates as possible is constrained by some properties of the system and the model. For example, the conserved quantities must be satisfied as well as rotational invariance of the model. Also, there are some freedoms to chose the moments that lead to different numbers of independent rotational invariant degrees of freedom. For instance, consider the third moments m_{120}, m_{102} and m_{012} as independent variables. Theses independent moments must be relaxed with different relaxation rates. However, constrains in the rotational invariant limit these three moments to have the same relaxation rate. If one set of these moments is devised as the combination of each moment such as $m_{120} + m_{102}$ and $m_{120} - m_{102}$, each set can have one independent relaxation rate because each of the two sets is not connected by the frame rotation anymore [10].

In the equilibrium state, all degrees of freedom must be statistically independent. Consequently, all random variables are independent. The joint probability for all degrees of freedom can be interpreted as a product of the individual variables or the independent degrees of freedom. The Maxwell distribution function has this property. The equilibrium distribution function is supposed to be a Maxwell distribution function which is a smooth and continuous function [10]. The moment generating function of the Maxwell distribution in three dimensions is:

$$M^{eq}(\Xi,\Upsilon,\mathrm{Z}) = \int_{-\infty}^{\infty}\int_{-\infty}^{\infty}\int_{-\infty}^{\infty} f^{eq}(\xi,\upsilon,\zeta)e^{\Xi\xi}e^{\Upsilon\upsilon}e^{\mathrm{Z}\zeta}d\xi d\upsilon d\zeta \tag{4.17}$$

where a Maxwell distribution function for three dimension is:

$$f^{eq}(\xi,\upsilon,\zeta) = \rho(\frac{1}{2\pi c_s^2})^{3/2} e^{-\frac{(c\xi-u)^2+(c\upsilon-v)^2+(c\zeta-w)^2}{2c_s^2}} \tag{4.18}$$

the equilibrium function is substituted into the moment generating function:

$$M^{eq}(\Xi,\Upsilon,\mathrm{Z}) = \rho(\frac{1}{2\pi c_s^2})^{3/2}\int_{-\infty}^{\infty} e^{-\frac{(c\xi-u)^2}{2c_s^2}+\Xi\xi}d\xi\int_{-\infty}^{\infty} e^{-\frac{(c\upsilon-v)^2}{2c_s^2}+\Upsilon\upsilon}d\upsilon\int_{-\infty}^{\infty} e^{-\frac{(c\zeta-w)^2}{2c_s^2}+\mathrm{Z}\zeta}d\zeta \tag{4.19}$$

after integration and simplification, a normalized Maxwell distribution function is:

$$M^{eq}(\Xi,\Upsilon,\mathrm{Z}) = e^{u\Xi/c+v\Upsilon/c+w\mathrm{Z}/c+\frac{c_s^2(\Xi^2+\Upsilon^2+\mathrm{Z}^2)}{2c^2}} \tag{4.20}$$

Now, the moments of the equilibrium are easily calculated by deriving the moment generating function, $M^{eq}(\Xi,\Upsilon,\mathrm{Z})$. The easiest way to calculate central moments used in the CLBM is to set the velocity equal to zero for all moments. Another way to calculate central moments is to shift the random variables with the local velocity u, v, w in three dimensions. A PDF for central moments can be written as:

$$f_c(\xi,\upsilon,\zeta) = \sum_{ijk} f(\xi_i,\upsilon_j,\zeta_k)\delta(\xi-(\xi_i-u/c))\delta(\upsilon-(\upsilon_i-v/c))\delta(\zeta-(\zeta_i-w/c)) \tag{4.21}$$

central moments can be calculated as:

$$k_{\xi^m \upsilon^n \zeta^l} = \int_{-\infty}^{\infty} \int_{-\infty}^{\infty} \int_{-\infty}^{\infty} f_c(\xi, \upsilon, \zeta) \xi^m \upsilon^n \zeta^l d\xi d\upsilon d\zeta \tag{4.22}$$

which can be rewritten as:

$$\begin{aligned}
&k_{\xi^m \upsilon^n \zeta^l} = \\
&\int \int \int \sum_{ijk} f(\xi_i, \upsilon_j, \zeta_k) \delta(\xi - (\xi_i - u/c)) \delta(\upsilon - (\upsilon_j - v/c)) \delta(\zeta - (\zeta_k - w/c)) \xi^m \upsilon^n \zeta^l d\xi d\upsilon d\zeta \\
&= \sum_{ijk} f(\xi_i, \upsilon_j, \zeta_k) \int \int \int \delta(\xi - (\xi_i - u/c)) \delta(\upsilon - (\upsilon_j - v/c)) \delta(\zeta - (\zeta_k - w/c)) \xi^m \upsilon^n \zeta^l d\xi d\upsilon d\zeta \\
&= \sum_{ijk} f(\xi_i, \upsilon_j, \zeta_k) (\xi_i - u/c)^m (\upsilon_j - v/c)^n (\zeta_k - w/c)^l
\end{aligned} \tag{4.23}$$

or

$$k_{\xi^m \upsilon^n \zeta^l} = \sum_{ijk} f(\xi_i, \upsilon_j, \zeta_k) (e_{\xi i} - u/c)^m (e_{\upsilon j} - v/c)^n (e_{\zeta k} - w/c)^l \tag{4.24}$$

The central moment generating function is acquired the same way as the raw moment generating function, as:

$$\widehat{M}(\Xi, \Upsilon, \mathrm{Z}) = e^{-\Xi u/c - \Upsilon v/c - \mathrm{Z} w/c} \sum_{ijk} f(\xi_i, \upsilon_j, \zeta_k) e^{\Xi \xi_i} e^{\Upsilon \upsilon_j} e^{\mathrm{Z} \zeta_k} \tag{4.25}$$

Therefore:

$$\widehat{M}(\Xi, \Upsilon, \mathrm{Z}) = e^{-\Xi u/c - \Upsilon v/c - \mathrm{Z} w/c} M(\Xi, \Upsilon, \mathrm{Z}) \tag{4.26}$$

Moreover, central moments can be directly obtained as:

$$k_{\xi^m \upsilon^n \zeta^l} = \frac{\partial^m \partial^n \partial^l}{\partial \Xi^m \partial \Upsilon^n \partial \mathrm{Z}^l} \widehat{M}(\Xi, \Upsilon, \mathrm{Z}) \bigg|_{\Xi = \Upsilon = \mathrm{Z} = 0} \tag{4.27}$$

It is easy to check the above equation by only calculating the first moment and see whether it is equal to zero or not.

$$\begin{aligned}
&k_1 = \tfrac{\partial}{\partial \Xi} \widehat{M} \Big|_{\Xi = 0} = \tfrac{\partial}{\partial \Xi} \left[e^{-\Xi u/c - \Upsilon v/c - \mathrm{Z} w/c} M(\Xi, \Upsilon, \mathrm{Z}) \right]_{\Xi = 0} = \\
&= \left[-(u/c) e^{-\Xi u/c - \Upsilon v/c - \mathrm{Z} w/c} M(\Xi, \Upsilon, \mathrm{Z}) + e^{-\Xi u/c - \Upsilon v/c - \mathrm{Z} w/c} \tfrac{\partial}{\partial \Xi} M(\Xi, \Upsilon, \mathrm{Z}) \right]_{\Xi, \Upsilon, \mathrm{Z} = 0} \\
&= -u/c + \mu_1 = 0
\end{aligned} \tag{4.28}$$

The cumulant generating function is (see Appendix A):

$$c_{\xi^m \upsilon^n \zeta^l} = \frac{\partial^m \partial^n \partial^l}{\partial \Xi^m \partial \Upsilon^n \partial \mathrm{Z}^l} \ln(M(\Xi, \Upsilon, \mathrm{Z})) \bigg|_{\Xi = \Upsilon = \mathrm{Z} = 0} \tag{4.29}$$

and the equilibrium value for the cumulant generating function is:

$$\begin{aligned} CGF^{eq} &= \ln M^{eq}(\Xi, \Upsilon, \mathrm{Z}) = \ln(e^{u\Xi/c+v\Upsilon/c+w\mathrm{Z}/c+\frac{c_s^2(\Xi^2+\Upsilon^2+\mathrm{Z}^2)}{2c^2}}) \\ CGF^{eq} &= u\Xi/c + v\Upsilon/c + w\mathrm{Z}/c + \frac{c_s^2(\Xi^2+\Upsilon^2+\mathrm{Z}^2)}{2c^2} \end{aligned} \tag{4.30}$$

Each relaxation process can be modeled for the cumulant with an independent rate ω as:

$$c^*_{\xi^m \upsilon^n \zeta^l} = c_{\xi^m \upsilon^n \zeta^l} + \omega_{\xi^m \upsilon^n \zeta^l}(c^{eq}_{\xi^m \upsilon^n \zeta^l} - c_{\xi^m \upsilon^n \zeta^l}) \tag{4.31}$$

where c_{eq} is the cumulants for the equilibrium state. Using cumulants instead of moments has the advantage that observable quantities can be separated from their rotational properties by combining the countable cumulants in various additive ways. This decouples e.g. shear viscosity from bulk viscosity.

4.2. Why do we use the cumulant LBM?

Although the cumulant LBM has been, in general, introduced and explained in the preceding sections, the significant advantages of this method has not been clarified yet. Most of the problems related to Galilean invariance have been solved by the CLBM. Thus, why do we use the cumulant LBM rather than the CLBM? To answer to this question, first of all, it must be mentioned that both methods are asymptotically equal and there is no obvious difference between the CLBM and the cumulant LBM in two dimensions. However, a significant difference is seen in three dimensions. The cumulants remove the violation of the Galilean invariance in both two and three dimensions. The asymptotic analysis (given in Appendix B) of the third order moment $\mu_{120+102} = \mu_{120} + \mu_{102}$ can be given by the following equivalent partial differential equation [10]:

$$\begin{aligned} &\bar{\mu}^{(3)}_{120+102} = \tfrac{2}{3}(\rho^{(0)}u^{(3)} + \rho^{(2)}u^{(1)}) + \rho^{(1)}u^{(0)}(v^{(1)}v^{(1)} + w^{(1)}w^{(1)}) \\ &-\tfrac{2\rho^{(0)}}{3}(\tfrac{1}{\omega_3} - \tfrac{1}{2})[v^{(1)}(\partial_x v^{(1)} + \partial_y u^{(1)}) + w^{(1)}(\partial_x w^{(1)} + \partial_z u^{(1)}) \\ &+w^{(1)}(\partial_y v^{(1)} + \partial_z w^{(1)}) + \tfrac{1}{3}(\tfrac{1}{\omega_1} - \tfrac{1}{2})(\partial_{yy}u^{(1)} + \partial_{zz}u^{(1)} + \partial_{xz}v^{(1)} + \partial_{xz}w^{(1)})] \end{aligned} \tag{4.32}$$

The shorthand $\bar{\mu}_{120+102}$ is the averaged moment of μ_{120} and μ_{102} ($\bar{\mu}_{120+102} = \frac{\mu_{120}+\mu_{102}}{2}$). The velocities $u^{(0)}$, $v^{(1)}$, and $w^{(1)}$ in the above equation imply that the Galilean invariance is not satisfied. This problem is solved by using central moments where the first moments are zero [10].

$$\begin{aligned} &\rho^{(0)}\bar{c}^{(3)}_{120+102} = \bar{k}^{(3)}_{120+102} = \\ &-\tfrac{2\rho^{(0)}}{9}(\tfrac{1}{\omega_3} - \tfrac{1}{2})(\tfrac{1}{\omega_1} - \tfrac{1}{2})(\partial_{yy}u^{(1)} + \partial_{zz}u^{(1)} + \partial_{xz}v^{(1)} + \partial_{xz}w^{(1)}) \end{aligned} \tag{4.33}$$

Up to this order, the central moments and the cumulants are identical and the CLBM and the cumulant LBM show the same behavior to simulate fluid flow. The stencil D3Q27 is a three dimensions model and moments with order four, five, and six have to be considered. Thus, the differences between the two methods become apparent in these cases. A main difference between the cumulant and the CLBM is found in the following example. The fourth and second order raw moments and central moments $\bar{\mu}^{(2)}_{221}$, $\bar{k}^{(2)}_{221}$, $\bar{\mu}^{(2)}_{011}$ and $\bar{k}^{(2)}_{011}$ are [10]:

$$\bar{\mu}^{(2)}_{221} = \frac{1}{3}(\rho^{(0)}v^{(1)}w^{(1)}) - \frac{\rho^{(0)}}{9}(\frac{1}{\omega_8} - \frac{1}{2})(\partial_y w^{(1)} + \partial_z v^{(1)}) \tag{4.34}$$

$$\bar{k}^{(2)}_{221} = -\frac{\rho^{(0)}}{9}(\frac{1}{\omega_8} - \frac{1}{2})(\partial_y w^{(1)} + \partial_z v^{(1)}) \tag{4.35}$$

$$\bar{\mu}^{(2)}_{011} = (\rho^{(0)}v^{(1)}w^{(1)}) - \frac{\rho^{(0)}}{3}(\frac{1}{\omega_1} - \frac{1}{2})(\partial_y w^{(1)} + \partial_z v^{(1)}) \tag{4.36}$$

$$\bar{k}^{(2)}_{011} = -\frac{\rho^{(0)}}{3}(\frac{1}{\omega_1} - \frac{1}{2})(\partial_y w^{(1)} + \partial_z v^{(1)}) \tag{4.37}$$

It is seen that the fourth order raw moments and central moments, $\bar{\mu}^{(2)}_{221}$, $\bar{k}^{(2)}_{221}$ are dependent on $\bar{\mu}^{(2)}_{011}$, $\bar{k}^{(2)}_{011}$ and a hyper-viscosity is created in the fourth order moment and central moment. These negative effects are removed by using cumulants. The fourth order cumulant $\bar{c}^{(2)}_{221}$and second cumulant $\bar{c}^{(2)}_{110}$ are [10]:

$$\bar{c}^{(2)}_{011} = -\frac{1}{3}(\frac{1}{\omega_1} - \frac{1}{2})(\partial_y w^{(1)} + \partial_z v^{(1)}) \tag{4.38}$$

$$\bar{c}^{(2)}_{211} = 0 \tag{4.39}$$

The hyper-viscosity is removed from equation 4.39 and the dependency of higher order to the lower order is minimized by using cumulants. These features of the cumulant LBM motivate researchers to use this method rather than other lattice Boltzmann methods.

4.3. The collision algorithm of the cumulant LBM

In this section, the procedure of the collision algorithm of the cumulant LBM is explained. This algorithm can be summarized into five main steps such that they must be carried out sequentially. The algorithm of this procedure is shown in algorithm 1.

Algorithm 1 The kernel algorithm of implementing the cumulant LBM. All the equations related to these five steps are given in Appendix C.

```
procedure PROCEDURE
loop over all computational nodes:
    (Step 1): obtain central moments from distributions
    (Step 2): calculate cumulants from central moments
    (Step 3): acquire post-collision cumulants from the collision operator
    (Step 4): extract post-collision central moments from the post-collision cumulants
    (Step 5): transfer back the post-collision central moments to the distributions
```

In this thesis, it is assumed that fluid is incompressible and thus, the LBM density, the zero moment, is equal to 1. The conservative moments are constant and are not changed during the transformation from central space to cumulant space, and vice versa. Therefore, their equations are not given in the Appendix. However, the effect of forces is only applied on these first moments as [10]:

$$u = m_{100} + F_x/2 \tag{4.40}$$

$$v = m_{010} + F_y/2 \tag{4.41}$$

$$w = m_{001} + F_z/2 \tag{4.42}$$

Steps one and five can be performed with 1/3 the number of operations in comparison with equations listed in the Appendix if we split equation 4.23 into three different directions [10]. Thus, step one can be performed by:

$$k_{ij|\gamma} = \sum_k f_{ijk}(\zeta_k - w/c)^\gamma \tag{4.43}$$

$$k_{i|\beta\gamma} = \sum_j k_{ij|\gamma}(\upsilon_j - v/c)^\beta \tag{4.44}$$

$$k_{\alpha\beta\gamma} = \sum_i k_{i|\beta\gamma}(\xi_i - u/c)^\alpha \tag{4.45}$$

and step five can be carried out in the same way and post-collision distributions are acquired three times faster than with direct computations [10]. It is noted that the final equations in both methods are the same and only the performance of the above method is three times faster than common computations.

There are 27 discrete velocities in the D3Q27 stencil and thus, the number of independent moments is limited to 27. This constraint causes higher order moments or cumulants to depend on the lower order ones. Therefore, Galilean invariance is violated. Moment μ_{300} is the first moment showing this dependency on lower order moment μ_{100}. Geier [10] proposed that correction terms including the derivative of velocities can be added to the second order moments to minimize this drawback. These terms are:

$$D_x u = -\frac{\omega_1}{2}(2c_{200} - c_{020} - c_{002}) - \frac{\omega_2}{2}(c_{200} + c_{020} + c_{002} + 1) \tag{4.46}$$

$$D_y v = D_x u + \frac{3\omega_1}{2}(c_{200} - c_{020}) \tag{4.47}$$

$$D_z w = D_x u + \frac{3\omega_1}{2}(c_{200} - c_{002}) \tag{4.48}$$

It is noted that the correction terms are obtained by known pre-collision cumulants. The modified post-collision cumulants are given by the following equations [10]:

$$c^*_{200} - c^*_{020} = (1 - \omega_1)(c_{200} - c_{020}) - 3(1 - \frac{\omega_1}{2})(u^2/c^2 D_x u/c - v^2/c^2 D_y v/c) \tag{4.49}$$

$$c^*_{200} - c^*_{002} = (1 - \omega_1)(c_{200} - c_{002}) - 3(1 - \frac{\omega_1}{2})(u^2/c^2 D_x u/c - w^2/c^2 D_z w/c) \tag{4.50}$$

$$\begin{aligned} c^*_{200} + c^*_{020} + c^*_{002} = \omega_2 + (1 - \omega_2)(c_{200} + c_{020} + c_{002}) \\ -3(1 - \tfrac{\omega_2}{2})(u^2/c^2 D_x u/c + v^2/c^2 D_y v/c + w^2/c^2 D_z w/c) \end{aligned} \tag{4.51}$$

The modified cumulants reduce the effect of non Galilean invariance in the system with little computational cost [10].

4.4. Propagation

As it is mentioned in the first section, the LBM consists of two main parts, collision and propagation. In the preceding sections the collision step which is the more complicated part is discussed and explained in detail. In the propagation part, particle distribution functions move to the neighboring nodes with their respective velocity. A simple algorithm can be defined for propagation as:

$$f_i(x + e_{xi}c\Delta t, y + e_{yi}c\Delta t, z + e_{zi}c\Delta t, t + \Delta t) = f_i{}^*(x, y, z, t) \tag{4.52}$$

It means that the post-collision distribution functions at position x, y, z and at time t are substituted into the neighbor's distribution functions in the next computational time step. At the first glance, two equal memories are required to allocate for distribution functions f and f^*. As long as a computation with the low number of nodes is performed, the necessity of the new technique using less memory is not felt. However, in most of the academic and industrial studies, high computational cost is demanded. Different schemes have been proposed to deal with this problem such as the AAP scheme [94].

Recently, a new sophisticated scheme named EsoTwist scheme [95] has been suggested. This is compatible with parallel computer architectures because of its thread-safeness. Linxweiler [96] showed the superior performance of this method in comparison with the common way. In this thesis the EsoTwist scheme is used to increase the performance of our computations.

4.5. Grid refinement method

Researchers have been looking for methods to decrease the cost of computations. For example, when they study turbulent flows, they must have a resolved domain to capture small vortexes. Moreover, when they deal with aggregates, enough resolution must be spent to calculate drag forces acting on each particle accurately. A big computational domain has to be considered to decrease boundary condition effects. Therefore, computational costs limit us to study these phenomena. One powerful method for the reduction of the cost of the computation is grid refinement. The grid refinement in the LBM like other computational methods causes the performance of computations to increase. Different methods have been proposed to carry out the grid refinement in the LBM [60, 97, 98]. In this thesis, the grid refinement proposed by Geier [60, 99] is used in three dimensions.

For the sake of simplicity only two grids are considered: the coarse grid and fine grid. An overlapping area including both kinds of grids is defined. The fine grid has twice the grid resolution of the coarse grid. A schematic of an interface between the fine and coarse grid is shown in the Fig 4.3. Unknown distributions of fine nodes (yellow nodes) are obtained by using distributions of known red nodes when interpolation from coarse nodes to fine nodes is required. The fine nodes are directly placed onto the coarse nodes in the prevalent grid refinement technique. Consequently, various schemes are used to recover different nodes in the interface. An interpolation scheme for time must be considered as well. In this new method, however, the center of the coordinate system is in the center of the cell in both two and three dimensions. The fine grid is located in the constant offset $\Delta_c/4$ in x, y, and z directions from the corner of the coarse cell. This offset results in a concise interpolation scheme between different resolutions. Time interpolation is not required anymore and only interpolation in a space is left.

Fig. 4.4 shows a magnification of a coarse to an fine interpolation zone in two and three dimensions. The size of the grid spacing in the coarse and fine level are Δ_c and Δ_f, respectively. Eight fine nodes are at the boundary of the fine cell (Fig. 4.4) and they are surrounded by eight coarse nodes (red nodes). Information stored in the coarse nodes is used to calculate required information in the fine nodes. The procedure of interpolation from fine to coarse is the same as the coarse to the fine interpolation (Fig. 4.5). One

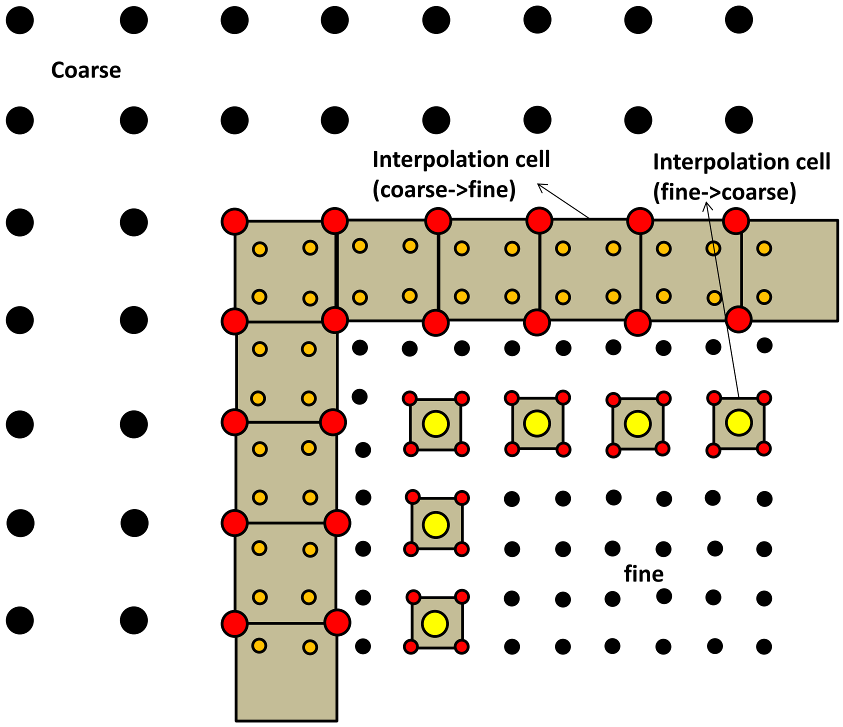

Figure 4.3.: A schematic of an overlapping interface between the fine and coarse grid. Distributions of yellow nodes which are unknown nodes are calculated by Red nodes which are known nodes in an interpolation process in both coarse and fine grids. Black nodes are not taken apart into the interpolation processes.

coarse node is surrounded by eight fine nodes and its information is obtained by the use of these eight fine nodes. It is noted that the center of the coordinate system is in the center of the coarse.

In the common grid refinement of the LBM, distribution functions are interpolated in the grid interface from the coarse to the fine and, vice versa. However, we use another approach in which the fluid dynamic quantities are utilized instead of using distributions directly. This method splits distributions into the equilibrium part and the non-equilibrium part. The equilibrium distribution functions depend on the velocities and pressure. The gradients of velocities determines the non-equilibrium distribution functions. In chapter 5.2 we show that this method has the second order accuracy in comparison to the linear interpolation which has the first order accuracy.

A polynomial function (bubble function with compact interpolation) [99] for the interpo-

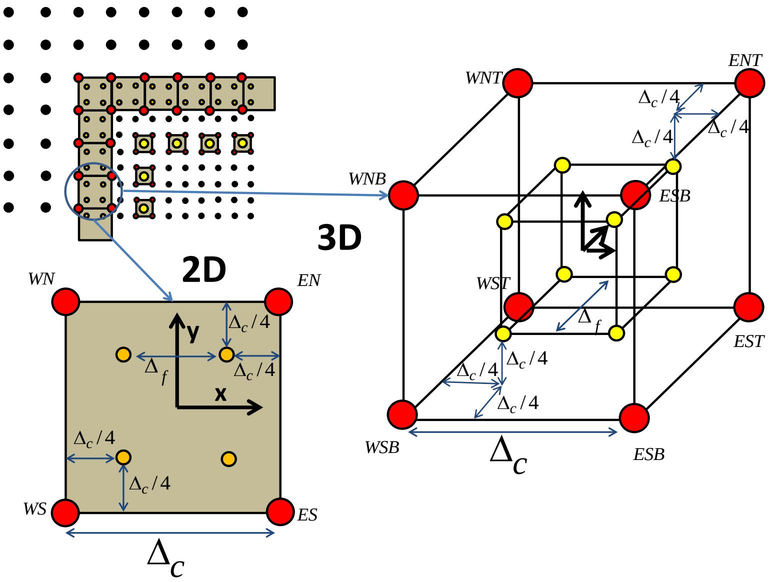

Figure 4.4.: A coarse to fine interpolation zone in two and three dimensions. Yellow nodes are unknown nodes and red nodes are known nodes in an interpolation process in both coarse and fine grids. Block nodes are not taken apart into the interpolation processes

lation with the second order accuracy in x, y, and z directions can be given by:

$$u(x,y,z) = a_0 + a_x x + a_y y + a_z z + a_{xx}x^2 + a_{yy}y^2 + a_{zz}z^2 + a_{xy}xy + a_{xz}xz + a_{yz}yz + a_{xyz}xyz \tag{4.53}$$

$$v(x,y,z) = b_0 + b_x x + b_y y + b_z z + b_{xx}x^2 + b_{yy}y^2 + b_{zz}z^2 + b_{xy}xy + b_{xz}xz + b_{yz}yz + b_{xyz}xyz \tag{4.54}$$

$$w(x,y,z) = c_0 + c_x x + c_y y + c_z z + c_{xx}x^2 + c_{yy}y^2 + c_{zz}z^2 + c_{xy}xy + c_{xz}xz + c_{yz}yz + c_{xyz}xyz \tag{4.55}$$

The coefficients of the bubble function are functions of the distributions. The velocity of each point inside the interpolation cell is easily calculated by using equations 4.53 to 4.55 [99]. The equilibrium distribution functions are not only dependent on velocities but also on pressure. Thus, we have to interpolate the pressure for the nodes inside the cell. A trilinear interpolation scheme is used for calculating the pressure [99].

4.6. Boundary conditions

Boundary conditions play a key role in numerical methods such as the LBM. They have profound effects on the results if they are not well defined. Since different simulations

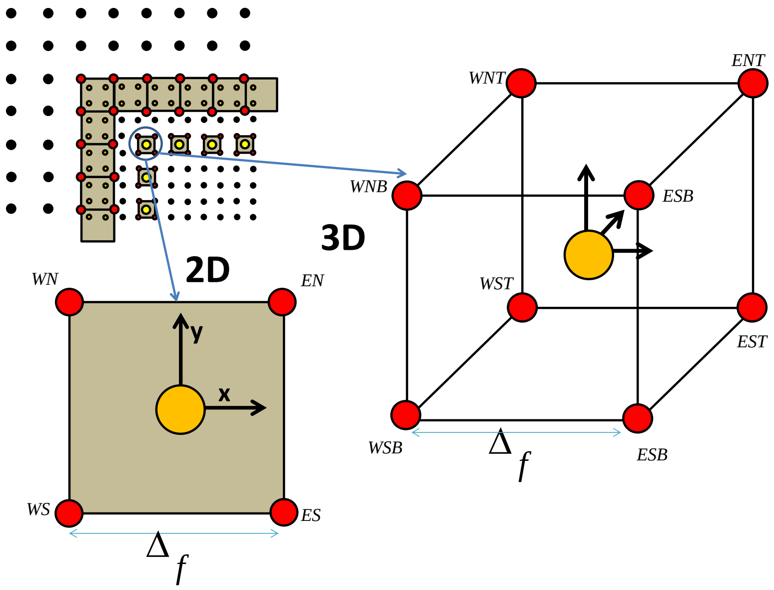

Figure 4.5.: A fine to coarse interpolation zone in two and three dimensions.Yellow nodes are unknown nodes and red nodes are known nodes in an interpolation process in both coarse and fine grids. Block nodes are not taken apart into the interpolation processes

have been carried out in this thesis, different boundary conditions are utilized. In general, boundary conditions in this method are applied after collision.

The boundary condition which does not allow fluid to slip on or enter in the solid surface is commonly called the no slip boundary condition. This boundary condition can be applied on walls, obstacle suspended in the fluid, or on any solid nodes in the simulation. The simplest form of this boundary condition in the LBM is the so-called bounce-back scheme [97]. However, this is not accurate enough at curve walls since the real distance of the wall to the closest computational grid node is not considered. Therefore, different boundary conditions with higher accuracy have been proposed [97, 99, 100]. These boundary conditions consider the distance of the closet lattice node to the wall and use an interpolation method to recover the desired distributions. At least two nodes in the common interpolation methods are exploited. A drawback of these methods appears when aggregates are studied with the LBM [101, 102]. The computation cost limits us to increase the ratio of the primary sphere to the lattice cell size. Thus, it can happen that a fluid node is located between two solid nodes. Consequently, adequate information for the interpolation is not available. Geier [99] suggested a new scheme to remove this problem. It only uses one fluid node for interpolation. Moreover, this method is compatible with our propagation

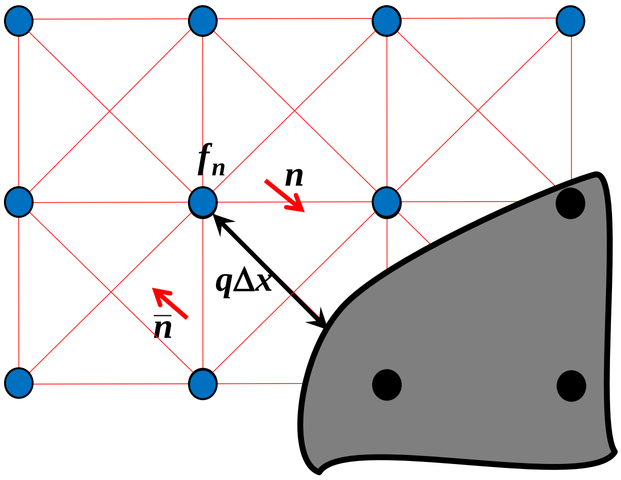

Figure 4.6.: A schematic of the implemented boundary condition.

algorithm. This method is given by:

$$f_{\bar{n}}(t+\Delta t)=\frac{1-q_n}{1+q_n}\frac{f_n^*(t)-\omega f_n^{eq}(t)}{1-\omega}+\frac{q_n}{1+q_n}(f_n^*(t)+f_{\bar{n}}^*(t)-2w_n\mathbf{u}\cdot\mathbf{e}_n/c_s^2) \qquad (4.56)$$

where ω is the relaxation parameter and q is the distance ratio of the node-wall to the node-node distance in the special direction. Fig. 4.6 shows a schematic of this method. The distribution entering to the wall has the flag n while returning back is assigned by $\bar{n}$. The velocity of wall is given by $\mathbf{u}$ and w is the weight factor of the link in the LBM. If the solid wall does not move, its velocity is zero.

The slip boundary condition is another type of boundary conditions which is used for far field conditions. The velocity in the last grid node is calculated in this method and its tangential component is imposed in to the above equation as the wall velocity. The same equation is applied for the velocity inflow boundary condition with the velocity substituted in the above equation as a given value. The pressure boundary condition is a sensitive boundary condition in the LBM especially for high Reynolds number flows. The use of non-equilibrium distributions in the last grid nodes gives more accurate results but it is not necessarily stable. Therefore, equilibrium distributions are used to satisfy the pressure boundary condition in this thesis.

4.7. Parallel computation

A sophisticated objected oriented code executed in parallel on CPU-cluster is used for the implementation of all the simulations in this thesis. It is called VirtualFluids. The code is run in the HPC cluster LUDWIG from TU Braunschweig including 1400 CPU cores. It was developed and extended at IRMB. The parallelized code employs MPI communication and utilizes a hybrid block data structure enabling us to partition the computational domain according to blocks rather than to nodes. Therefore, a massive datasets can be implemented. A METIS partitioning with load balancing is exploited to divide our computational domain between different processes. The explained grid refinement is added to the code using hierarchical block grids to improve the flexibility and decrease the computational costs. An example of METIS partitioning applied in the micro-machined disperser is demonstrated in Fig. 4.7. A process containing at least one block has its own rank. Each square in this figure represents a block including 16^3 grid nodes. In the micro-machined disperser model 960 processes are used for the simulation with 100 bar pressure drop. Two different views x-y and x-z are depicted in the figure, respectively.

4.8. Turbulent flow

Since a particularly efficient way is available in the LBM to compute the strain rate tensor, this model is widely used by researchers working on the LBM [56, 103, 104]. In fact, the strain rate tensor related to the Smagorinsky model [105] is calculated by the use of non-equilibrium components of the distribution functions in the LBM, $f^{neq} = f - f^{eq}$. The following equation derived from the asymptotic analysis helps us to avoid using the finite difference method for calculating s, [103].

$$s = \frac{-\omega}{2\rho c_s^2} \sum (f - f^{eq}) c_{i\alpha} c_{i\beta} \tag{4.57}$$

Uphoff [89] has compared the CLBM and the factorized central LBM (FCLBM) which do not use additional turbulent viscosity [106] with the MRT utilizing Smagorinsky model for a jet flow. Her results show a good agreement between these two different methods. The cumulant LBM inheriting the main positive characteristics of the CLBM has recently been investigated by Geier [10]. Different methods of the LBM are compared with the cumulant LBM in a turbulent flow in his work. The given results are in the close agreement in comparison to the other methods. The cumulant LBM is similar to

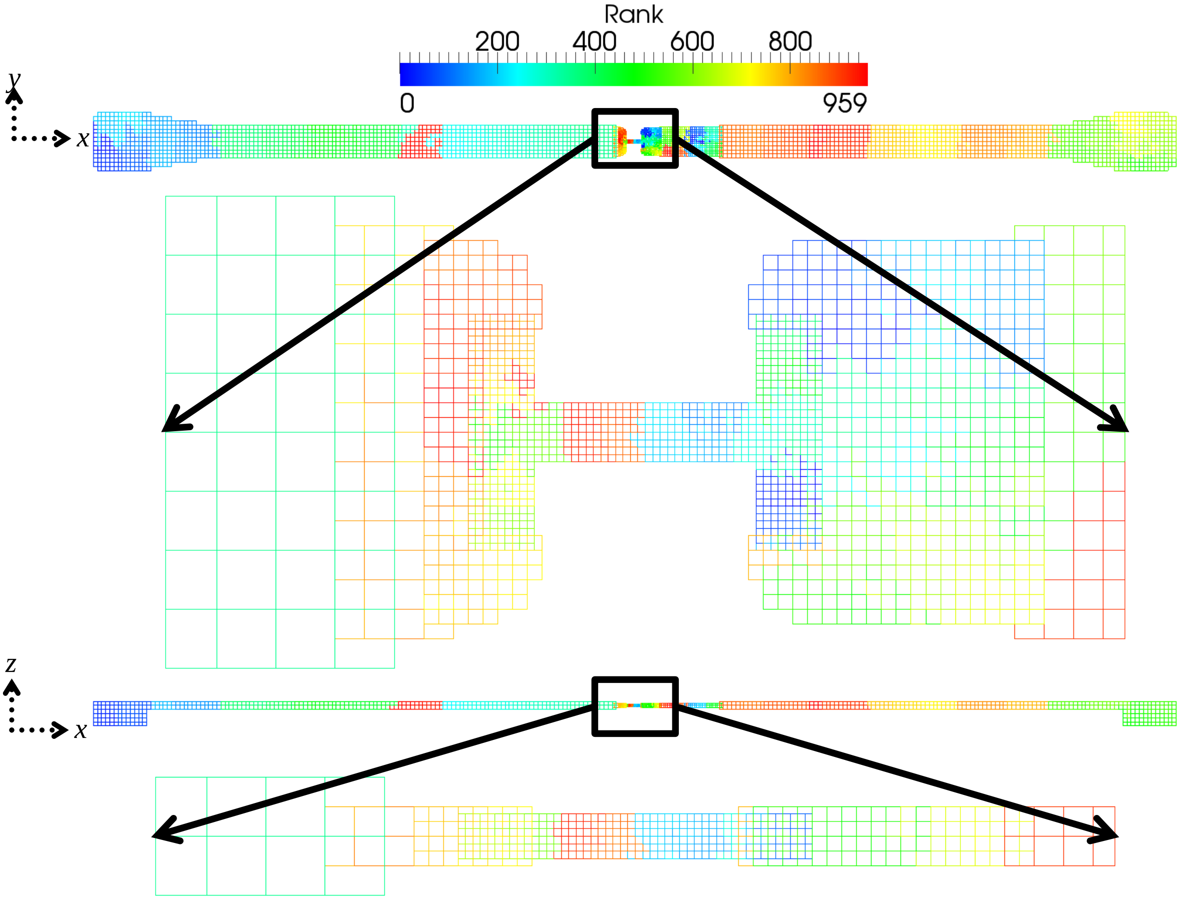

Figure 4.7.: METIS partitioning of the micro-machined disperser in two different views x-y and x-z. Each block has a rank. Each square has 16^2 nodes (in 3D, a cube has 16^3 nodes). The pressure drop is 100 bar.

the large eddy simulation (LES) method [105, 107] because only large eddies are explicitly resolved. However, unlike the LES, an additional turbulent viscosity is not required to be added to the molecular viscosity in the cumulant LBM [57, 90, 108] as long as sufficient resolution is implemented. The reason is that this method removes the instability problems originated by non Galilean invariance and makes the simulation stable even for large Reynolds number [9].

5. Pathlines

5.1. Introduction to pathlines

Streamlines and pathlines are convenient tools to describe and visualize flow fields in the computational domain [43]. A streamline is tangential to the velocity vector at every point in the flow at a given instant in time. In fact, a streamline shows the direction of a fluid element traveling at any point in space. Fig 5.1 shows an example of streamlines in a laminar flow close to the wall. Two streamlines never intersect each other because the instantaneous velocity vector at any given point is unique. The definition of streamline leads to the following equation [43]:

$$\frac{dx}{u(x,y,z)} = \frac{dy}{v(x,y,z)} = \frac{dz}{w(x,y,z)} \tag{5.1}$$

where u, v, and w are the velocity components in x, y, and z directions, respectively. A pathline is the actual path traveling by an individual fluid particle over a time period. Pathlines can be traced by injecting a dye into the fluid and following its path by photography. A schematic of pathlines is shown in Fig 5.2. Two pathlines can intersect each other as two particles, for example, can arrive at the same point at different instants of time. The pathlines are solutions of the equations [43]:

$$\frac{dx}{dt} = u(t,x,y,z), \ \frac{dy}{dt} = v(t,x,y,z), \ \frac{dz}{dt} = \mathrm{w(t,x,y,z)} \tag{5.2}$$

Pathlines are used in computational fluid dynamics to record the properties of fluid over a period of time. This tool allows us to obtain important data which can not be easily obtained with experimental methods. For example, in a turbulent flow, experimental results are barely able to estimate instantaneous velocities of a moving particle in a complex setup. We use pathlines to trace shear stresses and velocity of fluid particles over some period of time. In this chapter, we first show how to calculate the velocity of particles by the use of an interpolation method and then show the accuracy of the used interpolation method. Moreover, the procedure of implementation of pathlines is described in detail.

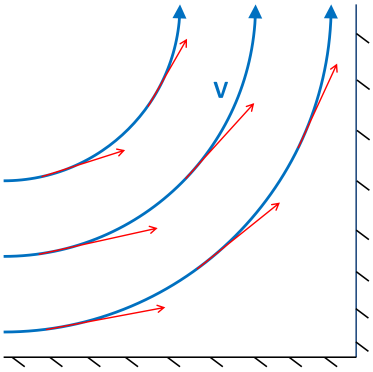

Figure 5.1.: A schematic of streamlines in a laminar flow close to the wall.

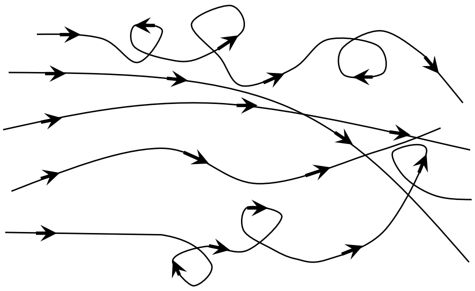

Figure 5.2.: A schematic of arbitrary pathlines in a flow field.

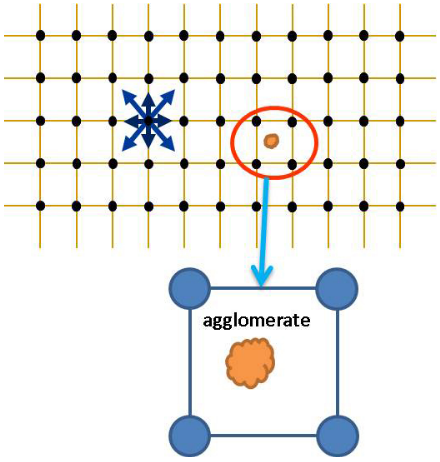

Figure 5.3.: Typical aggregate location in the lattice Boltzmann grid.

5.2. Interpolation methods for pathlines

Let us start calculating the pathlines by solving the partial diferential equations 5.2. Particles move from one point to another point with a known velocity in a period of time. Thus, velocities must be known in the above equations. Since the particle position, in general, does not coincide with the grid nodes of the LBM, interpolation in space is required to obtain the local fluid velocity. In addition, because the spatial derivatives of velocity in the particles position to compute the shear stresses imposed on the aggregate are needed, the interpolated velocity has to be at least second-order accurate. This velocity is obtained by using the interpolation method defined in the last chapter. This method has second-order accuracy for the velocity at low computational cost. Fig 5.3 shows a schematic of the particle (aggregate) movement in the LBM grid. The velocities of the particle at any position are calculated by equations 4.53 to 4.55 after knowing all coefficients in these equations. Heun's method [109] which is a modified Euler's method with second-order accuracy is used to discretize and solve equation 5.2. The intermediate value $\overrightarrow{\tilde{x}_{i+1}}$ in this method is calculated and then, the corrected value $\overrightarrow{x_{i+1}}$ at the next integration point is obtained. This method is given by following equations:

$$\begin{aligned} \overrightarrow{\tilde{x}_{i+1}} &= \overrightarrow{x_i} + h\overrightarrow{u'}(t_i, \overrightarrow{x_i}) \\ \overrightarrow{x_{i+1}} &= \overrightarrow{x_i} + \tfrac{h}{2}(\overrightarrow{u}(t_i, \overrightarrow{x_i}) + f(t_{i+1}, \overrightarrow{\tilde{x}_{i+1}})) \end{aligned} \tag{5.3}$$

The next position of the moving particle is acquired by using above equations.

The Taylor Green [110] flow which is a typical benchmark in computational fluid dynamics is implemented using the Cumulant LBM to show the accuracy of the pathline integration.

Velocities and the pressure are given for the Taylor Green flow as:

$$u = U_{\max}\sin(2\pi x/L_x)\cos(2\pi y/L_y) \tag{5.4}$$

$$v = -U_{\max}\cos(2\pi x/L_x)\sin(2\pi y/L_y) \tag{5.5}$$

$$w = 0 \tag{5.6}$$

$$P = U^2{}_{\max}(\rho_0/4)[\cos(4\pi x/L_x) + \cos(4\pi y/L_y)] \tag{5.7}$$

where $L_x = L_y = L$ are the lengths of the computational domain in the simulation and $U_{\max}$ is the maximum velocity calculated by the following equation:

$$U_{\max} = \frac{\mathrm{Re}\nu}{L} \tag{5.8}$$

here Re and ν are the Reynolds number and the kinematic viscosity, respectively. An external force is applied to the computational domain to keep the fluid flow in the simulation constant:

$$F_x = 2U_{\max}\rho\nu(2\pi/L)^2 sin(2\pi x/L)\cos(2\pi y/L) \tag{5.9}$$

$$F_y = -2U_{\max}\rho\nu(2\pi/L)^2\cos(2\pi x/L)\sin(2\pi y/L) \tag{5.10}$$

$$F_z = 0 \tag{5.11}$$

where ρ is the density of the fluid. The D3Q27 model of the LBM and a domain with $129 \times 129 \times 129$ nodes are used. The lattice Boltzmann viscosity and Reynolds number are chosen as 0.005 $\Delta x^2/\Delta t$ and 15, respectively. The x-velocity contour and pathlines in the Tayler Green vortex flow are depicted in Fig. 5.4. The fluid flow in the computational domain is divided into 4 subdomains. A massless particle is located randomly in one of these subdomains and starts moving in the transient flow. The non-dimensional transient shear stress ($\frac{\tau L}{\mu U_{\max}}$) is recorded for each particle position using a bilinear and a compact interpolation method (i.e. the explained bubble function in the previous chapter [99]). We calculate shear stresses according to the following equations which are the derivatives of equations 4.53 to 4.55.

$$\tau_{xx} = \mu(\frac{\partial u}{\partial x} + \frac{\partial u}{\partial x}) = 2\mu(a_x + 2a_{xx}x + a_{xy}y + a_{xz}z + a_{xyz}yz) \tag{5.12}$$

$$\tau_{yy} = \mu(\frac{\partial v}{\partial y} + \frac{\partial v}{\partial y}) = 2\mu(b_y + 2b_{yy}y + b_{xy}x + b_{yz}z + b_{xyz}xz) \tag{5.13}$$

$$\tau_{zz} = \mu(\frac{\partial w}{\partial z} + \frac{\partial w}{\partial z}) = 2\mu(c_z + 2c_{zz}z + c_{xz}x + c_{yz}y + c_{xyz}xy) \tag{5.14}$$

$$\tau_{xy} = \mu(\frac{\partial u}{\partial y}+\frac{\partial v}{\partial x}) = \mu((a_y+2a_{yy}y+a_{xy}x+a_{yz}z+a_{xyz}xz)+(b_x+2b_{xx}x+b_{xy}y+b_{xz}z+b_{xyz}yz)) \tag{5.15}$$

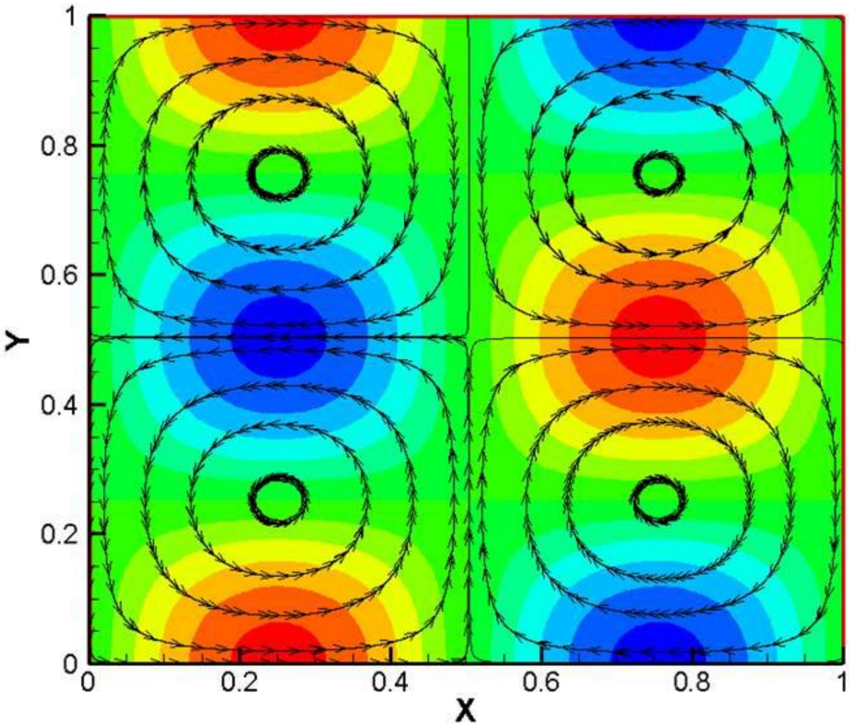

Figure 5.4.: Contour of x-velocity and streamlines in Tayler green vortex flow.

$$\tau_{xz} = \mu(\frac{\partial u}{\partial z}+\frac{\partial w}{\partial x}) = \mu((a_z+2a_{zz}z+a_{xz}x+a_{yz}y+a_{xyz}xy) + (c_x+2c_{xx}x+c_{xy}y+c_{xz}z+c_{xyz}yz)) \tag{5.16}$$

$$\tau_{yz} = \mu(\frac{\partial v}{\partial z}+\frac{\partial w}{\partial y}) = \mu((b_z+2b_{zz}z+b_{xz}x+b_{yz}y+b_{xyz}xy)+(c_y+2c_{yy}y+c_{xy}x+c_{yz}z+c_{xyz}xz)) \tag{5.17}$$

The bilinear interpolation method with first-order accurate interpolation leads to discontinuous shear rates as demonstrated for a Taylor Green flow in Fig. 5.5:

The compact method obtains second-order accurate interpolation at the expense of linear interpolation. Using the compact second-order interpolation, the recorded shear rates are continuous as demonstrated in Fig. 5.6. The convergence study shown in Fig. 5.7 demonstrates that the obtained shear rates are second-order accurate whereas they are first-order accurate with using the linear interpolation.

The LBM employs locally refined Cartesian grids. Arbitrary walls do not, in general, coincide with lattice nodes. A local interpolation method allowing to place no-slip boundaries off grid is designed. The lattice links that cut into a wall are collected and are assigned a subgrid-distance q to the wall. The local post-collision distribution function is equal to the pre-collision distribution function at the neighboring node in the local interpolation.

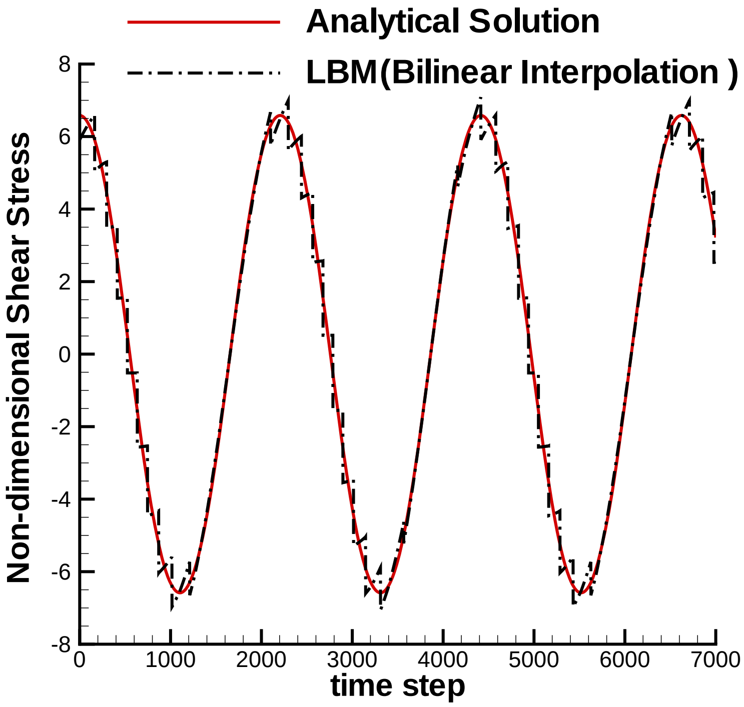

Figure 5.5.: Bilinear interpolation for Taylor Green flow. The non-dimensional shear stress is seen to be discontinuous between lattice nodes.

Hence, the distribution entering the wall can be interpolated along its characteristic to the point where it hits the wall. At this point the bounce back rule is applied that gives us the distribution entering the fluid domain from the wall. Another interpolation between this distribution and the distribution moving away from the node into the fluid domain gives the required boundary value for the next time step. This boundary condition allowing to place the walls at any points in the domain with second-order accuracy in space requires only local data. Consequently, the boundary itself is not a part of the simulation domain, which has implications on the pathline algorithm. There is always a small gap between the last grid node in the fluid domain and the boundary for which the flow field is unknown. A pathline entering this gap would leave the regular simulation domain and it is often observed in third-party post-processing tools that streamlines leave the domain. Such a behavior is unacceptable and requires a special near wall treatment.

When the particle approaches the wall, it will eventually leave the simulation domain, which means it is no longer enclosed in a complete cube of the lattice nodes. As a result, the particle is in the gap between the wall and the numerical grid. The interpolation function from the closest complete cube is now being evaluated outside of the cube to extrapolate the flow field.

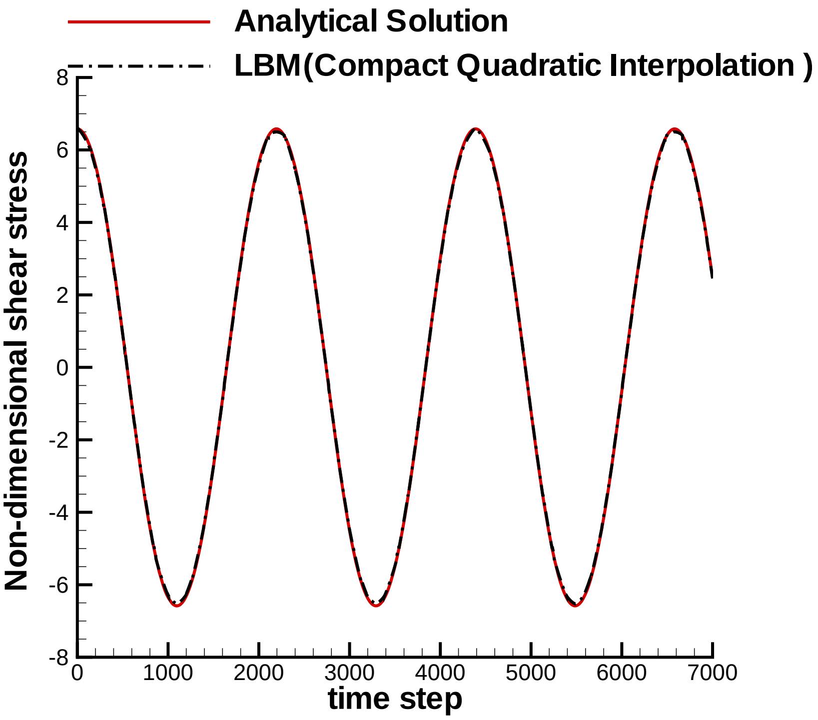

Figure 5.6.: Compact quadratic interpolation as in Fig. 4. Here the non-dimensional shear stress is continuous.

5.3. Correction in the extrapolation zone

Although massless particles were frequently found to cross the wall and leave the fluid domain, this extrapolation method was not sufficiently accurate on its own. In order to come to grips with this problem, a correction method for extrapolation is devised. In the coordinate system that originates in the center of the cube with 8 nodes at its verties the distance of the particle to the wall is computed and from the extrapolation function, the velocity $\overrightarrow{u}_{extra}$ at the location of the wall is obtained. Due to numerical errors the extrapolated value differs from the actual velocity of the wall $\overrightarrow{u}_w$. A corrector function with the following properties is designed: The correction is zero at the nodes of the cube, the second derivative of the correction is zero in the center of the cube, and the correction is minus the error from the extrapolation at the wall. From these constraints the following corrector function is obtained (Fig. 5.8):

$$\overrightarrow{u}_{correction} = \frac{\overrightarrow{u}_{extra}(x_w) - \overrightarrow{u}_w}{{x^3}_w - \frac{x_w}{4}}({x^3}_p - \frac{x_p}{4}) \tag{5.18}$$

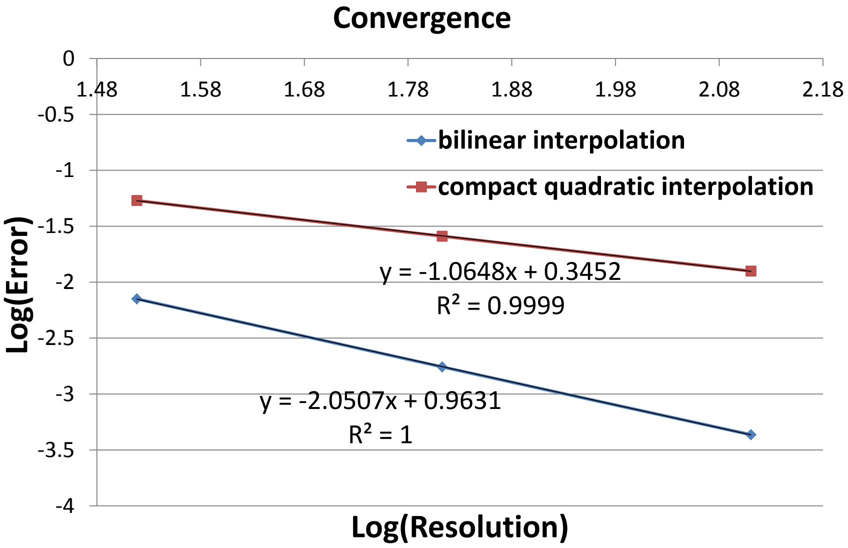

Figure 5.7.: Convergence of compact quadratic interpolation for the non-dimensional shear stress measurement in comparison to bilinear interpolation.

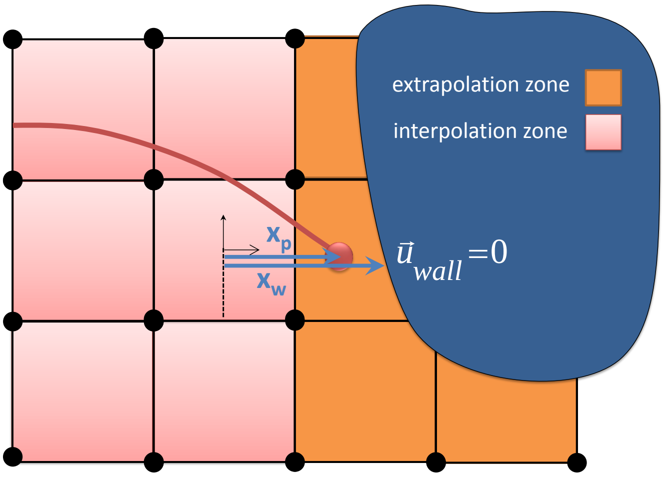

Figure 5.8.: Velocity correction in the extrapolation zone.

The correction is added to the extrapolated velocity. Using the correction, collisions with the wall do only happen for heavy and large particles for which this behavior is admissible.

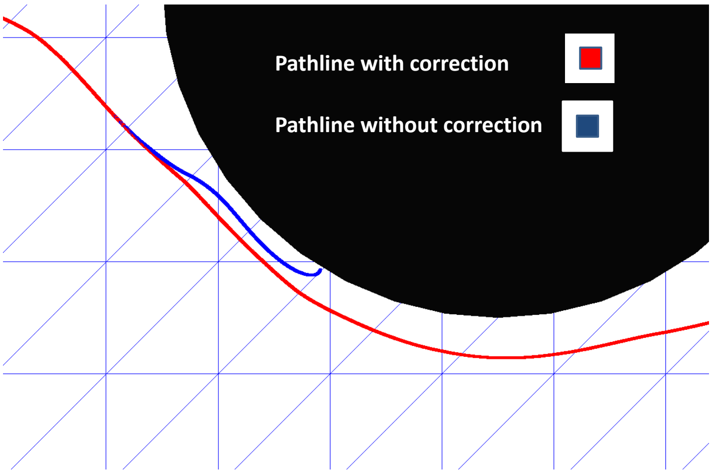

Figure 5.9.: Pathline pass over a cylinder with and without correction in the extrapolation zone.

Fig 5.8 shows the concept behind the correction in the extrapolation zone. The particle moves to the extrapolation zone where there is not enough information to calculate the velocity of the particle. This particle uses the closest interpolation cell in which all nodes are fluid. This correction is applied for all three components of velocity and for shear stresses. We implement this correction in a simulation where flow passes over a cylinder to see the difference between a pathline. The red line shows a pathline with correction while the blue line shows the pathline without correction in Fig 5.9. The blue pathline goes into the cylinder but the red pathline never goes inside the cylinder. The importance of this correction becomes more apparent when a large simulation with lots of pathlines including mass are studied and information such as shear stresses close to the wall must be acquired. Therefore this correction can play a critical role in this simulation. It should be mentioned that particles would go inside the wall even for the interpolation methods with higher order accuracy without the correction. This problem is not totally solved with higher resolutions (smaller Δx) or increasing the accuracy of interpolation.

5.4. Analytical solution for heavy particle velocity

In general, the force on a moving object with constant mass in the flow field is defined as:

$$\vec{F} = m\frac{d\vec{u}_p}{dt} \tag{5.19}$$

where u_p and m are the velocity and mass of the object, respectively. If one particle moves in the fluid flow with very small Reynolds numbers, the force can be computed for Stokes-flow as [111]:

$$\vec{F} = 6\pi\mu a(\vec{u} - \vec{u}_p) \tag{5.20}$$

where $\vec{F}$ is the Stokes drag force acting on the particle, $\mu = \rho\nu$ is the dynamic viscosity, a is the radius of the spherical object, $\vec{u}$ is the velocity of the fluid surrounding the particle and $\vec{u}_p$ is the velocity of the particle. A differential equation of the particle velocity is derived by substituting equation (5.24) into equation (5.19) as:

$$6\pi\mu a(\vec{u} - \vec{u}_p) = m\frac{d\vec{u}_p}{dt} \tag{5.21}$$

After simplification, the following form is obtained:

$$\frac{d\vec{u}_p}{dt} = \lambda(\vec{u} - \vec{u}_p) \tag{5.22}$$

where $\lambda = \frac{(6\pi\mu a)}{m}$ is the relaxation parameter for the particle that is computed from the particles mass and its drag coefficient. The above equation is solved analytically:

$$\vec{u}_p(t) = \vec{u}(t) + (\vec{u}_p(t - \Delta t) - \vec{u}(t))e^{-\lambda\Delta t} \tag{5.23}$$

The final goal in this thesis is to study the behavior of moving aggregates in the flow field. Later we will show that there is a linear relationship between the averaged hydrodynamic force on aggregates and the number of primary particles, (equation 5.24). This relationship can help us to analytically solve equation (5.19) for a random aggregate. In fact, a constant coefficient βN^α which is only dependent on the number of primary particles is multiplied to the right hand of equation (5.20).

$$\frac{|\left\langle \vec{F} \right\rangle|}{|\vec{F}_{pri}|} = \beta N^\alpha \tag{5.24}$$

here $\vec{F}_{pri}$ is the drag force on a sphere in the infinite domain given by equation (5.20) and coefficients α and β are constant and depend on the fractal dimension. The relaxation parameter for a random aggregate, λ, is modified as

$$\lambda = \frac{\beta N^\alpha (6\pi\mu a)}{m} \tag{5.25}$$

We use the modified λ and equation (5.23) to acquire the velocity of aggregates in our simulation.

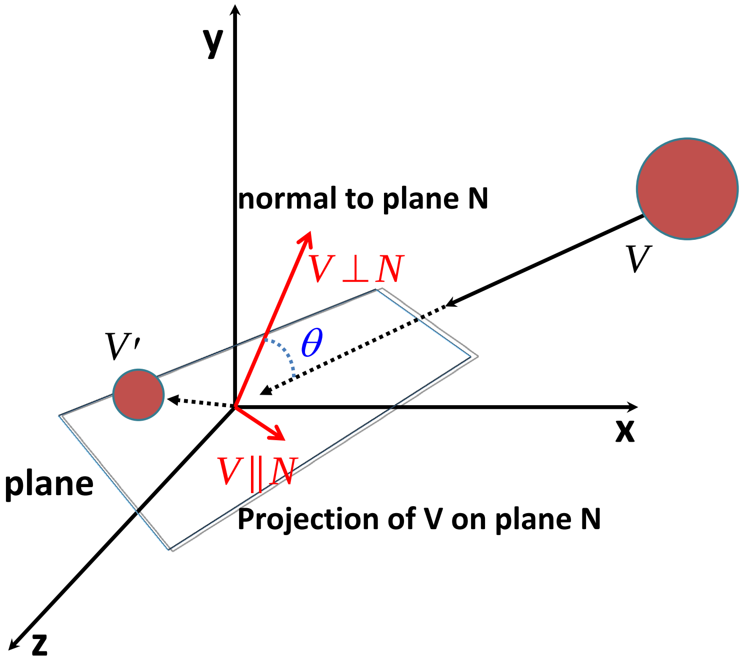

Figure 5.10.: Collision and reflection of a sphere with a plane locating in an angle θ with the horizontal plane.

5.5. Particle collisions with the wall

Particles without mass in the fluid flow should never touch the wall while particles with mass can collide with the wall and be reflected on. Therefore, the elasticity of the wall should be considered in the collision process. The reflection velocity of the particle with respect to the wall plane with the consideration of the coefficient of restitution is calculated in this section. We suppose that a particle with the velocity $V = \{u, v, w\}$ in the space x, y, z collides with a wall identified by equation $Ax + By + Cz = D$ and is reflected. The normal vector of the wall is specified by $\{A, B, C\}$.

Fig. 5.10 shows a particle which has a velocity V before the collision and a velocity V' after collision. The wall has the normal and the tangential coefficients of restitution e_n and e_{tz} respectively. In order to obtain the related equations, first of all, the components of the perpendicular and the parallel vector V with respect to the plane have to be calculated. The scalar magnitude of the projection on the plane is $|V|sin(\theta)$ and its direction is perpendicular to the normal N. The projection on the plane N is obtained by:

$$V||N = |V|sin(\theta)\overline{N} \times \overline{V \times N} \tag{5.26}$$

where $\overline{N} = \frac{N}{|N|}$, $\overline{V} = \frac{V}{|V|}$ and $\overline{V \times N} = \frac{V \times N}{|V \times N|}$. We use the relation $\overline{V} \times \overline{N} = \overline{V \times N} \sin(\theta)$ and simplify the above equation to:

$$V_{||} = V||N = N \times (V \times N/|N|)/N \tag{5.27}$$

the perpendicular component is calculated with the same procedure and it is equal to:

$$V_{\perp} = V \perp N = V \bullet N \times N/|N|^2 \tag{5.28}$$

It is supposed that the velocity of the wall is zero and the coefficient of restitution in two directions normal and parallel to the wall is applied. Therefore, the components of V' can be obtained by the following equations:

for the normal components:

$$u_n = -e_n \times A \times (A \times u + B \times v + C \times w)/(A \times A + B \times B + C \times C) \tag{5.29}$$

$$v_n = -e_n \times B \times (A \times u + B \times v + C \times w)/(A \times A + B \times B + C \times C) \tag{5.30}$$

$$w_n = -e_n \times C \times (A \times u + B \times v + C \times w)/(A \times A + B \times B + C \times C) \tag{5.31}$$

for the parallel components:

$$u_{tz} = e_{tz}(B \times B \times u + C \times C \times u - A \times B \times v - A \times C \times w)/(A \times A + B \times B + C \times C) \tag{5.32}$$

$$v_{tz} = e_{tz}(-(A \times B \times u) + A \times A \times v + C \times C \times v - B \times C \times w)/(A \times A + B \times B + C \times C) \tag{5.33}$$

$$w_{tz} = e_{tz}(-(A \times C \times u) - B \times C \times v + A \times A \times w + B \times B \times w)/(A \times A + B \times B + C \times C) \tag{5.34}$$

and finally the components of velocity, V', are calculated by adding the two components of the normal and parallel velocity.

A collision is called elastic when e_n and e_{yz} are equal to 1 and it is called a plastic collision when the coefficients of restitution are zero. The magnitude of the velocity is conserved in elastic collision which means the velocity magnitude of the particle before and after collision are the same. A simulation is implemented to show the influence of the normal coefficients of restitution with the LBM on the particle movement. In this simulation, a cylinder is located in the center of the computational domain and flow passes over the cylinder. About 50 sphere-shaped particles which have mass are released into the flow. This simulation is repeated for two different normal coefficients of restitution, $e_n = 0.9$ and $e_n = 0.01$. The influence of the normal coefficients of restitution e_n is shown in Fig. 5.11. As expected, when the normal coefficient of restitution is 0.9, the collision looks like an elastic collision and when e_n is 0.01, the collision is similar to a plastic collision.

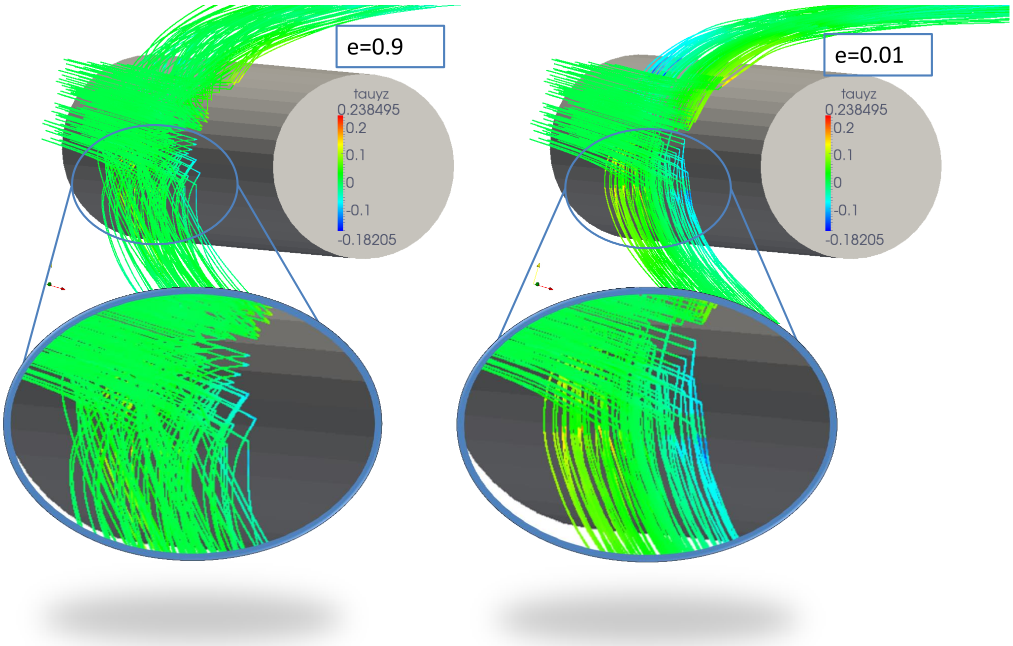

Figure 5.11.: Influence of the normal coefficient of restitution e_n. The collision is considered to be elastic when e_n is 1 and plastic when is 0.

5.6. Parallelizing the pathlines algorithm

Calculating a pathline seemingly is not difficult and is not a time consuming job. However, one wants to calculate hundreds of pathlines supposed to move in a big computational domain decomposed between lots of processes, considers an efficient and a precise algorithm. Thus, this algorithm has to be implemented with a parallel programming concept.

The procedure of implementing an algorithm for pathline tracing in different processes is demonstrated with one example. A big computational domain is considered and particles are distributed in the domain. Particles are allowed to move according to the flow field. Fig. 5.12(a) shows a decomposed domain consisting of 20 processes and Fig. 5.12(b) depicts the distribution of some particles in this domain. The processes do not have any information about each other and if one particle moves from one process to another, all information of this particle must be sent to the target process. Therefore, first of all, particles must know in which process they are and they must recognize their target processes where they want to go. A magnification of Fig. 5.12 is shown in the Fig. 5.13. In this picture only 9 processes exist and the particle in each process has its own color. Particles supposed to leave their process have a direction flag (Fig. 5.13(a)) that allows them to know about their target process. For example, only 4 among 7 particles in P_{22}, which are red, want to leave the process. These four particles leave P_{22} and go to P_{21}, P_{12}, and P_{23}. Moreover, the process P_{22} receives particles from P_{21}, P_{32}, and P_{13}. The same behavior is observed in other processes. Thus, each process with moving particles sends all particle information to the destination process and delete its memory of these particles. This process is demonstrated in Fig. 5.13(b) where 4 red particles move to different processes and are not in P_{22} anymore. This procedure described above is the basic concept of the pathline algorithm. This algorithm can be explained as fallows: First of all, each process gets its own particles and inserts them into a list. The particles start moving in the domain according to the computational time step. When they leave the domain, the statement of 'if' is satisfied. Then, they are sent to the target processes and deleted from their list. Finally, entering particles are added to the list and the loop is repeated (algorithm 2). It is noted that this algorithm is executed for each process.

Algorithm 2 pathline algorithm for each process

```
procedure PROCEDURE
    ← particles
loop over time:
    move particles
    if particles are out of domain then
        send particles to the target processes
        delete these particles in local list
    receive particles coming from other processes
    add these particles into local list
```

The main solver of the LBM uses blocks of grid nodes to decompose the computational domain. In the grid refinement a coarse block is divided into 8 fine sub-blocks in 3D. Two Blocks are connected to each other by a connector to send and receive information. These two blocks can be on two different processes since, in general, a process may include one or more blocks. Therefore, three different kinds of connectors are required, a connector between same level where both sender and receiver blocks are in the the same grid level. A connector between the coarse block and the fine block and finally a connector between the fine block to the coarse block are needed. A schematic picture of connectors is shown in the Fig. 5.14. The black connectors connect blocks with the same level and the green connectors deal with the fine to coarse blocks while the purple connectors transfer information from the coarse block to the fine block. Interface blocks are represented by yellow color and have both coarse and fine blocks.

If a particle starts moving in the coarse block and enters into the fine block due to flow field, it will pass through an interface block. The particle in this situation, at first, uses

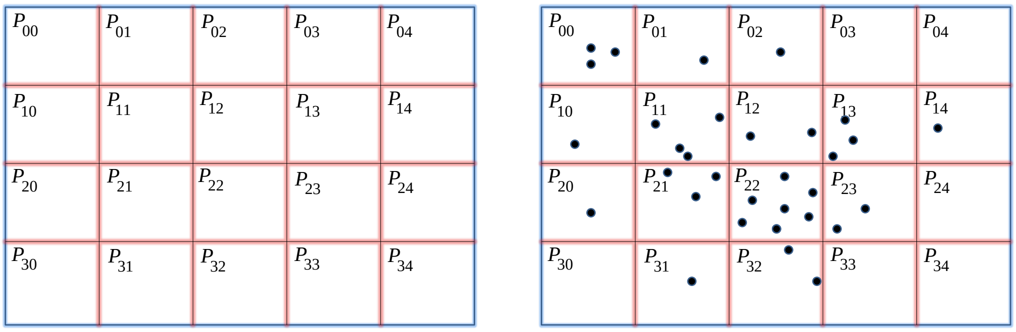

(a) Decomposed domain

(b) Distributed particles in the decomposed domain

Figure 5.12.: Distributed particles in decomposed domain consisting of 20 processes

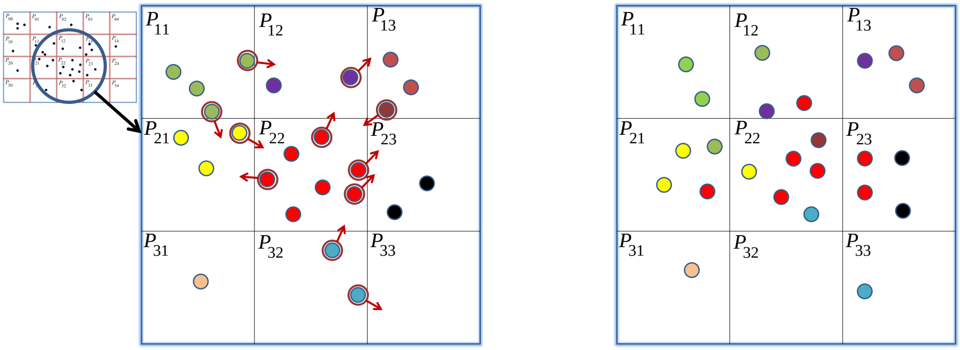

(a) Particles before streaming in the domain. Particles has direction flag will leave their process in the next computational time step.

(b) Particles after streaming in the domain. Each process may send and receive other particles.

Figure 5.13.: A close up of Fig. 5.12 including 9 processes. Each particle has a color identifying its process in a computational time step.

the same grid level connector in which its information is sent by this connector to the interface block. Then, the arrived particle utilizes the coarse block to the fine block connector to send its information. Finally, the particle only uses the connector with the same grid level as long as this particle travels in the fine grid level. If the particle wants to leave the fine grid level and returns back to the coarse grid level, connector blocks of green and black are utilized respectively.

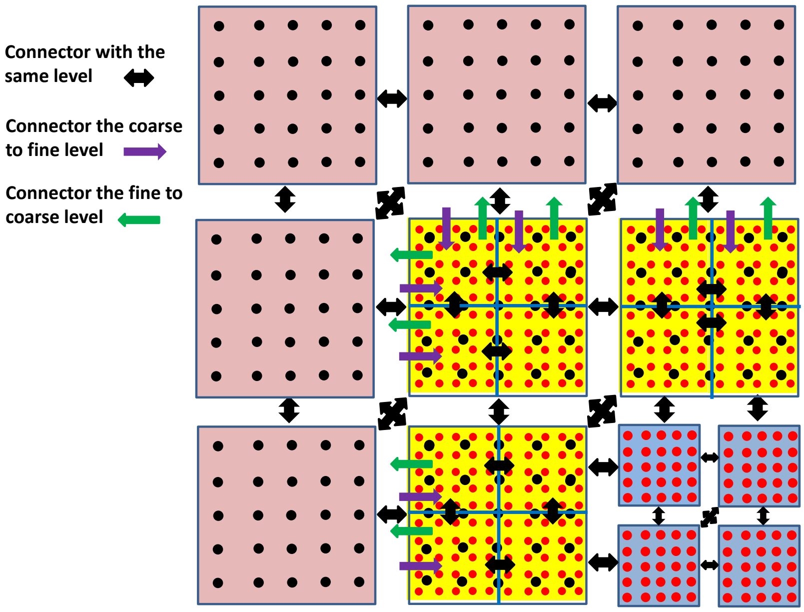

Figure 5.14.: A schematic of three kinds of connector for blocks with the LB nodes.

In the LBM solver, data related to particles are sent from one block to another block when data of the distributions are transferred. Thus, it does not need to consider the extra sending and receiving operations for the pathline algorithm in the LBM solver. Consequently, the performance of computing pathlines is significantly increased.

5.6.1. A sophisticated algorithm for the extrapolation zone

When a particle travels in the computational domain where there are no solid nodes, a interpolation process is used in the pathline algorithm. However, when the particle reaches the extrapolation zone, an extra consideration has to be implemented. We have applied a correction to the velocity of the particle to avoid entering to the solid domain. This correction is obtained from the closest cell data. Thus, a search algorithm for finding the closest cell should be added to our pathline algorithm. As long as the particle travels through cells in the extrapolation zone, the closest cell must be selected and used according to the shortest distance of the particle position to the center of neighbor cells. This method is implemented to increase the accuracy of our pathline algorithm.

Nevertheless, if a particle moving in the extrapolation zone leaves the block, a problem appears when the destination block belongs to a different process. The search algorithm fails since the information for suitable cells is not available in the new process anymore. In order to solve this problem we use ghost nodes which are available in the main kernel

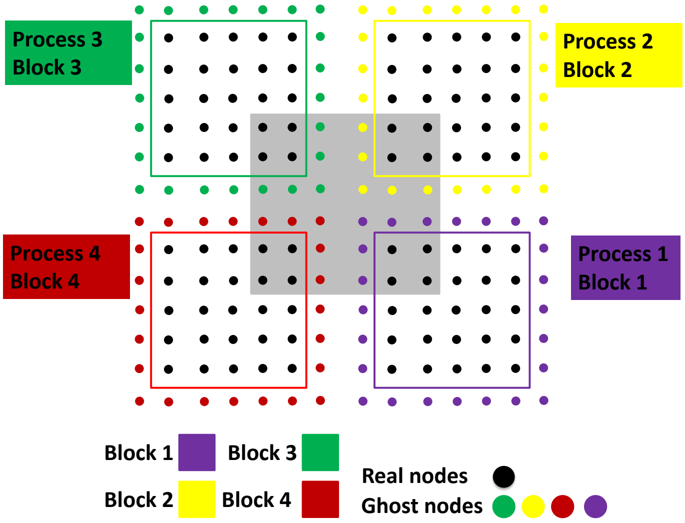

Figure 5.15.: Four different blocks in four different process. Each block is surrounded by ghost nodes and has a specific color. Four different processes are jointed together in the gray area demonstrated with a solid body in Fig. 5.16 to show the extrapolation pathline algorithm.

of the LBM. Each block is surrounded by ghost nodes. A schematic of ghost nodes for four different blocks located in the four different process is shown in the Fig. 5.15. Each block has a color which is similar to its ghost node color. The gray area in the center of this figure is a critical area since four different processes are jointed together in this zone. If a solid body locates in this area and a particle moves close to the wall, an extrapolation process is required in the pathline algorithm in this zone. In the post processing part of the simulations, ghost nodes are disregarded and only real nodes are represented. Fig. 5.16 depicts the gray area shown in Fig. 5.15 but with hidden ghost nodes. Every node may have different colors expressing different roles. For example, the nodes in this figure have four different colors: blue, red, purple, and green. It means that in reality, four nodes coincide in one node, one real fluid node of block 2, three ghost nodes of blocks 1, 3, and 4. Ghost nodes help us to solve extrapolation problems in the critical area.

A schematic of a particle pathline is shown in Fig. 5.16. This particle starts moving from the interpolation area, cell one, and approaches to the extrapolation zone. One of the Cells one to four, which are the closest and valid cells, is selected sophisticatedly by the search algorithm. The particle passing through the extrapolation zone uses the information extracted by the selected cell. However, these cells are in different processes such that they do not have shared memory. If we do not implement ghost nodes in the algorithm, when this particle leaves block four located in process four and enters to block one, the information of this particle is sent to process one in the switched position of the particle between processes shown by P_1 in the figure. Moreover, its information is removed

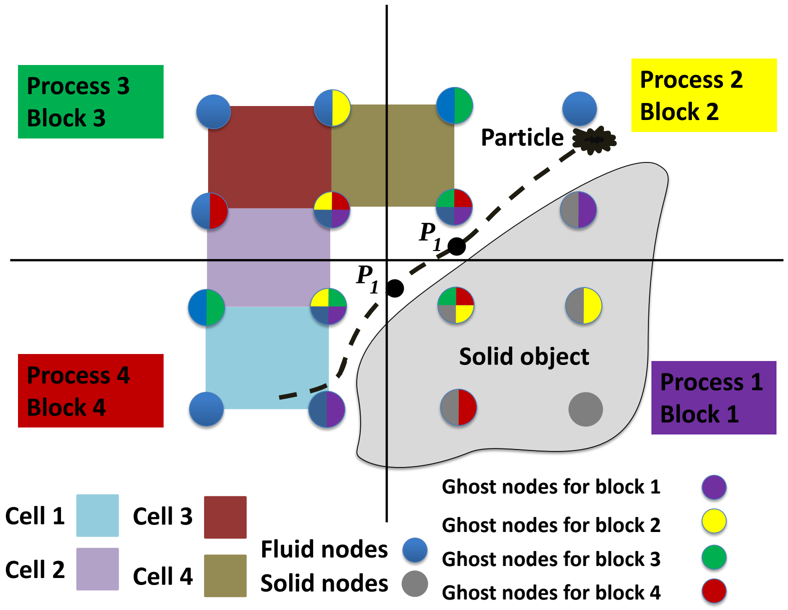

Figure 5.16.: A pathline of a particle in the gray area of Fig. 5.15. A suitable cell is selected according to the search algorithm. Ghost nodes coincide with real nodes; thus, a node in the picture can have different roles as it has different colors.

from the memory of process four. Now, the particle is in process one and its block has been filled out only with solid nodes. Besides, process one is not allowed to access cells two to four to obtain needed cell information. Consequently, the pathline algorithm will fail.

This problem is solved by using the ghost node. The particle entering to the location p_1 does not need to send its information to process one. Ghost nodes allow the particle to move further and use cell one. The particle continues its path up to position P_2. The process of the particle changes from process four to process two in this point. Process two has ghost nodes as well. Thus, cell four can be used by this particle and the algorithm continues successfully .

This efficient algorithm not only selects the best cell for the extrapolation, but also solves the problems related to the critical point in the decomposed domain.

6. A numerical study of aggregates

6.1. Introduction

The flow around a moving sphere in an unbounded domain was first examined by Stokes [112]. Lambs [113] solved Stokes's equations for many sphere-shaped and non-spherical particles. Brenner and Happel [114], Cox [115], Batchelor [116], Neil [117] and Ganatos [118] were pioneers in this field. Different methods were implemented by these researchers to study moving particles [114, 119, 120]. The hydrodynamic interaction between two freely moving particles was investigated by Neill [117] and Batchelor [116]. Hasimoto [121] studied the behavior of a periodic array of spheres in a fluid flow. He used Fourier series to formulate the periodic fundamental solutions of the Stokes equations.

When particles are stuck together and form colloidal aggregates moving through the fluid, additional research is required to determine their behavior. Colloidal aggregates, which are an essential topic in chemical, biological, and pharmaceutical industries, are considered in various fields of CFD. Hydrodynamic forces play a key factor in the suspension characteristics of aggregates in fluid flow [122, 123]. The sedimentation velocity [124], the diffusion constant [125, 126], and the rheology of the suspension [127] are some of the relevant features.

The shape of aggregates can be distorted due to the hydrodynamic stresses acting on them. In order to estimate the hydrodynamic forces, many methods with various levels of complexity have been used by scientists. A model is that an aggregates is considered as a pseudo-continuous porous sphere. Both Brinkman and Stokes equations are solved simultaneously to simulate an aggregate in this method [37, 128–130]. Different correlations between the fractal dimension and the porosity are proposed by Vanni [131]. Higashitani et al. [47] improved the method by applying a correction to the sum of the hydrodynamic drag forces. They validated their results with experimental values.

To evaluate hydrodynamic interactions of particles, another method was introduced, which followed the Kirkwood-Riseman theory [132]. In this method, the force exerted to whole spheres in the aggregate was evaluated as a summation of the drag forces on a single particle if it did not experience any effects from other particles. This method gave good results regarding the modeling of the hydrodynamic properties of polymer chains and random coils. However, the results of it are not acceptable when the interactions in close contact are evaluated. Torre and Bloomfield modified the approach [133]. Meakin et al. [134] applied the theory to clusters generated through a Monte Carlo cluster-cluster aggregation mechanism and determined their hydrodynamic radii. Lattuada et al. [135] developed an analytical formula for the hydrodynamic radius of fractal clusters based on the particle-particle correlation function.

Another method utilizes the free-draining approximation [136–140]. This method was implemented based on the Stokes drag force experienced by each particle as if there were no other particles in the flow domain. An estimation of the screening hydrodynamic forces occurring in aggregates was obtained by either the fraction of the surface area of a primary particle or by applying a reflection method [128]. Stokesian dynamics was also used as a method for the simulation of the fluid dynamics of aggregates. Brady et al. [140, 141] were the pioneers of this method. They proposed the method for the calculation of hydrodynamic forces. Stokesian dynamics was adopted for modeling the response of porous clusters in uniform flows [142, 143], shear flows [128, 144], and general linear flows [145, 146].

Solving the full Navier-Stokes equations at the surface of the particles is another method. Maury [147] used a finite element method to solve the Navier-Stokes equations for the two-dimensional motion of a non-spherical particle by using a re-meshing algorithm. More recently, new methods such as the immersed boundary method (IBM) have been developed to a point where they are capable of simulating moving particles in laminar and turbulent flows. A vast number of studies have been carried out on the IBM and its application on moving particles [148, 149]. However, this method does not resolve the interface exactly.

The intrinsic properties of the LBM increase the numerical efficiency significantly and allow us to simulate a moving sphere [150, 151] accurately. Ladd [51] simulated a moving particle by the LBM for the first time. Moreover, in the LBM suitable boundary conditions can be implemented on the surface of the sphere to estimate the curved boundary correctly. Thus, a complex particle-fluid boundary can be studied with high accuracy in the LBM.

The main reason for simulations of aggregates suspended in fluid is the calculation of the drag force. With the drag force known , the irregularity of the aggregate can be modeled efficiently. The drag force also determines important physical properties like settling velocity, coagulation rate, sedimentation behavior and equivalent particle size. In order to reach this goal, we study different aggregates with different number of primary particles primary particles and find a simple model such that it can satisfy the properties of aggregates.

6.2. Calculation of the drag force

All computational simulations are influenced by the domain boundaries. They can effect the result significantly and may lead to wrong interpretations. However, the cost of the computation does not allow us to increase the domain size unlimitedly. A reasonable computational domain can be acquired by assessing the ratio of the domain size to the sphere diameter and the ratio of the sphere diameter to the cell size. We simulate the flow passing over a sphere with a periodic boundary condition at all borders except inflow and outflow and calculate the drag force. The inflow condition is considered to be constant velocity while a constant pressure is applied at outflow. In the following, all the drag forces obtained from the LBM are calculated by the momentum-exchange method [51, 143, 152]. Moreover, they are normalized by the Stokes drag force, $6\pi\mu a u$, on a single sphere suspended in an infinite flow with the inflow velocity u and viscosity μ and radius a.

In this section, we study the effect of the ratio of the domain size to the sphere diameter for Stokes flow, which is a flow with low Reynolds number. We fix the ratio of sphere diameter to the cell size. The analytical drag force on the sphere in Stokes flow can be given by [153]:

$$F_{analytic} = 6\pi\mu a u \tag{6.1}$$

If the drag force on the sphere is correctly calculated and normalized by the analytical solution, the result must be equal to one.

The viscosity of the LBM is set to 0.13 $\Delta x^2/\Delta t$ to avoid being in the under-relaxation zone. The Reynolds number is equal to 0.1, small enough to satisfy Stokes flow conditions. The Mach number also is small enough to assume incompressiblity for the flow. Fig. 6.1 shows the influence of the ratio of the domain size to sphere diameter on the drag force deviation. The ratio of the sphere diameter to the cell size is fixed to be 14. Later we will show that this is a reasonable value for our simulations. It is seen that the drag force deviation of the analytical solution is reduced by increasing the ratio of the domain size to the sphere diameter. The influence of the boundary condition is significantly higher for small domains and with increasing this ratio up to 50, an underestimation of the drag forces is seen. It is concluded from Fig. 6.1 that the number 45 can be a reasonable value for the ratio of the domain size to the sphere diameter in our simulation. If we plot the logarithm form of the deviation force versus the logarithm form of the ratio of the domain size to sphere diameter, the slope of this plot is about equal to one, Fig. 6.2.

$$Log(F_{d_{deviation}}) = -0.9402 Log(\frac{H}{D}) + 0.1376 \tag{6.2}$$

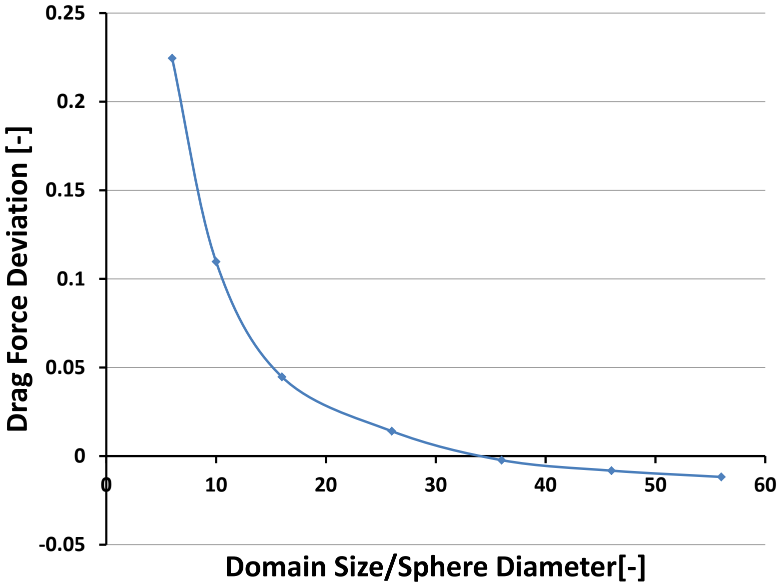

Figure 6.1.: The influence of the ratio of the domain size to the sphere diameter in the fixed ratio of the sphere diameter to the cell size, 14.

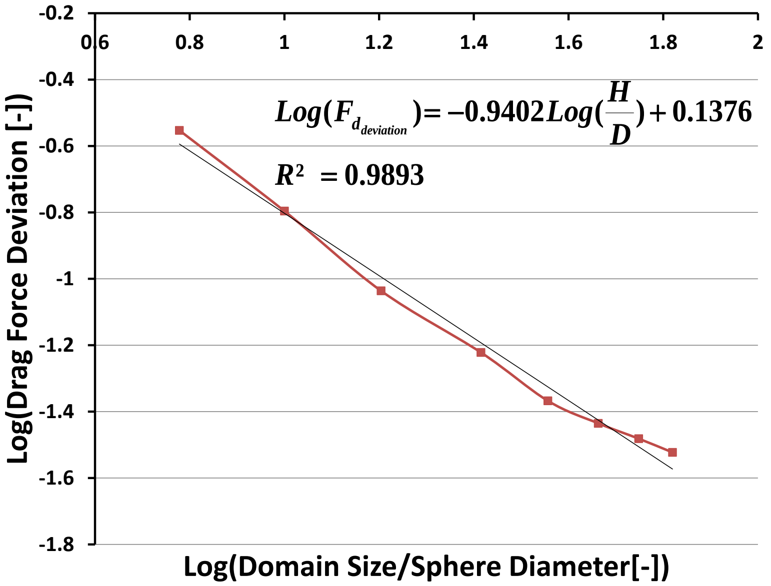

Figure 6.2.: The influence of the ratio of the domain size to the sphere diameter in the fixed ratio of the sphere diameter to the cell size, 14, in the logarithm form.

where H and D are the domain size and the sphere diameter, respectively. Different lattice radii for the sphere are investigated to find out the influence of the ratio of the sphere diameter to the cell size on the drag force. The sphere is located in the center

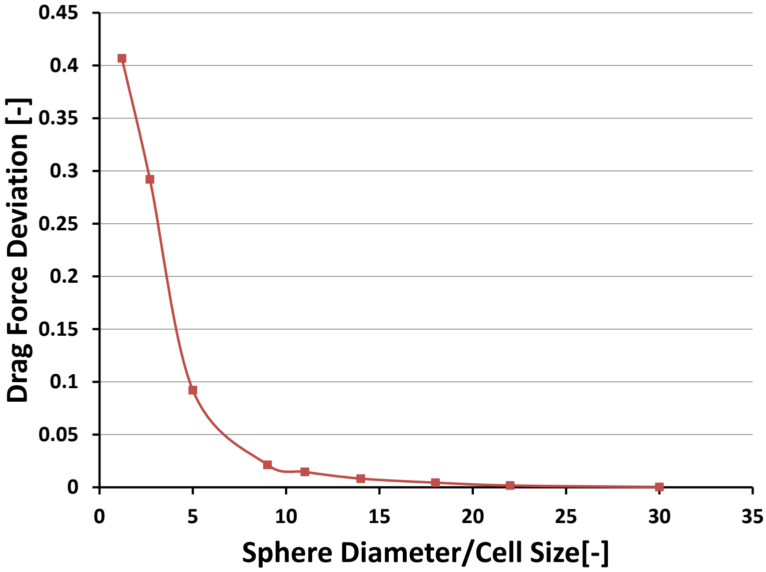

Figure 6.3.: The influence of the ratio of sphere diameter to the cell size in the fixed domain size to the sphere diameter 45.

of the fluid domain and the LBM viscosity is considered to be the same as before. The Reynolds number is kept constant by decreasing the inflow velocity when the number of the lattice cells is increasing. The ratio of the domain size to the sphere diameter is assumed to be 45 which is obtained from the blockage ratio plot.

For very small radii of 1 or 2, a poor approximation of the drag force is obtained but with increasing the number of the lattice cell, the drag force deviation is decreased. Binder [143] claimed that a resolution of six cells is good enough to calculate the drag force without any deviation force but he did not pay attention to the LBM viscosity and he selected a high value leading the simulation to be implemented in the under-relaxation zone. In this zone, the continuity assumption of the fluid is questionable and thus, the obtained results are not trustworthy. Fig. 6.3 shows the influence of the ratio of the sphere diameter to the cell size with the ratio of the domain size to sphere diameter fixed at 45. The figure implies that the selection of 14 lattice cells to recover hydrodynamic forces of a sphere is sufficient to get an error less than 3% which is acceptable for our simulations. A logarithm form of the error is demonstrated in the Fig. 6.4. This relationship is fitted to:

$$Log(F_{d_{deviation}}) = -2.1684Log(\frac{D}{C}) + 0.2287 \tag{6.3}$$

where D and C are the sphere diameter and the cell size, respectively. The error decreases with the second-order in the grid spacing. The slope of the plot demonstrates that the effect of this ratio is remarkably critical in comparison to the blockage ratio.

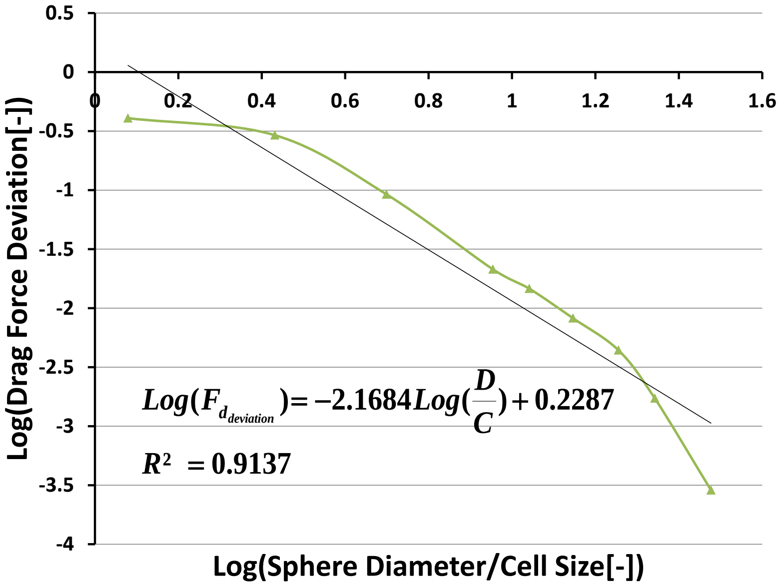

Figure 6.4.: The influence of the ratio of sphere diameter to the cell size in the fixed domain size to sphere diameter 45 in the in the logarithm form.

A question raised here is that if an aggregate with a high number of primary particles is used in a simulation, whether the above ratios are still valid. In order to reassess the above statement about the blockage ratio, a doublette consisting of two attaching spheres is studied. A schematic of the doublette is shown in Fig. 6.5. Fortunately, there is an analytical solution of the drag force in the Stokes flow regime. Happel and Brenner [114] calculated the analytical solution of the drag force in the Stokes flow for a fluid containing two spheres as:

$$F_{analytic} = 6\pi\mu a u(1 - 3a/4r + 9a^2/16r^2 ...) \tag{6.4}$$

where r is the inter-particle center-to-center distance. If the distance between two particles vanishes, the following equation to calculate the drag force on each sphere is obtained by [154]:

$$F = 6\pi\mu a u[\frac{4}{3}\int_0^\infty \frac{1}{4}(1 - \frac{4\sinh^2 x - 4x^2}{2\sinh 2x + 4x^2})dx)] \tag{6.5}$$

In stationary fluid flow, the bracket in the above equation evaluates to 1.29 for the case where two spheres are aligned parallel into the direction of the flow and 1.432 for the case where two spheres are located perpendicular to the direction of the flow. In Fig. 6.5, these flows are depicted with blue and red color, respectively.

The influence of the ratio of the domain size to the equivalent diameter on the drag force with the ratio of the domain size to sphere diameter fixed at 14 is demonstrated in Fig. 6.6. The equivalent diameter is defined as the wet area of two spheres and it is different

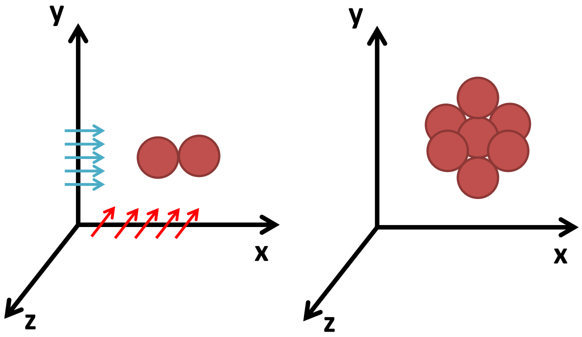

Figure 6.5.: A doublette and a symmetry star-shaped aggregate suspended in the flow. Flow passing over the doublette in two directions parallel and perpendicular is shown in the left figure while a symmetry star-shaped aggregate is depicted in the right hand side.

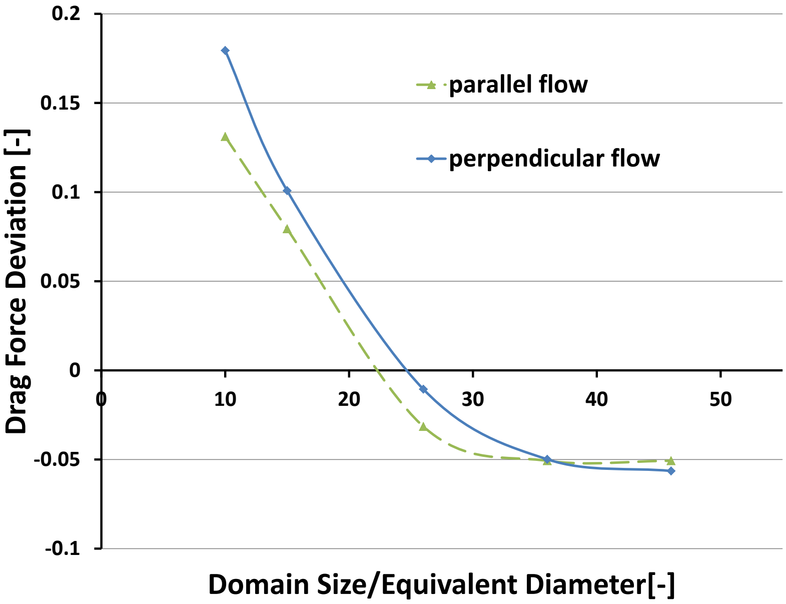

Figure 6.6.: The influence of the ratio of domain size to equivalent diameter in the fixed ratio of the sphere diameter to the cell size 14.

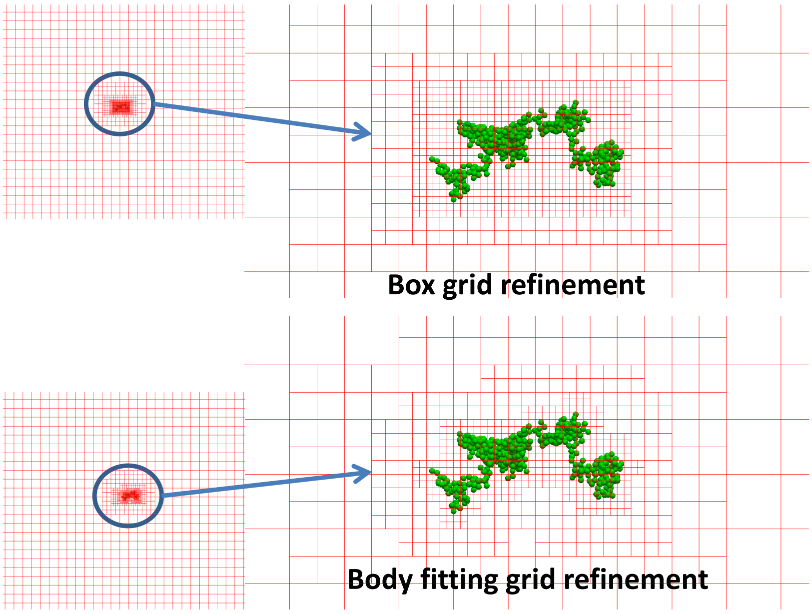

Figure 6.7.: An body fitting and a box grid refinement around an aggregate with 500 primary particles in the $x - y$ view.

for these two different simulations. Periodic boundary conditions are used and the lattice Boltzmann viscosity and Reynolds number are the same as before. It is seen that by increasing the blockage ratio up to 30, the drag force deviation decreases rapidly in both cases. A constant deviation of about 5 percent is observed at a ratio of the domain size to the equivalent diameter of more than 40. This figure confirms the previous results and declares that 45 as the blockage ratio is suitable for our simulation. Therefore, in the rest of following simulation the blockage ratio is set up to be 45 in order to minimize the error created by boundary conditions.

In order to get a pattern of the drag force applied on the aggregates we should study different aggregates including different numbers of primary particles. In general, aggregates are not symmetric and a random aggregate can have different drag forces at different orientations to the flow field direction. The aggregates considered in our studies are limited to the fractal dimension 1.85. A grid refinement method is necessary to implement a suitable blockage ratio while resolving the primary particles sufficiently. The grid refinement significantly decreases the cost of the computations and allows us to simulates large aggregates with more than 5000 primary particles.

In order to study aggregates with low fractal dimensions a body fitting grid refinement is required because a box grid refinement considers a box zone where some parts of this zone are empty of primary particles. Therefore, these parts of the zone do not need to be refined. It must be noted that the most grid nodes are in the finest level where

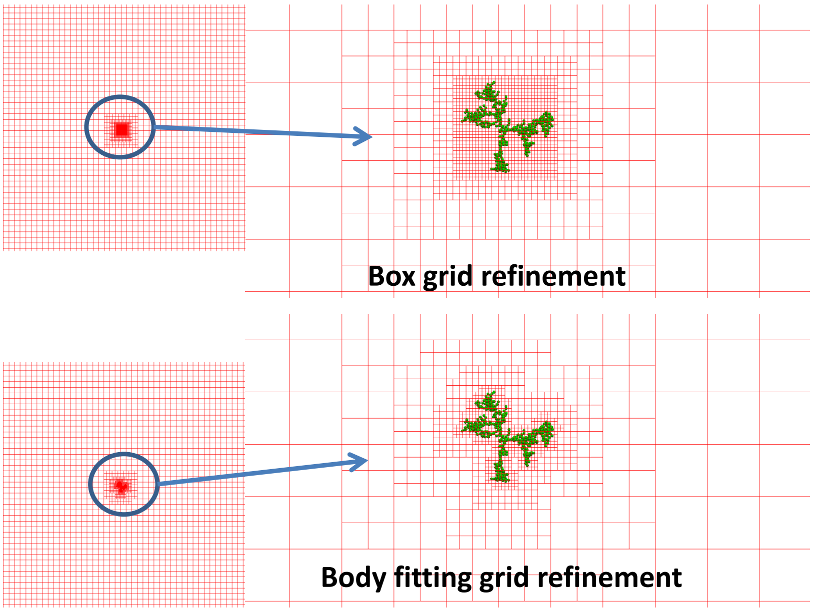

Figure 6.8.: An body fitting and a box grid refinement around an aggregate with 500 primary particles in the $x - z$ view.

method	Number of nodes$\times 10^6$
body fitting grid refinement	825
box grid refinement	418

Table 6.1.: comparison between two different grid refinements

the computational cost is high. Consequently, the performance of the computations is tremendously reduced by using only body fitting grid refinement. Fig. 6.7 and Fig. 6.8 demonstrate an aggregate with 500 primary particles in different views in two types of grid refinements with 5 levels and more than 852 million grid nodes. Each square of this figure corresponds to a box including 16^3 grid nodes. A comparison between two different grid refinements is shown in the table 6.1. The cost of computation is about half for the body fitting grid refinement in comparison to the box grid refinement. Two views are depicted to emphasize how many node blocks can be saved only by using the suitable grid refinement.

Unfortunately, there are not more analytical solutions for aggregates to validate our results; thus, a commercial software, ANSYS, for solving Navier-Stokes equations based on the finite element methods is used. The results obtained by the LBM are compared with ANSYS results. A prototype volume mesh generated by ANSYS for a random aggregate with 60 primary particles is shown in Fig. 6.9. We use one million elements and 0.18 million computational nodes. The elements must be small enough to capture intersections

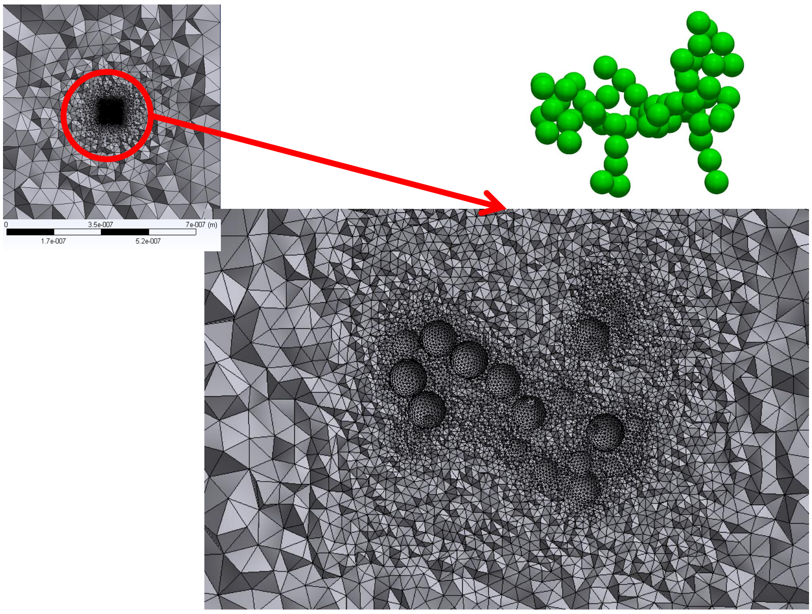

Figure 6.9.: A grid refinement generated by ANSYS for a aggregate with 60 primary particles. One million elements and 180000 nodes are used.

between spheres correctly; otherwise, results do not converge to the correct drag force.

An star-shaped aggregate with seven primary particles is shown in Fig. 6.5. This aggregate is symmetric and the drag force in each direction should have the same value. Therefore, the drag force is only calculated in x direction. The result is compared with results acquired by ANSYS. A good agreement is achieved between the LBM method and ANSYS in which the deviation is only 1.1%. The results are also compared with the ASD method [155] to ensure the accuracy of our results, table 6.2. The drag force obtained by the ASD method is close to our result. All these values are given by numerical methods and certainly have deviations from the real value. However, they are close to each other and this confirms the validity of our result. The star-shaped aggregate is a symmetric object but real aggregates are not symmetric. Thus, drag forces are obtained in different orientations. Four random aggregates with 20, 40, 60 and 80 primary particles are studied and LBM results are compared with ANSYS result under the same conditions. Our goal is to find a relationship between aggregates and their drag force. These aggregate geometries are located in their three main orientations and their drag forces are calculated

Direction/method	LBM	ANSYS	ASD([155])	deviation(LBM and ANSYS)%
(1,0,0)	2.48	2.51	2.55	1.1

Table 6.2.: Normalized drag force of a star-shaped aggregate

by the LBM. A body fitting mesh is used to decrease the computational cost in order to satisfy the discussed blockage ratio requirements in all these simulations.

Direction/method	LBM	ANSYS	deviation%
(1,0,0)	4.41	4.37	2.1
(0,1,0)	4.12	4.07	1.2
(0,0,1)	4.19	4.11	1.9

Table 6.3.: Normalized drag force for an aggregates with 20 primary particles

Direction/method	LBM	ANSYS	deviation%
(1,0,0)	6.21	6.35	2.5
(0,1,0)	6.38	6.2	2.8
(0,0,1)	6.32	6.44	1.8

Table 6.4.: Normalized drag force for an aggregates with 40 primary particles

Direction/method	LBM	ANSYS	deviation%
(1,0,0)	7.57	7.7	1.7
(0,1,0)	8.2	8.4	2.4
(0,0,1)	7.76	7.66	2.01

Table 6.5.: Normalized drag force for an aggregates with 60 primary particles

Tables 6.3 to 6.6 show the drag forces acting on the aggregates. Results obtained by the LBM are in a close agreement with ANSYS results. Deviations are not larger than 4 percent in these aggregates. Moreover, it is seen that there are no obvious differences between drag forces on the aggregates in the various orientations.

A random aggregate with 586 primary particles is shown in the Fig. 6.10 in three directions $x-y$, $x-z$, and $y-z$. The projected areas are in the same ranges. Therefore, one can expect to obtain similar drag forces for different orientations. The x-velocity profile close to this aggregate is demonstrated in Fig. 6.11.

Another random aggregate with 500 primary particles is studied to see how large the difference between drag forces in the various orientations is, when a large aggregate is simulated. The hydrodynamic drag forces on the aggregate when flow passes over in the x and y directions are 24.45 and 28.01, respectively, table 6.7. The maximum deviation of the drag in these three directions is observed to be less than 15% which is acceptable for large aggregates. It is noted that large aggregates need more computational cost and therefore need more grid refinement levels. Different levels are used according to how

Direction/method	LBM	ANSYS	deviation%
(1,0,0)	9.44	9.64	2.1
(0,1,0)	8.31	8.38	1.2
(0,0,1)	9.15	9.44	3.1

Table 6.6.: Normalized drag force for an aggregates with 80 primary particles

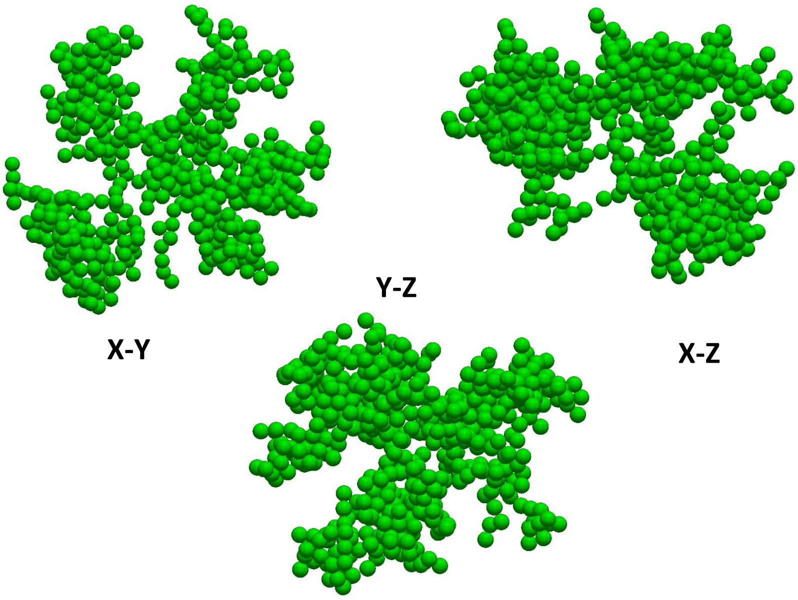

Figure 6.10.: A random aggregate with 586 primary particles in three view directions.

large the aggregate is. The blockage ratio and the number of the lattice cells used to consider one primary particle are similar in all test cases.

Up until now, various aggregates have been studied and their hydrodynamic drag forces have been calculated with the LBM and compared with other methods to assess the validity of our results. A simple relationship between the drag force on aggregates and the number of primary particles is observed by plotting a logarithm form of these two parameters. In order to get a relationship independent of the orientation, drag forces on the different orientations are averaged. A nonlinear behavior between the averaged drag forces and the number of primary particles is acquired due to the shielding effect, Fig. 6.12. Because the outer particles of the aggregates are faced to the flow and inner particles screened from the flow, the latter contribute less to the drag forces. Our aggregates, which have the fractal dimension 1.85, are compared to a volume equivalent sphere (fractal dimension 3) of the given number of particles. The drag force on the aggregates with the fractal number 1.85 is larger than those of the fractal number 3 with the same number of primary particles. Moreover, the difference is grown by increasing the number of primary

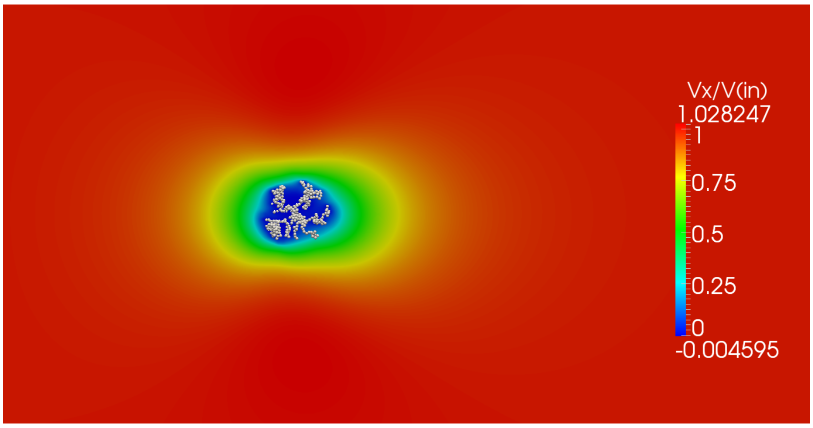

Figure 6.11.: The x-velocity profile close to the random aggregate with 586 primary particles shown in the Fig. 6.10.

Direction/method	LBM
(1,0,0)	24.45
(0,1,0)	28.01
(0,0,1)	24.58

Table 6.7.: Normalized drag force for an aggregates with 500 primary particles

particles. The mean drag force is correlated to the number of particles with fractal dimensions 1.85 and 3 by the following approximations respectively:

$$\frac{F_d}{F_{d,prim}} = \beta N^{\alpha} = 0.9141 N^{0.5403} \quad for\ D_f = 1.85 \tag{6.6}$$

$$\frac{F_d}{F_{d,prim}} = N^{0.3333} \quad for\ D_f = 3 \tag{6.7}$$

Our correlation is comparable to the equation proposed by Kim and Yuan [156], in which an ideal fractal aggregate, $D_f = 5/3$, is examined. The functional relations 6.6 and 6.7 are used to compute the relaxation parameter for our pathline algorithm.

$$\lambda = \frac{\beta N^{\alpha}(6\pi\mu a)}{m} \tag{6.8}$$

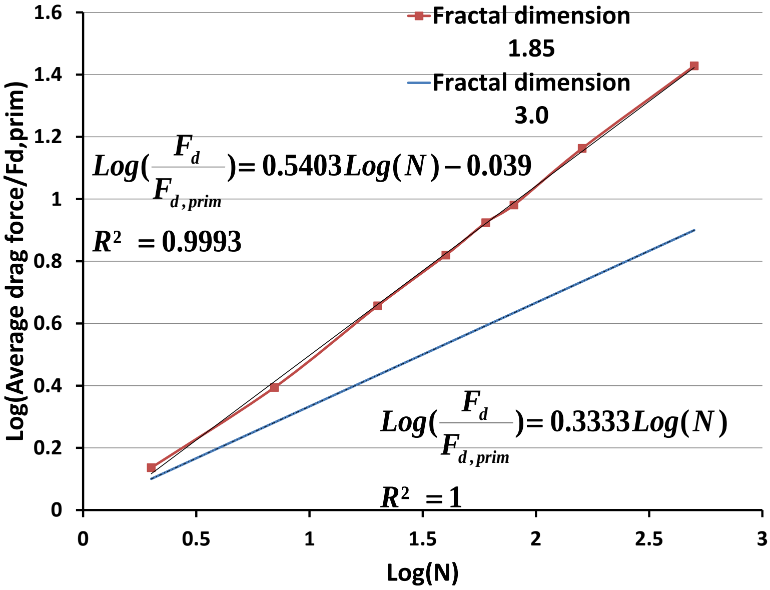

Figure 6.12.: Influence of the particle number on the drag force for aggregates with the fractal dimension 1.85 and a volume equivalent sphere (fractal dimension 3).

where β and α are obtained from equations 6.6 and 6.7. The variables m, a, and a are the mass of primary particle, the dynamic viscosity, and the radius of the primary particle, respectively. Albeit the relaxation parameter is relatively large for small agglomerates, it turns out that there is no clear scale separation between the relaxation of the particle to the velocity of the surrounding fluid and the time step of the simulation. Therefor the mass of the particle cannot be neglected a priority.

Another useful relation showing the influence of the gyration radius on the drag force is obtained by our simulation. This is demonstrated in the Fig.6.13 for aggregates with the fractal dimension 1.85 and a volume equivalent sphere (fractal dimension 3). The slope of the logarithmic plot is about one in both cases and thus, a linear relationship is seen in both kinds of aggregates unlike the previous relationships (6.6 and 6.7).

$$\frac{F_d}{F_{d,prim}} = 1.1096(\frac{R_{gyr}}{Rprim})^{1.0261} \quad for\ D_f = 1.85 \tag{6.9}$$

$$\frac{F_d}{F_{d,prim}} = \frac{R_{gyr}}{Rprim} \quad for\ D_f = 3 \tag{6.10}$$

It is observed that aggregates with lower fractal dimension have slightly larger drag forces.

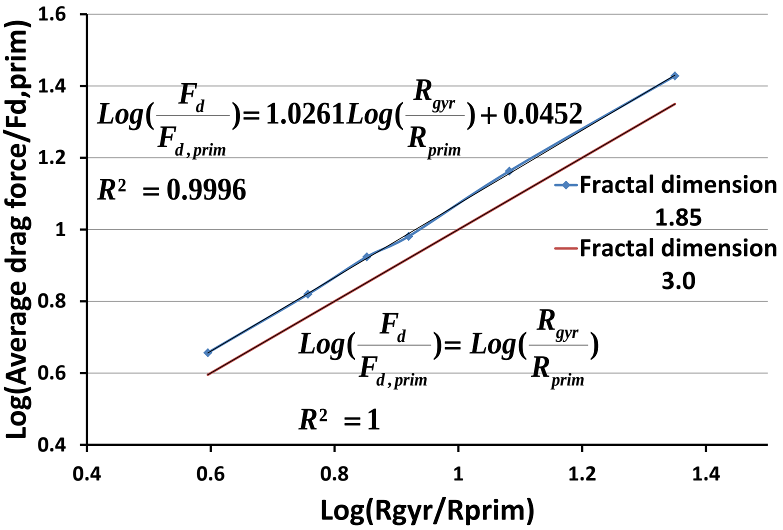

Figure 6.13.: Influence of the gyration radius on the drag force for aggregates with the fractal dimension 1.85 and a volume equivalent sphere (fractal dimension 3).

6.3. Studying aggregates under elongational flow, pure rotational flow and simple shear flow

In this section, three classical flow fields, the elongational flow, the pure rotational flow and the simple shear flow, are briefly studied. We first define these flow fields and then implement them with the LBM. Fig. 6.14 and 6.15 show the set of velocity profiles and streamlines for two dimensional flows related to these fields. The reason of studying these kinds of flow fields is that they are suspected to be the main reasons of the aggregate dispersion. Derivatives of velocities in three directions assign the type of the flow fields. The rate of strain tensor and vorticity tensor which are the main characteristics of the flow are also determined as derivatives of velocities. The rate of strain tensor, E, and vorticity tensor , Ω, are defined by $(\Gamma + \Gamma^T)/2$ and $(\Gamma - \Gamma^T)/2$, respectively. The variable Γ is equal to ∇V and can be varied in the different flow fields. Every flow field can be generated by a combination of these flows. For example, when an aggregate goes through an orifice at high Reynolds numbers, elongational flow is created before the entrance of the orifice, shear flow is seen inside of the orifice and pure rotation is observed in the corners where vorticities are observed. In the following sub-section these classical fluid flows are introduced and their simulations are implemented by the LBM.

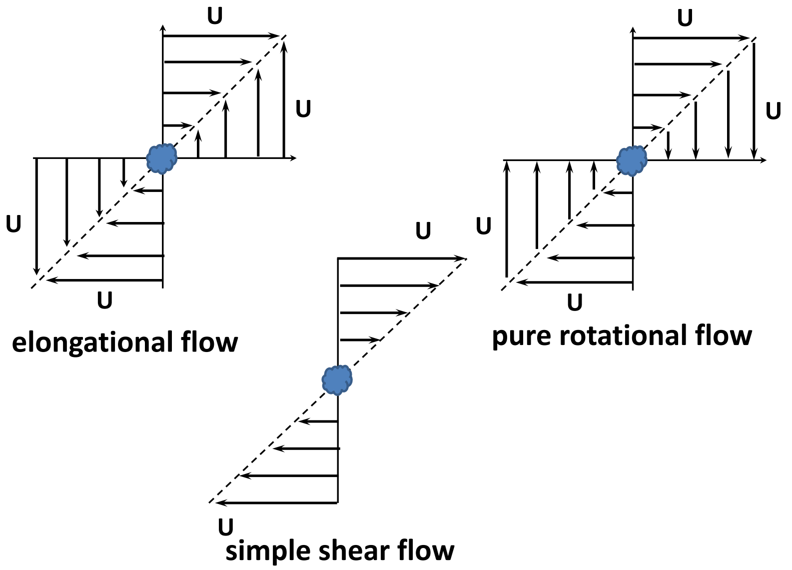

Figure 6.14.: The velocity profile for two dimensional flows for elongational flow, pure rotational flow and simple shear flow.

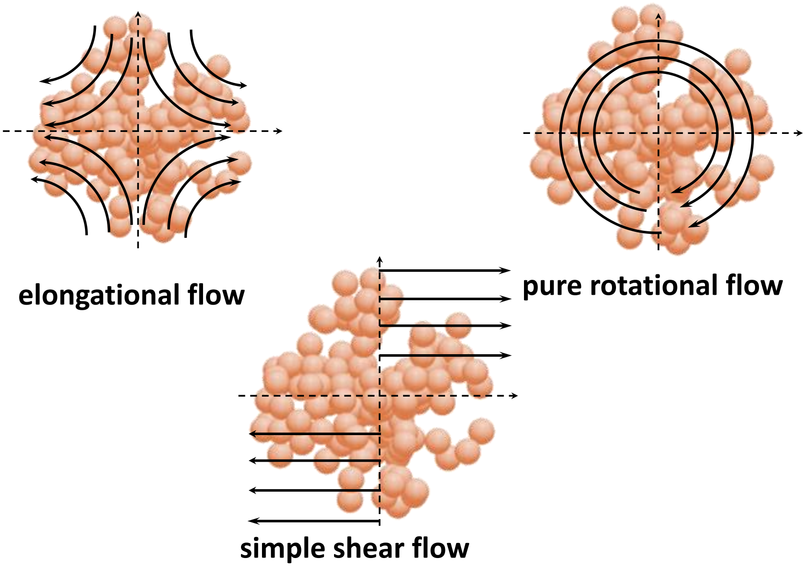

Figure 6.15.: The streamlines for two dimensional flows for elongational flow, pure rotational flow and simple shear flow.

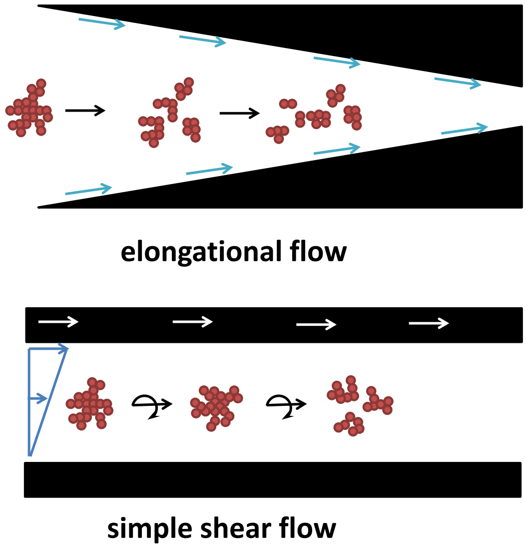

Figure 6.16.: Two common physical example of elongational flow and simple shear flows.

6.3.1. Elongational flow

A pure deformation without rotation is called elongational flow. The components of this velocity field tend to stretch out fluid elements. The main characteristic of this flow is that the curl of the velocity field is zero, $\nabla \times V = 0$. The center of the coordinate system is the stagnation point where the velocity is equal to zero and it allows us to study deformation of an object without considering the translational motion. One common example of elongational flow is seen in the Fig. 6.16 where a large aggregate is broken up by elongational flow field into smaller aggregates. The elongational flow here is created by decreasing the area. The elongational flow is defined by the following equation:

$$\Gamma = \begin{bmatrix} \gamma_e & 0 & 0 \\ 0 & -\gamma_e & 0 \\ 0 & 0 & 0 \end{bmatrix} \tag{6.11}$$

where γ_e is the elongational rate. the flow is incompressible because $du_x/dx + du_y/dy + du_z/dz = \gamma_e - \gamma_e = 0$. The streamlines are calculated according to the equations:

$$\gamma_e = du_x/dx \tag{6.12}$$

$$\gamma_e = -du_y/dy \tag{6.13}$$

6.3.2. Pure rotational flow

In the dispersion process, usually pure rotational flow is not considered [146]. However, this flow is simulated here to see its effects on the aggregates. The streamline and velocity profile for the pure rotation are depicted in Fig. 6.14 and 6.15. The pure rotational flow is clarified by a simple example. The velocity components are given in two dimensions as:

$$\begin{aligned} v_x &= y \\ v_y &= -x \end{aligned} \tag{6.14}$$

the curl of the velocity field is obtained by:

$$\nabla \times V = -i_z \tag{6.15}$$

This flow is rotated in the z-axis and is normal to the plane of the flow. The pure rotational flow is defined by following equation:

$$\Gamma = \begin{bmatrix} 0 & \gamma_r & 0 \\ -\gamma_r & 0 & 0 \\ 0 & 0 & 0 \end{bmatrix} \tag{6.16}$$

where γ_r is the pure rotational rate. The streamline is generated in the same way as elongational flow:

$$\gamma_r = du_x/dy \tag{6.17}$$

$$\gamma_r = -du_y/dx \tag{6.18}$$

6.3.3. Simple shear flow

The shear flow has the capability to break-up aggregates although its effect is smaller than that of the elongational flow. Kao and Mason [23] claimed that the flow energy in the simple shear flow is consumed to rotate the aggregate while the rotation in the elongational flow is disregarded. Consequently, with less energy in the elongational flow, aggregated particles can break-up. A physical example of simple shear flow is demonstrated in Fig. 6.16, where the upper wall moves with a constant velocity while the lower wall is fixed. Figs. 6.14 and 6.15 show the streamline and velocity profile for the simple shear flow. The variable Γ for this flow is defined by the following equation:

$$\Gamma = \begin{bmatrix} 0 & \gamma_s & 0 \\ 0 & 0 & 0 \\ 0 & 0 & 0 \end{bmatrix} \tag{6.19}$$

where γ_s is the shear rate. The streamlines for shear flow are calculated by solving following equation:

$$\gamma_s = du_x/dy \tag{6.20}$$

6.4. Simulation of aggregates under elongational flow, pure rotational flow, and simple shear flow

The simulation of aggregates suspended in elongational flow, pure rotational flow and the simple shear flow are studied with the LBM in this section. Aggregates are located in the center of computational domains and suitable boundary conditions corresponding to the flow fields are applied. Forces and torques are calculated for each primary particle in the simulations. The Reynolds number in the simulations is defined as $R_e = \gamma \times a^2/\nu$, where a is the radius of a primary particle and ν is the viscosity of the fluid, which is water here. The elongational, shear and rotational flow rate, γ, are considered to be 500000 in all three cases to satisfy Stokes flow ($Re = 1.8 \times 10^{-5}$).

Forces are normalized by $6\gamma\pi\nu a^2$, which is equal to the analytical solution of the force on the sphere in the infinite domain in the Stokes flow. Moreover, torques are normalized by $8\gamma\pi\nu a^3$, which is the torque acting on the same sphere in the pure rotation flow following from the Stokes approximation. Equations 6.12, 6.13, 6.17, 6.18 and 6.20 give us the variable γ according to the desirable boundary condition in the flow. For example, γ in the simple shear flow is equal to $\gamma = du/dy = 2U/H$, where U is the velocity of the boundary and H is the height of the domain. Periodic boundary conditions in x direction are implemented for the shear flow. We use 14 lattice cells for each primary particle to have enough resolution to capture an accurate force on the particle. A body fitting grid refinement with 4 levels is used to reduce the cost of computation.

An aggregate with 500 primary particles under the described conditions in different flow fields is simulated. Streamlines around elongational flow, pure rotational flow and simple shear flow are shown in Fig. 6.7 from top to bottom, respectively. The velocity in this figure is the magnitude of the velocity, which is normalized by a variable $V(ref)$. This velocity, $V(ref)$, is equal to the the velocity of the boundary, U in the Fig. 6.14. For each flow field, there is a close up picture to magnify flow fields around the aggregate.

The magnitude of the forces applied on each primary particle in different flow fields are normalized and then depicted in Fig. 6.18. Arrows in this figure show the magnitude of the forces. Forces in the elongational flow are two times larger than in shear flow for this aggregate. Forces in pure rotation are larger than forces in shear flow but lower than in elongational flow. Particles which are far from the center of the aggregate in all flow

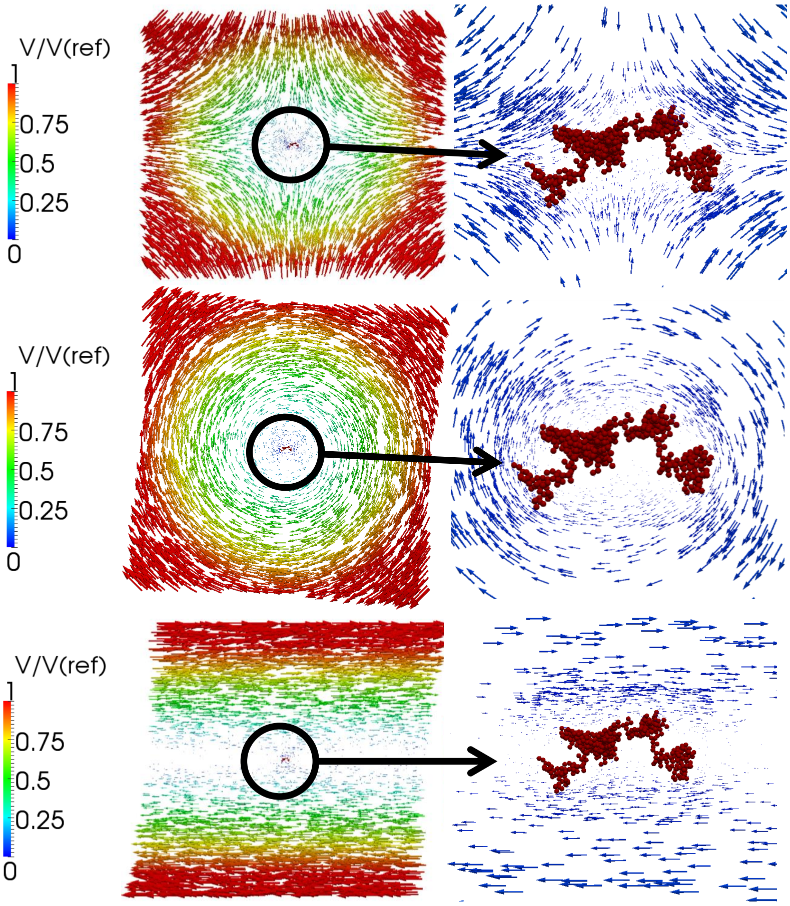

Figure 6.17.: Streamlines around three kinds of flow fields. The elongational flow, the pure rotational flow and simple shear flow are shown from up to down, respectively.

fields are exposed to larger forces. The same behavior is observed regarding the torques acting on each primary particle. These torques are calculated by multiplying forces acting on each particle with the distance of the particle from the center of the aggregate. The magnitude of the normalized torque acting on each primary particle in different flow fields is demonstrated in Fig. 6.19.

Particles in the elongational flow experience larger torque in comparsion to other flow fields. Forces and torques in pure rotational flow are larger than in shear flow for this aggregate as it is seen in these figures since this aggregate is aligned parallel to the flow. Therefore, the majority of primary particles are close to the center line where the derivative of velocities is zero. In reality, the shear flow has more potential to break-up aggregates compared to the pure rotation [146].

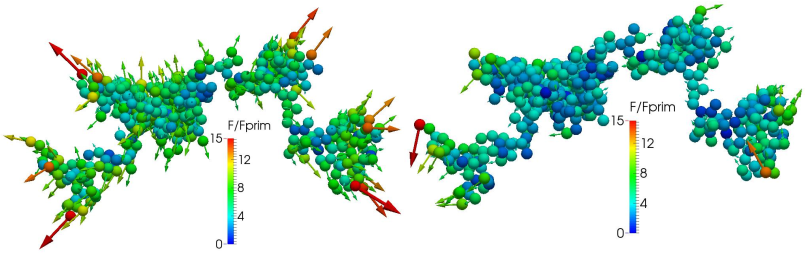

elongational flow **pure rotational flow**

simple shear flow

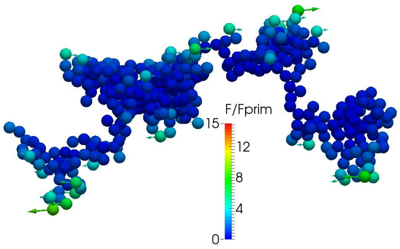

Figure 6.18.: The magnitude of normalized forces applied on each primary particle in different flow fields.

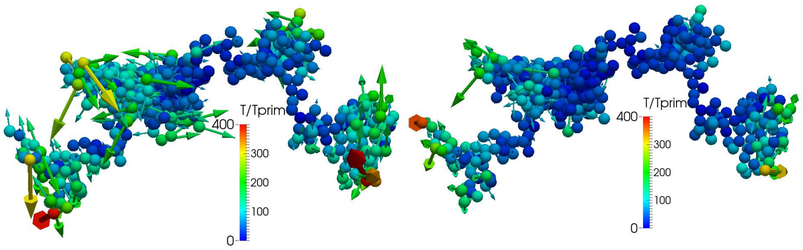

elongational flow **pure rotational flow**

simple shear flow

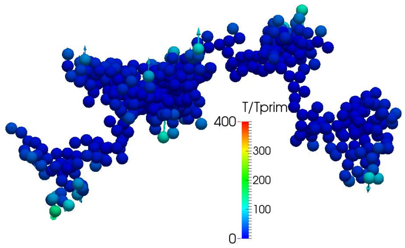

Figure 6.19.: The magnitude of normalized torque applied on each primary particle in different flow fields.

7. Numerical results for the dispersion reactor

In this chapter the micro-machined disperser is studied at high Reynolds numbers to investigate the break-up process due to the stresses acting on the aggregates. This chapter is divided into two main parts. In the first part, turbulent flow fields are shown for three different pressure differences. The acquired flow rates are compared with the experimental results to validate the simulations. The stresses generated in the flow are shown. The dissipation rate as an important factor is calculated for different input pressures. In the second part, the tracking of aggregates is studied to obtain estimations of the break-up process. In addition, the effects of the fractal dimension and the number of primary particles per aggregate on the Stokes number are investigated.

7.1. Methodology

A schematic of the micro-machined disperser is shown in Fig. 7.1. Different groups of the large aggregates are inserted on the left hand side of the disperser and pass through the orifice together with the flow. In the orifice the flow becomes turbulent. It is assumed that the generated Reynolds stresses and the time-average stresses including the elongation and shear cause the aggregates to break-up. These stresses are recorded by the pathlines of the aggregates. Three input pressures corresponding to pressure drop of 100 bar, 200 bar, and 500 bar between entrance and exit of the disperser are considered in this study.

Velocity measurements with micro PIV were only available until a pressure drop of 200 bar since the necessary glass cover broke at higher pressures. Consequently, the simulation setup, including time step and grid resolution, was chosen to accurately simulate the flow at a pressure drop of 200 bar. In CFD simulations, more resolution is required when higher pressure drops are applied on the boundaries. The simulation for a pressure drop of 500 bar is already slightly under-resolved. Therefor, the results for this case have to be used with some caution as they are expected to be less accurate than the results for the pressure drop of 200 bar.

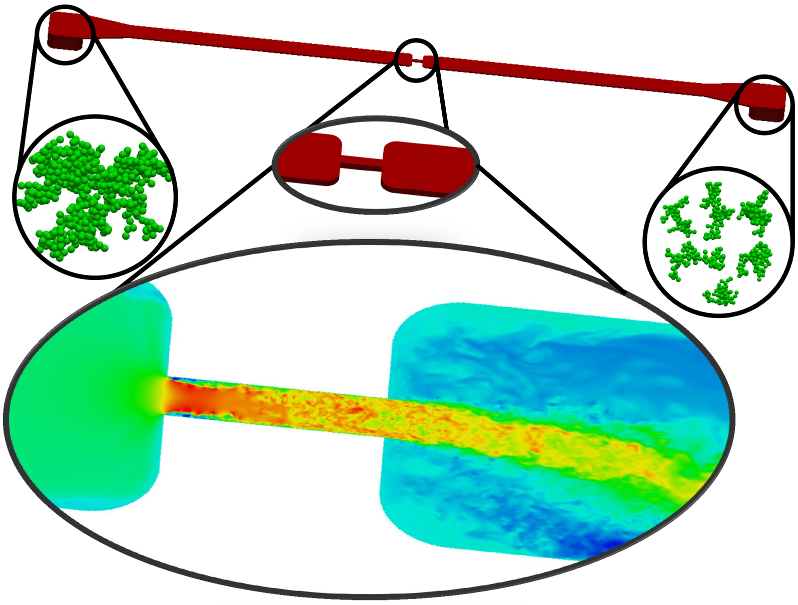

Figure 7.1.: A schematic of the breakage process due to stresses acting on the aggregates released ate the left hand side of the micro-machined disperser.

The cumulant LBM is used to study the disperser. Stresses exerted on the aggregates are recorded using compact second-order interpolation.

7.2. Geometry, meshing, and boundary conditions

The micro-machined disperser [58] considered in this study is a channel of two centimeters in length with an orifice in the center of 80 microns width, 50 microns height, and 300 microns length (Fig. 7.2). Only half of the disperser geometry is displayed since the shape is symmetric in x-direction.

In general, high velocity gradients are observed close to the wall which is why the highest grid resolution has to be spent there. A commonly used grid independent criterion for CFD simulations is a $y+$ value of the order of one or smaller [157]. In terms of the LBM $y+$ is the non dimensional resolution at the wall perpendicular to the wall. When this value is close to one, the turbulent eddies in the boundary layer are appropriately resolved. When the pressure drops of 200 bar and 500 bar are applied on the system, one more grid level in comparison to the 100 bar case is added to the orifice to keep the $y+$ value close to one.

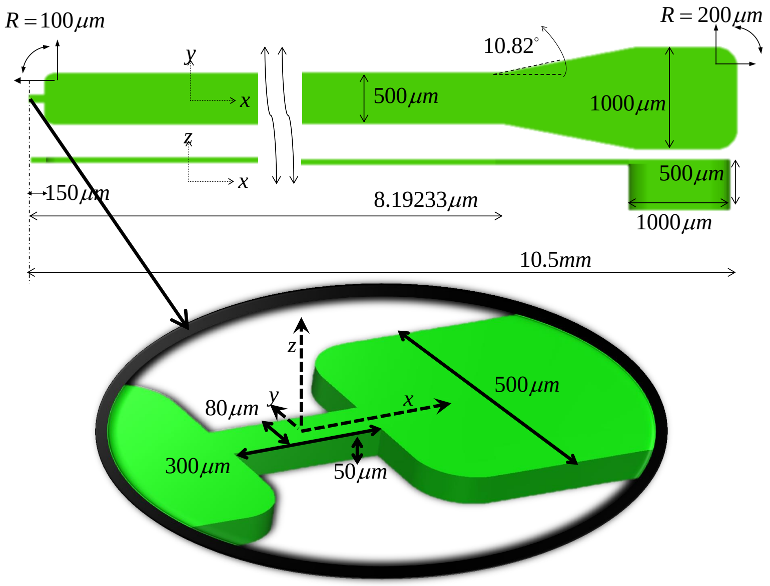

Figure 7.2.: A schematic of the micro-machined disperser.

A zoom into the orifice region of the disperser for three pressure drops are demonstrated in Fig. 7.3. Four grid levels for pressure drops of 200 bar and 500 bar and three grid levels for a pressure drop of 100 bar are used. Each square of the grid in this figure corresponds to a cube of 16^3 grid nodes resulting in a total number of 65×10^6 grid points and 1.7×10^{10} degrees of freedom for the flow computation at the pressure drop of 200 bar. The coarsest grid with a grid spacing of $\Delta x = 4.96$ micro meter is where the velocity gradients are low. The finest grids close to the wall in the orifice have $\Delta x = 0.62$ micro meter and $\Delta x = 0.31$ micro meter for the pressure drops of 100 bar and 500 bar, respectively. In the 200 bar case the area close to the wall in the orifice is only partly refined to the highest resolution.

A pressure differences of 100 bar and 200 bar between inlet and outlet is imposed to compare the results with available micro PIV measurements [1]. Since the device is designed to operate at higher pressure drops than those for which micro PIV measurements are available we also study a case with a pressure drop of 500 bar.

A no-slip boundary condition is applied on the wall. The viscosity of water is imposed and the time step is set to be $6.125 \times 10^{-10}s$ in all three cases.

The computation is carried out on 120 Intel Nehalem compute nodes (2.6 GHZ) with eight cores each. A sample of the METIS partitioning is shown in chapter 4. The related information to the number of nodes, the number of blocks, run time for one time step, and the performances per process for each simulation are given in table (7.1).

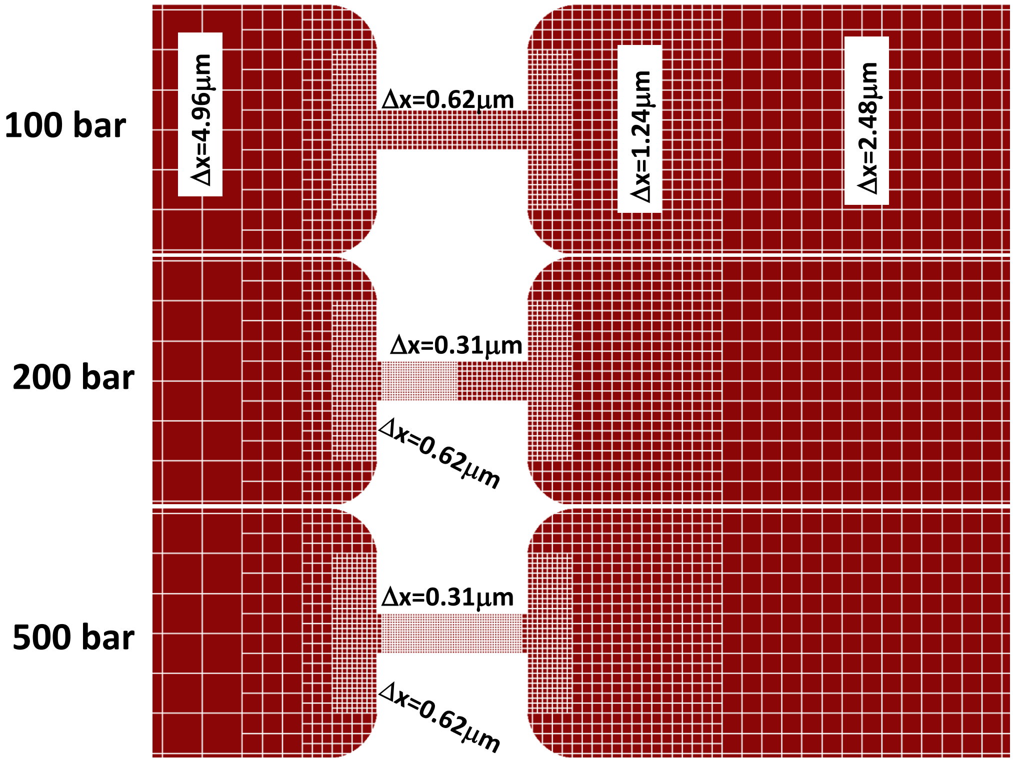

Figure 7.3.: Zoom into the grid of the disperser close to the wall for three pressure differences. Each cell contains 16^3 lattice nodes.

The 500 bar case requires 38% more nodes than the 100 bar case. Only the area close to the wall of the orifice has been refined with level four in the 500 bar case since resolving the complete orifice with level four would require more than one billion grid nodes. Simulations with such a large number of nodes are not feasible within our hardware constraints. With our strategy we obtain a $y+$ value close to one with an acceptable computational effort as depicted in Fig. 7.4.

After the flow field develop turbulent profile, aggregates are released in the disperser at random positions in front of the orifice. The simulation is continued until at least 95% of the aggregates have passed through the orifice. The complete history of stresses experienced by the aggregates is recorded. The density and radius of the primary particles are 2200kg/m^3 and 6 nano-meter, respectively.

Pressure	# Nodes	# Blocks	Time / time step	Performance / process
100(bar)	57(million)	13936	0.7181(s)	0.33474(MNUPS)
200(bar)	65(million)	15857	1.5352(s)	0.24195(MNUPS)
500(bar)	79(million)	19312	2.292(s)	0.2693(MNUPS)

Table 7.1.: Information on the simulation setups and their performance. MNUPS means Million Node Updates Per Second. The performance values are obtained without recording pathlines. Including 4000 pathlines, the calculation of the stresses, and averaging of the particle velocity and the dissipation increase the computational time per time step by about 50% in the 100 bar case.

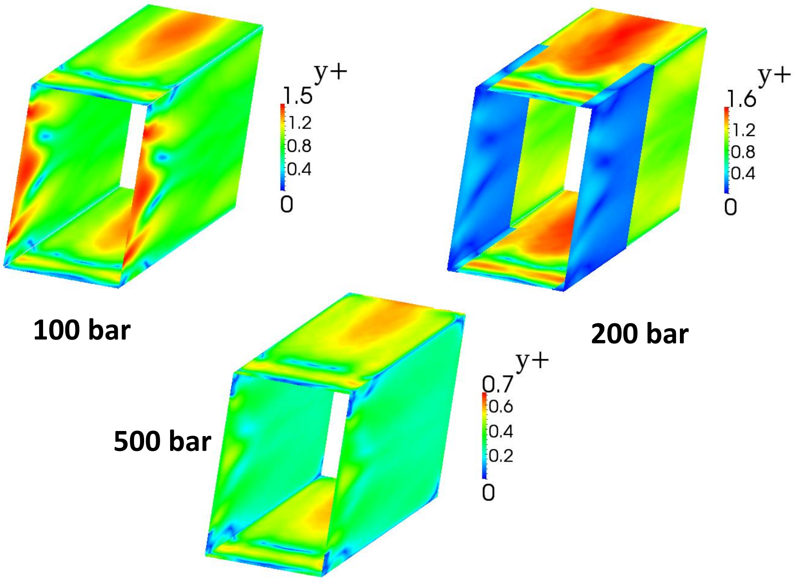

Figure 7.4.: The variable $y+$ for the three pressure drops of 100 bar, 200 bar, and 500 bar. In the 200 bar case two different resolutions are used close to the wall. The better resolved part at the entrance of the orifice appears in blue in the figure.

7.3. Flow simulations

The flow rates acquired by our simulations are compared with the experimental measurement to validate our results. The results are shown in Fig. 7.5. The deviations between the LBM simulation and the experiment for the pressure drops 100 bar, 200 bar, and 500 bar are 1.57%, 1.51%, and 2.84%, respectively. It is observed that our results are in close agreement to the experimental results.

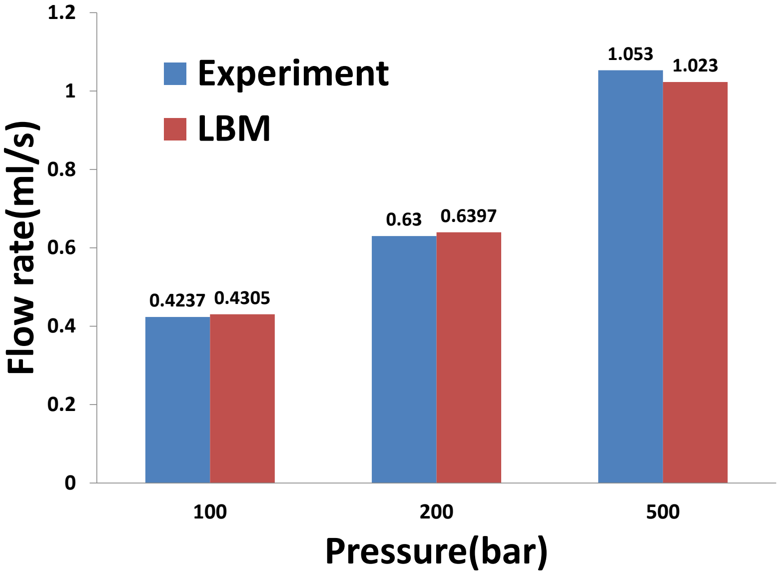

Figure 7.5.: Comparison between flow rates obtained by the LBM simulation and by experiment for the three pressure drops of 100 bar, 200 bar, and 500 bar.

The average velocity obtained by PIV and the LBM in the orifice of the disperser for two pressure drops are shown in the Fig. 7.6. The upper picture of each part shows the average of 600 PIV measurements of the disperser at a pressure difference of 100 bar and 200 bar [1]. The lower picture shows an average velocity from the simulation of the same device in center plane. The averaging interval corresponds to 24.5 microseconds real time. In addition, the average velocity acquired by the LBM for pressure drop 500 bar is shown in 7.7. The micro PIV measurement for 500 bar is not available as the setup broke down for pressure differences lager than 200 bar.

The device is symmetric along its x-axis as depicted in Fig. 7.2. Consequently our simulation setup is also symmetric. However, the resulting fluid field is not symmetric as the jet attaches randomly to either the left or the right wall and stays there for the whole duration of the measurement or the simulation. Coincidentally, the jet attached to the left wall in the measurement and to the right wall in the simulation. In order to facilitate the comparison of the two pictures we show a mirror image of the simulation result in Fig. 7.6. The reattachment point, where the flow close to the wall changes direction, is measured in the 200 bar simulation to be 885 microns away from the entrance of the orifice. This is compatible to the PIV measurements. The reattachment points are almost the same for all three cases. It is seen that the magnitude of the velocity at the entrance is high. Two vortexes are observed at the corners of the device in upstream of the orifice. Downstream of the orifice, very large asymmetric vortexes are observed.

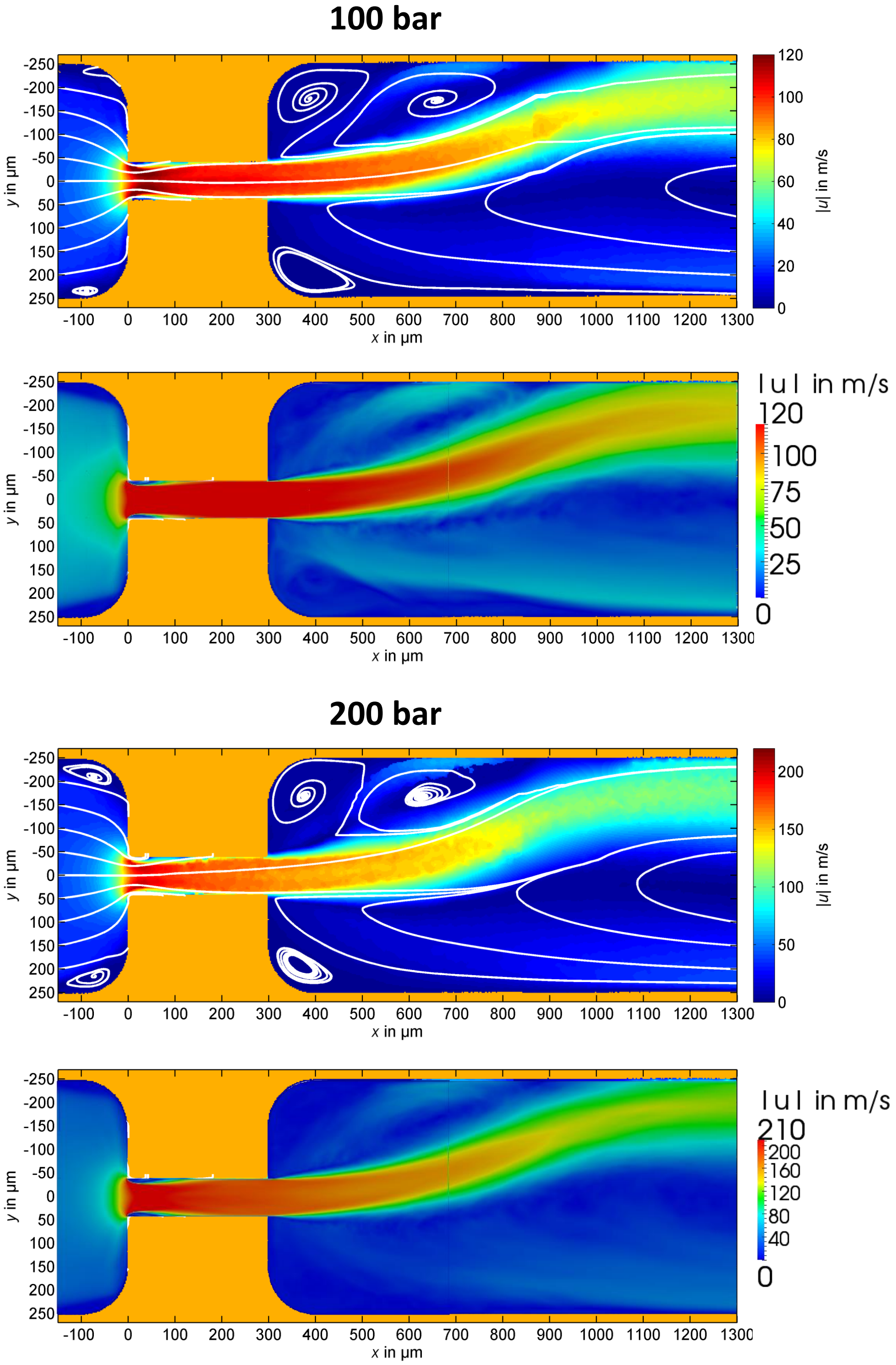

Figure 7.6.: Comparison of PIV velocity measurements to the LBM simulation. The first and third pictures from top show the average of 600 PIV measurements of the micro-machined disperser at a pressure difference of 100 bar and 200 bar, respectively [1]. Pictures two and four show an average of 40000 time steps of the simulation of the same device in center plane corresponding to a real time interval of 24.5 microseconds.

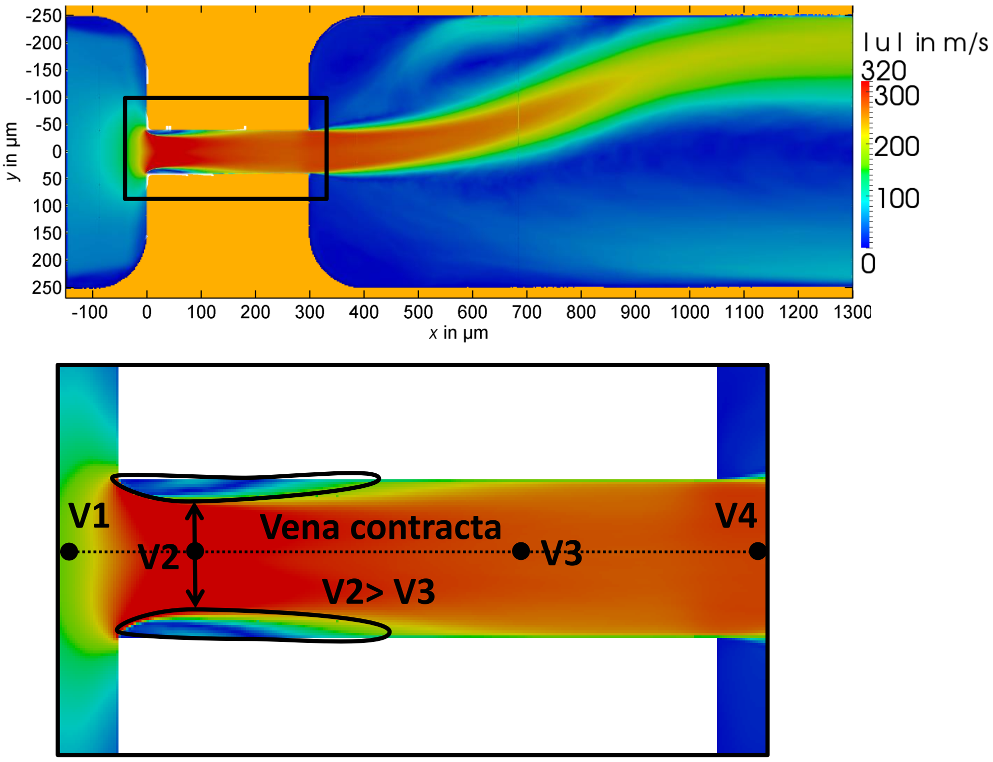

Figure 7.7.: The upper picture shows an average of 40000 time steps of the simulation of the disperser at a pressure difference of 500 bar. The lower picture shows a zoom into the velocity field. The effect of the vena contracta is demonstrated.

In addition to the average velocity Fig. 7.7 demonstrates the vena contracta effect. The vena contracta reduces the effective area and increases the velocity. Thus, it is observed that the velocity in position 2, V_2, is bigger that the velocity in position 3, V_3. This phenomenon is a classical problem in fluid mechanics and researchers try to eliminate it in some ways such as rounding the entrance region [43]. An orifice usually has two loss coefficients: the loss coefficient for a sudden contraction and the loss coefficient for a sudden expansion. Streeter [158] calculated the loss coefficient for a sudden contraction and the sudden expansion and provided approximations for these coefficients in relation to the ratios of the cross sections. For our disperser, the loss coefficients extracted from his plot are 0.42 and 0.68 for the sudden expansion and the sudden contraction, respectively. In general, these loss coefficients are related to the head loss calculated from the energy equation between points 1 and 2, points 3 and 4 [43].

The center line magnitude velocities for three different pressure drops of 100 bar, 200 bar and 500 bar are shown in Fig. 7.8. The lines go from 50 micro meter before the orifice entrance and 50 micro meter after the orifice exit. The position $x = 0$ coincides with the entrance of the orifice. The velocity in each case reaches the maximum value at point V_2

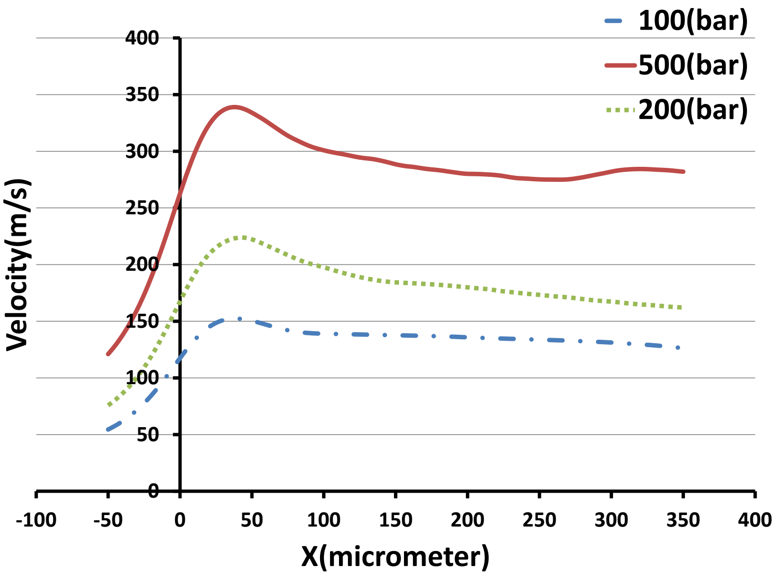

Figure 7.8.: The center line magnitude velocity for three cases. The positions $x = 0$ and $x = 300$ micro meter coincide with the entrance and the exit of the orifice, respectively.

(Fi. 7.7). The velocity growths over a short distance when entering.

The time averaged pressure in and behind the orifice is depicted for the 100 bar and 500 bar cases in Fig. 7.9. It is shown for two different planes: $z = -17$ micro meter and $z = -34$ micro meter according to Fig. 7.2.

Fig. 7.9 shows the reason why the jet is attached to the wall after leaving the orifice. In the volume confined by the jet and the wall in negative y direction the pressure drops due to the suction effect of the moving jet. This lowers the pressure in the confined volume relative to the pressure in the open volume on the other side of the jet. The pressure difference between the confined and the open volume drives the jet towards the confined volume. While the jet oscillates downstream of the orifice it was never observed in the simulation or the experiment that the jet would switch to the other wall once it was attached.

The time averaged pressure is averaged over $y - z$ planes and plotted along the main flow direction (x direction) for the 100 bar and 500 bar cases in Fig. 7.10. The orifice entrance is located at x=0. The pressure drops suddenly at the entrance and reaches its minimum value where the velocity has its maximum. The pressure drops further at the exit of the orifice. This effect is much more pronounced in the 500 bar case than in the 100 bar case. Fig. 7.10 helps us to calculate the head loss between two points along the x direction

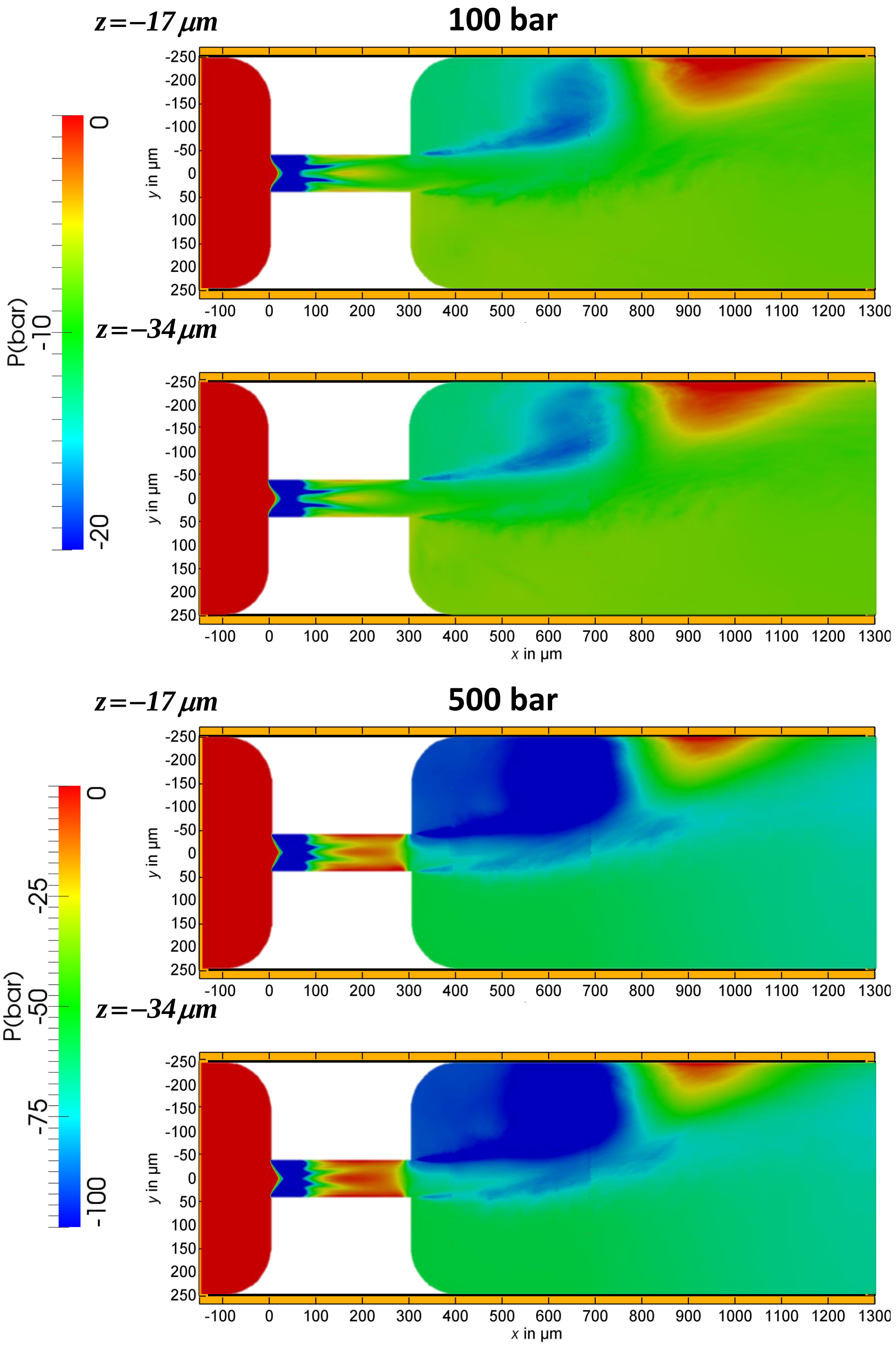

Figure 7.9.: The time averaged pressure for the 100 bar and and the 500 bar cases at two different planes. The upper picture for each set shows the pressure for plane $z = -17$ micro meter and the lower shows the pressure for $z = -34$ micro meter.

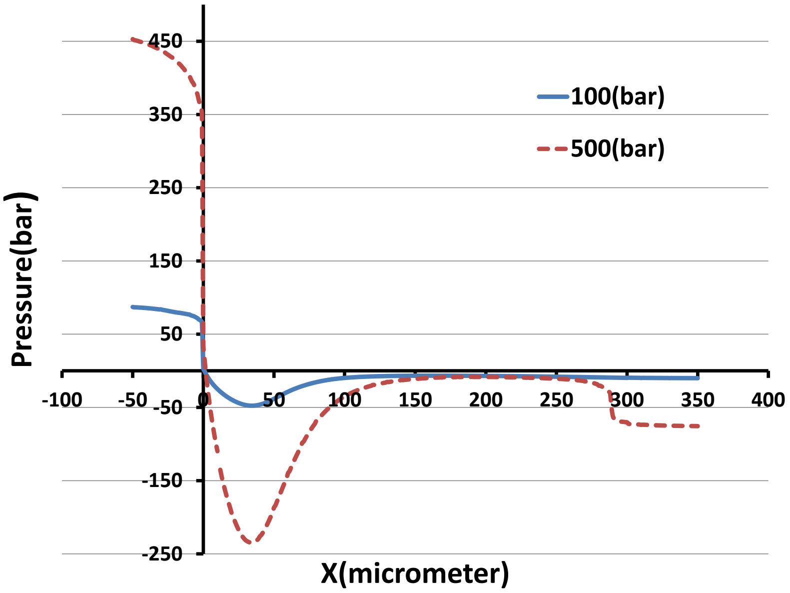

Figure 7.10.: The time averaged pressure over z direction through the orifice for the 100 bar case and the 500 bar case. The position $x = 0$ and $x = 300$ micro meter coincide with the entrance and the exit of the orifice, respectively.

[43]. With the flow rate known the only required parameter for the energy equation is the pressure drop between the two points.

7.3.1. Fluid flow intensity

The normal and tangential fluid forces acting on the surface of the aggregates deform and subsequently disrupt the aggregates. The stresses are calculated by the velocity-gradient components. The strain rate tensor is composed of the nine velocity-gradient components of which three are normal strain components and six are tangential strains components. The magnitude of the strain rate tensor is an indicator for the deformation forces causing the aggregate breakage to occur. It can be written in terms of velocity-gradients as:

$$\begin{aligned} S^2 = &\left[\frac{\partial u}{\partial x}\left(\frac{\partial u}{\partial x}+\frac{\partial u}{\partial x}\right)+\frac{\partial u}{\partial y}\left(\frac{\partial u}{\partial y}+\frac{\partial v}{\partial x}\right)+\frac{\partial u}{\partial z}\left(\frac{\partial u}{\partial z}+\frac{\partial w}{\partial x}\right)\right]+\\ &\left[\frac{\partial v}{\partial x}\left(\frac{\partial v}{\partial x}+\frac{\partial u}{\partial y}\right)+\frac{\partial v}{\partial y}\left(\frac{\partial v}{\partial y}+\frac{\partial v}{\partial y}\right)+\frac{\partial v}{\partial z}\left(\frac{\partial v}{\partial z}+\frac{\partial w}{\partial y}\right)\right]+\\ &\left[\frac{\partial w}{\partial x}\left(\frac{\partial w}{\partial x}+\frac{\partial u}{\partial z}\right)+\frac{\partial w}{\partial y}\left(\frac{\partial w}{\partial y}+\frac{\partial v}{\partial z}\right)+\frac{\partial w}{\partial z}\left(\frac{\partial w}{\partial z}+\frac{\partial w}{\partial z}\right)\right] \end{aligned} \tag{7.1}$$

In order to obtain the velocity-gradients in this equation a finite difference scheme is implemented in common CFD methods. Thus, each grid node needs information from its neighbors. In the LBM the strain rate can be computed locally from the non-equilibrium part of the distribution function. The above equation is rewritten according to the strain rate instead of the velocity-gradients as:

$$S^2 = 2({s_{xx}}^2 + {s_{yy}}^2 + {s_{zz}}^2 + 2{s_{xy}}^2 + 2{s_{xz}}^2 + 2{s_{yz}}^2) \tag{7.2}$$

By convention the magnitude of the strain rate tensor is defined as [159, 160]:

$$S^2 = 2s : s = 2s_{ij}s_{ji} \tag{7.3}$$

where the strain rate component s_{ij} is:

$$s_{ij} = \frac{1}{2}\left(\frac{\partial u_i}{\partial x_j} + \frac{\partial u_j}{\partial x_i}\right) \tag{7.4}$$

The dissipation rate is a useful parameter for the characterization of the local hydrodynamic conditions and flow field intensities.

$$\epsilon = \nu S^2 \tag{7.5}$$

The total dissipation rate is obtained from the sum of the averaged energy dissipation rate and the turbulent dissipation rate according to the following equation [161]:

$$\epsilon_{total} = \epsilon_{fluctuation} + \epsilon_{mean} = 2\nu\overline{s'_{ij}s'_{ij}} + 2\nu\bar{s}_{ij}\bar{s}_{ij} \tag{7.6}$$

The corresponding stress can be acquired as:

$$\tau = \mu\sqrt{\epsilon/\nu} \tag{7.7}$$

The higher the dissipation, the more aggregate breakage is observed in the system [8]. Fig. 7.11 shows the logarithm of the dissipation rates for the 100 bar and 500 bar cases from 50 micro meter before to 50 micro meter after the orifice. There is a substantial increase in the dissipation rate at the entrance of the orifice in comparison to 50 micro meter before the entrance. Two peaks are observed in the dissipation, one is exactly at the entrance and another one is at position $x = 46$ micro meter. It is the same position where the maximal velocity and the minimal pressure is observed.

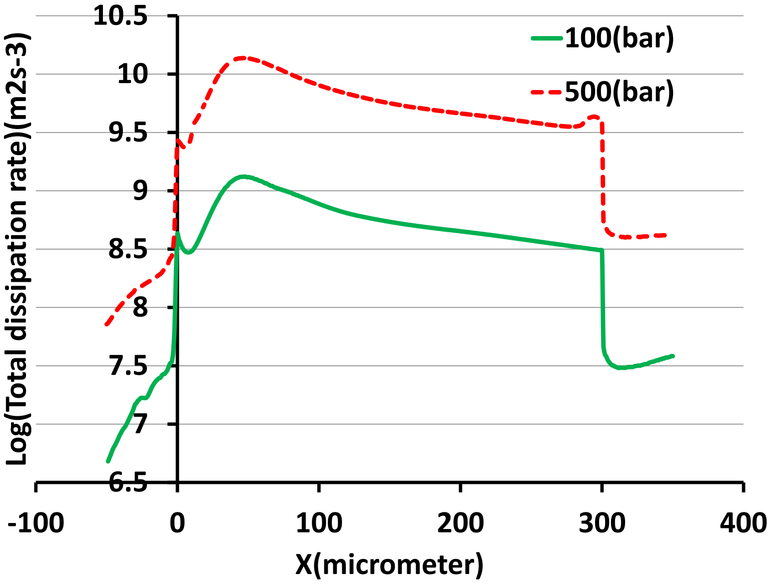

Figure 7.11.: The logarithm form of the total dissipation rates versus x-direction for two pressure drops. The dissipation rates are averaged over the z direction. The position $x = 0$ coincides with the orifice entrance.

Q-criterion

There are Eulerian and Lagrangian methods to detect coherent structures (eddies) in a flow [162, 163]. Many of the Eulerian methods are based on the velocity gradient tensor [163–165]. One such method is the Q-criterion [166]. The second invariant of the velocity gradient tensor is called Q and can be given by:

$$Q = \frac{1}{2}[|\Omega^2| - |s|^2] \tag{7.8}$$

where the antisymmetric part or the vorticity tensor is:

$$\Omega_{ij} = \frac{1}{2}\left(\frac{\partial u_i}{\partial x_j} - \frac{\partial u_j}{\partial x_i}\right) \tag{7.9}$$

The Q-criterion is applied to detect the dominance of the vorticity over the strain. The vorticity is dominant when $Q > 0$ while strain is dominant for $Q < 0$. A zero contour of Q can be used to visualize vortexes.

Fig. 7.12 to Fig. 7.14 show contours for $Q = 0$ for the three cases. Q is calculated for the averaged velocity fields in this figures. Long vortex tubes are observed at the entrance of

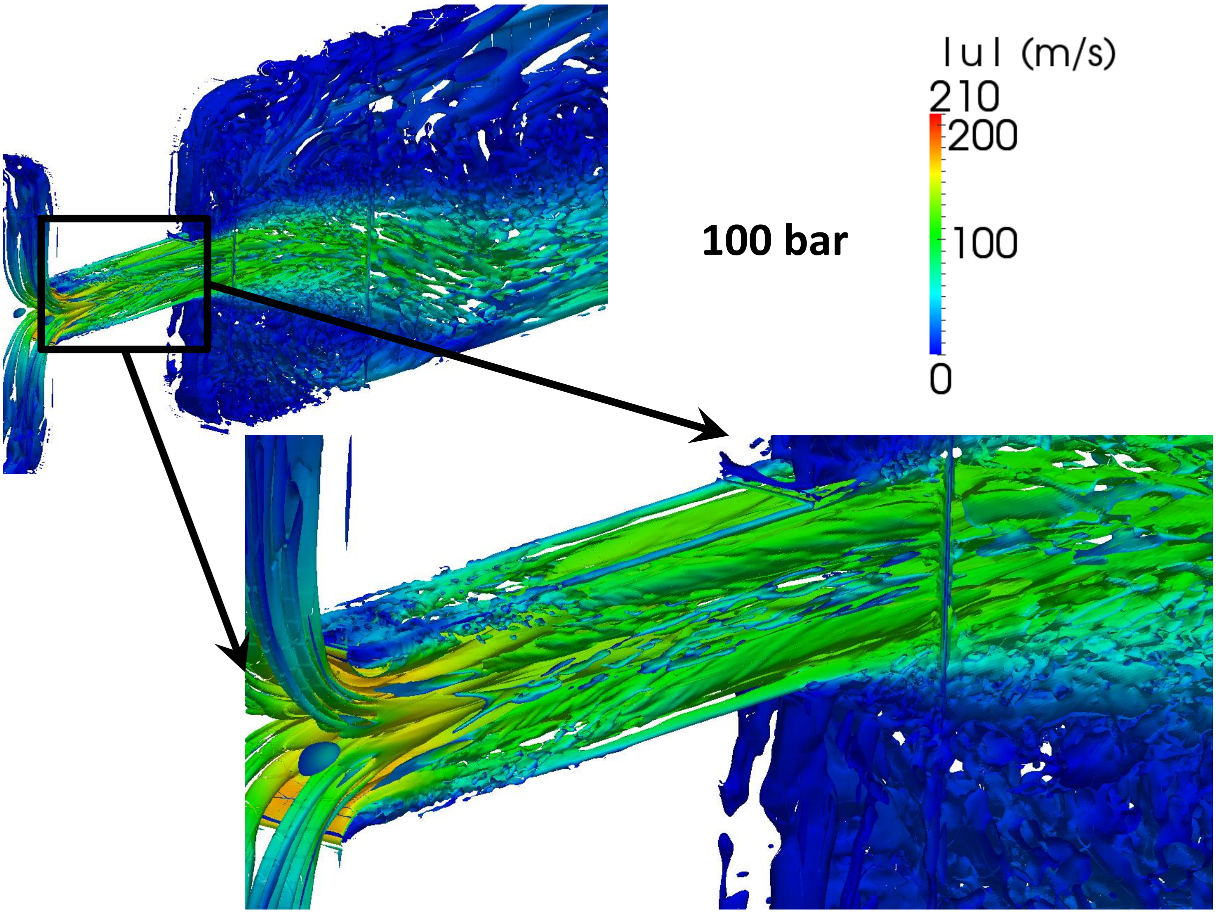

Figure 7.12.: The Q-criterion for the time averaged flow through the disperser for the 100 bar case. The color shows the magnitude of the velocity.

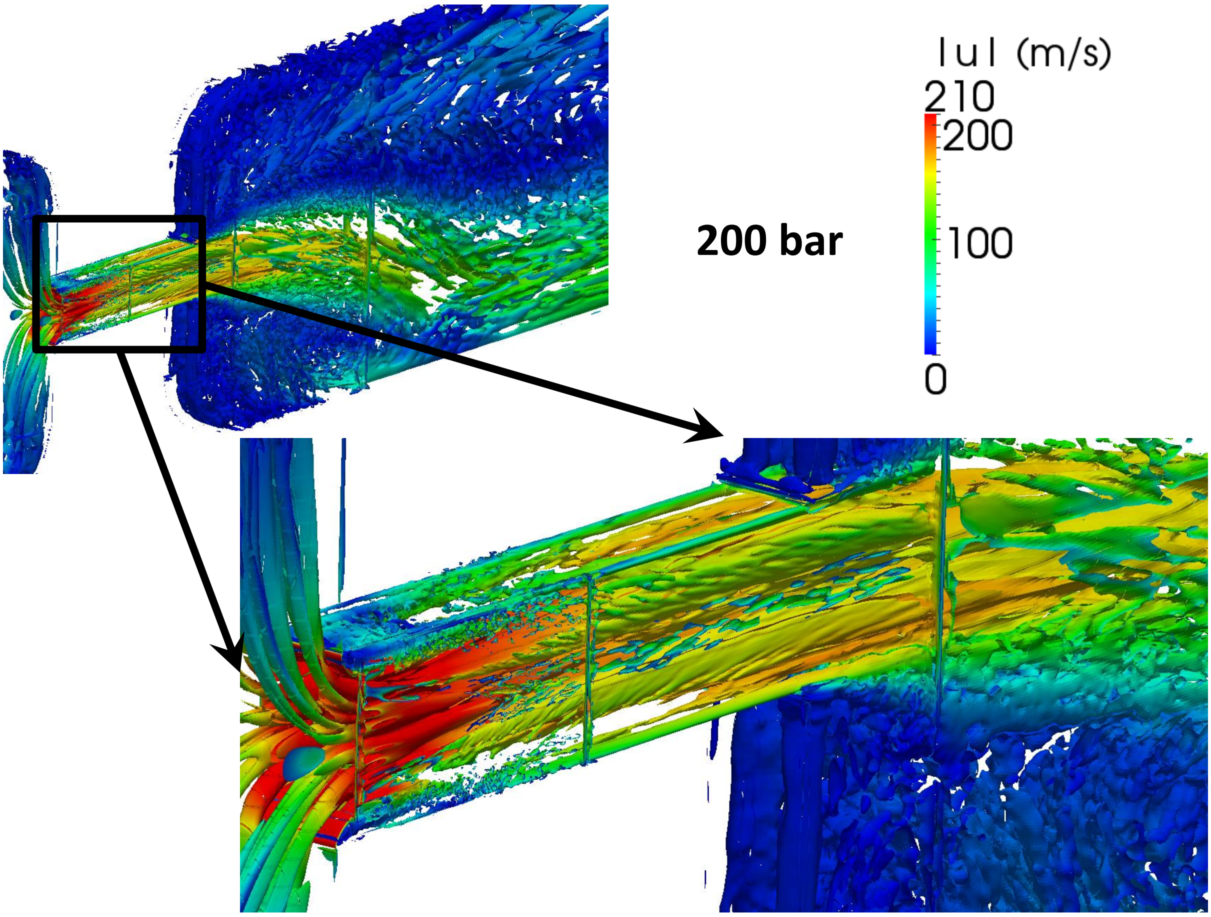

Figure 7.13.: The Q-criterion for the time averaged flow through the disperser for the 200 bar case. The color shows the magnitude of the velocity.

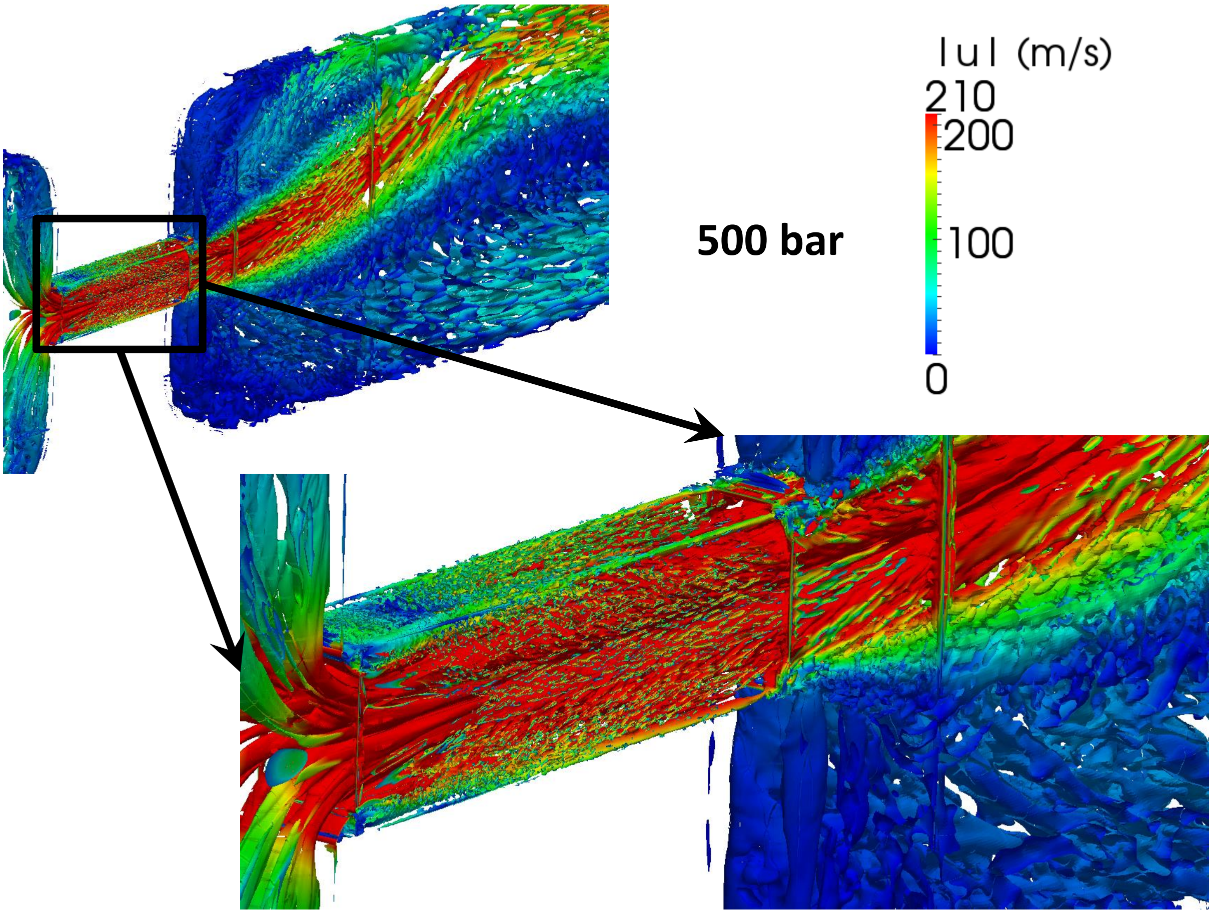

Figure 7.14.: The Q-criterion for the time averaged flow through the disperser for the 500 bar case. The color shows the magnitude of the velocity.

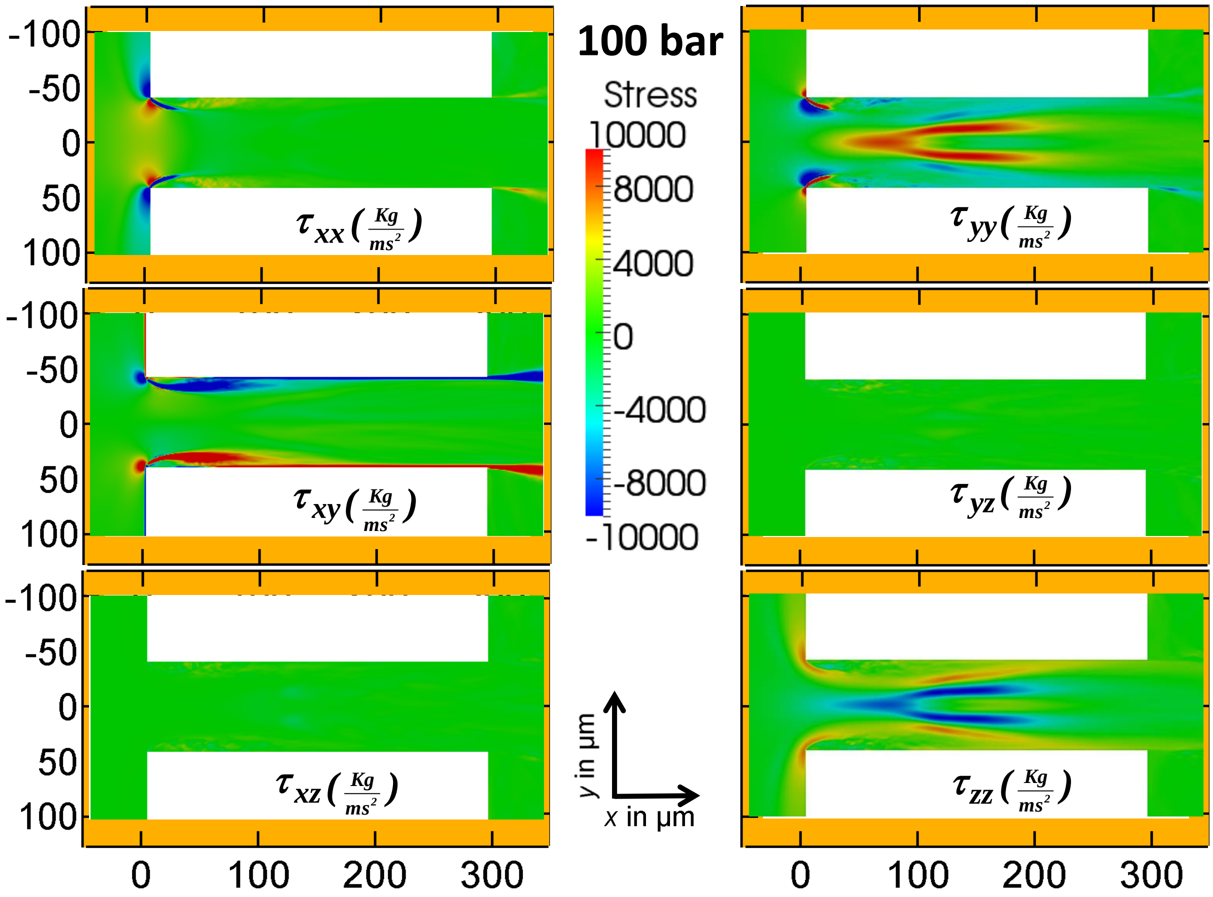

Figure 7.15.: The laminar stress components generated in the orifice in the mid plane for a pressure drop of 100 bar.

the orifice. With increasing pressure drop and Reynolds number finer vortex structures develop in the orifice.

Laminar and turbulent stresses

The stresses generated by the fluid flow and acting on the aggregates can be divided into laminar stresses and turbulent stresses [167–170].

$$\tau = \tau_l + \tau_t \tag{7.10}$$

where τ_l and τ_t are the laminar stress tensor and turbulent stress tensor, respectively. A stress tensor is given by:

$$\tau = \begin{bmatrix} \tau_{xx} & \tau_{xy} & \tau_{xz} \\ \tau_{yx} & \tau_{yy} & \tau_{yz} \\ \tau_{zx} & \tau_{zy} & \tau_{zz} \end{bmatrix} \tag{7.11}$$

The laminar stress tensor consists of the average velocity derivatives [167]:

$$\tau_l = \mu \begin{bmatrix} \tau_{xx} & \tau_{xy} & \tau_{xz} \\ \tau_{yx} & \tau_{yy} & \tau_{yz} \\ \tau_{zx} & \tau_{zy} & \tau_{zz} \end{bmatrix} = \mu \begin{bmatrix} \frac{\partial \overline{u}}{\partial x} + \frac{\partial \overline{u}}{\partial x} & \frac{\partial \overline{u}}{\partial y} + \frac{\partial \overline{v}}{\partial x} & \frac{\partial \overline{u}}{\partial w} + \frac{\partial \overline{w}}{\partial x} \\ \frac{\partial \overline{v}}{\partial x} + \frac{\partial \overline{u}}{\partial y} & \frac{\partial \overline{v}}{\partial y} + \frac{\partial \overline{v}}{\partial y} & \frac{\partial \overline{v}}{\partial z} + \frac{\partial \overline{w}}{\partial y} \\ \frac{\partial \overline{w}}{\partial x} + \frac{\partial \overline{u}}{\partial z} & \frac{\partial \overline{w}}{\partial y} + \frac{\partial \overline{v}}{\partial z} & \frac{\partial \overline{w}}{\partial z} + \frac{\partial \overline{w}}{\partial z} \end{bmatrix} \tag{7.12}$$

The turbulent stress tensor is the same as the Reynolds stress tensor ($\tau_{ij}^R = -\rho\overline{u_i'u_j'}$) [161, 171]:

$$\tau_t = \begin{bmatrix} \tau_{xx} & \tau_{xy} & \tau_{xz} \\ \tau_{yx} & \tau_{yy} & \tau_{yz} \\ \tau_{zx} & \tau_{zy} & \tau_{zz} \end{bmatrix} = -\rho \begin{bmatrix} \overline{u'u'} & \overline{u'v'} & \overline{u'w'} \\ \overline{u'v'} & \overline{v'v'} & \overline{v'w'} \\ \overline{u'w'} & \overline{v'w'} & \overline{w'w'} \end{bmatrix} \tag{7.13}$$

The laminar stresses produced in the orifice for the 100 bar and 500 bar cases in the mid plane are demonstrated in Fig. 7.15 and 7.16. The six independent stress components are depicted in each figure. In general, if the coordinate system is aligned with the flow direction, the diagonal components of the stress tensor cause a fluid element to be elongated. The diagonal components of the stress tensor in Fig. 7.15 and 7.16 are dominant. They can have significant effects on the aggregates breakage. From the non-diagonal components only τ_{xy} has a significant contribution to the stress in the mid plane. However, closer to the wall the non-diagonal parts of the stress tensor become dominate as depicted in Fig. 7.17.

In order to distinguish the effects of each stress component quantitatively, the magnitude of the stress is averaged over $y - z$ planes and plotted along the length of the orifice (Fig. 7.18). The upper figure shows the stress components from 50 micro meter before to 50 micro meter after the orifice. The lower figure demonstrates a close-up of the upper figure. At the entrance, the diagonal components of stress tensor τ_{xx} and τ_{yy} are dominant. The stress component τ_{xx} decreases along the orifice. The stress component τ_{xy} shows a complicated behavior. It starts from a low value and reach its maximum among at a short distance before the entrance. After a short distance from the entrance it reaches a local minimum.

The turbulent stresses can have different effects on the aggregate breakage dependent on the turbulent length scale. It has been suggested that the breakage mechanism of aggregates is controlled by the Kolmogorov microscale [36, 172]. Aggregates are more likely to break into large fragmentation where the aggregate diameter is notably lager than the Kolmogorov scale. Surface erosion is considered to dominate the break-up where the aggregate diameter is remarkably smaller than Kolmogorov scale. Therefor, knowing

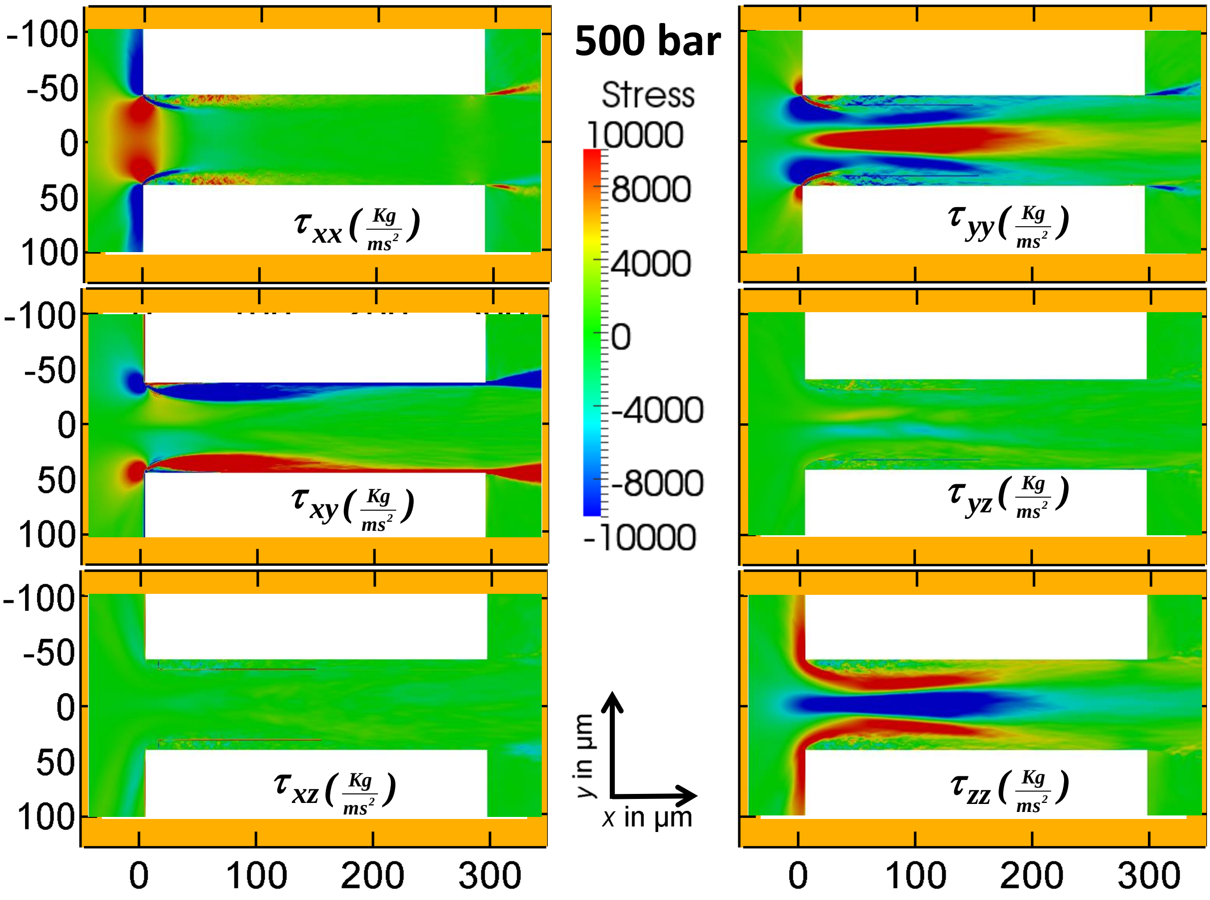

Figure 7.16.: The laminar stress components generated in the orifice in the mid plane for a pressure drop of 500 bar.

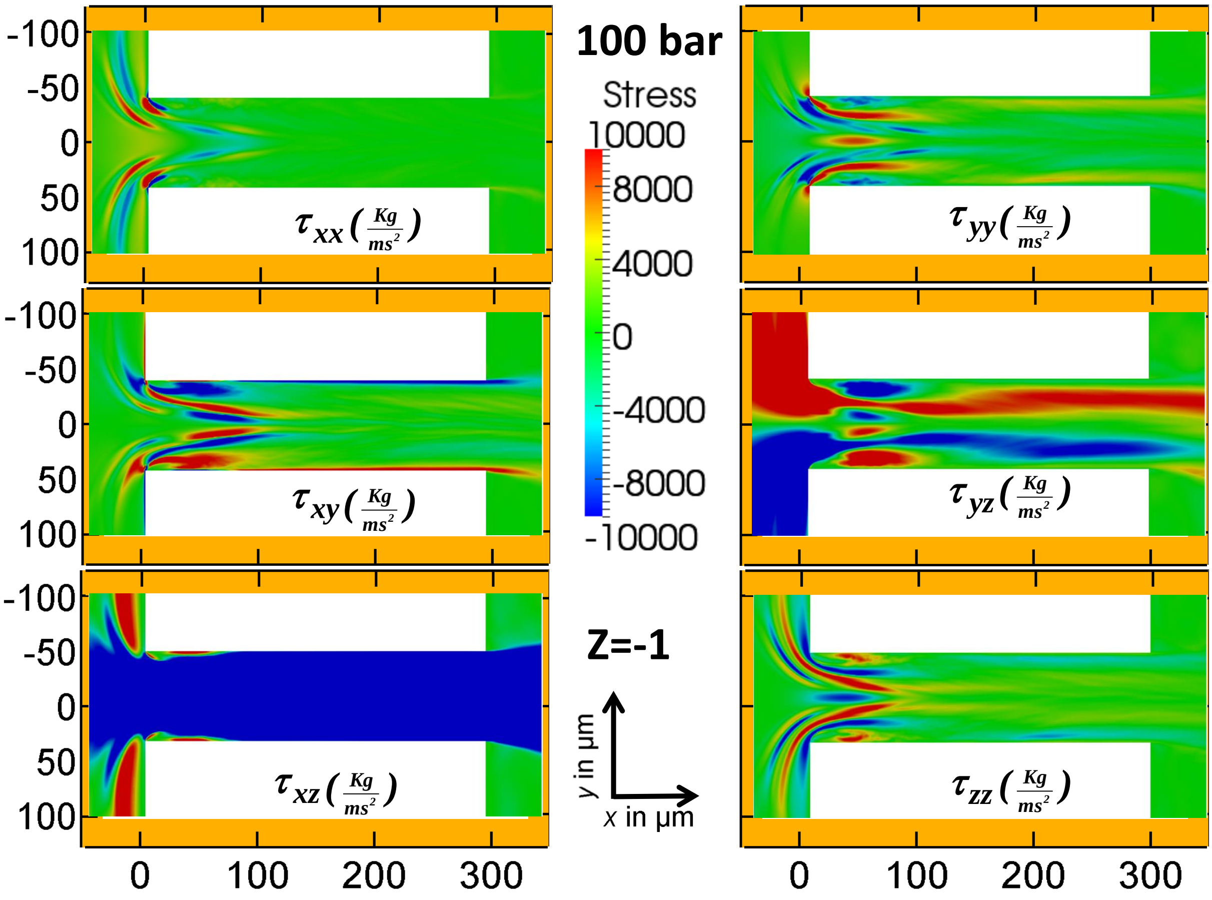

Figure 7.17.: The laminar stress components generated in the orifice in plane $z = -1$ for a pressure drop of 100 bar.

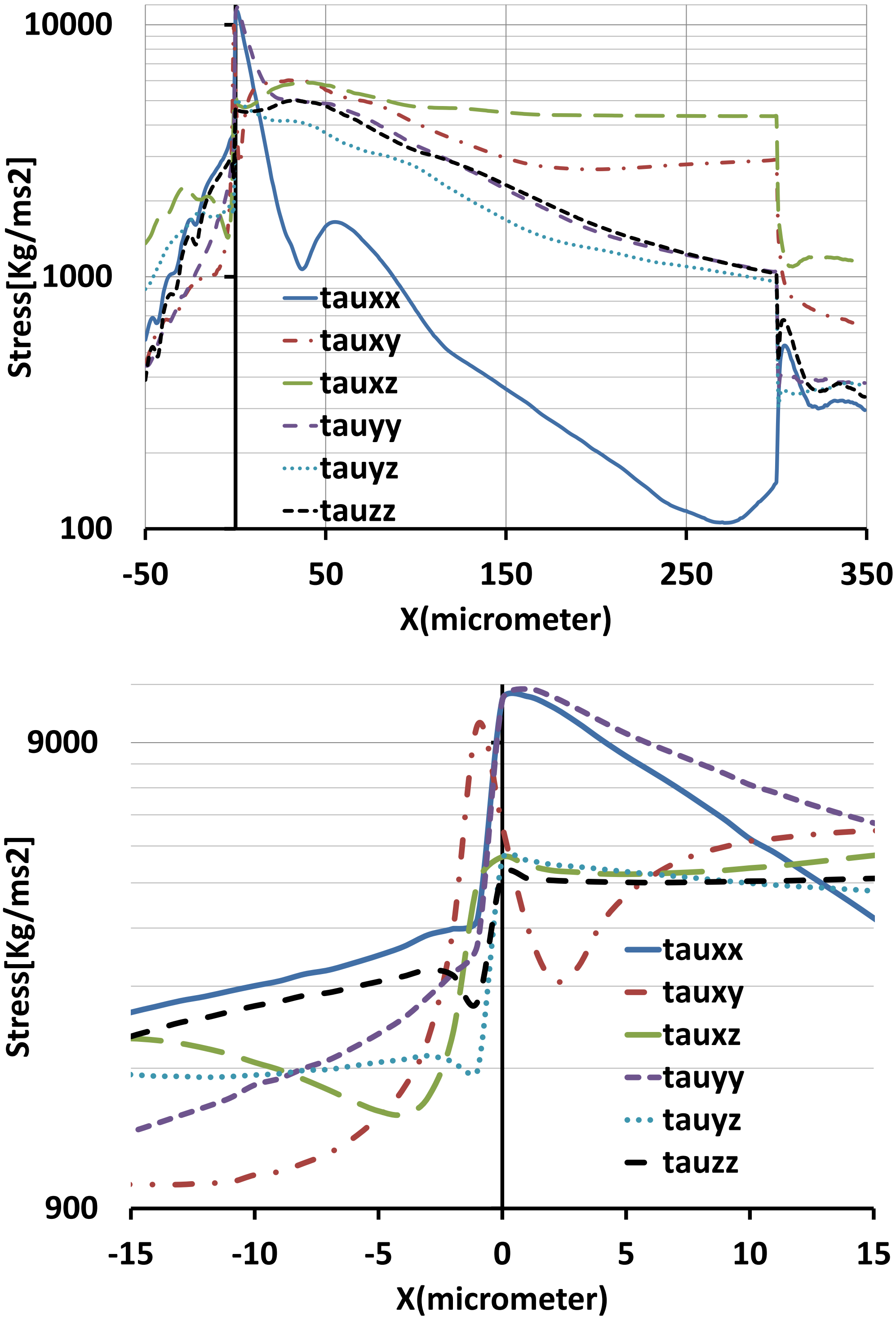

Figure 7.18.: The laminar stress components averaged over $y-z$ planes plotted in x direction for a pressure drop of 100 bar.

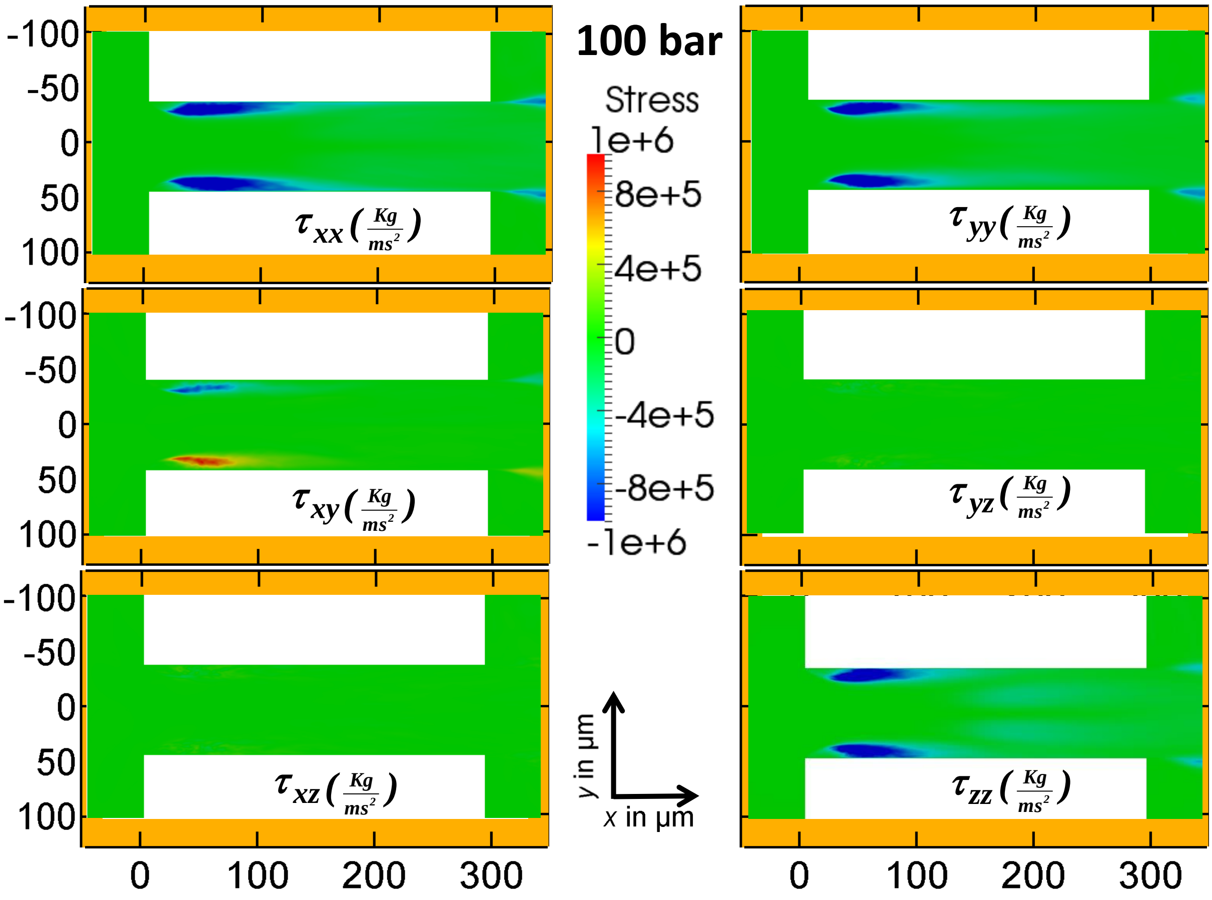

Figure 7.19.: The turbulent stress components generated in the orifice in the mid plane for pressure drop of 100 bar.

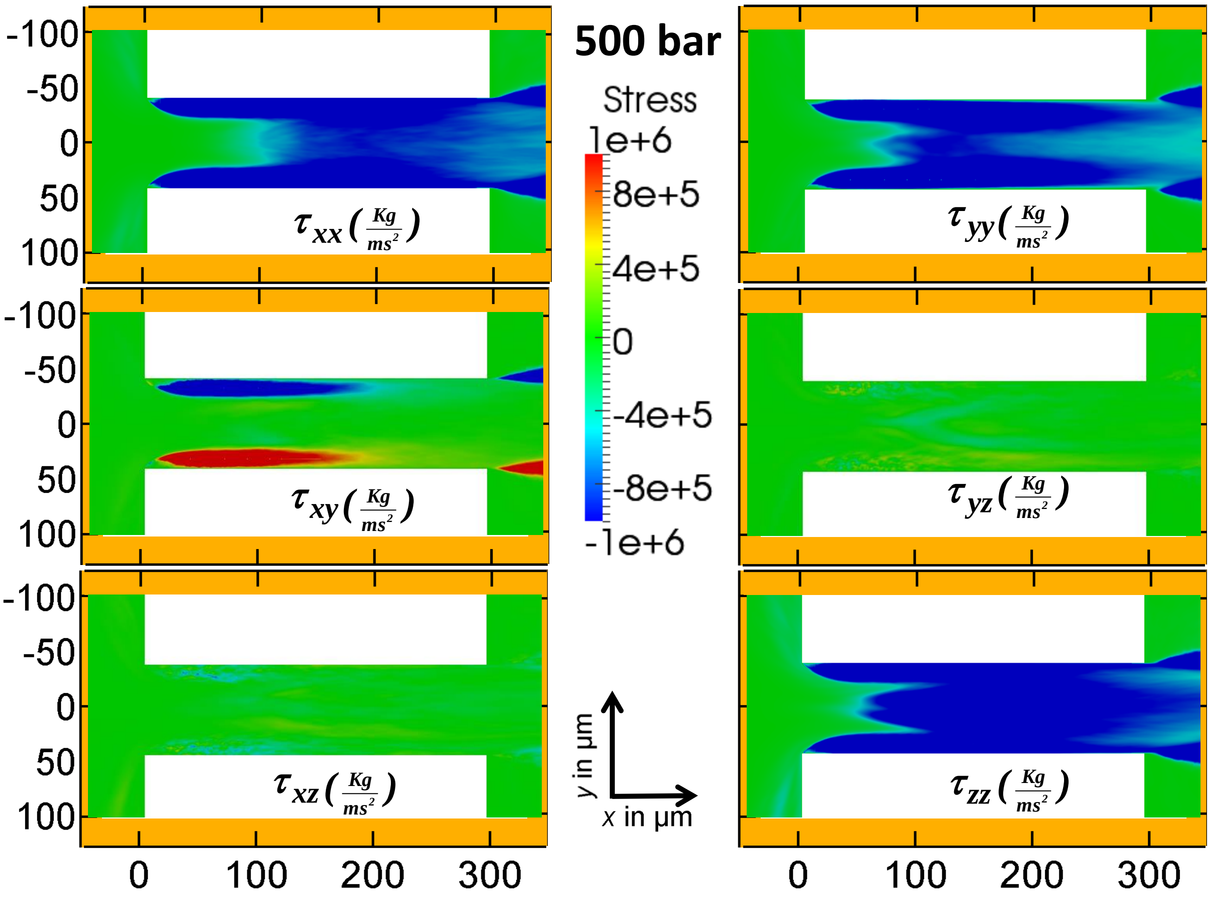

Figure 7.20.: The turbulent stress components generated in the orifice in the mid plane for pressure drop of 500 bar.

about the turbulent stresses, can help to understand and predict the aggregates breakage mechanism.

The components of the turbulent stress tensor for the 100 bar and 500 bar cases are shown in Fig. 7.19 and Fig. 7.20. These figures are taken in the mid plane of the orifice. The trace of the turbulent stress tensor constitutes the turbulent kinetic energy of the fluid flow. The magnitude of the diagonal components is considerably larger than non diagonal components in the mid plane. As for for the laminar stresses only τ_{xy} has a significant contribution among the non-diagonal stresses.

Unlike the laminar stresses turbulent stresses play no role at the entrance of the orifice. The turbulence is produced where the laminar stresses are high and moves downstream with the flow. The turbulence flow near the wall in the plane $z = -1$ is shown in Fig. 7.21. The values for the turbulent stresses are seen to be smaller close to the wall than

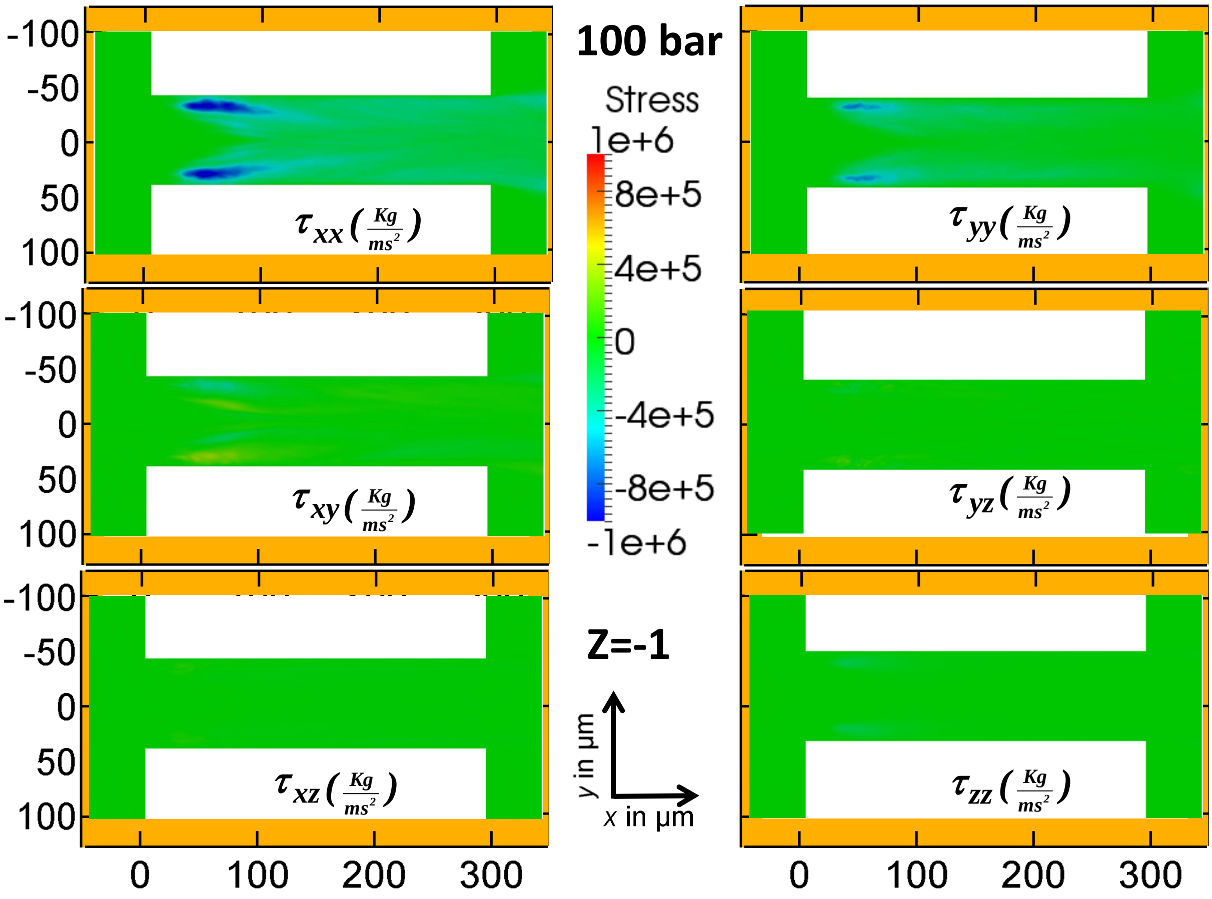

Figure 7.21.: The averaged stress components generated in the orifice in the plane $z = -1$ for the pressure drop of 100 bar.

in the mid plane. The diagonal components of the turbulent stress tensor are dominant before, after, and inside of the orifice. This behavior can be seen in Fig. 7.22. The upper figure shows the average magnitude of the turbulence stress for each component. The lower figure is the close-up of the upper figure. The maximums of the turbulent stresses is observed where the velocity is maximal at about 50 micro meter behind the entrance of the orifice.

7.4. Aggregate simulation

In this section, the breakage of aggregates with the use of information extracted by the tracer particles is studied. While moving through the disperser the particles record the stresses they experience. A statistical assessment is carried out according to the collected

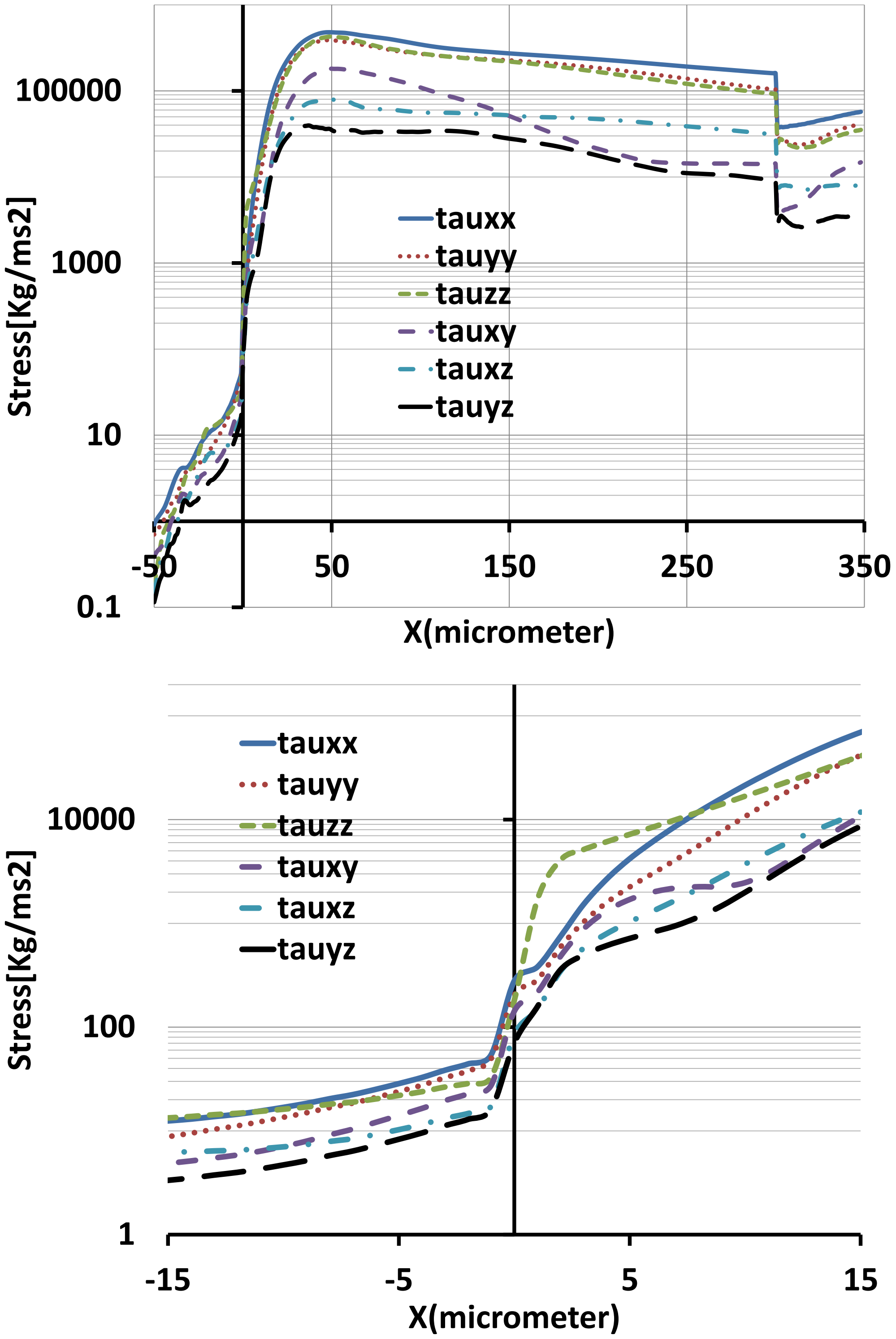

Figure 7.22.: The turbulent stress components averaged over $y-z$ planes plotted in x direction for a pressure drop of 100 bar.

data in order to obtain relationships between the breakage of aggregates and different parameters such as the fractal dimension.

Three different pressure drops studied in the preceding section lead to turbulent flow. Since the cumulant LBM as an implicit LES is used and since sufficient resolution is provided at the critical sections of the device, the exact stresses or strains can be calculated. This distinguishes the current study from simulations with RANS models where assumptions have to be made to extract these quantities from the turbulence model.

7.4.1. Fluidic time scale versus particle time scale

When an aggregate moves in the fluid its velocity is not exactly the same as that of the surrounding fluid. The time that a particle needs to reach the speed of the surrounding fluid is defined as the relaxation time. The order of this time scale compared to the time scale of the fluid determines whether the relative velocity of the oparticle to the fluid is significant. Some researchers [36, 41, 50] assumed that the particles follow the fluid instantaneously. In order to check whether particle inertia must be taken into account for CFD model or not, a comparison of the relaxation time of the aggregate to the time step of the simulation is carried out. As a crude assumption, an aggregate is considered as a spherical shape with mass $m = 2.3 \times 10^{-17} kg$ and a radius $a = 300nm$. A relative Reynolds number can be defined around the aggregate in the following way:

$$Re = \frac{U_{rel}(2a)}{\nu} \tag{7.14}$$

The relative velocity instead of the fluid velocity in this Reynolds number definition is considered. In 7.4.3 we show that the maximum relative velocity reaches 10% of the fluid velocity. Therefore, the maximum relative Reynolds number around the aggregate is assumed to be lower than 100. If the particle moves with velocity U_P in comparison to the the surrounding fluid velocity, U_F, the following equation of motion is obtained for the particle velocity:

$$m\dot{U_P} \approx \alpha 6\pi\mu a(U_F - U_P) \tag{7.15}$$

where α is a coefficient modifying the drag coefficient for the range from the Stokes flow to $Re = 10^6$ [173]. This equation can be solved for for a particle with resting initial condition to give:

$$U_P(t) = U_F\left(1 - e^{\frac{t}{\tau}}\right) \tag{7.16}$$

where $\tau = \frac{6\pi\mu a\alpha}{m} = 2.2\alpha \times 10^{-6}s$ is the relaxation time. when Re approaches to zero, α goes to one (Stokes drag) and for $Re = 10$, this coefficient is 1.653. In addition, the maximum numerical time step under the consideration of the CFL condition, a grid spacing of $\Delta x = 1\mu m$, and a maximal velocity of $300m/s$ is calculated as:

$$\Delta t = U_{\max Numeric} \frac{\Delta x}{U_{\max Physic}} = 0.1 \frac{10^{-6} m}{300 \frac{m}{s}} = 3.3 \times 10^{-9} s \tag{7.17}$$

The actual numerical time step for our simulations is, $6.125 \times 10^{-10} s$, which is less than the critical value. Therefore, the ratio of the relaxation time to the numerical time step under the crude approximation is about 1000 for $Re = 1$ and 1653 for $Re = 10$ which are significant values. As a result, particle mass and autonomous movement must be considered and modeled in the simulations. In chapter 6, the relationship between the drag force acting on the aggregate and its number of primary particles has been given for two two fractal dimensions. The analytical solution with the modified relaxation time has been obtained in chapter 5.2. We use this information to compute the relaxation time of our tracer particles as a function of their mass and fractal dimension.

7.4.2. Classes of particles

In each simulation of the disperser, a specific distribution of aggregates is used. For the 100 bar case, aggregates with two different fractal dimensions, 1.85 and 3 are considered. In either group particles with 500 and 4000 primary particles are considered. The total number of aggregates in this simulation is 4000 such that each of the four categories has 1000 aggregates. The particles are inserted at random locations in front of the orifice. Each aggregate shares its initial position with one aggregate out of each of the other categories.

For the 200 bar case 400 aggregates with randomly chosen mass are used. All aggregate have fractal dimension 1.85. The distribution of the primary particles in the agglomerates is shown in Fig. 7.23. For example, about 12 percent of the aggregates have between 1400 and 2000 primary particles.

For the 500 bar case aggregates with 500, 1000, 2000, and 3000 primary particles are used with fractal dimension 1.85 and 3. Each of the eight categories has 350 aggregates such that 2800 aggregates are simulated in total. Each aggregate shares its initial position with one aggregate from the other seven groups.

In each of the simulations about 5% of the aggregates did not pass through the orifice after 20 days of simulation. These aggregates have been disregarded in the analysis.

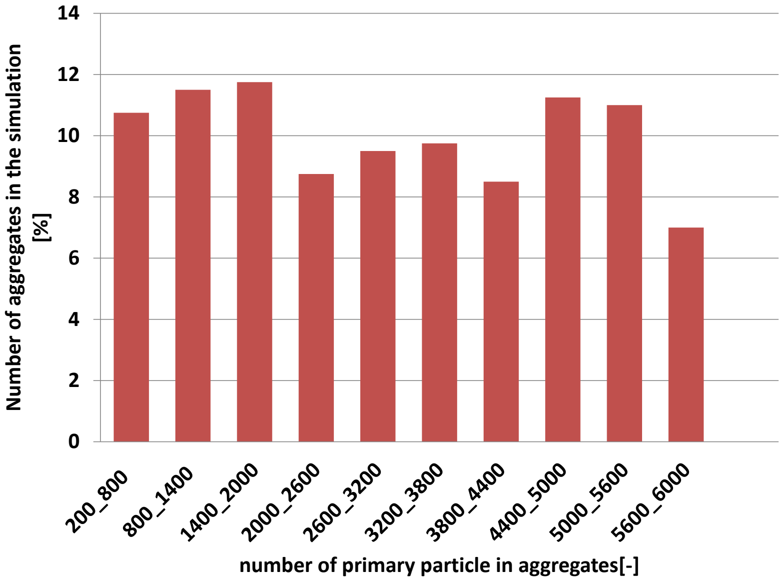

Figure 7.23.: Distribution of primary particles in the aggregates for pressure drop 200 bar.

7.4.3. Analysis of aggregate histories

In order to compare between the obtained results for the different pressure drops, a non-dimensional magnitude of the strain rate is defined as:

$$C = \frac{\mu S}{\Delta p} \tag{7.18}$$

where Δp denotes the pressure difference between inlet and outlet of the disperser.

No data from experiments is available for the shear rate suffered by the particles. This data can only be obtained from our simulation. The highest shear rates are observed close to the wall at the entrance of the orifice. This causes aggregates passing through this area to experience the highest probability of breaking-up. Fig. 7.24 shows three aggregates entering the orifice at different distances to the wall for the 200 bar case. The aggregate passing close to the centerline experiences a reduced strain rate, as is depicted in Fig. 7.24.

Collisions to the wall were monitored but were rarely observed. Particles could come very close to the wall (see Fig. 7.25) but if they actually hit the wall they would hit it at a very low angle such that the particle would rather scratch along the wall than bounce of the wall. The model used in this simulation considers the reflection of colliding particles with a coefficient of restitution equal to 0.75. Albeit only about 10 out of 400 particles collided

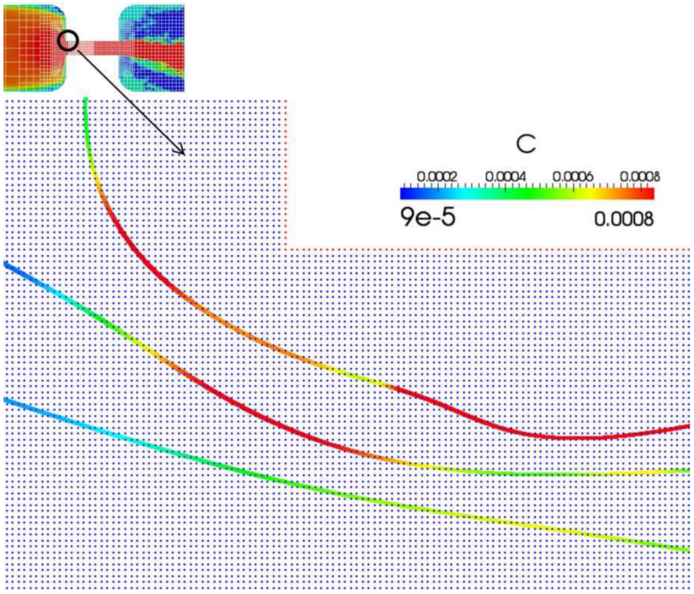

Figure 7.24.: Non-dimensional strain rate of 3 aggregates at different distances to the wall moving into the orifice part of the disperser from the left to the right. The pressure drop is 200 bar.

with the wall it goes with out saying that in the presence of many more particles, these relatively rare events have a significant influence on the abrasion of the microstructure. Since collisions to the wall are rare from the point of view of the particles they are not considered to have a significant effect on the break-up frequency.

It is instructive to identify the regions in which aggregates suffer the highest strain. Fig. 7.26 shows where the dimensionless strain rate exceeds 0.004 for the pressure drop of 100 bar including. We study the four different categories of aggregates to see the effect of the fractal dimension and the size of the aggregates on the area of highest strain. This figure shows that the fractal number and the number of the primary particles have no influence on the highest strain zone. Even though the highest absolute strain is observed at the entrance of the orifice, only very few particles are actually affected by this stress. While the stress in the turbulent flow in the middle of the orifice is lower than at the entrance, it affects significantly more particles. Some particles experience their maximum stress only in the turbulent jet leaving the orifice. High shear rates are never observed in the center of the entrance of the orifice.

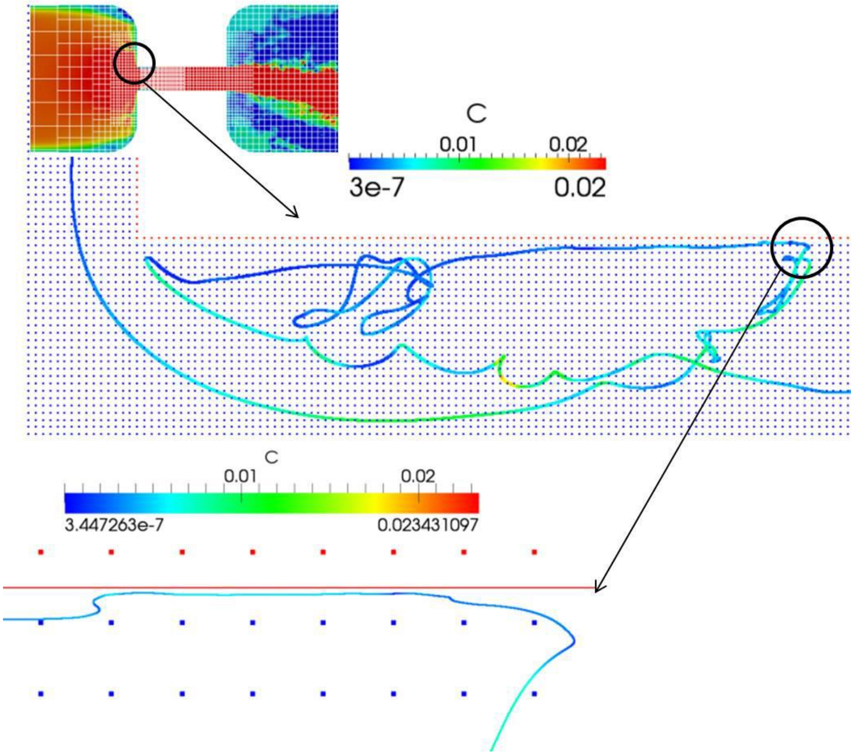

Figure 7.25.: Tracer particles come close to the wall but the corrected extrapolation from equation 5.18 hinders almost all particles from hitting the wall. The particle in this picture cames so close to the wall that, taking its radius into account, the physical aggregate would have touched the wall. These events were found to happen too rarely to obtain enough data for a statistical analysis.

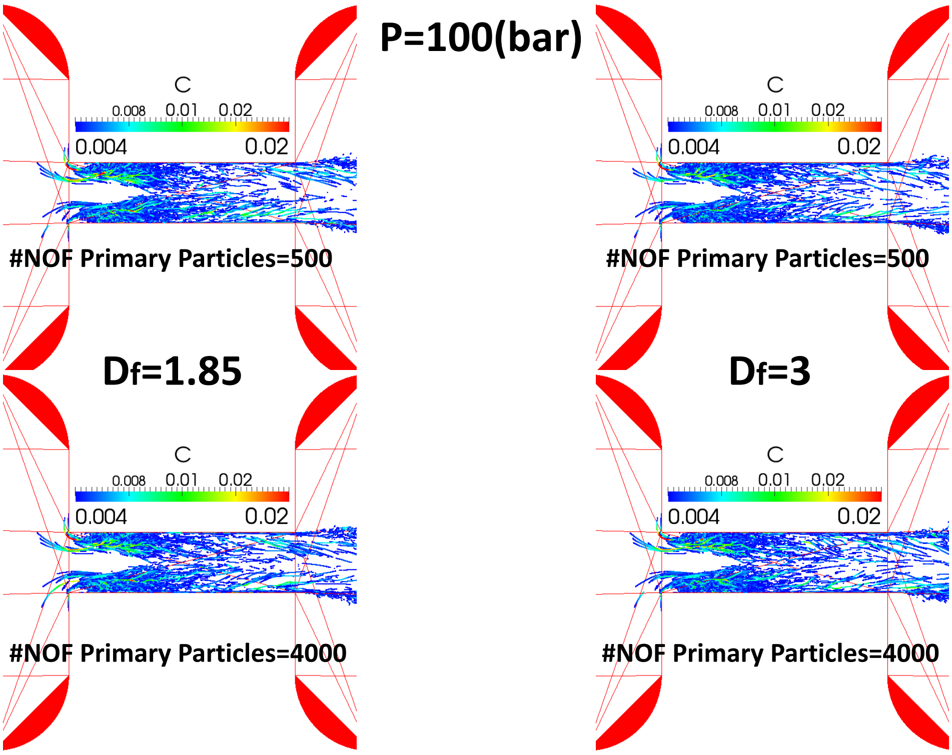

Figure 7.26.: Areas of high strain rate identified from the pathlines at a pressure drop of 100 bar for four different categories of aggregates. The upper and the lower figures show aggregates with the 500 and 4000 primary particles, respectively. The left and the right figures show aggregates with the the fractal dimension 1.85 and 3, respectively. Only dimensionless stresses exceeding 0.004 are shown.

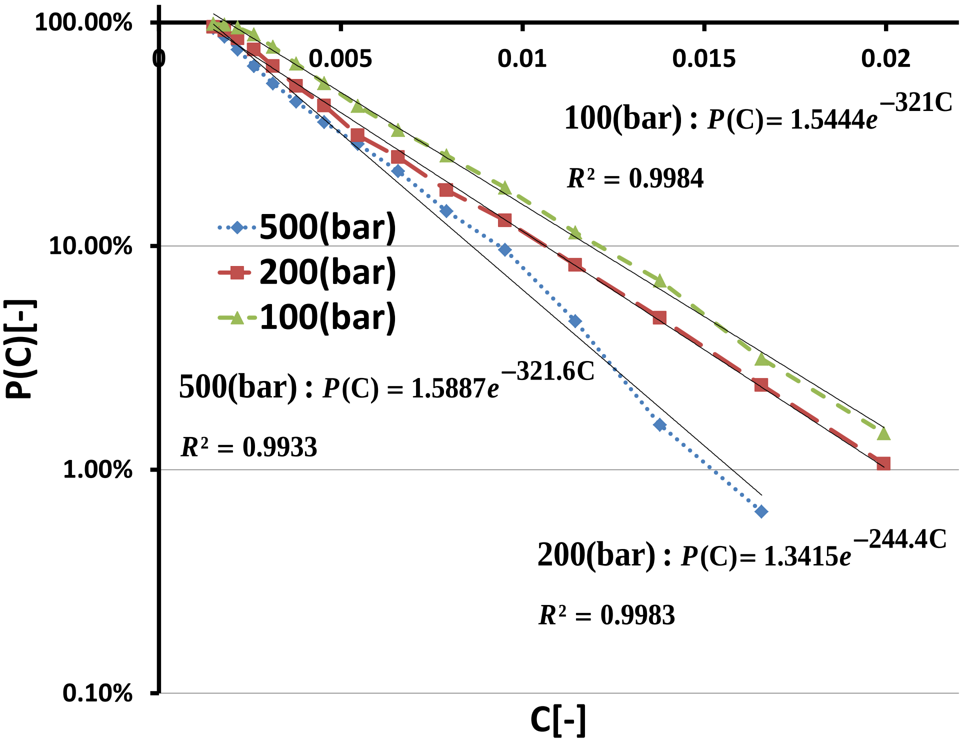

Figure 7.27.: Probability for a particle to experience at least the strain rate C in percent for three pressure drops. The data from the simulation (triangles) is well approximated by an exponential function.

Maximum strain

The data obtained by the simulation can be used together with various models for aggreagte break-up. First we consider a simple model for the aggregates break-up that depends only on the maximum load aggregates experience while passing through the disperser. Because ceramic aggregates are considered to be hard nano-particles, a memoryless model is expected to be sufficient. To begin with, the maximum of the dimensionless strain is collected for each aggregate. A cumulative histogram for a set of threshold loads suffered by the particles is used to determine the cumulative probability distribution for the load. The procedure is repeated with different bin sizes to assure independence of the discrete threshold values. The cumulative distribution function can be interpreted as the probability that a particle passing through the disperser suffers at least a certain amount of stress. This distribution shown in Fig. 7.27 is clearly identified to be of exponential type and can be fitted to the following function with high accuracy:

$$P(c) = \begin{cases} 1 & if(c < c_{\min}) \\ e^{-\frac{(c-c_{\min})}{c_{ref}}} & else \end{cases} \tag{7.19}$$

This model has only two parameters c_{min} and c_{ref} that can be fitted to the simulation data.

These parameters are $c_{min} = 0.001354, c_{ref} = 0.0031152$ for the 100 bar case, $c_{min} = 0.001202, c_{ref} = 0.0040965$ for the 200 bar case, and $c_{min} = 0.0014394, c_{ref} = 0.003109$ for the 500 bar case. Parameters c_{min} and c_{ref} have been obtained with a coefficient of determination for the fit of 0.9984, 0.9983, and, 0.9933 for the 100 bar case, the 200 bar case and the 500 bar case, respectively. This probability function is a very useful tool for computing the number of particle break-ups. Assuming that an aggregate breaks after experiencing a threshold stress c_{th}, the percentage of broken-up aggregates is $P(c_{th})$.

The function decouples the simulation of the disperser from the investigation of the break-up threshold. The number of broken aggregates for any known threshold can be determined. A condensed model like the probability function also simplifies further analysis. For example, the percentage of broken aggregates after n passages of the disperser under the same conditions can be estimated from the conditional probability that the aggregate does not break-up in each of the passages.

$$P(c,n) = \begin{cases} 1 & if(c < c_{\min}) \\ 1-(1-e^{-\frac{(c-c_{\min})}{c_{ref}}})^n & else \end{cases} \tag{7.20}$$

With the condensed model the dispersion result of many passages through the disperser can be inferred by simulating only a single passage. Fig. 7.28 shows the probability for

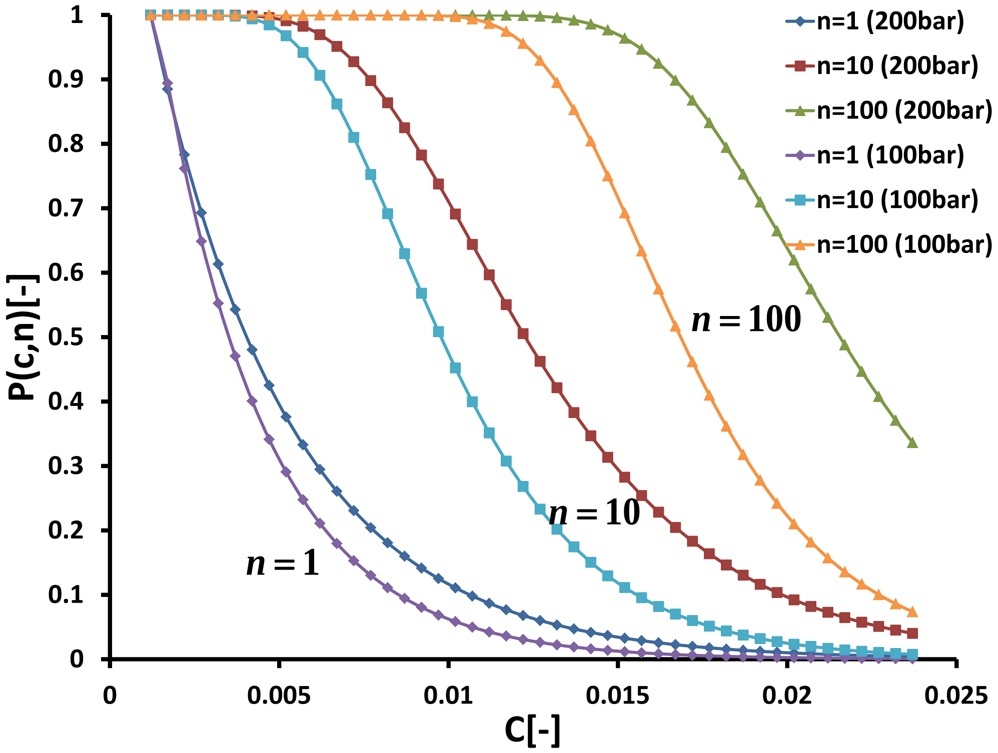

Figure 7.28.: Probability for a particle to experience at least the strain rate C after one, ten, and hundred passages through the disperser for the 100 bar and 200 bar cases. The model equation 7.20 allows us to determine these probabilities from a single simulation.

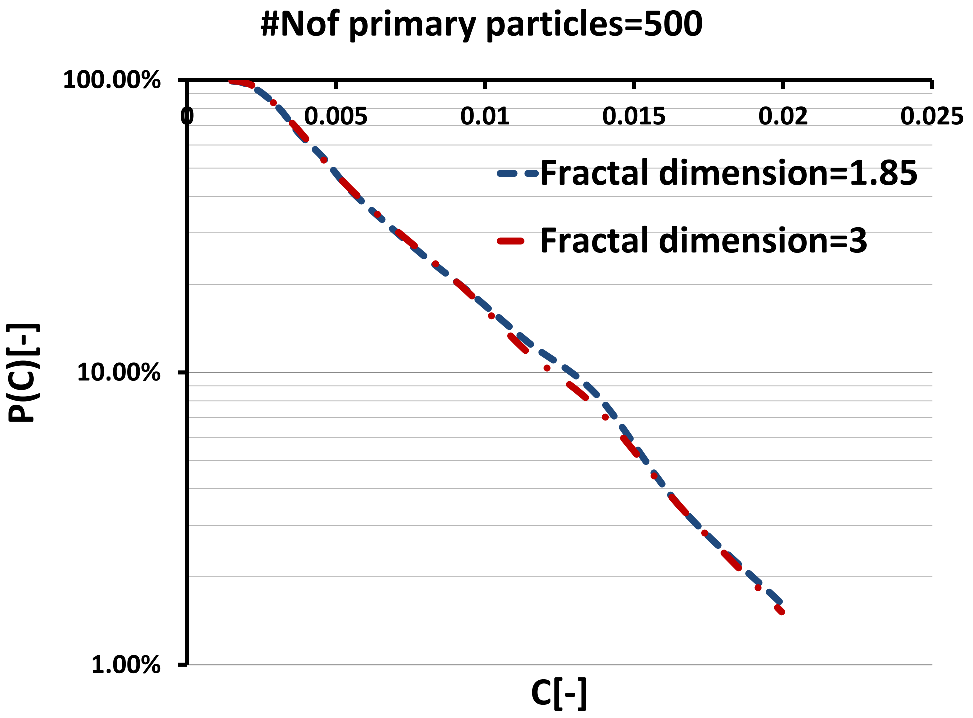

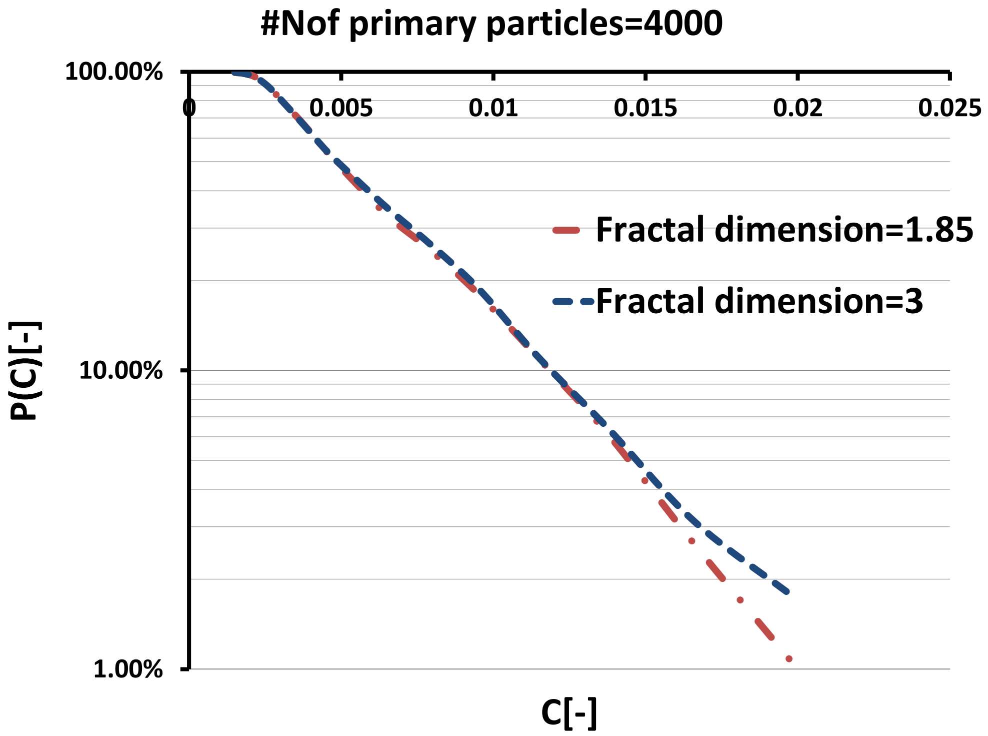

Figure 7.29.: The effect of the fractal dimension on the probability for an aggregate to experience at least the strain rate C in percent for a pressure drop of 100 bar. Only the probability higher than 1% is shown. The upper and lower figure refer to 500 and 4000 primary particles, respectively.

a particle to experience at least the strain rate C after one, ten, and hundred passages through the disperser for the 100 bar and the 200 bar cases. The difference between the 100 bar and 200 bar case increases with the number of passages.

It is observed that the behavior of the probability for many passages is always similar to the function for a single passage. Up to a certain minimum stress the probability is almost unity. Above the minimal stress the probability decays exponentially. The same behavior is observed when c_{min} is equal to zero. Multiple passages can also be efficiently modeled by the original equation. In fact, we assume that the observed behavior described by equation 7.19 arises from a combination of different events inside the disperser. Some aggregates experience their maximum stress when entering the orifice, whereas others experience their maximum stress due to the turbulence inside the orifice or in the turbulent jet behind the orifice. Equation 7.19 models the combination these events.

The effect of the fractal dimension for a fixed number of primary particles on the probability of the aggregate breakage for the 100 bar case is depicted in Fig. 7.29. The upper and lower plots show aggregates with 500 and 4000 primary particles, respectively. Only probabilities larger than 1% are shown. In these plots the fractal dimension has no perceivable effect on the probability to suffer a certain stress.

In other to investigate the effects of the number of primary particles on the probability to experience at least a certain amount of stress, the results from the 100 bar case is used. The probability for the fractal dimensions 1.85 and 3 versus the normalized strain rate is shown in Fig. 7.36. It is concluded that probability for a particle to experience at least the strain rate C is independent of the number of primary particles. As a result, the fractal dimension and the number of primary particle have no influence on the strain rate.

Exposure time

Exposure time is defined as the cumulative time during which a particle experiences at least a specific magnitude of strain rate. It is possible that the probability of the break-up is also affected by the duration of the load. Fig. 7.31 shows averaged exposure times of 400 particles versus strain rate for the 200 bar case. An exponential relationship with a coefficient of determination for the fit of 0.9983 ($R^2 = .9926$) can be observed:

$$T_{exp}(C) = 1.4002e^{-512.2C} \tag{7.21}$$

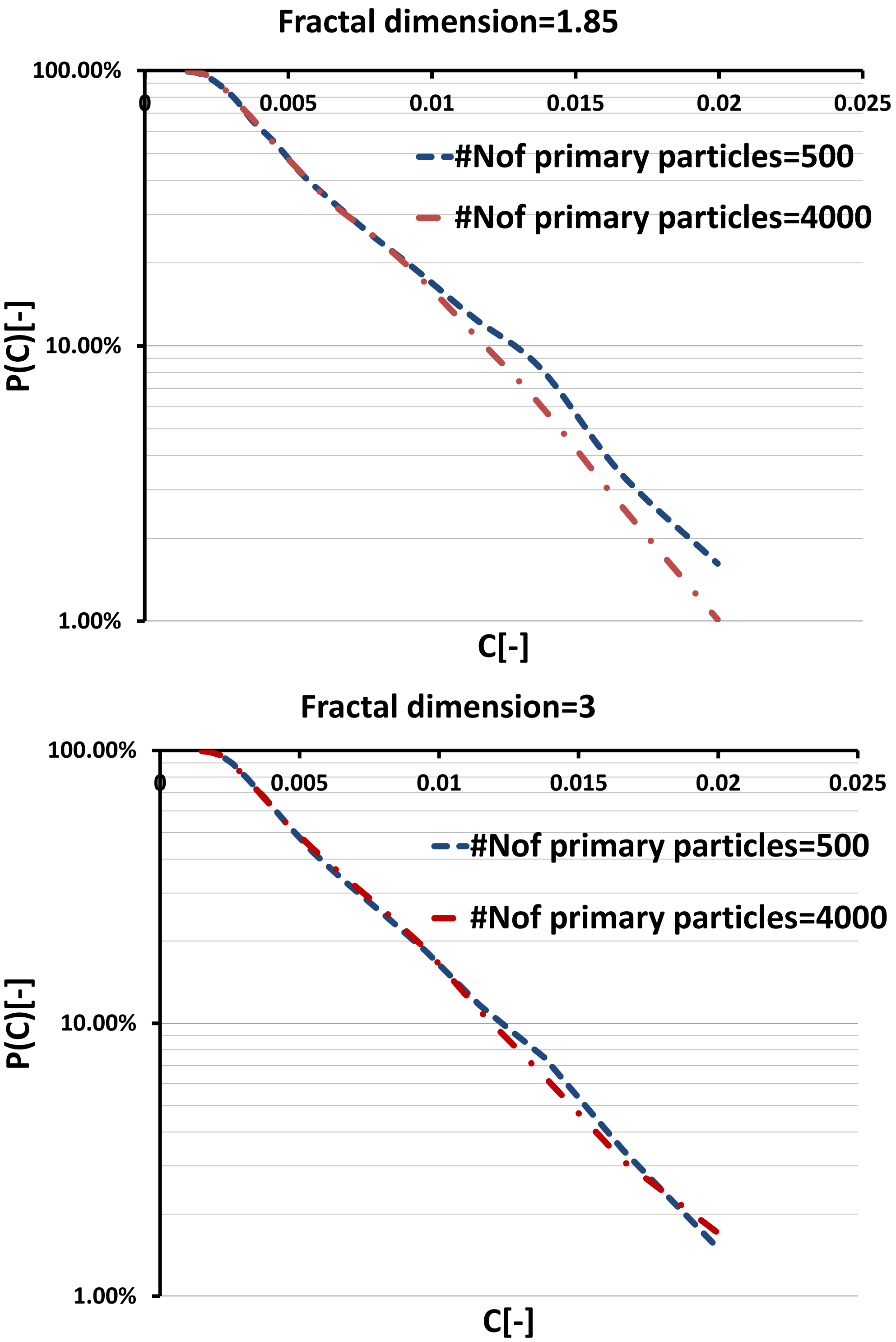

Figure 7.30.: The effect of the the number of primary particles with fixed fractal dimension on the probability for an aggregate to experience at least the strain rate C in percent for pressure a drop of 100 bar. The upper and lower figures are related to aggregates with fractal dimension 1.85 and 3, respectively. Only probabilities higher than 1% are shown.

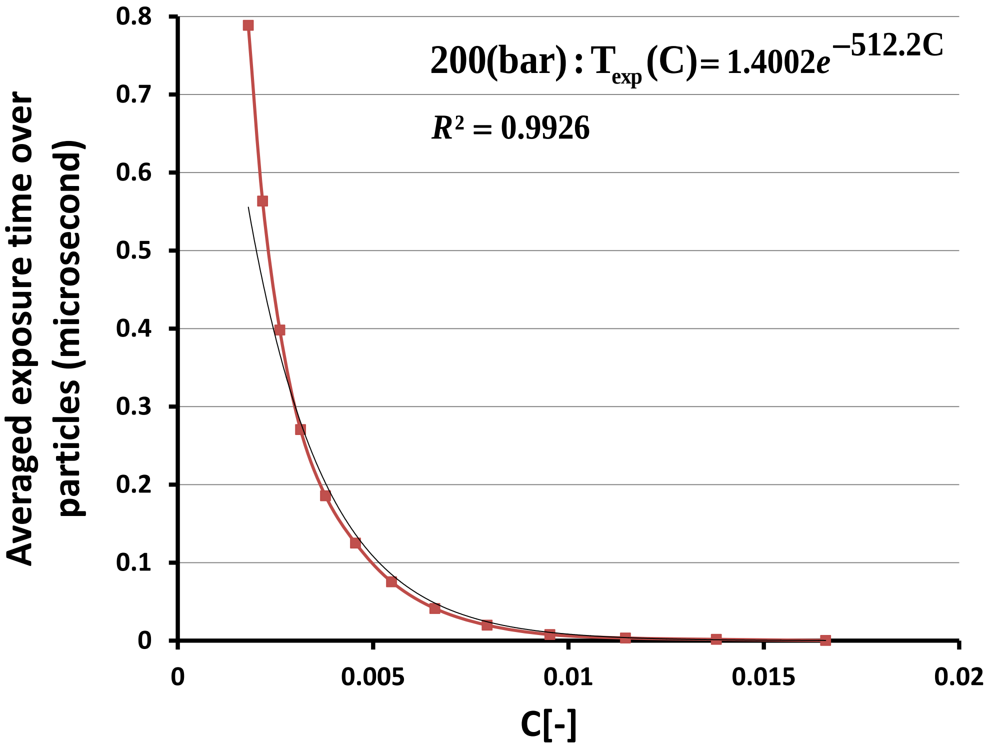

Figure 7.31.: Averaged exposure time over particles versus strain rate C for a pressure drop of 200 bar.

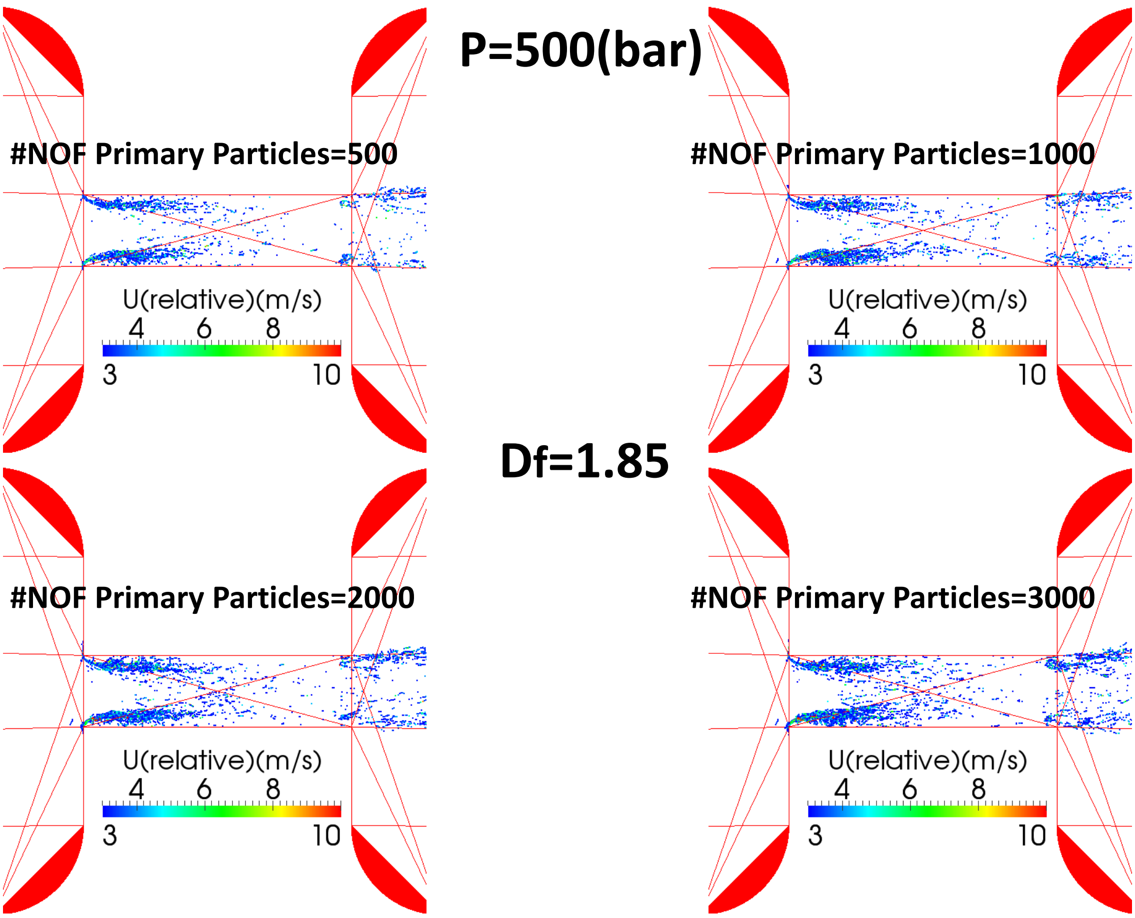

Figure 7.32.: The relative velocity between aggregates and the surrounding fluid for a pressure drop of 500 bar with the fractal dimension 1.85. The upper left, upper right, lower left, and lower right figures show aggregates with 500, 1000, 2000, and 3000 primary particles, respectively. Only relative velocities exceeding 3 m/s are shown.

Relative velocity

In our simulation, the effect of the aggregates on the fluid is neglected. In order to check the validity of this assumption, the relative velocity between particle and the surrounding fluid at a pressure drop of 500 bar is investigated. Fig. 7.32 and 7.33 show the relative velocity for the fractal dimension 1.85 and 3, respectively. Four different numbers of primary particles (500, 1000, 2000, and 3000) in the aggregates are shown in each figure. Only relative velocities more than 3 m/s are shown in these figures.

The maximal relative aggregate velocity for aggregates with fractal dimension 1.85 reaches up to 1% of the maximal fluid velocity. This behavior is sensitive to the fractal dimension of the aggregates since this ratio increase to 10% for the aggregates with the fractal dimension 3. Aggregates with realistic geometry (fractal number 1.85) follow the fluid velocity more closely than spherical particles (fractal number 3.0).

A approximation of the maximum relative Reynolds number for a large aggregate with the number of primary particles 3000 and fractal dimension 3 is obtained as:

$$Re = \frac{U_{rel} D}{\nu} = \frac{40(m/s) \times 140(m) \times 10^{-9}}{10^{-6}(m^2/s)} = 5.6 \tag{7.22}$$

the same procedure can be applied for the aggregate with fractal dimension 1.85 and the same number of primary particles:

$$Re = \frac{U_{rel} D}{\nu} = \frac{3(m/s) \times 700(m) \times 10^{-9}}{10^{-6}(m^2/s)} = 2.1 \tag{7.23}$$

in both cases the relative Reynolds number are less than 10. It is seen in Fiq. 7.32 and Fig. 7.33 that the sensitivity of the relative velocity to the mass of the particles is larger for spherical particles than for realistic aggregates. The relative velocity increases with increasing number of primary particles slightly for aggregates with the fractal dimension 1.85. For fractal dimension 3 the effect is more pronounced. The maximal relative velocities are observed close to the wall at the entrance of the orifice where strain rates are high as well.

The behavior of the aggregates suspended in a flow can be related to the particle Stokes number, which is the ratio of the characteristic time of an aggregate to a characteristic time of the flow [112]. In this thesis, this number is written as:

$$St = \frac{U_{rel}/d}{S} \tag{7.24}$$

where d is the diameter of the aggregate, and U_{rel} is the relative velocity between particle and fluid. When this number is higher than one, it means that the stress due to the relative velocity of the particle dominates the stress of the surrounding fluid. Consequently, these effects must be considered and modeled in the simulation.

The Stokes numbers for the aggregates with the fractal dimension 3 are shown in Fig. 7.34. The pressure drop for this simulation is 500 bar and only Stokes numbers exceeding 1 are shown. This figure shows that the effect of the relative velocity for these aggregates are considerable in comparison to the strain rate from the surrounding flow. The Stokes number is larger at the entrance of the orifice and it increases with the number of primary particles. For lager aggregates the dominance of the relative velocity over the strain from the surrounding fluid is extended further upstream.

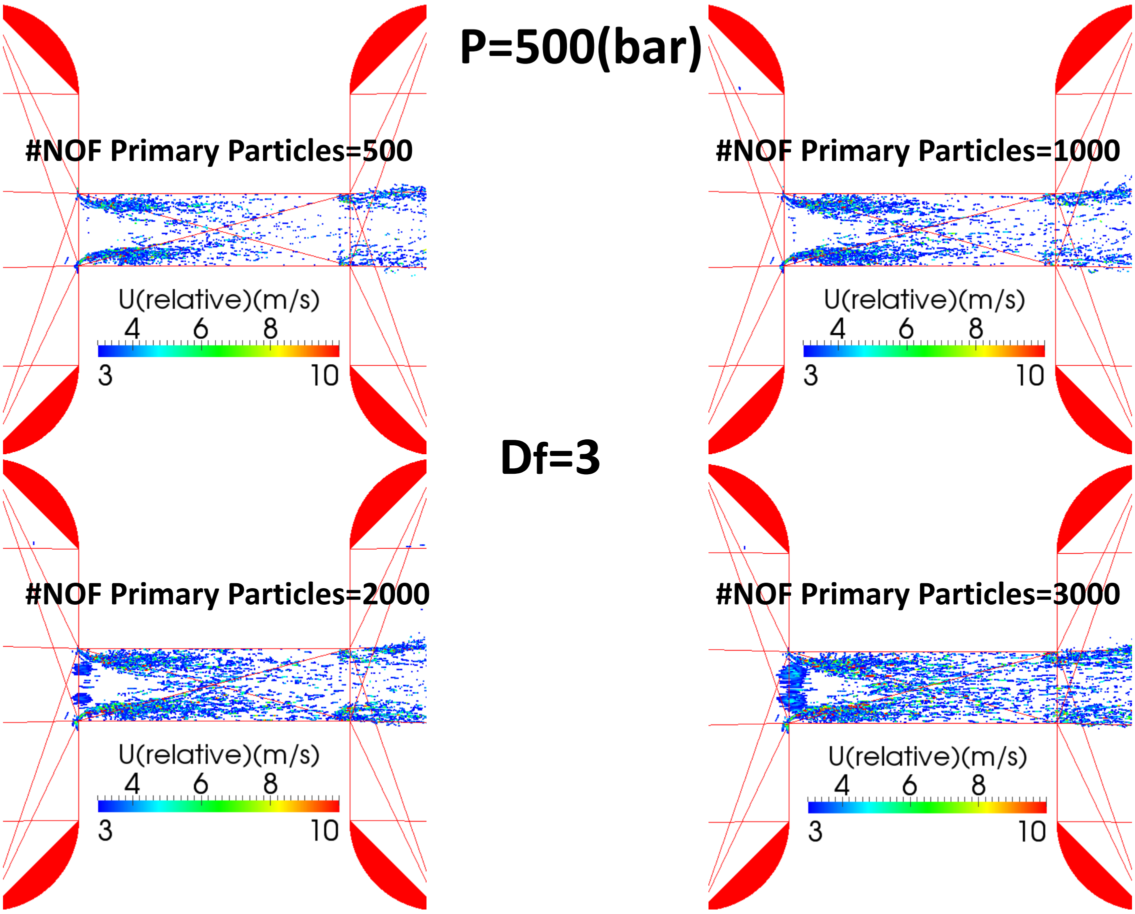

Figure 7.33.: The relative velocity between aggregates and the surrounding fluid for a pressure drop of 500 bar with the fractal dimension 3. The upper left, upper right, lower left, and lower right figures show aggregates with 500, 1000, 2000, and 3000 primary particles, respectively. Only relative velocities exceeding 3 m/s are shown.

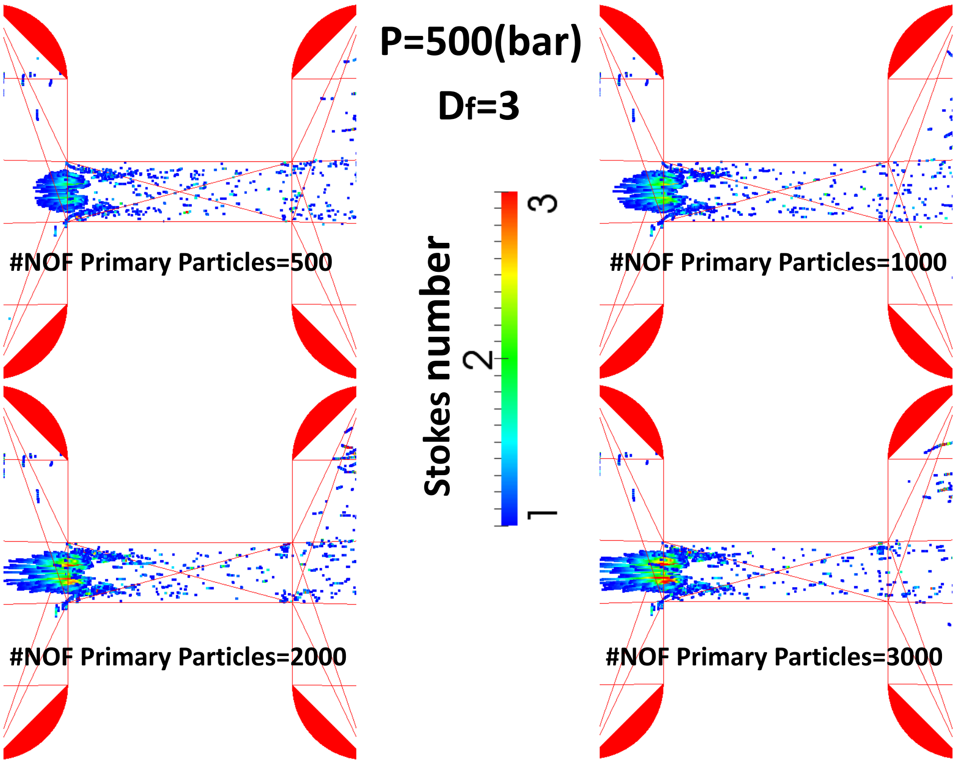

Figure 7.34.: The Stokes number for the aggregates with the fractal dimension 3. The upper left, upper right, lower left, and lower right figures show aggregates with 500, 1000, 2000, and 3000 primary particles, respectively. Only Stokes numbers exceeding 1 are shown. The pressure drop is 500 bar.

The Stokes numbers for the aggregates with the fractal dimension 1.85 is calculated as well. However, the Stokes number of the realistic aggregates does not exceed one. This means that the strain from the surrounding fluid always dominates the relative velocity of the aggregates with fractal dimension 1.8.

The relative velocities of the aggregates with fractal dimension 3 are not negligible according to their Stokes number. The relative velocity causes forces acting on the aggregates and may lead to aggregate break-up. Thus, we investigate this effect in the same way as we have studied the normalized strain rate. The maximum relative velocity for each aggregate is extracted from our data for the 100 bar case. A probability for an aggregates to experience at least the maximum relative velocity is obtained.

The fractal dimension effects the relative velocities. When an aggregate moving in the flow is of spherical shape it experiences a lower hydrodynamic drag in comparison with realistic aggregates. Consequently, it does not follow the movements of the surrounding fluid as closely as a realistic aggregate.

Fig. 7.35 confirms this conclusion since the probability for an aggregate to experience at least a certain relative velocity is smaller for aggregates with a lower fractal dimension. Only the probabilities higher than 1% are shown in this figure. An exponential correlations with a coefficient of determination for the fit of $R^2 = 0.9941$ and $R^2 = 0.9965$ are obtained for the fractal dimension 3 and 1.85 respectively. These correlations are given as:

$$P(U)_{D_f=3} = 1.9265e^{-0.937U} \tag{7.25}$$

$$P(U)_{D_f=1.85} = 1.6392e^{-1.087U} \tag{7.26}$$

where U is the maximum relative velocity experienced by an aggregate. The same behavior is observed for heavier aggregates (lower plot in Fig. 7.35). Although the large aggregates with fractal dimension 1.85 show complex behaviors, the relative velocity for the hard sphere with the same number of primary particles is higher than for the realistic aggregates.

The behavior of the aggregates with fractal dimension 3 and 40000 primary particles is accurately correlated with a high coefficient of determination $R^2 = 0.9955$ to:

$$P(U)_{D_f=3} = 1.6498e^{-0.654U} \tag{7.27}$$

However, a good correlation is not obtained for the fractal dimension 1.85.

$$P(U)_{D_f=1.85} = 1.0541e^{-0.583U} \tag{7.28}$$

where the coefficient of determination is $R^2 = 0.9394$. The behavior of spherical aggregates can be accurately represented by an exponential function while the behavior of

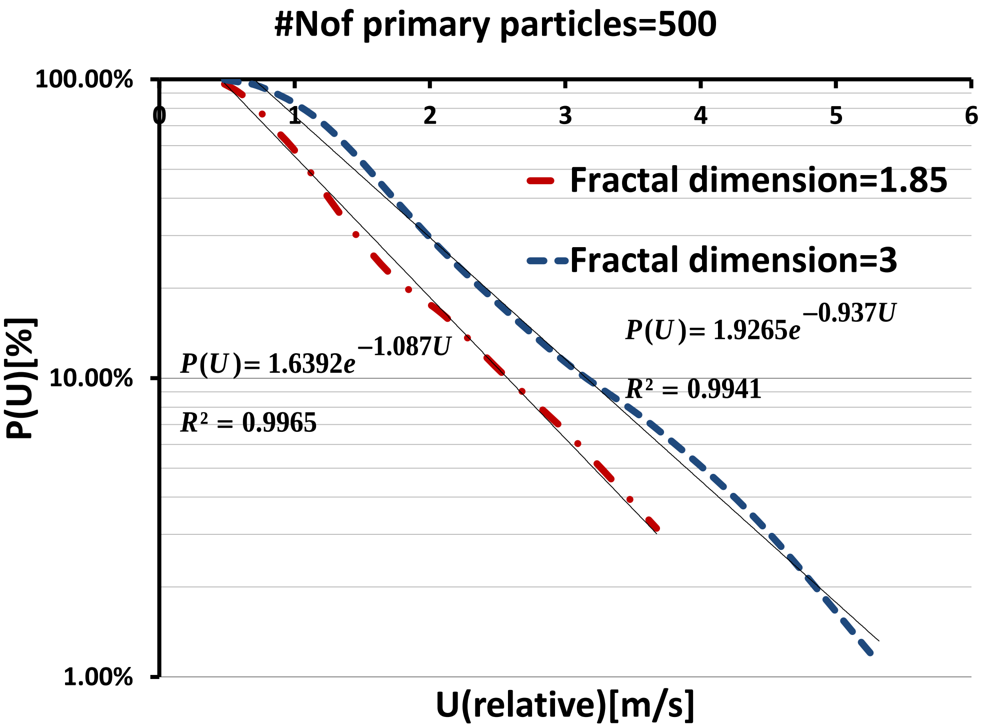

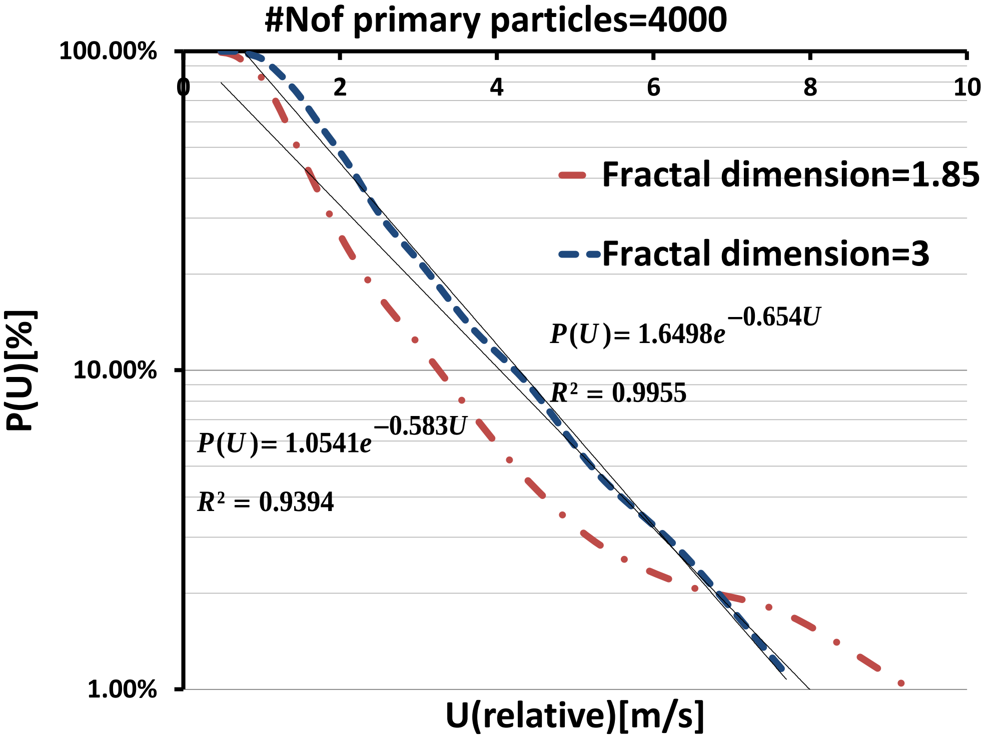

Figure 7.35.: The effect of the fractal dimension on the probability for an aggregate to experience at least the maximum relative velocity in percent for the 100 bar case. Only probabilities higher than 1% are shown.

aggregates with fractal dimension 1.85 is sensitive to the number of primary particles. Fig. 7.36 and Fig. 7.37 depict the influence of the number of primary particles on the probability for an aggregate to experience at least the maximum relative velocity for the 100 bar 200 bar cases. Only probabilities higher than 1% are taken into account. Smaller aggregates with fractal dimension 1.85 follow the exponential function much better than large aggregates.

The pressure drop effect of 100 bar and 500 bar on the probability for a particle to experience at least the maximum relative velocity is shown in Fig. 7.38. In order to make it independent of the primary particles, the probabilities belong to the similar fractal dimension are averaged over the different primary particles. A correlation (the coefficient of determination is $R^2 = 0.9759$) between the spherical aggregates and the relative velocity at the pressure drop of 500 bar are given as:

$$P(U)_{D_f=3} = 1.3402e^{-0.136U} \tag{7.29}$$

Moreover, for the realistic aggregates the correlation ($R^2 = 0.9536$) is obtained as:

$$P(U)_{D_f=1.85} = 1.079e^{-0.176U} \tag{7.30}$$

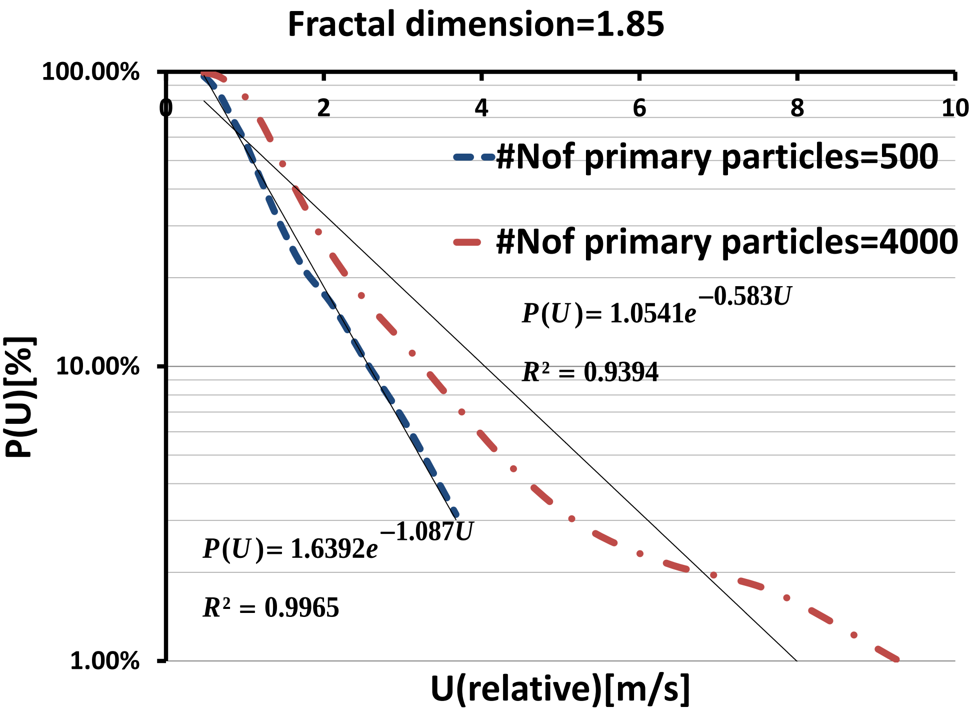

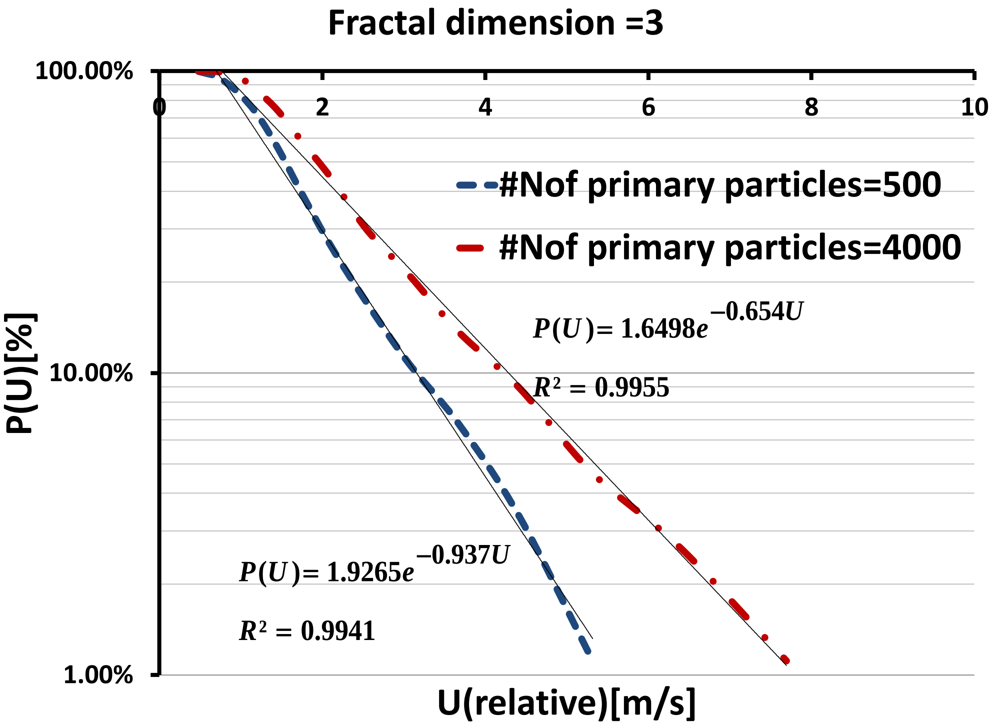

Figure 7.36.: The effect of the number of primary particles on the probability for a particle to experience at least the maximum relative velocity in percent for the 100 bar case. The upper and lower plots are related to aggregates with fractal dimension 1.85 and 3, respectively. Only probabilities higher than 1% are shown.

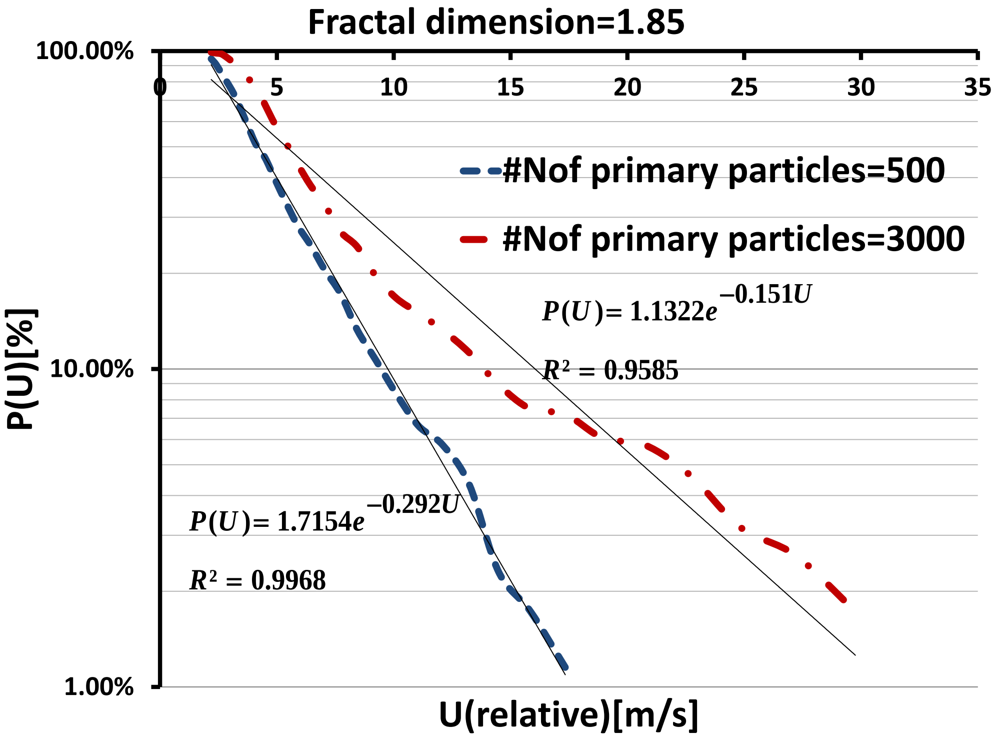

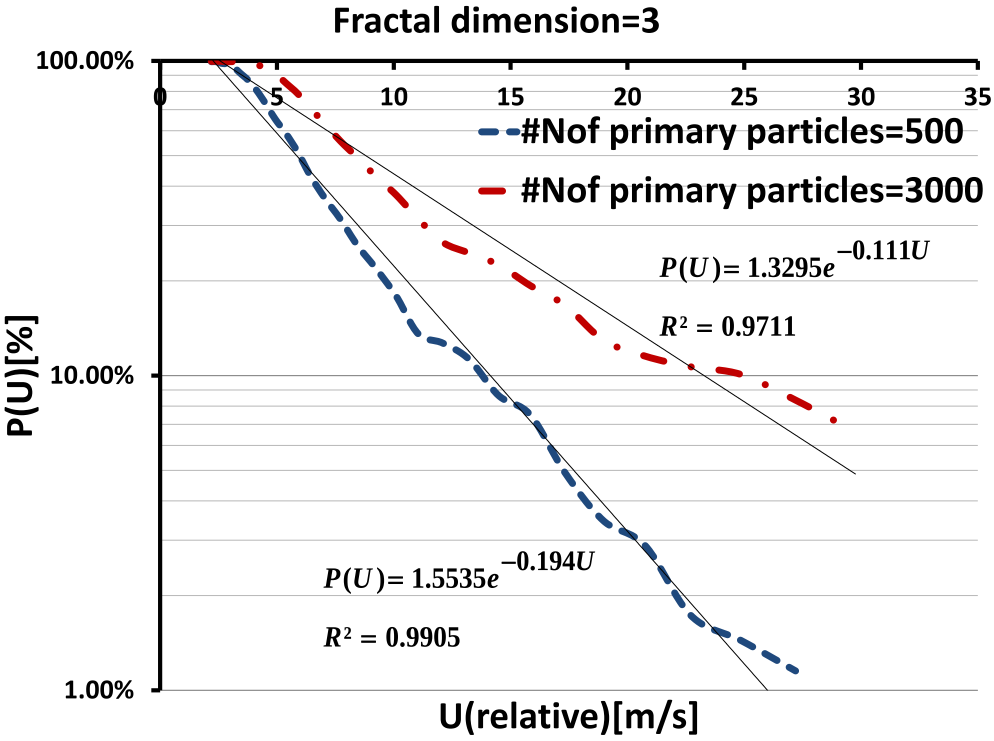

Figure 7.37.: The effect of the number of primary particles on the probability for a particle to experience at least the maximum relative velocity in percent for the 500 bar case. The upper and lower plots are related to aggregates with fractal dimension 1.85 and 3, respectively. Only probabilities higher than 1% are shown.

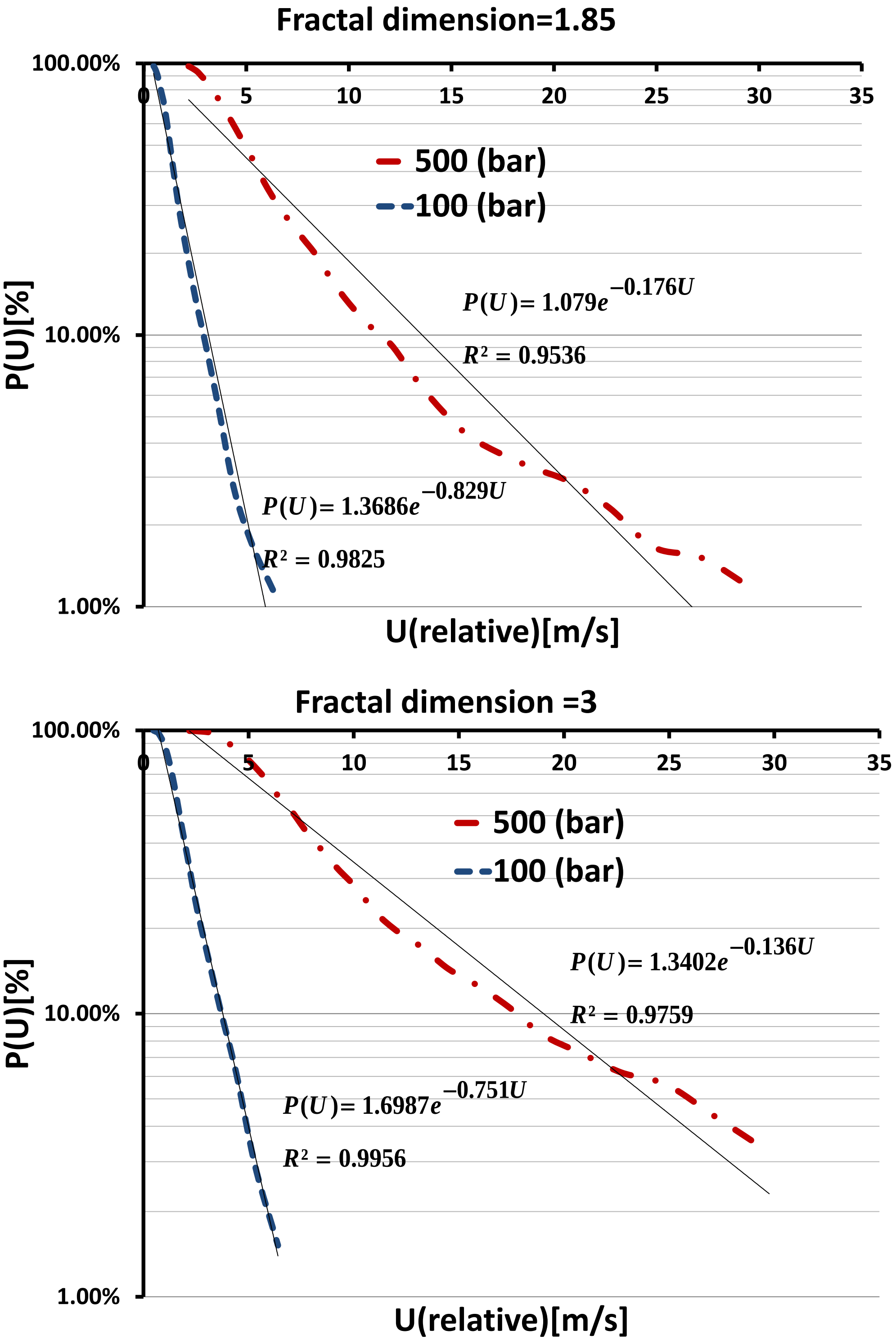

Figure 7.38.: The pressure drop effect of 100 bar and 500 bar on the probability for a particle to experience at least the maximum relative velocity in percent. The upper and lower plots are related to aggregates with fractal dimension 1.85 and 3, respectively. Only probabilities higher than 1% are shown. The aggregates have been averaged over the number of primary particles in each sub-category.

8. Conclusion

The main objective of this thesis is to demonstrate the feasibility of the cumulant LBM approach to accurately simulate the hydrodynamic loads on aggregates. Concerning the main flow filed the velocity profile, the flow rate, and the reattachment point seen in experiments can be quantitatively reproduced. To evaluate the break-up probability of aggregates, a simple statistical model is derived from the shear stress history recorded by the tracer particles.

This chapter reviews the obtained results and gives an outlook on how this research can be continued.

8.1. Summary

In order to study the dispersion of ceramic aggregates numerically the aggregates are modelled at two different scales in this thesis. On the particle scale drag coefficients for various aggregates are obtained to derive a reduced order model that can be used for a large number of tracer particles on the device scale.

The passage of the aggregates through the disperser is simulated at different pressure drops with an wall resolved LES using the cumulant LBM. Finally the load history of the tracer particles are analyzed with statistical methods.

In chapters (2 to 3), a literature review of previous works has been given. The basic concept of aggregates and fluid dynamics are briefly explained.

Chapter (4) addresses the cumulant LBM. This method is an improved LBM with respect to stability and accuracy in the low as well as in the high Reynolds number regime. Appendixes give additional information in order to clarify the concept of the cumulant LBM.

In Chapter (5.2), a parallelized pathline algorithm is developed for the tracer particles. This algorithm uses compact quadratic interpolation which has the second-order accuracy for the strain at the expense of linear interpolation. A correction term is proposed in the extrapolation zone, where particles get very close to the wall, to prevent pathlines from crossing the wall.

In Chapter (6), various aggregates are simulated on the particle scale and their hydrodynamic drag forces are calculated. The results are validated with analytical solutions or other numerical results. A body fitting grid refinement is used to reduce the cost of computation considerably. A precise and simple correlation between the drag force and the number of primary particles is acquired. The pathlines uses this correlation to move through the disperser in the simulation on the device scale.

In the last chapter, the data aquired by the pathline simulation is analyzed. The device is simulated for three different input pressures. The resolution of the grid spacing is checked by the variable dimensionless distance to the wall $y+$. For all three cases a value of order unity is obtained in the orifice. The boundary layer of the flow is hence well resolved. The flow rates acquired by our simulation are in the close agreement to the experimental result. Moreover, the reattachment point coincides with the micro PIV measurement. These two criteria are used to verify our results. The center line velocities and average pressure over the cross section are plotted along the orifice. The velocity increases at the entrance of the orifice while the pressure drops suddenly. After the exit of the orifice, the pressure decreases on one side of the disperser and attracts the jet towards the wall. This behavior is stable and results in an asymmetric mean flow.

The total dissipation rate is an important parameter for the breakage of the aggregates. It reaches the maximum value inside of the orifice with a second local maximum at the entrance of the orifice.

The highest strain rate areas for the 100 bar case has been shown for different fractal dimensions and different numbers of primary particles. The relative velocity between an aggregate and its surrounding fluid and the Stokes number are depicted to represent the areas affected by these parameters. The relative velocity grows with the fractal dimension and with the number of primary particles. For aggregates with fractal dimension 3 the relative velocity is more sensitive to the number of primary particles than for aggregates with realistic geometry. An exponential relationships between the cumulative probability for a tracer particle to experience at least a certain value of relative velocity is obtained for sphere-shaped particles. The behavior of the relative velocity of realistic aggregates is not well captured by by the same function.

An empirical model is proposed to evaluate the aggregate breakage. This model has only two parameters and shows the probability for an aggregate to experience at least the strain rate C. The data from the simulation is well approximated by an exponential function. This model has been extracted from one passage of the aggregates through the orifice. However, it can be easily extended to the several passages. The probability for an aggregate to experience at least the strain rate C after one, ten, and hundred passages through the disperser is calculated. The model equation allows us to determine these probabilities from a single simulation.

8.2. Outlook and Future Work

In this thesis we calculated the load acting on aggregates but the mechanics of the aggregates are not considered. In a future study, the obtained loads could be imposed on a Discrete Element Model of the aggregates to obtain their actual probability of breaking-up.

Also the influence of the particles on the flow has been completely neglected in our simulations. This was because the number of tracer particles in our simulation was not even close to realistic numbers of aggregates in the real disperser. If a two-way coupling is considered in future work it will require many more tracer particles to be realistic. The effect of the aggregates on the flow could also be modeled by a non-Newtonian fluid model.

Another effect neglected in this thesis is cavitation, which is observed when the pressure in the devices is lower than the vapor pressure of the fluid. The results in this thesis can be used to detect areas susceptible to cavitation but the actual consideration of bubbles in the flow require further modeling.

The disperser should also be simulated at higher input pressure rates in order to get closer to the regime in which the device is operated in practice. This will increase the cost of the simulation.

In this thesis, only the dispersion of aggregates has been investigated. However, the coagulation process could be simulated as well.

A. Introduction to the moments and cumulants

In this section some basic properties of the moments, central moments, and cumulants with some examples are explained.

A.1. Expectation of a random variable

An expectation of a random variable is the mean taken by possible values of the random variable. It is also called the first moment of the random variable. In this section, first, the expectation of a discrete random variable is explain and then, the expectation of a continuous random variable is described.

A.1.1. The expectation of a discrete and a continuous random variable

To begin with, let us suppose that X is a discrete random variable with the probability mass function (PMF) $P_X(x)$ in the range of $\chi = \{x_1, x_2, x_3 ...\}$. The expectation of discrete random variable X about a value c can be defined as:

$$E(X) = \sum_{x_i \in \chi} (x_i - c) P_X(x_i) \tag{A.1}$$

Another notation which is often used is μ (the moment or the raw moment, usually refers to the above expression with c= 0). The first moment or the expected value of X is:

$$\mu_x = E[X] = \sum_{x_i \in \chi} x_i P_X(x_i) \tag{A.2}$$

x	2	3	4	5	6
$P_X(x)$	0.2	0.1	0.4	0.2	0.1

Table A.1.: A distribution of the random variables

In general, the $k-th$ moment of a discrete random variable can be written as

$$\mu_k = E[X^k] = \sum_{x_i \in \chi} x_i^k P_X(x_i) \tag{A.3}$$

The abstract concept of the moment can be clarified with some examples. We suppose that the average of numbers 2, 2, 3, 4, 4, 4, 4, 5, 5, 5, 6 is desired. A way is to divide the sum of all numbers by the count of the numbers.

$$\begin{array}{l} average = \frac{2+2+3+4+4+4+4+5+5+6}{10} = \\ = \frac{2(2)+1(3)+4(4)+2(5)+1(6)}{10} = 0.2*2+0.1*3+0.4*4+0.2*5+0.1*6 = 3.9 \end{array} \tag{A.4}$$

Another way to calculate the average is the use of the first moment. Coefficients 0.2, 0.1, 0.4, 0.2, 0.1 in equation A.4 are our PMF of numbers 2, 3, 4, 5, 6 respectively. For simplicity, we put this information in table A.1 showing the distribution of the random variable. The possible values of χ for this random variable are $\{2,3,4,5,6\}$. Thus, the expectation of the discrete random variable is:

$$\begin{array}{l} \mu_x = E[X] = \sum\limits_{i=0}^{5} x_i P_X(x_i) = \\ 2P_X(2) + 3P_X(3) + 4P_X(4) + 5P_X(5) + 6P_X(6) \\ = 2(0.2) + 3(0.1) + 4(0.4) + 5(0.2) + 6(0.1) = 3.9 \end{array} \tag{A.5}$$

As a result, the first moment is mathematically equal to the mean (compare equation A.4 with A.5). However, a PMF can be more complicated than a weight factor of some numbers such that calculating the mean is not straightforward without using the moment. We assume that a PMF is given by $P_X(x) = \frac{4-x}{6}$ in the range $x = 1,2,3$ and the expectation of the discrete random variable is required in the second example. Thus, the first moment according to equation A.2 can be calculated as:

$$\begin{array}{l} \mu_x = E[X] = \sum\limits_{i=0}^{2} x_i P_X(x_i) = 1P_X(1) + 2P_X(2) + 3P_X(3) \\ = 1(3/6) + 2(2/6) + 3(1/6) = 10/6 \end{array} \tag{A.6}$$

Now let us assume that Y is a continuous random variable instead of the discrete random variable with a probability density function (PDF) in the range of χ. The expectation of the continuous random variable about a value c is defined as:

$$\mu = E[Y] = \int_{\chi} (y - c) f_Y(y) dy \tag{A.7}$$

where c=0 for the raw moment. For instance, it is supposed that a PDF is given by:

$$f_Y(y) = 3y \tag{A.8}$$

where $0 \leq y \leq 2$. Therefore, the expectation of the random variable is calculated as:

$$\mu = E[Y] = \int_0^2 y f_Y(y) dy = \int_0^2 y 3y dy = 8 \tag{A.9}$$

So far, the expectation of a discrete and a continuous random variable have been described. Sometimes, the expectation of a function of a random variable is required. We suppose that Y is a random variable, then $g(y)$ is a function of this random variable. In this case, the expectation of a function of that random variable is defined as:

$$E[g(Y)] = \sum_{y_i \in \chi} g(y_i) P_Y(y_i) \quad for\, discrete\, variables \tag{A.10}$$

$$E[g(Y)] = \int_{y \in \chi} g(y) P_Y(y) dy \quad for\, continuous\, variables \tag{A.11}$$

For example, we suppose that $P_Y(y_i) = (\frac{1}{6})^{y_i+1}$ and $g(y_i) = e^{y_i}$ with a range of $y = 0, 1, 2, ...$, the expectation of $g(y_i) = e^{y_i}$ is calculated as:

$$E[g(Y)] = \sum_{i=0}^{\infty} e^{y_i} (\frac{1}{6})^{y_i+1} = (\frac{1}{6}) \sum_{i=0}^{\infty} (\frac{e}{6})^{y_i} = (\frac{1}{6}) \frac{1}{1 - \frac{e}{6}} = \frac{1}{6 - e} \tag{A.12}$$

where

$$\sum_{k=0}^{\infty} r^n = \frac{1}{1 - r} \quad if\ 0 < r < 1 \tag{A.13}$$

Three important properties of a expected value operator can be written as:

$$\begin{aligned} &E[kX] = kE[X] \\ &E[X + k] = E[X] + k \\ &E[X + Y] = E[X] + E[Y] \end{aligned} \tag{A.14}$$

A.2. Moment generating function (MGF)

The moment generating function $M_X(t)$ or a two-sided Laplace transform of $f_X(x)$ of a random variable X in the range of χ is defined as.

$$M_X(t) = E[e^{tx}] = \begin{cases} \sum_{\chi} e^{tx_i} P_X(x_i) & when\ X\ is\ discrete \\ \int_{\chi} e^{tx} f_X(x) dx & when\ X\ is\ continuous \end{cases} \tag{A.15}$$

A question raised is that why the expectation of e^{tx} is called the moment generating function. In fact, we call it the moment generating function because the moment can be calculated directly by $M_X(t)$:

$$\mu_k = E[X^k] = \frac{d^k}{dt^k} M_X(t)\bigg|_{t=0} \tag{A.16}$$

For example, the first and second moments can be obtained by (remember that the first moment is defined as $E(X)$, the second moment as $E(X^2)$ and $K-th$ moment as $E(X^k)$):

$$\begin{aligned} \mu_1 &= E[X] = \tfrac{d}{dt} M_X(t)\big|_{t=0} = M'{}_X(0) \\ \mu_2 &= E[X^2] = \tfrac{d^2}{dt^2} M_X(t)\Big|_{t=0} = M''{}_X(0) \end{aligned} \tag{A.17}$$

We apply a PMF as an illustration to show the use of equation A.16. We suppose that $P_X(x_i) = (\frac{1}{10})^{x_i}$ in the range of $x = 0, 1, 2, 3, ...$ to calculate the first moment by using the moment generating function:

$$\begin{aligned} & M_X(t) = E[e^{tx}] = \sum_{\chi} e^{tx} P_X(x) \ = \sum_{i=0}^{\infty} e^{tx_i} (\tfrac{1}{10})^{x_i} \\ & = \sum_{i=0}^{\infty} (\tfrac{e^t}{10})^{x_i} = (\tfrac{1}{1-\frac{e^t}{10}}) \end{aligned} \tag{A.18}$$

in the above example, we assume that $0 < (\frac{e^t}{10}) < 1$ (equation A.13). The first moment can be directly calculated just with making the derivation of the moment generating function:

$$\mu_1 = E[X] = \frac{d}{dt} M_X(t)\bigg|_{t=0} = \frac{\frac{1}{10} e^t}{(1 - \frac{e^t}{10})^2}\Bigg|_{t=0} = \frac{10}{81} \tag{A.19}$$

It could be also useful to know a MGF is a series of expected values:

$$\begin{aligned}&M_X(t) = E[e^{tx}] = E(\tfrac{[tx]^0}{0!} + \tfrac{[tx]^1}{1!} + \tfrac{[tx]^2}{2!} + ...) = 1 + E[X] + \tfrac{t^2}{2!}E[X^2] + ...\\ &M_X(t) = \sum_{k=0}^{\infty} \tfrac{t^k}{k!}E[X^k] = \sum_{k=0}^{\infty} \tfrac{t^k}{k!}\mu_k\end{aligned} \tag{A.20}$$

A.3. Central moments

The moments have been calculated about the origin of coordinate system (the value c in the moment definition is equal to zero) but in the probability theory, knowing about the moment which has the deviation from the mean is preferred to raw moments. The $k-th$ central moment of the random variable X is defined as:

$$k_k = E[(X - E[X])^k] = E[(X - \mu)^k] \tag{A.21}$$

In other words, we shift the coordinate system to the mean μ $(c = \mu)$. The central moment for a discrete or continuous random variable X with a probability density function $f_X(x)$ is:

$$k_k = \begin{cases} \sum\limits_{\chi} (x_i - \mu)^k P_X(x_i) \;\; \textit{when X is discrete} \\ \int_{\chi} (x - \mu)^k f_X(x)dx \;\; \textit{when X is continuous} \end{cases} \tag{A.22}$$

In the lattice Boltzmann method, it is vital to transform raw moments to central moments. The following example demonstrates how to calculate the third central moment according to the raw moments:

$$\begin{aligned}&k_3 = E[(x - \mu)^3] = E[x^3 - 3x^2\mu + 3\mu^2 x - \mu^3]\\ &= E[x^3] - 3E[x^2]\mu + 3\mu^2 E[x] - \mu^3\\ &= \mu_3 - 3\mu_2\mu + 3\mu_1\mu^2 - \mu^3 = \mu_3 - 3\mu_2\mu + 3\mu^3 - \mu^3\\ &= \mu_2 - 3\mu_2\mu + 2\mu^3\end{aligned} \tag{A.23}$$

A general equation for this transforming can be given by the binomial transform:

$$K_n = \sum_{j=0}^{n} \begin{pmatrix} n \\ j \end{pmatrix} (-1)^{n-j} \mu_j \mu^{n-j} \tag{A.24}$$

where $\begin{pmatrix} n \\ j \end{pmatrix} = \frac{n!}{j!(n-j)!}$.

The first few central moments in the probability theory have important meanings and interpretations.

The zeroth central moment is equal to one:

$$k_0 = E[(x-\mu)^0] = E[1] = 1 \tag{A.25}$$

The first central moment is zero

$$k_1 = E[(x-\mu)^1] = E[x] - \mu = \mu - \mu = 0 \tag{A.26}$$

The second central moment μ is called the variance

$$\begin{aligned} &\text{var}(X) = E[(x-\mu)^2] \\ &= E[X^2 - 2X\mu + \mu^2] = E[X^2] - 2\mu E[X] + \mu^2 \\ &= E[X^2] - 2\mu\mu + \mu^2 = E[X^2] - \mu^2 \end{aligned} \tag{A.27}$$

The third central moment is named the standardized moment or is defined as the skewness.

A.4. Cumulant generating functions (CGF) and cumulants

Sometimes it is significantly easier to have a logarithmic form of a function for doing some mathematical calculations rather than the raw function. Therefore, a logarithm of the moment generating function is defined and called the cumulant generating function:

$$CGF = \ln(M_X(t)) = \ln(E[e^{tx}]) \tag{A.28}$$

For example, a MGF of the Poisson distribution is given by $M_X(t) = e^{\lambda(e^t-1)}$, with using the above equation, the CGF of this function is $CGF = \lambda(e^t - 1)$. It is much easier to work with the function $\lambda(e^t - 1)$ rather than $e^{\lambda(e^t-1)}$ to calculate moments. Let us take the logarithm of the moment generating function (equation A.20):

$$CGF = \ln(M_X(t)) = \ln(\sum_{0}^{\infty} \frac{t^k}{k!} E[X^k]) \tag{A.29}$$

The Taylor series of function ln is:

$$\ln(x) = -\sum_{n=1}^{\infty} \frac{1}{n}(1-x)^n \tag{A.30}$$

with using equation A.30, the CGF is:

$$\begin{aligned} CGF &= \ln(E[e^{tX}]) = -\sum_{n=1}^{\infty} \tfrac{1}{n}(1 - E[e^{tX}])^n = -\sum_{n=1}^{\infty} \tfrac{1}{n}(\sum_{m=1}^{\infty} \tfrac{t^m}{m!}\mu_m)^n \\ &= \mu_1 t + (\mu_2 - \mu_1)\tfrac{t^2}{2!} + (\mu_3 - 3\mu_2\mu_1 + 2\mu_1)\tfrac{t^3}{3!} + ... = \sum_{m=1}^{\infty} \tfrac{t^m}{m!} c_m \end{aligned} \tag{A.31}$$

where c_m is the $m-th$ cumulant. The $m-th$ cumulant is calculated by differentiating the CGF m times and evaluating the result at wave number zero:

$$c_k = \frac{d^k}{dt^k} CGF_X(t)\Big|_{t=0} \tag{A.32}$$

For example, the first and second cumulants are calculated the following ways.

For the first cumulant:

$$\begin{aligned} c_1 &= \tfrac{d^1}{dt^1} CGF_X(t)\Big|_{t=0} = \tfrac{d^1}{dt^1}\ln(M_X(t))\Big|_{t=0} = \tfrac{d^1}{dt^1}\ln(E[e^{tX}])\Big|_{t=0} = \\ &= \tfrac{1}{E[e^{tX}]|_{t=0}} \tfrac{d^1}{dt^1}(E[e^{tX}])\Big|_{t=0} = \tfrac{1}{1}\mu_1 = \mu_1 \end{aligned} \tag{A.33}$$

For the second cumulant:

$$\begin{aligned} c_2 &= \tfrac{d^2}{dt^2} CGF_X(t)\Big|_{t=0} = \tfrac{d^2}{dt^2}\ln(M_X(t))\Big|_{t=0} = \tfrac{d^2}{dt^2}\ln(E[e^{tX}])\Big|_{t=0} = \\ &= \tfrac{d}{dt}\Big[\tfrac{1}{E[e^{tX}]}\tfrac{d^1}{dt^1}(E[e^{tX}])\Big]_{t=0} = \Big[-\tfrac{1}{(E[e^{tX}])^2}(\tfrac{d^1}{dt^1}(E[e^{tX}])^2 + \tfrac{1}{E[e^{tX}]}(\tfrac{d^2}{dt^2}(E[e^{tX}])\Big]_{t=0} \\ &= -{\mu_1}^2 + \mu_2 \end{aligned} \tag{A.34}$$

A.5. Joint probability distribution

Up until now, just one random variable has been considered when the moments, central moments and cumulants have been studied in the previous sections. Joint probability distribution simply means how to work with distributions including more than one random variable. A joint probability distribution gives the probebilities of one random varibale given other random variables. When the random variables are independent, the joint probability distribution is the product of the individual random variable. We assume, for example, that there are three random variables X, Y, and Z and we want to calculate the first moment. Because of these three random variables we can define three independent moments in which each of them is in the first order of moments, μ_x, μ_y, μ_z. A new notation is introduced for simplicity when three random variables are used:

$$\begin{aligned} \mu_5 &= \mu_{\underbrace{xxxxx}_{5\ times}} = \mu_{x^5} \\ \mu_{x^3y^4z^2} &= \mu_{\underbrace{xxx}_{3times}\underbrace{yyyy}_{4times}\underbrace{zz}_{2times}} = \mu_{342} \end{aligned} \tag{A.35}$$

where μ_{x^5} is the fifth moment of one random variable X and μ_{342} is a ninth moment of three random variables X, Y, and Z. The definition of the moments, moment generating function, central moments and cumulants can be simply rewritten in the following equations:

For the moment:

$$\begin{aligned} &\mu_{mnl} = E[X^mY^nZ^l] = \\ &= \begin{cases} \sum\limits_{x_i \in \chi_1} \sum\limits_{y_j \in \chi_2} \sum\limits_{z_k \in \chi_3} x_i^m y_j^n z_k^l P_{XYZ}(x_i, y_j, z_k) & when\ X, Y, Z\ are\ discrete \\ \int_{x \in \chi_1} \int_{y \in \chi_2} \int_{z \in \chi_3} x^m y^n z^l f_{XYZ}(x, y, z) dxdydz & when\ X, Y, Z\ are\ continuous \end{cases} \end{aligned} \tag{A.36}$$

For independent random variables the moment definition can be simplified as a product of three independent random variables:

$$\mu_{x^my^nz^l} = E[X^mY^nZ^l] = E[X^m]E[Y^n]E[Z^l] \tag{A.37}$$

For the moment generating function:

$$\begin{aligned} &M_{XYZ}(t_1, t_2, t_3) = E[e^{t_1x+t_2y+t_3z}] = \\ &= \begin{cases} \sum\limits_{x_i \in \chi_1} \sum\limits_{y_j \in \chi_2} \sum\limits_{z_k \in \chi_3} e^{t_1x_i} e^{t_2y_j} e^{t_3z_k} P_{XYZ}(x_i, y_j, z_k) & when\ X, Y, Z\ are\ discrete \\ \int_{x \in \chi_1} \int_{y \in \chi_2} \int_{z \in \chi_3} e^{t_1x} e^{t_2y} e^{t_3z} f_{XYZ}(x, y, z) dxdydz & when\ X, Y, Z\ are\ continuous \end{cases} \end{aligned} \tag{A.38}$$

The relationship between the moment and the moment generating function:

$$\mu_{mnl} = E[X^mY^nZ^l] = \frac{\partial^m \partial^n \partial^l}{\partial t_1^m \partial t_2^n \partial t_3^l} M_{XYZ}(t_1, t_2, t_3) \bigg|_{t_1=t_2=t_3=0,} \tag{A.39}$$

For the central moment (the moment about the mean $\mu = (\mu_x, \mu_y, \mu_z)$):

$$\begin{array}{l}
k_{mnl} = E[(X-\mu_x)^m(Y-\mu_y)^n(Z-\mu_z)^l] = \\
\quad \textit{when } X,Y,Z \textit{ are discrete} \\
\qquad \sum\limits_{x_i\in\chi_1}\sum\limits_{y_i\in\chi_2}\sum\limits_{z_k\in\chi_3}(x_i-\mu_x)^m(y_j-\mu_y)^n(z_k-\mu_z)^l P_{XYZ}(x_i,y_j,z_k) \\
\quad \textit{when } X,Y,Z \textit{ are continuous} \\
\qquad \int_{x\in\chi_1}\int_{y\in\chi_2}\int_{y\in\chi_3}(x-\mu_x)^m(y-\mu_y)^n(z-\mu_z)^l f_{XYZ}(x,y,z)dxdydz
\end{array} \tag{A.40}$$

The cumulant generating function is:

$$CGF_{XYZ}(t_1,t_2,t_3) = \ln(E[e^{t_1X+t_2Y+t_3Z}]) = \ln(M_{XYZ}(t_1,t_2,t_3)\,) \tag{A.41}$$

And the cumulant is given by:

$$c_{nml} = \frac{\partial^m\partial^n\partial^l}{\partial t_1^m\partial t_2^n\partial t_3^l}\ln(M_{XYZ}(t_1,t_2,t_3))\bigg|_{t_1=t_2=t_3=0} \tag{A.42}$$

Let us make some examples to clarify the new definitions. We start calculating the second cumulant as:

$$\begin{array}{l}
c_{11} = \frac{\partial\partial}{\partial t_1\partial t_2}\ln(M_{XY}(t_1,t_2))\Big|_{t_1=t_2=0} = \\
\frac{\partial\partial}{\partial t_1\partial t_2}\ln(E[e^{t_1X+t_2Y}])\Big|_{t_1=t_2=0} = \frac{\partial}{\partial t_1}\left[\frac{1}{E[e^{t_1X+t_2Y}]}\frac{\partial}{\partial t_2}(E[e^{t_1X+t_2Y}])\right]_{t_1=t_2=0} = \\
\left[-\frac{1}{(E[e^{t_1X+t_2Y}])^2}\frac{\partial}{\partial t_1}(E[e^{t_1X+t_2Y}])\frac{\partial}{\partial t_2}(E[e^{t_1X+t_2Y}]) + \frac{1}{E[e^{t_1X+t_2Y}]}\frac{\partial\partial}{\partial t_1\partial t_2}(E[e^{t_1X+t_2Y}])\right]_{t_1=t_2=0} = \\
= -\mu_x\mu_y + \mu_{xy}
\end{array} \tag{A.43}$$

If we apply the same procedure for c_{111}, then:

$$c_{111} = \mu_{111} - \mu_{110}\mu_{001} - \mu_{101}\mu_{010} - \mu_{011}\mu_{100} + 2\mu_{100}\mu_{010}\mu_{001} \tag{A.44}$$

and also for c_{201}:

$$c_{201} = \mu_{201} - \mu_{200}\mu_{001} - 2\mu_{101}\mu_{100} + 2\mu_{200}\mu_{001} \tag{A.45}$$

k_{xyz} can be simply calculated by equation A.44 with knowing that in the central moment, first moments or the means are equal to zero ($\mu_{100} = \mu_{010} = \mu_{001} = 0$):

$$c_{111} = \mu_{111} \tag{A.46}$$

Let X, Y, and Z be three random variables such that Z is an independent random variable from X and Y. Thus cumulant c_{112} is:

$$
\begin{aligned}
c_{112} &= \frac{\partial^1\partial^1\partial^2}{\partial t_1^1\partial t_2^1\partial t_3^2} \ln(M_{XYZ}(t_1,t_2,t_3))\Big|_{t_1=t_2=t_3=0} \\
&= \frac{\partial^1\partial^1\partial^2}{\partial t_1^1\partial t_2^1\partial t_3^2} \ln(M_{XY}(t_1,t_2)M_Z(t_3))\Big|_{t_1=t_2=t_3=0} \\
&= \frac{\partial^1\partial^1\partial^2}{\partial t_1^1\partial t_2^1\partial t_3^2} (\ln M_{XY}(t_1,t_2) + \ln M_Z(t_3))\Big|_{t_1=t_2=t_3=0} = 0
\end{aligned}
\tag{A.47}
$$

The above equation tells us that if one variable is independent of others, all the cumulants of these three random variables are zero. However, this behavior is not observed in the moment because μ_{112} is not zero in the same situation:

$$
\mu_{112} = \frac{\partial^1\partial^1\partial^2}{\partial t_1^1\partial t_2^1\partial t_3^2}(M_{XYZ}(t_1,t_2,t_3))\Big|_{t_1=t_2=t_3=0} = \frac{\partial^1\partial^1\partial^2}{\partial t_1^1\partial t_2^1\partial t_3^2}(M_{XY}(t_1,t_2)M_Z(t_3))\Big|_{t_1=t_2=t_3=0} \\
(\frac{\partial^1\partial^1}{\partial t_1^1\partial t_2^1}M_{XY}(t_1,t_2)\frac{\partial^2}{\partial t_3^2}M_Z(t_3))\Big|_{t_1=t_2=t_3=0} = \mu_{110}\mu_{002}
\tag{A.48}
$$

A.6. The combinatorial interpretation of cumulant

We suppose that B is the set divided into subsets B_n such that $B = \cup_n B_n$ and $|B|$ is the size of set B and the numerator π runs through set B. The moments can be calculated with the polynomials of the cumulants as:

$$
\mu_n = \sum_{\pi} \prod_{B\in\pi} c_{|B|}
\tag{A.49}
$$

The bove equation has a combinatorial meaning of the expression of the moments in terms of cumulans. For more than one random variable:

$$
\mu_{x_1x_2..x_n} = \sum_{\pi} \prod_{B\in\pi} c(X_i : i \in B)
\tag{A.50}
$$

For example, μ_{111} is calculated as:

$$
\mu_{111} = c_{111} + c_{100}c_{011} + c_{010}c_{101} + c_{001}c_{110} + c_{100}c_{101}c_{001}
\tag{A.51}
$$

Let us calculate moments up the fourth order with the above equation.

$$\begin{aligned}
\mu_1 &= c_1 \\
\mu_2 &= c_2 + c_1^2 \\
\mu_3 &= c_3 + 3c_2c_1 + c_1^3 \\
\mu_4 &= c_4 + 4c_3c_1 + 3c_2^2 + 6c_2c_1^2 + c_1^4
\end{aligned} \tag{A.52}$$

cumulants in the polynomial form of the moments are obtained by rearranging above equations as:

$$\begin{aligned}
c_1 &= \mu_1 \\
c_2 &= \mu_2 - \mu_1^2 \\
c_3 &= \mu_3 - 3\mu_2\mu_1 + 2\mu_1^3 \\
c_4 &= \mu_4 - 4\mu_3\mu_1 - 3\mu_2^2 + 12\mu_2\mu_1^2 - \mu_1^4
\end{aligned} \tag{A.53}$$

the polynomial form of the central moments in terms of the cumulants can be acquired by dropping the first moment in all terms:

$$\begin{aligned}
c_2 &= k_2 \\
c_3 &= k_3 \\
c_4 &= k_4 - 3k_2^2
\end{aligned} \tag{A.54}$$

these equations imply that the second and third central moments and cumulants are identical. This result becomes more important in the cumulant LBM where moments and cumulants are transformed to each other.

A.7. Calculating a PDF from a PMF

Remember that a PDF is not used for a discrete random variable (it has the finite or countable number of values) because of discontinuances in the cumulative distribution function (CDF). However, we can define a PDF for discrete random variables if we somehow differentiate from the CDF at discontinuances. It can be carried out by the Dirac delta function. Thus, the Dirac delta function is used to extend the definition of the PDF to the discrete random variable. Some properties of the Dirac delta function can be written in the following equations:

$$1- \quad \delta(x-x_0) = \begin{cases} \infty & for\ x = x_0 \\ 0 & otherwise \end{cases} \tag{A.55}$$

$$2- \quad \delta(x-x_0) = \frac{d}{dx}u(x-x_0) \tag{A.56}$$

where $u(x - x_0)$ is a continuous unit step function.

$$3 - \quad \int_{-\infty}^{+\infty} \delta(x - x_0) = 1 \tag{A.57}$$

$$4 - \quad \int_{-\infty}^{+\infty} f(x)\delta(x - x_0) = f(x_0), \tag{A.58}$$

where $f(x)$ a continuous function.

Suppose X as a discrete random variable in the range $\chi = \{x_1, x_2, x_3 ...\}$ with the PMF $P_X(x_k)$. The CDF for the variable X is defined as:

$$CDF_x(x) = \sum_{x_k \in \chi} P_X(x_k) u(x - x_k) \tag{A.59}$$

By differentiating the CDF for X, the probability density function (PDF) is obtained as:

$$\begin{aligned} &PDF = f_X(x) = \tfrac{d}{dx}(CDF_X(x)) = \sum_{x_k \in \chi} P_X(x_k) \tfrac{d}{dx} u(x - x_k) \\ &= \sum_{x_k \in \chi} P_X(x_k) \delta(x - x_k) \end{aligned} \tag{A.60}$$

It is also called the generalized PDF. An advantage of the generalized PDF is that the same formula for both the discrete and continuous random variable can be used. A random variable X is a discrete random variable if the generalized PDF of this variable can be written as the sum of delta functions and if not; it is a continuous random variable. However, other definitions like the expectation, moment generating function, etc. are not influenced by this behavior. Let us suppose that Y is a discrete random variable and the expected value is required. Then:

$$\begin{aligned} &E[Y] = \textstyle\int_{-\infty}^{\infty} y f_Y(y) dy = \int_{-\infty}^{\infty} y \sum\limits_{y_k \in \chi} P_Y(y_k) \delta(y - y_k) dy = \\ &= \sum_{y_k \in \chi} P_Y(y_k) \textstyle\int_{-\infty}^{\infty} y \delta(y - y_k) dy = \sum\limits_{y_k \in \chi} P_Y(y_k) y_k \end{aligned} \tag{A.61}$$

It is seen that the original definition of the expected value and the moment generating function remain unchangeable with using the Dirac delta function.

$$\begin{aligned} &M_X(t) = E[e^{tX}] = \int_{-\infty}^{\infty} e^{tX} \sum_{x_k \in \chi} P_X(x_k)\delta(x - x_k)dx \\ &= \sum_{x_k \in \chi} P_X(x_k) \int_{-\infty}^{\infty} e^{tx}\delta(x - x_k)dx = \sum_{x_k \in \chi} P_X(x_k)e^{tx_k} \end{aligned} \tag{A.62}$$

In the LBM, continuous functions are used although the random variables are discrete. Therefore, fully realizing this section can help to understand the basic concept of the LBM better.

B. Asymptotic Analysis

The Navier-Stokes equations can be derived by the LB equation through a combination of Taylor expansions and asymptotic expansions. We show this procedure in detail in this appendix.

The propagation step in the LBM is:

$$f_i(x + e_{xi}c\Delta t, y + e_{yi}c\Delta t, z + e_{zi}c\Delta t, t + \Delta t) = {f_i}^*(x, y, z, t) \tag{B.1}$$

Or in the other words:

$$f_i(x, y, z, t + \Delta t) = {f_i}^*(x - e_{xi}c\Delta t, y - e_{yi}c\Delta t, z - e_{zi}c\Delta t, t) \tag{B.2}$$

We use Taylor expansion to expand equation B.2 in order to acquire partial differential equations. The Taylor expansion of both sides of equation B.2 results in:

$$\sum_{p=0}^{\infty} \frac{\Delta t^p}{p!} \partial_{t^p} f_i = \sum_{m,n,l=0}^{\omega} \frac{{e_{xi}}^m {e_{yi}}^n {e_{zi}}^l (-c\Delta t)^{m+n+l}}{m!n!l!} \partial_{x^m y^n z^l} {f_i}^* \tag{B.3}$$

where $\partial_{t^p} f$ is the p_{th} derivative of f with respect to t. We remove the index of space and time from now. The above equation can be rewritten in the moment form. The definition of the moment for the LBM is:

$$\mu_{\alpha\beta\gamma} = \sum_{ijk} f_{ijk} (e_i)^\alpha (e_j)^\beta (e_k)^\gamma$$

Therefore, a Taylor expansion of the moments in space and time can be given as:

$$\begin{aligned} &\sum_{ijk} \left(\sum_{p=0}^{\infty} \tfrac{\Delta t^p}{p!} \partial_{t^p} f_i \right) (e_i)^\alpha (e_j)^\beta (e_k)^\gamma = \\ &\sum_{ijk} \left(\sum_{m,n,l=0}^{\infty} \tfrac{{e_i}^m {e_i}^n {e_i}^l (-c\Delta t)^{m+n+l}}{m!n!l!} \partial_{x^m y^n z^l} {f_i}^* \right) (e_i)^\alpha (e_j)^\beta (e_k)^\gamma \end{aligned} \tag{B.4}$$

and thus:

$$\sum_{p=0}^{\infty} \frac{\Delta t^p}{p!}\partial_{t^p}\mu_{\alpha\beta\gamma} = \sum_{m,n,l=0}^{\infty} \frac{(-c\Delta t)^{m+n+l}}{m!n!l!}\partial_{x^m y^n z^l}\mu^*{}_{(\alpha+m)(\beta+n)(\gamma+l)} \tag{B.5}$$

Note that c is $\Delta x/\Delta t$; then, $c\Delta t = (\Delta x/\Delta t)\Delta t = \Delta x$. The left side of the equation is Δt while the right hand is Δx. There are two kinds of time scales, one is the acoustic and another is the diffusive time scale which is used ($\Delta t = (\Delta x)^2 = \epsilon^2$). After substituting the time and space scaling in equation B.5, the following equation is acquired:

$$\sum_{p=0}^{\infty} \frac{\varepsilon^{2p}}{p!}\partial_{t^p}\mu_{\alpha\beta\gamma} = \sum_{m,n,l=0}^{\infty} \frac{(-\varepsilon)^{m+n+l}}{m!n!l!}\partial_{x^m y^n z^l}\mu^*{}_{(\alpha+m)(\beta+n)(\gamma+l)} \tag{B.6}$$

We use asymptotic expansion for the moments according to the scaling parameter ϵ:

$$\mu_{\alpha\beta\gamma} = \sum_{q}^{\infty} \varepsilon^q \mu_{\alpha\beta\gamma}^{(q)} \tag{B.7}$$

with substituting equation B.7 into equation B.6 a final expanded equation can be obtained by:

$$\sum_{p=0}^{\infty} \frac{\varepsilon^{2p}}{p!}\partial_{t^p} \sum_{q}^{\infty} \varepsilon^q \mu_{\alpha\beta\gamma}^{(q)} = \sum_{m,n,l=0}^{\infty} \frac{(-\varepsilon)^{m+n+l}}{m!n!l!}\partial_{x^m y^n z^l} \sum_{q}^{\infty} \varepsilon^q \mu^{*(q)}_{(\alpha+m)(\beta+n)(\gamma+l)} \tag{B.8}$$

The rest of this appendix is obtained from the expansion of equation B.8 and equalizing both sides of the equation such that each side has the same power of ϵ. The equivalent partial differential equations are extracted from ordering the moments according to ϵ. A D3Q27 model is assumed which has 27 independent raw countable moments in three dimensions.

Higher order moments are considered to follow aliasing conditions such as:

$$\begin{aligned} \mu_{300} &= \mu_{100} \\ \mu_{400} &= \mu_{200} \\ \mu_{500} &= \mu_{100} \\ \mu_{310} &= \mu_{110} \end{aligned} \tag{B.9}$$

To show how the above equations are obtained, one of them is proved and other can be calculated in the same way. We suppose that there are three discrete random variables X, Y, and Z with the probability mass function $f_{XYZ}(x = e_{xi}, y = e_{yi}, z = e_{zi})$. For the D3Q27 model, ranges $R_x = (e_{x1}, e_{x2}, e_{x3}) = (-1, 0, 1)$, $R_y = (e_{y1}, e_{y2}, e_{y3}) = (-1, 0, 1)$ and $R_z = (e_{z1}, e_{z2}, e_{z3}) = (-1, 0, 1)$ are defined. Therefore, moment μ_{300} is:

$$\begin{aligned} \mu_{300} &= \sum_{i \in R_x} \sum_{j \in R_y} \sum_{k \in R_z} (e_{xi})^3 (e_{yj})^0 (e_{zk})^0 f \\ &= \sum_{i \in R_x} \sum_{j \in R_y} \sum_{k \in R_z} (e_{xi})^1 f \ = \mu_{100} \end{aligned} \tag{B.10}$$

The following equation is established if the left hand side (lhs) of equation B.8 is rearranged by orders of ϵ.

$$\begin{aligned} &lhs = \sum_{p=0}^{\infty} \tfrac{\varepsilon^{2p}}{p!} \partial_{t^p} \left(\varepsilon^0 \mu^{(0)}_{\alpha\beta\gamma} + \varepsilon^1 \mu^{(1)}_{\alpha\beta\gamma} + \varepsilon^2 \mu^{(2)}_{\alpha\beta\gamma} + \varepsilon^3 \mu^{(3)}_{\alpha\beta\gamma} ... \right) = \\ &\varepsilon^0 \left(\mu^{(0)}_{\alpha\beta\gamma} \right) + \varepsilon^1 \left(\mu^{(1)}_{\alpha\beta\gamma} \right) + \varepsilon^2 \left(\mu^{(2)}_{\alpha\beta\gamma} + \partial_t \mu^{(0)}_{\alpha\beta\gamma} \right) + \varepsilon^3 \left(\mu^{(3)}_{\alpha\beta\gamma} + \partial_t \mu^{(1)}_{\alpha\beta\gamma} \right) + ... \end{aligned} \tag{B.11}$$

For the right hand side (rhs), some categories are defined to simplify the procedure of acquiring the coefficients of ϵ. These categories are related to m, n and l. The expansion is limited up to order ϵ^3 because higher orders are not utilized in this thesis.

$$\begin{aligned} &rhs = \sum_{m,n,l=0}^{\infty} \tfrac{(-\varepsilon)^{m+n+l}}{m!n!l!} \partial_{x^m y^n z^l} (\varepsilon^0 \mu^{*(0)}_{(\alpha+m)(\beta+n)(\gamma+l)} + \varepsilon^1 \mu^{*(1)}_{(\alpha+m)(\beta+n)(\gamma+l)} \\ &+ \varepsilon^2 \mu^{*(2)}_{(\alpha+m)(\beta+n)(\gamma+l)} + \varepsilon^3 \mu^{*(3)}_{(\alpha+m)(\beta+n)(\gamma+l)} + ...) \end{aligned} \tag{B.12}$$

The first category is defined when the summation m, n, and l are equal to zero (m+n+l=0) in the above equation:

$$\begin{aligned} &m = n = l = 0 \\ &rhs = \varepsilon^0 \mu^{*(0)}_{(\alpha)(\beta)(\gamma)} + \varepsilon^1 \mu^{*(1)}_{(\alpha)(\beta)(\gamma)} + \varepsilon^2 \mu^{*(2)}_{(\alpha)(\beta)(\gamma)} + \varepsilon^3 \mu^{*(3)}_{(\alpha)(\beta)(\gamma)} + ... \end{aligned}$$

The second category has three different possibilities for the expansion where the summation of m, n, and l is equal to one (m+n+l=1):

$$\begin{aligned}
&m = 1, n = l = 0\\
&rhs = -\partial_x \left(\varepsilon^1 \mu^{*(0)}_{(\alpha+1)(\beta)(\gamma)} + \varepsilon^2 \mu^{*(1)}_{(\alpha+1)(\beta)(\gamma)} + \varepsilon^3 \mu^{*(2)}_{(\alpha+1)(\beta)(\gamma)} + ...\right)\\
&n = 1, m = l = 0\\
&rhs = -\partial_y \left(\varepsilon^1 \mu^{*(0)}_{(\alpha)(\beta+1)(\gamma)} + \varepsilon^2 \mu^{*(1)}_{(\alpha)(\beta+1)(\gamma)} + \varepsilon^3 \mu^{*(2)}_{(\alpha)(\beta+1)(\gamma)} + ...\right)\\
&l = 1, m = n = 0\\
&rhs = -\partial_z \left(\varepsilon^1 \mu^{*(0)}_{(\alpha)(\beta)(\gamma+1)} + \varepsilon^2 \mu^{*(1)}_{(\alpha)(\beta)(\gamma+1)} + \varepsilon^3 \mu^{*(2)}_{(\alpha)(\beta)(\gamma+1)} + ...\right)
\end{aligned}$$

third category is where m+n+l=2:

$$\begin{aligned}
&m = 1, n = 1, l = 0\\
&rhs = \partial_{xy} \left(\varepsilon^2 \mu^{*(0)}_{(\alpha+1)(\beta+1)(\gamma)} + \varepsilon^3 \mu^{*(1)}_{(\alpha+1)(\beta+1)(\gamma)} + \varepsilon^4 \mu^{*(2)}_{(\alpha+1)(\beta+1)(\gamma)} + ...\right)\\
&m = 1, n = 0, l = 1\\
&rhs = \partial_{xz} \left(\varepsilon^2 \mu^{*(0)}_{(\alpha+1)(\beta)(\gamma+1)} + \varepsilon^3 \mu^{*(1)}_{(\alpha+1)(\beta)(\gamma+1)} + \varepsilon^4 \mu^{*(2)}_{(\alpha+1)(\beta)(\gamma+1)} + ...\right)\\
&m = 0, n = 1, l = 1\\
&rhs = \partial_{yz} \left(\varepsilon^2 \mu^{*(0)}_{(\alpha)(\beta+1)(\gamma+1)} + \varepsilon^3 \mu^{*(1)}_{(\alpha)(\beta+1)(\gamma+1)} + \varepsilon^4 \mu^{*(2)}_{(\alpha)(\beta+1)(\gamma+1)} + ...\right)
\end{aligned}$$

$$\begin{aligned}
&m = 2, n = l = 0\\
&rhs = \tfrac{1}{2}\partial_{x^2} \left(\varepsilon^2 \mu^{*(0)}_{(\alpha+2)(\beta)(\gamma)} + \varepsilon^3 \mu^{*(1)}_{(\alpha+2)(\beta)(\gamma)} + \varepsilon^4 \mu^{*(2)}_{(\alpha+2)(\beta)(\gamma)} + ...\right)\\
&n = 2, m = l = 0\\
&rhs = \tfrac{1}{2}\partial_{y^2} \left(\varepsilon^2 \mu^{*(0)}_{(\alpha)(\beta+2)(\gamma)} + \varepsilon^3 \mu^{*(1)}_{(\alpha)(\beta+2)(\gamma)} + \varepsilon^4 \mu^{*(2)}_{(\alpha)(\beta+2)(\gamma)} + ...\right)\\
&l = 2, m = n = 0\\
&rhs = \tfrac{1}{2}\partial_{z^2} \left(\varepsilon^2 \mu^{*(0)}_{(\alpha)(\beta)(\gamma+2)} + \varepsilon^3 \mu^{*(1)}_{(\alpha)(\beta)(\gamma+2)} + \varepsilon^4 \mu^{*(2)}_{(\alpha)(\beta)(\gamma+2)} + ...\right)
\end{aligned}$$

And finally, forth category is where m+n+l=3:

$$\begin{aligned}
&m = n = l = 1\\
&rhs = -\partial_{xyz}\left(\varepsilon^{3}\mu^{*(0)}_{(\alpha+1)(\beta+1)(\gamma+1)} + ...\right)\\
&m = 2, n = 1, l = 0\\
&rhs = -\partial_{x^2y}\left(\varepsilon^{3}\mu^{*(0)}_{(\alpha+2)(\beta+1)(\gamma)} + ...\right)\\
&m = 2, n = 0, l = 1\\
&rhs = -\partial_{x^2z}\left(\varepsilon^{3}\mu^{*(0)}_{(\alpha+2)(\beta)(\gamma+1)} + ...\right)\\
&m = 0, n = 2, l = 1\\
&rhs = -\partial_{y^2z}\left(\varepsilon^{3}\mu^{*(0)}_{(\alpha)(\beta+2)(\gamma+1)} + ...\right)\\
&m = 1, n = 2, l = 0\\
&rhs = -\partial_{xy^2}\left(\varepsilon^{3}\mu^{*(0)}_{(\alpha+1)(\beta+2)(\gamma)} + ...\right)\\
&m = 0, n = 1, l = 2\\
&rhs = -\partial_{yz^2}\left(\varepsilon^{3}\mu^{*(0)}_{(\alpha)(\beta+1)(\gamma+2)} + ...\right)\\
&m = 1, n = 0, l = 2\\
&rhs = -\partial_{xz^2}\left(\varepsilon^{3}\mu^{*(0)}_{(\alpha+1)(\beta)(\gamma+2)} + ...\right)
\end{aligned}$$

$$\begin{aligned}
&m = 3, n = l = 0\\
&rhs = \tfrac{1}{6}\partial_{x^3}\left(\varepsilon^{2}\mu^{*(0)}_{(\alpha+3)(\beta)(\gamma)} + ...\right)\\
&n = 3, m = l = 0\\
&rhs = \tfrac{1}{6}\partial_{y^3}\left(\varepsilon^{2}\mu^{*(0)}_{(\alpha)(\beta+2)(\gamma)} + ...\right)\\
&l = 3, m = n = 0\\
&rhs = \tfrac{1}{6}\partial_{z^3}\left(\varepsilon^{2}\mu^{*(0)}_{(\alpha)(\beta)(\gamma+2)} + ...\right)
\end{aligned}$$

All the above categories are gathered and rearranged according to ϵ and then, terms consisting of the same power of ϵ in both side of equation B.8 are equalized separately:

For ϵ^0

$$\mu^{(0)}_{\alpha\beta\gamma} = \mu^{*(0)}_{\alpha\beta\gamma} \tag{B.13}$$

It is seen that to the zeroth order that all observable quantities are collision invariant. This means that all zeroth order moments are equal to their equilibrium moments. For ϵ^1

$$\mu^{(1)}_{\alpha\beta\gamma} = \mu^{*(1)}_{\alpha\beta\gamma} - \partial_x\mu^{*(0)}_{(\alpha+1)(\beta)(\gamma)} - \partial_y\mu^{*(0)}_{(\alpha)(\beta+1)(\gamma)} - \partial_z\mu^{*(0)}_{(\alpha)(\beta)(\gamma+1)} \tag{B.14}$$

For ϵ^2

$$\begin{aligned}&\mu^{(2)}_{\alpha\beta\gamma}+\partial_t\mu^{(0)}_{\alpha\beta\gamma}=\mu^{*(2)}_{(\alpha)(\beta)(\gamma)}-\partial_x\mu^{*(1)}_{(\alpha+1)(\beta)(\gamma)}-\partial_y\mu^{*(1)}_{(\alpha)(\beta+1)(\gamma)}-\partial_z\mu^{*(1)}_{(\alpha)(\beta)(\gamma+1)}\\&+\partial_{xy}\mu^{*(0)}_{(\alpha+1)(\beta+1)(\gamma)}+\partial_{xz}\mu^{*(0)}_{(\alpha+1)(\beta)(\gamma+1)}+\partial_{yz}\mu^{*(0)}_{(\alpha)(\beta+1)(\gamma+1)}+\\&\tfrac{1}{2}\partial_{x^2}\mu^{*(0)}_{(\alpha+2)(\beta)(\gamma)}+\tfrac{1}{2}\partial_{y^2}\mu^{*(0)}_{(\alpha)(\beta+2)(\gamma)}+\tfrac{1}{2}\partial_{z^2}\mu^{*(0)}_{(\alpha)(\beta+2)(\gamma)}\end{aligned}\tag{B.15}$$

For ϵ^3

$$\begin{aligned}&\mu^{(3)}_{\alpha\beta\gamma}+\partial_t\mu^{(1)}_{\alpha\beta\gamma}=\mu^{*(3)}_{(\alpha)(\beta)(\gamma)}-\partial_x\mu^{*(2)}_{(\alpha+1)(\beta)(\gamma)}-\partial_y\mu^{*(2)}_{(\alpha)(\beta+1)(\gamma)}-\partial_z\mu^{*(2)}_{(\alpha)(\beta)(\gamma+1)}+\\&\partial_{xy}\mu^{*(1)}_{(\alpha+1)(\beta+1)(\gamma)}+\partial_{xz}\mu^{*(1)}_{(\alpha+1)(\beta)(\gamma+1)}+\partial_{yz}\mu^{*(1)}_{(\alpha)(\beta+1)(\gamma+1)}+\\&\tfrac{1}{2}\partial_{x^2}\mu^{*(1)}_{(\alpha+2)(\beta)(\gamma)}+\tfrac{1}{2}\partial_{y^2}\mu^{*(1)}_{(\alpha)(\beta+2)(\gamma)}+\tfrac{1}{2}\partial_{z^2}\mu^{*(1)}_{(\alpha)(\beta)(\gamma+2)}\\&-\partial_{xyz}\mu^{*(0)}_{(\alpha+1)(\beta+1)(\gamma+1)}-\partial_{x^2y}\mu^{*(0)}_{(\alpha+2)(\beta+1)(\gamma)}-\partial_{x^2z}\mu^{*(0)}_{(\alpha+2)(\beta)(\gamma+1)}\\&-\partial_{y^2z}\mu^{*(0)}_{(\alpha)(\beta+2)(\gamma+1)}-\partial_{xy^2}\mu^{*(0)}_{(\alpha+1)(\beta+2)(\gamma)}-\partial_{yz^2}\mu^{*(0)}_{(\alpha)(\beta+1)(\gamma+2)}-\partial_{xz^2}\mu^{*(0)}_{(\alpha+1)(\beta)(\gamma+2)}\\&+\tfrac{1}{6}\partial_{x^3}\mu^{*(0)}_{(\alpha+3)(\beta)(\gamma)}+\tfrac{1}{6}\partial_{y^3}\mu^{*(0)}_{(\alpha)(\beta+2)(\gamma)}+\tfrac{1}{6}\partial_{z^3}\mu^{*(0)}_{(\alpha)(\beta)(\gamma+2)}\end{aligned}\tag{B.16}$$

There are some zeroth order moments in equation B.14 which need to be simplified with substituting equilibrium moments in the following way:

$$\mu^{(1)}_{\alpha\beta\gamma}=\mu^{*(1)}_{\alpha\beta\gamma}-\partial_x\mu^{eq(0)}_{(\alpha+1)(\beta)(\gamma)}-\partial_y\mu^{eq(0)}_{(\alpha)(\beta+1)(\gamma)}-\partial_z\mu^{eq(0)}_{(\alpha)(\beta)(\gamma+1)}\tag{B.17}$$

assume that $\alpha=\beta=\gamma=0$, then:

$$\mu^{(1)}_{000}=\mu^{*(1)}_{000}-\partial_x\mu^{eq(0)}_{100}-\partial_y\mu^{eq(0)}_{010}-\partial_z\mu^{eq(0)}_{001}\tag{B.18}$$

Let us calculate the zeroth order equilibrium moments of the above equation. We know that $\mu^{eq}_{100}=\rho u$, $\mu^{eq}_{010}=\rho v$ and $\mu^{eq}_{001}=\rho w$; thus, with using the asymptotic expansion over the density and the velocities, the zeroth order equilibrium moments are calculated:

$$\begin{aligned}&\mu^{eq}_{10}=\mu^{eq(0)}_{10}+\varepsilon\mu^{eq(1)}_{10}+\varepsilon^2\mu^{eq(2)}_{10}+...\\&=\rho u=(\rho^{(0)}+\varepsilon\rho^{(1)}+\varepsilon^2\rho^{(2)}+\varepsilon^3\rho^{(3)}...)(u^{(0)}+\varepsilon u^{(1)}+\varepsilon^2u^{(2)}+\varepsilon^3u^{(3)}...)\\&=\rho^{(0)}u^{(0)}+\varepsilon(\rho^{(0)}u^{(1)}+\rho^{(1)}u^{(0)})+\varepsilon^2(\rho^{(0)}u^{(2)}+\rho^{(1)}u^{(1)}+\rho^{(2)}u^{(0)})+...\end{aligned}\tag{B.19}$$

Because the zeroth order of velocity is zero, it is concluded that $\mu^{eq(0)}_{100}=\rho^{(0)}u^{(0)}=0$. The same procedure is applied for $\mu^{eq(0)}_{010}$ and $\mu^{eq(0)}_{001}$. Then, the following equation is obtained:

$$\mu^{(1)}_{000}=\mu^{*(1)}_{000}\tag{B.20}$$

Let us try with $\alpha=1,\beta=\gamma=0$:

$$\mu^{(1)}_{100}=\mu^{*(1)}_{100}-\partial_x\mu^{eq(0)}_{200}-\partial_y\mu^{eq(0)}_{110}-\partial_z\mu^{eq(0)}_{101}\tag{B.21}$$

Among the equilibrium moments $\mu^{eq(0)}_{200}$, $\mu^{eq(0)}_{110}$, and $\mu^{eq(0)}_{101}$, only the equilibrium $\mu^{eq(0)}_{200}$ is not zero:

$$\begin{aligned} &\mu^{eq}_{200} = \rho c_s^2 + \rho u^2 = \\ &= (\rho^{(0)} c_s^2 + \rho^{(0)} u^{(0)} u^{(0)}) + \varepsilon(\rho^{(1)} c_s^2 + 2\rho^{(0)} u^{(0)} u^{(1)} + \rho^{(1)} u^{(0)} u^{(0)}) + ... \end{aligned} \tag{B.22}$$

Then:

$$\mu^{eq(0)}_{200} = \rho^{(0)} c_s^2 + \rho^{(0)} u^{(0)} u^{(0)} = \rho^{(0)} c_s^2 = \mu^{(0)}_{000} c_s^2 \tag{B.23}$$

for the incompressible flow, $\mu^{(0)}_{000} c_s^2$ is a constant value; thus, derivatives of this term are zero. The first order pre-collision moments are equal to their post-collision moments as a result of the above explanation.

The continuity equation is obtained by equation B.15 at $\alpha = \beta = \gamma = 0$:

$$\partial_t \mu^{(0)}_{000} + \partial_x \mu^{*(1)}_{100} + \partial_y \mu^{*(1)}_{010} + \partial_z \mu^{*(1)}_{001} = 0 \tag{B.24}$$

By replacing the first moments with the velocities $\mu_{100} = \rho u$, $\mu_{010} = \rho v$, and $\mu_{001} = \rho w$ and the zeroth moment by density $\mu_{000} = \rho$:

$$\partial_t \rho^{(0)} + \partial_x((\rho u)^{(1)}) + \partial_y((\rho v)^{(1)}) + \partial_z((\rho w)^{(1)}) = 0 \tag{B.25}$$

for the incompressible flow:

$$\partial_t \mu^{(0)}_{000} = \partial_x \mu^{*(1)}_{100} + \partial_y \mu^{*(1)}_{010} + \partial_z \mu^{*(1)}_{001} = 0 \tag{B.26}$$

$$\partial_t \rho^{(0)} = \partial_x(u^{(1)}) + \partial_y(v^{(1)}) + \partial_z(w^{(1)}) = 0 \tag{B.27}$$

The Navier-Stokes equations for incompressible flow can be derived by setting all terms of order zero to zero in equation B.16 and $\alpha = 1, \beta = \gamma = 0$:

$$\begin{aligned} &\partial_t \mu^{(1)}_{100} = \mu^{*(3)}_{100} - \mu^{(3)}_{100} - (\partial_x \mu^{*(2)}_{200} + \partial_y \mu^{*(2)}_{110} + \partial_z \mu^{*(2)}_{101}) + \\ &(\partial_{xy} \mu^{*(1)}_{210} + \partial_{xz} \mu^{*(1)}_{201} + \partial_{yz} \mu^{*(1)}_{111}) + (\tfrac{1}{2}\partial_{x^2} \mu^{*(1)}_{300} + \tfrac{1}{2}\partial_{y^2} \mu^{*(1)}_{120} + \tfrac{1}{2}\partial_{z^2} \mu^{*(1)}_{102}) \end{aligned} \tag{B.28}$$

above equation can be rewritten by substituting equilibrium moments for first order terms:

$$\begin{aligned} &\partial_t \mu^{(1)}_{100} = \mu^{*(3)}_{100} - \mu^{(3)}_{100} - (\partial_x \mu^{*(2)}_{200} + \partial_y \mu^{*(2)}_{110} + \partial_z \mu^{*(2)}_{101}) + \\ &(\partial_{xy} \mu^{eq(1)}_{210} + \partial_{xz} \mu^{eq(1)}_{201} + \partial_{yz} \mu^{eq(1)}_{111}) + (\tfrac{1}{2}\partial_{x^2} \mu^{eq(1)}_{300} + \tfrac{1}{2}\partial_{y^2} \mu^{eq(1)}_{120} + \tfrac{1}{2}\partial_{z^2} \mu^{eq(1)}_{102}) \end{aligned} \tag{B.29}$$

There are some unknown moments such as $\mu^{*(2)}_{200}$, $\mu^{*(2)}_{110}$, and $\mu^{*(2)}_{101}$ which have to be derived by further equivalent partial differential equations. For calculating unknown moments, equation B.15 can be used again in the following way:

For calculating $\mu^{*(2)}_{200}$, we consider $\alpha = 2, \beta = \gamma = 0$ in equation B.15:

$$\mu^{(2)}_{200} + \partial_t \mu^{(0)}_{200} = \mu^{*(2)}_{200} - \partial_x \mu^{*(1)}_{300} - \partial_y \mu^{*(1)}_{210} - \partial_z \mu^{*(1)}_{201} \tag{B.30}$$

in addition, we know that:

$$\begin{aligned}&\partial_t\mu_{200}^{(0)}=0\\&\mu_{300}^{*(1)}=\mu_{100}^{*(1)}=\mu_{100}^{eq(1)}\\&\mu_{210}^{*(1)}=\mu_{210}^{eq(1)}\\&\mu_{201}^{*(1)}=\mu_{201}^{eq(1)}\end{aligned}\tag{B.31}$$

thus the following equation is acquired:

$$\mu_{200}^{(2)}=\mu_{200}^{*(2)}-\partial_x\mu_{100}^{eq(1)}-\partial_y\mu_{210}^{eq(1)}-\partial_z\mu_{201}^{eq(1)}\tag{B.32}$$

for calculating $\mu_{020}^{*(2)}$, we set $\alpha=0,\beta=2,\gamma=0$ in equation B.15:

$$\mu_{020}^{(2)}=\mu_{020}^{*(2)}-\partial_x\mu_{120}^{eq(1)}-\partial_y\mu_{010}^{eq(1)}-\partial_z\mu_{021}^{eq(1)}\tag{B.33}$$

for calculating $\mu_{002}^{*(2)}$, with $\alpha=0,\beta=0,\gamma=2$ in equation B.15:

$$\mu_{002}^{(2)}=\mu_{002}^{*(2)}-\partial_x\mu_{102}^{eq(1)}-\partial_y\mu_{012}^{eq(1)}-\partial_z\mu_{001}^{eq(1)}\tag{B.34}$$

for calculating $\mu_{110}^{*(2)}$, with $\alpha=1,\beta=1,\gamma=0$ in equation B.15:

$$\mu_{110}^{(2)}=\mu_{110}^{*(2)}-\partial_x\mu_{210}^{eq(1)}-\partial_y\mu_{120}^{eq(1)}-\partial_z\mu_{111}^{eq(1)}\tag{B.35}$$

for calculating $\mu_{101}^{*(2)}$, with $\alpha=1,\beta=0,\gamma=1$ in equation B.15:

$$\mu_{101}^{(2)}=\mu_{101}^{*(2)}-\partial_x\mu_{201}^{eq(1)}-\partial_y\mu_{111}^{eq(1)}-\partial_z\mu_{102}^{eq(1)}\tag{B.36}$$

some equilibrium moments are seen in the above equations which we can calculate directly, for example, μ_{210} is acquired by:

$$\begin{aligned}&\mu_{210}^{eq}=v\rho(c_s^2+u^2)=\\&(v^{(0)}+\varepsilon v^{(1)}...)[(\rho^{(0)}c_s^2+\rho^{(0)}u^{(0)}u^{(0)})+\varepsilon(\rho^{(1)}c_s^2+2\rho^{(0)}u^{(0)}u^{(1)}+\rho^{(1)}u^{(0)}u^{(0)})+...]\\&=0+\varepsilon(\rho^{(0)}v^{(1)}c_s^2)+...\end{aligned}\tag{B.37}$$

Therefore:

$$\mu_{210}^{eq(1)}=\rho^{(0)}v^{(1)}c_s^2\tag{B.38}$$

In the same way:

$$\mu_{201}^{eq(1)}=\rho^{(0)}w^{(1)}c_s^2\tag{B.39}$$

$$\mu_{300}^{eq(1)}=\mu_{100}^{eq(1)}=u^{(1)}\rho^{(0)}\tag{B.40}$$

$$\mu_{120}^{eq(1)}=\mu_{102}^{eq(1)}=\rho^{(0)}u^{(1)}c_s^2=\frac{1}{3}\rho^{(0)}u^{(1)}=\frac{1}{3}\mu_{100}^{eq(1)}\tag{B.41}$$

$$\mu_{111}^{eq(1)}=0\tag{B.42}$$

we can use relaxation operators to obtain relationships between pre and post collision moments and substitute them into equation B.29 to obtaine the Navier-Stokes equations. In this thesis cumulants are relaxed instead of moments although there is no difference between the moment and the cumulant method up to leading order. The relaxation of second cumulants can be written in the following form:

$$c_{110}^{*(2)} = (1-\omega_1)c_{110}^{(2)} \tag{B.43}$$

$$c_{101}^{*(2)} = (1-\omega_1)c_{101}^{(2)} \tag{B.44}$$

$$c_{200}^{*(2)} - c_{020}^{*(2)} = (1-\omega_1)(c_{200}^{(2)} - c_{020}^{(2)}) \tag{B.45}$$

$$c_{200}^{*(2)} - c_{002}^{*(2)} = (1-\omega_1)(c_{200}^{(2)} - c_{002}^{(2)}) \tag{B.46}$$

$$c_{200}^{*(2)} + c_{020}^{*(2)} + c_{003}^{*(2)} = 3c_s^2\omega_2 + (1-\omega_2)(c_{200}^{(2)} + c_{020}^{(2)} + c_{002}^{(2)}) \tag{B.47}$$

first of all, we substitute moments into the above equations to acquire new equations according to the moments and then we use the new obtained equations and equations B.32 to B.36 to calculate the unknown moments in equation B.29. Let us start with calculation μ_{110}:

$$c_{110}^{*} = \frac{\mu_{110}}{\mu_{000}} - \frac{\mu_{100}\mu_{010}}{\mu_{000}^2} \tag{B.48}$$

with using asymptotic expansions:

$$c_{110} = \frac{\mu_{110}^{(0)}}{\mu_{000}^{(0)}} + \varepsilon\left(\frac{\mu_{000}^{(0)}\mu_{110}^{(1)} - \mu_{010}^{(0)}\mu_{100}^{(1)}}{\left(\mu_{000}^{(0)}\right)^2}\right) - \varepsilon^2\left(\frac{\mu_{010}^{(1)}\mu_{100}^{(1)} + \mu_{010}^{(0)}\mu_{100}^{(2)} + \mu_{000}^{(2)}\mu_{110}^{(0)} - \mu_{000}^{(0)}\mu_{110}^{(2)}}{\left(\mu_{000}^{(0)}\right)^2}\right) + ... \tag{B.49}$$

therefore:

$$c_{110}^{(2)} = \frac{-\mu_{010}^{(1)}\mu_{100}^{(1)} + \mu_{000}^{(0)}\mu_{110}^{(2)}}{\left(\mu_{000}^{(0)}\right)^2} = \frac{\mu_{110}^{(2)}}{\mu_{000}^{(0)}} - \frac{\mu_{010}^{(1)}\mu_{100}^{(1)}}{\left(\mu_{000}^{(0)}\right)^2} \tag{B.50}$$

we replace the above equation into equation B.43 as:

$$
\begin{aligned}
&\frac{\mu^{*(2)}_{110}}{\mu^{*(0)}_{000}} - \frac{\mu^{*(1)}_{100}\mu^{*(1)}_{010}}{(\mu^{*(0)}_{000})^2} = (1-\omega_1)\Big(\frac{\mu^{(2)}_{110}}{\mu^{(0)}_{000}} - \frac{\mu^{(1)}_{100}\mu^{(1)}_{010}}{(\mu^{(0)}_{000})^2}\Big)\\
&\frac{\mu^{*(2)}_{110}}{\mu^{*(0)}_{000}} - \frac{\mu^{*(1)}_{100}\mu^{*(1)}_{010}}{(\mu^{*(0)}_{000})^2} = (1-\omega_1)\frac{\mu^{(2)}_{110}}{\mu^{(0)}_{000}} - \frac{\mu^{(1)}_{100}\mu^{(1)}_{010}}{(\mu^{(0)}_{000})^2} + \omega_1\frac{\mu^{(1)}_{100}\mu^{(1)}_{010}}{(\mu^{(0)}_{000})^2}\\
&\Rightarrow \mu^{*(2)}_{110} = \mu^{(2)}_{110}(1-\omega_1) + \frac{\mu^{(1)}_{100}\mu^{(1)}_{010}}{\mu^{(0)}_{000}}\omega_1 = \mu^{(2)}_{110}(1-\omega_1) + \frac{\mu^{eq(1)}_{100}\mu^{eq(1)}_{010}}{\mu^{eq(0)}_{000}}\omega_1
\end{aligned}
\tag{B.51}
$$

equations B.51 and B.35 give us $\mu^{*(2)}_{110}$:

$$
\begin{cases}
\mu^{(2)}_{110} = \mu^{*(2)}_{110} - \partial_x\mu^{eq(1)}_{210} - \partial_y\mu^{eq(1)}_{120} - \partial_z\mu^{eq(1)}_{111}\\
\mu^{(2)}_{110} = \frac{1}{(1-\omega_1)}\mu^{*(2)}_{110} - \frac{\omega_1}{(1-\omega_1)}\frac{\mu^{eq(1)}_{100}\mu^{eq(1)}_{010}}{\mu^{eq(0)}_{000}}
\end{cases}
\tag{B.52}
$$

and finally:

$$
\mu^{*(2)}_{110} = \Big[\frac{\mu^{eq(1)}_{100}\mu^{eq(1)}_{010}}{\mu^{eq(0)}_{000}} + (1-\frac{1}{\omega_1})\partial_x\mu^{eq(1)}_{210} + (1-\frac{1}{\omega_1})\partial_y\mu^{eq(1)}_{120} + (1-\frac{1}{\omega_1})\partial_z\mu^{eq(1)}_{111}\Big]
\tag{B.53}
$$

with the same procedure for $\mu^{(2)}_{101}$:

$$
\begin{cases}
\mu^{(2)}_{101} = \mu^{*(2)}_{101} - \partial_x\mu^{eq(1)}_{201} - \partial_y\mu^{eq(1)}_{111} - \partial_z\mu^{eq(1)}_{102}\\
\mu^{(2)}_{101} = \frac{1}{(1-\omega_1)}\mu^{*(2)}_{101} - \frac{\omega_1}{(1-\omega_1)}\frac{\mu^{eq(1)}_{100}\mu^{eq(1)}_{001}}{\mu^{(0)}_{000}}
\end{cases}
\tag{B.54}
$$

$$
\mu^{*(2)}_{101} = \Big[\frac{\mu^{eq(1)}_{100}\mu^{eq(1)}_{001}}{\mu^{eq(0)}_{000}} + (1-\frac{1}{\omega_1})\partial_x\mu^{eq(1)}_{201} + (1-\frac{1}{\omega_1})\partial_y\mu^{eq(1)}_{111} + (1-\frac{1}{\omega_1})\partial_z\mu^{eq(1)}_{102}\Big]
\tag{B.55}
$$

calculating $\mu^{*(2)}_{200}$, $\mu^{*(2)}_{020}$, and $\mu^{*(2)}_{002}$ are more complicated than $\mu^{*(2)}_{101}$ and need more algebraic operations. Asymptotic expansions give the following equations which transfer the second cumulant to the moments:

$$
c^{(2)}_{200} = \frac{\mu^{(2)}_{200}}{\mu^{(0)}_{000}} - \frac{(\mu^{(1)}_{100})^2}{(\mu^{(0)}_{000})^2} - \frac{(\mu^{(2)}_{000}\mu^{(0)}_{200})}{(\mu^{(0)}_{000})^2}
\tag{B.56}
$$

$$
c^{(2)}_{020} = \frac{\mu^{(2)}_{020}}{\mu^{(0)}_{000}} - \frac{(\mu^{(1)}_{010})^2}{(\mu^{(0)}_{000})^2} - \frac{(\mu^{(2)}_{000}\mu^{(0)}_{020})}{(\mu^{(0)}_{000})^2}
\tag{B.57}
$$

$$c_{002}^{(2)} = \frac{\mu_{002}^{(2)}}{\mu_{000}^{(0)}} - \frac{\left(\mu_{001}^{(1)}\right)^2}{\left(\mu_{000}^{(0)}\right)^2} - \frac{\left(\mu_{000}^{(2)}\mu_{002}^{(0)}\right)}{\left(\mu_{000}^{(0)}\right)^2} \tag{B.58}$$

we gather all the above equations into 9 main equations :

$$\begin{array}{l}
\mu_{200}^{(2)} = \mu_{200}^{*(2)} - \partial_x \mu_{100}^{eq(1)} - \partial_y \mu_{210}^{eq(1)} - \partial_z \mu_{201}^{eq(1)} \\
\mu_{020}^{(2)} = \mu_{020}^{*(2)} - \partial_x \mu_{120}^{eq(1)} - \partial_y \mu_{010}^{eq(1)} - \partial_z \mu_{021}^{eq(1)} \\
\mu_{002}^{(2)} = \mu_{002}^{*(2)} - \partial_x \mu_{102}^{eq(1)} - \partial_y \mu_{012}^{eq(1)} - \partial_z \mu_{001}^{eq(1)} \\
c_{200}^{*(2)} - c_{020}^{*(2)} = (1-\omega_1)(c_{200}^{(2)} - c_{020}^{(2)}) \\
c_{200}^{*(2)} - c_{002}^{*(2)} = (1-\omega_1)(c_{200}^{(2)} - c_{002}^{(2)}) \\
c_{200}^{*(2)} + c_{020}^{*(2)} + c_{003}^{*(2)} = (1-\omega_2)(c_{200}^{(2)} + c_{020}^{(2)} + c_{002}^{(2)}) \ \cdot \\
c_{200}^{(2)} = \frac{\mu_{200}^{(2)}}{\mu_{000}^{(0)}} - \frac{(\mu_{100}^{(1)})^2}{(\mu_{000}^{(0)})^2} - \frac{(\mu_{000}^{(2)}\mu_{200}^{(0)})}{(\mu_{000}^{(0)})^2} \\
c_{020}^{(2)} = \frac{\mu_{020}^{(2)}}{\mu_{000}^{(0)}} - \frac{(\mu_{010}^{(1)})^2}{(\mu_{000}^{(0)})^2} - \frac{(\mu_{000}^{(2)}\mu_{020}^{(0)})}{(\mu_{000}^{(0)})^2} \\
c_{002}^{(2)} = \frac{\mu_{002}^{(2)}}{\mu_{000}^{(0)}} - \frac{(\mu_{001}^{(1)})^2}{(\mu_{000}^{(0)})^2} - \frac{(\mu_{000}^{(2)}\mu_{002}^{(0)})}{(\mu_{000}^{(0)})^2}
\end{array}$$

after the simplification, we obtain 6 equations and 6 unknown moments:

$$\begin{array}{l}
\mu_{200}^{(2)} = \mu_{200}^{*(2)} - \partial_x \mu_{100}^{eq(1)} - \partial_y \mu_{210}^{eq(1)} - \partial_z \mu_{201}^{eq(1)} \\
\mu_{020}^{(2)} = \mu_{020}^{*(2)} - \partial_x \mu_{120}^{eq(1)} - \partial_y \mu_{010}^{eq(1)} - \partial_z \mu_{021}^{eq(1)} \\
\mu_{002}^{(2)} = \mu_{002}^{*(2)} - \partial_x \mu_{102}^{eq(1)} - \partial_y \mu_{012}^{eq(1)} - \partial_z \mu_{001}^{eq(1)} \\
\mu_{200}^{*(2)} - \mu_{020}^{*(2)} = (1-\omega_1)(\mu_{200}^{(2)} - \mu_{020}^{(2)}) + \omega_1\left(\frac{(\mu_{100}^{eq(1)})^2 - (\mu_{010}^{eq(1)})^2}{\mu_{000}^{(0)}}\right) + \omega_1\left(\frac{\mu_{000}^{(2)}\mu_{200}^{(0)} - \mu_{000}^{(2)}\mu_{020}^{(0)}}{\mu_{000}^{(0)}}\right) \\
\mu_{200}^{*(2)} - \mu_{002}^{*(2)} = (1-\omega_1)(\mu_{200}^{(2)} - \mu_{002}^{(2)}) + \omega_1\left(\frac{(\mu_{100}^{eq(1)})^2 - (\mu_{001}^{eq(1)})^2}{\mu_{000}^{(0)}}\right) + \omega_1\left(\frac{\mu_{000}^{(2)}\mu_{200}^{(0)} - \mu_{000}^{(2)}\mu_{002}^{(0)}}{\mu_{000}^{(0)}}\right) \\
\mu_{200}^{*(2)} + \mu_{020}^{*(2)} + \mu_{002}^{(2)} = (1-\omega_2)(\mu_{200}^{(2)} + \mu_{020}^{(2)} + \mu_{002}^{(2)}) \\
+\omega_2\left(\frac{(\mu_{100}^{eq(1)})^2 + (\mu_{010}^{eq(1)})^2 + (\mu_{001}^{eq(1)})^2}{\mu_{000}^{(0)}}\right) + \omega_2\left(\frac{\mu_{000}^{(2)}\mu_{200}^{(0)} + \mu_{000}^{(2)}\mu_{020}^{(0)} + \mu_{000}^{(2)}\mu_{002}^{(0)}}{\mu_{000}^{(0)}}\right)
\end{array} \tag{B.59}$$

we use the continuity equation B.27 to simplify above set of equations:

$$
\begin{array}{l}
\mu_{200}^{(2)} = \mu_{200}^{*(2)} - \frac{2}{3}\partial_x \mu_{100}^{eq(1)} \\
\mu_{020}^{(2)} = \mu_{020}^{*(2)} - \frac{2}{3}\partial_y \mu_{010}^{eq(1)} \\
\mu_{002}^{(2)} = \mu_{002}^{*(2)} - \frac{2}{3}\partial_z \mu_{001}^{eq(1)} \\
\mu_{200}^{*(2)} - \mu_{020}^{*(2)} = (1-\omega_1)(\mu_{200}^{(2)} - \mu_{020}^{(2)}) + \omega_1(\frac{{(\mu_{100}^{eq(1)})}^2 - {(\mu_{010}^{eq(1)})}^2}{\mu_{000}^{(0)}}) + \omega_1(\frac{\mu_{000}^{(2)}\mu_{200}^{(0)} - \mu_{000}^{(2)}\mu_{020}^{(0)}}{\mu_{000}^{(0)}}) \\
\mu_{200}^{*(2)} - \mu_{002}^{*(2)} = (1-\omega_1)(\mu_{200}^{(2)} - \mu_{002}^{(2)}) + \omega_1(\frac{{(\mu_{100}^{eq(1)})}^2 - {(\mu_{001}^{eq(1)})}^2}{\mu_{000}^{(0)}}) + \omega_1(\frac{\mu_{000}^{(2)}\mu_{200}^{(0)} - \mu_{000}^{(2)}\mu_{002}^{(0)}}{\mu_{000}^{(0)}}) \\
\mu_{200}^{*(2)} + \mu_{020}^{*(2)} + \mu_{002}^{(2)} = (1-\omega_2)(\mu_{200}^{(2)} + \mu_{020}^{(2)} + \mu_{002}^{(2)}) \\
+\omega_2(\frac{{(\mu_{100}^{eq(1)})}^2 + {(\mu_{010}^{eq(1)})}^2 + {(\mu_{001}^{eq(1)})}^2}{\mu_{000}^{(0)}}) + \omega_2(\frac{\mu_{000}^{(2)}\mu_{200}^{(0)} + \mu_{000}^{(2)}\mu_{020}^{(0)} + \mu_{000}^{(2)}\mu_{002}^{(0)}}{\mu_{000}^{(0)}})
\end{array}
\tag{B.60}
$$

and

$$
\left\{
\begin{array}{l}
\mu_{200}^{*(2)} - \mu_{020}^{*(2)} = (1-\omega_1)((\mu_{200}^{*(2)} - \frac{2}{3}\partial_x \mu_{100}^{eq(1)}) - (\mu_{020}^{*(2)} - \frac{2}{3}\partial_y \mu_{010}^{eq(1)}))+ \\
\omega_1(\frac{{(\mu_{100}^{eq(1)})}^2 - {(\mu_{010}^{eq(1)})}^2}{\mu_{000}^{(0)}}) + \omega_1(\frac{\mu_{000}^{(2)}\mu_{200}^{(0)} - \mu_{000}^{(2)}\mu_{020}^{(0)}}{\mu_{000}^{(0)}}) \\
\mu_{200}^{*(2)} - \mu_{002}^{*(2)} = (1-\omega_1)((\mu_{200}^{*(2)} - \frac{2}{3}\partial_x \mu_{100}^{eq(1)}) - (\mu_{002}^{*(2)} - \frac{2}{3}\partial_z \mu_{001}^{eq(1)})) \\
+\omega_1(\frac{{(\mu_{100}^{eq(1)})}^2 - {(\mu_{001}^{eq(1)})}^2}{\mu_{000}^{(0)}}) + \omega_1(\frac{\mu_{000}^{(2)}\mu_{200}^{(0)} - \mu_{000}^{(2)}\mu_{002}^{(0)}}{\mu_{000}^{(0)}}) \\
\mu_{200}^{*(2)} + \mu_{020}^{*(2)} + \mu_{002}^{(2)} = (1-\omega_2)(\mu_{200}^{*(2)} + \mu_{020}^{*(2)} + \mu_{002}^{*(2)}) \\
-\frac{2}{3}(1-\omega_2)(\partial_x \mu_{100}^{eq(1)} + \partial_y \mu_{010}^{eq(1)} + \partial_z \mu_{001}^{eq(1)}) \\
+\omega_2(\frac{{(\mu_{100}^{eq(1)})}^2 + {(\mu_{010}^{eq(1)})}^2 + {(\mu_{001}^{eq(1)})}^2}{\mu_{000}^{(0)}}) + \omega_2(\frac{\mu_{000}^{(2)}\mu_{200}^{(0)} + \mu_{000}^{(2)}\mu_{020}^{(0)} + \mu_{000}^{(2)}\mu_{002}^{(0)}}{\mu_{000}^{(0)}})
\end{array}
\right.
\tag{B.61}
$$

$$
\left\{
\begin{array}{l}
\mu_{200}^{*(2)} - \mu_{020}^{*(2)} = -\frac{2}{3}\frac{(1-\omega_1)}{\omega_1}(\partial_x \mu_{100}^{eq(1)} - \partial_y \mu_{010}^{eq(1)}) + (\frac{{(\mu_{100}^{eq(1)})}^2 - {(\mu_{010}^{eq(1)})}^2}{\mu_{000}^{(0)}}) \\
+(\frac{\mu_{000}^{(2)}\mu_{200}^{(0)} - \mu_{000}^{(2)}\mu_{020}^{(0)}}{\mu_{000}^{(0)}}) \\
\mu_{200}^{*(2)} - \mu_{002}^{*(2)} = -\frac{2}{3}\frac{(1-\omega_1)}{\omega_1}(\partial_x \mu_{100}^{eq(1)} - \partial_z \mu_{001}^{eq(1)}) + (\frac{{(\mu_{100}^{eq(1)})}^2 - {(\mu_{001}^{eq(1)})}^2}{\mu_{000}^{(0)}}) \\
+(\frac{\mu_{000}^{(2)}\mu_{200}^{(0)} - \mu_{000}^{(2)}\mu_{002}^{(0)}}{\mu_{000}^{(0)}}) \\
\mu_{200}^{*(2)} + \mu_{020}^{*(2)} + \mu_{002}^{(2)} = (\frac{{(\mu_{100}^{eq(1)})}^2 + {(\mu_{010}^{eq(1)})}^2 + {(\mu_{001}^{eq(1)})}^2}{\mu_{000}^{(0)}}) \\
+(\frac{\mu_{000}^{(2)}\mu_{200}^{(0)} + \mu_{000}^{(2)}\mu_{020}^{(0)} + \mu_{000}^{(2)}\mu_{002}^{(0)}}{\mu_{000}^{(0)}})
\end{array}
\right.
\tag{B.62}
$$

then, $\mu_{200}^{*(2)}$, $\mu_{020}^{*(2)}$, and $\mu_{002}^{*(2)}$ are:

$$
\mu_{200}^{*(2)} = \frac{2}{3}\partial_x \mu_{100}^{eq(1)}(1 - \frac{1}{\omega_1}) + \frac{{(\mu_{100}^{eq(1)})}^2}{\mu_{000}^{(0)}} + \frac{\mu_{000}^{(2)}\mu_{200}^{(0)}}{\mu_{000}^{(0)}}
\tag{B.63}
$$

$$\mu_{020}^{*(2)} = \frac{2}{3}\partial_y\mu_{010}^{eq(1)}(1-\frac{1}{\omega_1}) + \frac{\left(\mu_{010}^{eq(1)}\right)^2}{\mu_{000}^{(0)}} + \frac{\mu_{000}^{(2)}\mu_{020}^{(0)}}{\mu_{000}^{(0)}} \tag{B.64}$$

$$\mu_{020}^{*(2)} = \frac{2}{3}\partial_z\mu_{001}^{eq(1)}(1-\frac{1}{\omega_1}) + \frac{\left(\mu_{001}^{eq(1)}\right)^2}{\mu_{000}^{(0)}} + \frac{\mu_{000}^{(2)}\mu_{002}^{(0)}}{\mu_{000}^{(0)}} \tag{B.65}$$

or in the forms of pre-collision moments:

$$\mu_{200}^{(2)} = \mu_{200}^{eq(2)} - \frac{2}{3\omega_1}\rho\partial_x u^{(1)} \tag{B.66}$$

$$\mu_{020}^{(2)} = \mu_{020}^{eq(2)} - \frac{2}{3\omega_1}\rho\partial_y v^{(1)} \tag{B.67}$$

$$\mu_{020}^{(2)} = \mu_{020}^{eq(2)} - \frac{2}{3\omega_1}\rho\partial_z w^{(1)} \tag{B.68}$$

where $\mu_{200}^{eq(2)}$, $\mu_{020}^{(2)}$, and $\mu_{020}^{(2)}$ are calculated by asymptotic expansion:

$$\mu_{200}^{eq(2)} = \frac{\left(\mu_{100}^{eq(1)}\right)^2}{\mu_{000}^{(0)}} + \frac{\mu_{000}^{(2)}\mu_{200}^{(0)}}{\mu_{000}^{(0)}}$$
$$\mu_{020}^{(2)} = \frac{\left(\mu_{010}^{eq(1)}\right)^2}{\mu_{000}^{(0)}} + \frac{\mu_{000}^{(2)}\mu_{020}^{(0)}}{\mu_{000}^{(0)}}$$
$$\mu_{020}^{(2)} = \frac{\left(\mu_{001}^{eq(1)}\right)^2}{\mu_{000}^{(0)}} + \frac{\mu_{000}^{(2)}\mu_{002}^{(0)}}{\mu_{000}^{(0)}}$$

All unknown moments have been calculated. We again gather all useful equations in one following set of equations:

$$\left\{ \begin{array}{l} \mu_{200}^{*(2)} = \tfrac{2}{3}(1-\tfrac{1}{\omega_1})\partial_x\mu_{100}^{eq(1)} + \tfrac{\left(\mu_{100}^{eq(1)}\right)^2}{\mu_{000}^{(0)}} + \tfrac{\mu_{000}^{(2)}\mu_{200}^{(0)}}{\mu_{000}^{(0)}} \\ \mu_{101}^{*(2)} = (1-\tfrac{1}{\omega_1})\partial_x\mu_{201}^{eq(1)} + (1-\tfrac{1}{\omega_1})\partial_y\mu_{111}^{eq(1)} + (1-\tfrac{1}{\omega_1})\partial_z\mu_{102}^{eq(1)} + \tfrac{\mu_{100}^{eq(1)}\mu_{001}^{eq(1)}}{\mu_{000}^{eq(0)}} \\ \mu_{110}^{*(2)} = (1-\tfrac{1}{\omega_1})\partial_x\mu_{210}^{eq(1)} + (1-\tfrac{1}{\omega_1})\partial_y\mu_{120}^{eq(1)} + (1-\tfrac{1}{\omega_1})\partial_z\mu_{111}^{eq(1)} + \tfrac{\mu_{100}^{eq(1)}\mu_{010}^{eq(1)}}{\mu_{000}^{eq(0)}} \\ \partial_t\mu_{100}^{(1)} = \mu_{100}^{*(3)} - \mu_{100}^{(3)} - (\partial_x\mu_{200}^{*(2)} + \partial_y\mu_{110}^{*(2)} + \partial_z\mu_{101}^{*(2)}) + \\ (\partial_{xy}\mu_{210}^{*(1)} + \partial_{xz}\mu_{201}^{*(1)} + \partial_{yz}\mu_{111}^{*(1)}) + (\tfrac{1}{2}\partial_{x^2}\mu_{300}^{*(1)} + \tfrac{1}{2}\partial_{y^2}\mu_{120}^{*(1)} + \tfrac{1}{2}\partial_{z^2}\mu_{102}^{*(1)}) \end{array} \right.$$

with substituting $\mu_{200}^{*(2)}$, $\mu_{101}^{*(2)}$, and $\mu_{110}^{*(2)}$ into B.29:

$$\begin{aligned}
&\partial_t\mu_{100}^{(1)} = \mu_{100}^{*(3)} - \mu_{100}^{(3)} - \\
&\{\partial_x(\tfrac{2}{3}(1-\tfrac{1}{\omega_1})\partial_x\mu_{100}^{eq(1)} + \tfrac{(\mu_{100}^{eq(1)})^2}{\mu_{000}^{(0)}} + \tfrac{\mu_{000}^{(2)}\mu_{200}^{(0)}}{\mu_{000}^{(0)}}) + \\
&\partial_y((1-\tfrac{1}{\omega_1})\partial_x\mu_{210}^{eq(1)} + (1-\tfrac{1}{\omega_1})\partial_y\mu_{120}^{eq(1)} + (1-\tfrac{1}{\omega_1})\partial_z\mu_{111}^{eq(1)} + \tfrac{\mu_{100}^{eq(1)}\mu_{010}^{eq(1)}}{\mu_{000}^{eq(0)}}) + \\
&\partial_z((1-\tfrac{1}{\omega_1})\partial_x\mu_{201}^{eq(1)} + (1-\tfrac{1}{\omega_1})\partial_y\mu_{111}^{eq(1)} + (1-\tfrac{1}{\omega_1})\partial_z\mu_{102}^{eq(1)} + \tfrac{\mu_{100}^{eq(1)}\mu_{001}^{eq(1)}}{\mu_{000}^{eq(0)}})\} + \\
&(\partial_{xy}\mu_{210}^{eq(1)} + \partial_{xz}\mu_{201}^{eq(1)} + \partial_{yz}\mu_{111}^{eq(1)}) + (\tfrac{1}{2}\partial_{x^2}\mu_{300}^{eq(1)} + \tfrac{1}{2}\partial_{y^2}\mu_{120}^{eq(1)} + \tfrac{1}{2}\partial_{z^2}\mu_{102}^{eq(1)})
\end{aligned} \tag{B.69}$$

$$\begin{aligned}
&\partial_t\mu_{100}^{(1)} = \mu_{100}^{*(3)} - \mu_{100}^{(3)} - \partial_x\tfrac{\mu_{000}^{(2)}\mu_{200}^{(0)}}{\mu_{000}^{(0)}} - \partial_x(\tfrac{\mu_{100}^{eq(1)}\mu_{100}^{eq(1)}}{\mu_{000}^{(0)}}) - \partial_y(\tfrac{\mu_{100}^{eq(1)}\mu_{010}^{eq(1)}}{\mu_{000}^{eq(0)}}) - \partial_z(\tfrac{\mu_{100}^{eq(1)}\mu_{001}^{eq(1)}}{\mu_{000}^{eq(0)}}) + \\
&(-\tfrac{2}{3}\partial_{x^2}\mu_{100}^{eq(1)} - \partial_{xy}\mu_{210}^{eq(1)} - \partial_{y^2}\mu_{120}^{eq(1)} - \partial_{zy}\mu_{111}^{eq(1)} - \partial_{xz}\mu_{201}^{eq(1)} - \partial_{yz}\mu_{111}^{eq(1)} - \partial_{z^2}\mu_{102}^{eq(1)}) + \\
&(\tfrac{1}{\omega_1})(\tfrac{2}{3}\partial_{x^2}\mu_{100}^{eq(1)} + \partial_{xy}\mu_{210}^{eq(1)} + \partial_{y^2}\mu_{120}^{eq(1)} + \partial_{zy}\mu_{111}^{eq(1)} + \partial_{xz}\mu_{201}^{eq(1)} + \partial_{yz}\mu_{111}^{eq(1)} + \partial_{z^2}\mu_{102}^{eq(1)}) \\
&+(\partial_{xy}\mu_{210}^{eq(1)} + \partial_{xz}\mu_{201}^{eq(1)} + \partial_{yz}\mu_{111}^{eq(1)}) + (\tfrac{1}{2}\partial_{x^2}\mu_{300}^{eq(1)} + \tfrac{1}{2}\partial_{y^2}\mu_{120}^{eq(1)} + \tfrac{1}{2}\partial_{z^2}\mu_{102}^{eq(1)})
\end{aligned} \tag{B.70}$$

with using B.41 and continuity equation B.27, the above equation can be reduced to:

$$\begin{aligned}
&\partial_t\mu_{100}^{(1)} = \mu_{100}^{*(3)} - \mu_{100}^{(3)} - \partial_x\tfrac{\mu_{000}^{(2)}\mu_{200}^{(0)}}{\mu_{000}^{(0)}} - \partial_x(\tfrac{\mu_{100}^{eq(1)}\mu_{100}^{eq(1)}}{\mu_{000}^{(0)}}) - \partial_y(\tfrac{\mu_{100}^{eq(1)}\mu_{010}^{eq(1)}}{\mu_{000}^{eq(0)}}) - \partial_z(\tfrac{\mu_{100}^{eq(1)}\mu_{001}^{eq(1)}}{\mu_{000}^{eq(0)}}) + \\
&\tfrac{1}{6}(-\partial_{x^2}\mu_{100}^{eq(1)} - \partial_{y^2}\mu_{100}^{eq(1)} - \partial_{z^2}\mu_{100}^{eq(1)}) + (\tfrac{1}{3\omega_1})(\partial_{x^2}\mu_{100}^{eq(1)} + \partial_{y^2}\mu_{100}^{eq(1)} + \partial_{z^2}\mu_{100}^{eq(1)})
\end{aligned} \tag{B.71}$$

The Navier-Stokes equation is acquired by rearranging the above equation:

$$\begin{aligned}
&\partial_t\mu_{100}^{(1)} = \mu_{100}^{*(3)} - \mu_{100}^{(3)} - \partial_x\tfrac{\mu_{000}^{(2)}\mu_{200}^{(0)}}{\mu_{000}^{(0)}} - \tfrac{(\mu_{100}^{eq(1)}\partial_x\mu_{100}^{eq(1)} + \mu_{010}^{eq(1)}\partial_y\mu_{100}^{eq(1)} + \mu_{001}^{eq(1)}\partial_z\mu_{100}^{eq(1)})}{\mu_{000}^{(0)}} + \\
&\tfrac{1}{3}(\tfrac{1}{\omega_1} - \tfrac{1}{2})(\partial_{x^2}\mu_{100}^{eq(1)} + \partial_{y^2}\mu_{100}^{eq(1)} + \partial_{z^2}\mu_{100}^{eq(1)})
\end{aligned} \tag{B.72}$$

or in another form:

$$\begin{aligned}
&\partial_t(\rho^{(0)}u^{(1)}) = F_x^{(3)} - \partial_x(\rho^{(2)}c_s^2) - [u^{(1)}\partial_x(\rho^{(0)}u^{(1)}) + v^{(1)}\partial_y(\rho^{(0)}u^{(1)}) + w^{(1)}\partial_z(\rho^{(0)}u^{(1)})] + \\
&\tfrac{1}{3}(\tfrac{1}{\omega_1} - \tfrac{1}{2})(\partial_{x^2}(\rho^{(0)}u^{(1)}) + \partial_{y^2}(\rho^{(0)}u^{(1)}) + \partial_{z^2}(\rho^{(0)}u^{(1)}))
\end{aligned} \tag{B.73}$$

and the final form of the Navier-Stokes equation is:

$$\begin{aligned}
&\partial_t(u^{(1)}) = \tfrac{F_x^3}{\rho^{(0)}} - \tfrac{\partial_x(\rho^{(2)})}{3\rho^{(0)}} - (u^{(1)}\partial_x u^{(1)} + v^{(1)}\partial_y u^{(1)} + w^{(1)}\partial_z u^{(1)}) + \\
&\tfrac{1}{3}(\tfrac{1}{\omega_1} - \tfrac{1}{2})(\partial_{x^2}u^{(1)} + \partial_{y^2}u^{(1)} + \partial_{z^2}u^{(1)})
\end{aligned} \tag{B.74}$$

C. The kernel of the cumulant LBM

In this appendix, the equations of the cumulant kernel are given.

Step 1: obtaining central moments by distributions.

part a

$$\begin{aligned}\mu_{200} = (&f^{E} + f^{W} + f^{NE} + f^{SW} + f^{SE} + f^{NW} + f^{TE} + f^{BW} + f^{BE}\\ &+f^{TW} + f^{TNE} + f^{BNE} + f^{TSE} + f^{BSE} + f^{TNW} + f^{BNW} + f^{TSW} + f^{BSW})\end{aligned} \tag{C.1}$$

$$\begin{aligned}\mu_{020} = (&f^{N} + f^{S} + f^{NE} + f^{SW} + f^{SE} + f^{NW} + f^{TN} + f^{BS} + f^{BN}\\ &+f^{TS} + f^{TNE} + f^{BNE} + f^{TSE} + f^{BSE} + f^{TNW} + f^{BNW} + f^{TSW} + f^{BSW})\end{aligned} \tag{C.2}$$

$$\begin{aligned}\mu_{002} = (&f^{T} + f^{B} + f^{TE} + f^{BW} + f^{BE} + f^{TW} + f^{TN} + f^{BS}\\ &+f^{BN} + f^{TS} + f^{TNE} + f^{BNE} + f^{TSE} + f^{BSE} + f^{TNW} + f^{BNW} + f^{TSW} + f^{BSW})\end{aligned} \tag{C.3}$$

$$\begin{aligned}\mu_{110} = (&f^{NE} - f^{SE} + f^{SW} - f^{NW} + f^{TNE} - f^{TSE} + f^{BNE} - f^{BSE}\\ &+f^{TSW} - f^{TNW} + f^{BSW} - f^{BNW})\end{aligned} \tag{C.4}$$

$$\begin{aligned}\mu_{101} = (&f^{TE} + f^{BW} - f^{BE} - f^{TW} + f^{TNE} - f^{BNE} + f^{TSE} - f^{BSE}\\ &-f^{TNW} + f^{BNW} - f^{TSW} + f^{BSW})\end{aligned} \tag{C.5}$$

$$\begin{aligned}\mu_{011} = (&f^{TN} + f^{BS} - f^{BN} - f^{TS} + f^{TNE} - f^{BNE} - f^{TSE} + f^{BSE}\\ &+f^{TNW} - f^{BNW} - f^{TSW} + f^{BSW})\end{aligned} \tag{C.6}$$

$$\begin{aligned}\mu_{210} = (&f^{NE} - f^{SW} - f^{SE} + f^{NW} + f^{TNE} + f^{BNE} - f^{TSE} - f^{BSE}\\ &+f^{TNW} + f^{BNW} - f^{TSW} - f^{BSW}) - 2u\mu_{110} - v\mu_{200}\end{aligned} \tag{C.7}$$

$$\begin{aligned}\mu_{120} = (&f^{NE} - f^{SW} + f^{SE} - f^{NW} + f^{TNE} - f^{TNW} + f^{BNE} - f^{BNW}\\ &+f^{TSE} - f^{TSW} + f^{BSE} - f^{BSW})\end{aligned} \tag{C.8}$$

$$\begin{aligned}\mu_{102} = (&f^{TE} - f^{BW} + f^{BE} - f^{TW} + f^{TNE} - f^{TNW} + f^{BNE} - f^{BNW}\\ &+f^{TSE} - f^{TSW} + f^{BSE} - f^{BSW})\end{aligned} \tag{C.9}$$

$$\mu_{111} = (f^{TNE} - f^{BNE} - f^{TSE} + f^{BSE} - f^{TNW} + f^{BNW} + f^{TSW} - f^{BSW}) \tag{C.10}$$

$$\begin{aligned}\mu_{201} = (&f^{TE} - f^{BW} - f^{BE} + f^{TW} + f^{TNE} - f^{BNE} + f^{TSE} - f^{BSE}\\ &+ f^{TNW} - f^{BNW} + f^{TSW} - f^{BSW})\end{aligned} \tag{C.11}$$

$$\begin{aligned}\mu_{021} = (&f^{TN} - f^{BS} - f^{BN} + f^{TS} + f^{TNE} - f^{BNE} + f^{TSE} - f^{BSE}\\ &+ f^{TNW} - f^{BNW} + f^{TSW} - f^{BSW})\end{aligned} \tag{C.12}$$

$$\begin{aligned}\mu_{012} = (&f^{TN} - f^{BS} + f^{BN} - f^{TS} + f^{TNE} + f^{BNE} - f^{TSE} - f^{BSE}\\ &+ f^{TNW} + f^{BNW} - f^{TSW} - f^{BSW})\end{aligned} \tag{C.13}$$

$$\begin{aligned}\mu_{220} = (&f^{NE} + f^{SW} + f^{SE} + f^{NW} + f^{TNE} + f^{BNE} + f^{TSE} + f^{BSE}\\ &+ f^{TNW} + f^{BNW} + f^{TSW} + f^{BSW})\end{aligned} \tag{C.14}$$

$$\mu_{121} = (f^{TNE} - f^{BNE} + f^{TSE} - f^{BSE} - f^{TNW} + f^{BNW} - f^{TSW} + f^{BSW}) \tag{C.15}$$

$$\begin{aligned}\mu_{202} = (&f^{TE} + f^{BW} + f^{BE} + f^{TW} + f^{TNE} + f^{BNE} + f^{TSE} + f^{BSE}\\ &+ f^{TNW} + f^{BNW} + f^{TSW} + f^{BSW})\end{aligned} \tag{C.16}$$

$$\mu_{211} = (f^{TNE} - f^{BNE} - f^{TSE} + f^{BSE} + f^{TNW} - f^{BNW} - f^{TSW} + f^{BSW}) \tag{C.17}$$

$$\mu_{112} = (f^{TNE} + f^{BNE} - f^{TSE} - f^{BSE} - f^{TNW} - f^{BNW} + f^{TSW} + f^{BSW}) \tag{C.18}$$

$$\begin{aligned}\mu_{022} = (&f^{TN} + f^{BS} + f^{BN} + f^{TS} + f^{TNE} + f^{BNE} + f^{TSE} + f^{BSE}\\ &+ f^{TNW} + f^{BNW} + f^{TSW} + f^{BSW})\end{aligned} \tag{C.19}$$

$$\mu_{221} = (f^{TNE} - f^{BNE} + f^{TSE} - f^{BSE} + f^{TNW} - f^{BNW} + f^{TSW} - f^{BSW}) \tag{C.20}$$

$$\mu_{122} = (f^{TNE} - f^{TNW} + f^{BNE} - f^{BNW} + f^{TSE} - f^{TSW} + f^{BSE} - f^{BSW}) \tag{C.21}$$

$$\mu_{212} = (f^{TNE} + f^{BNE} - f^{TSE} - f^{BSE} + f^{TNW} + f^{BNW} - f^{TSW} - f^{BSW}) \tag{C.22}$$

$$\mu_{222} = (f^{TNE} + f^{BNE} + f^{TSE} + f^{BSE} + f^{TNW} + f^{BNW} + f^{TSW} + f^{BSW}) \tag{C.23}$$

part b

$$k_{200} = \mu_{200} - \rho uu/c^2 \tag{C.24}$$

$$k_{002} = \mu_{002} - \rho ww/c^2 \tag{C.25}$$

$$k_{020} = \mu_{020} - \rho vv/c^2 \tag{C.26}$$

$$k_{110} = \mu_{110} - \rho uv/c^2 \tag{C.27}$$

$$k_{101} = \mu_{101} - \rho uw/c^2 \tag{C.28}$$

$$k_{011} = \mu_{011} - \rho vw/c^2 \tag{C.29}$$

$$k_{021} = \mu_{021} - (w/c\mu_{020} + 2v/ck_{011}) \tag{C.30}$$

$$k_{012} = \mu_{012} - (v/c\mu_{002} + 2w/ck_{011}) \tag{C.31}$$

$$k_{102} = \mu_{102} - (u/c\mu_{002} + 2w/ck_{101}) \tag{C.32}$$

$$k_{201} = \mu_{201} - (w/c\mu_{200} + 2u/ck_{101}) \tag{C.33}$$

$$k_{210} = \mu_{210} - (v/c\mu_{200} + 2u/ck_{110}) \tag{C.34}$$

$$k_{120} = \mu_{120} - (u/c\mu_{020} + 2v/ck_{110}) \tag{C.35}$$

$$k_{111} = \mu_{111} - (uvw/c^3 + u/ck_{011} + v/ck_{101} + w/ck_{110}) \tag{C.36}$$

$$k_{121} = \mu_{121} - (w/c\mu_{120} + 2uv/c^2k_{011} + u/ck_{021} + vv/c^2k_{101} + 2.0v/ck_{111}) \tag{C.37}$$

$$k_{112} = \mu_{112} - (v/c\mu_{102} + 2uw/c^2k_{011} + v/ck_{012} + ww/c^2k_{110} + 2w/ck_{111}) \tag{C.38}$$

$$k_{211} = \mu_{211} - (w/c\mu_{210} + 2uv/c^2k_{101} + v/ck_{201} + uu/c^2k_{011} + 2u/ck_{111}) \tag{C.39}$$

$$k_{220} = \mu_{220} - (uu/c^2\mu_{020} + 4uv/c^2k_{110} + 2u/ck_{120} + vv/c^2k_{200} + 2v/ck_{210}) \tag{C.40}$$

$$k_{022} = \mu_{022} - (vv/c^2\mu_{002} + 4vw/c^2k_{011} + 2v/ck_{012} + ww/c^2k_{020} + 2w/ck_{021}) \tag{C.41}$$

$$k_{202} = \mu_{202} - (uu/c^2\mu_{002} + 4uw/c^2k_{101} + 2u/ck_{102} + ww/c^2k_{200} + 2w/ck_{201}) \tag{C.42}$$

$$\begin{split} k_{221} = \mu_{221} - (w/c\mu_{220} + 2uuv/c^3k_{011} + uu/c^2k_{021} + 2uvv/c^3k_{101} + 4uv/c^2k_{111} \\ +2u/ck_{121} + vv/c^2k_{021} + 2v/ck_{211}) \end{split} \tag{C.43}$$

$$\begin{split} k_{122} = \mu_{122} - (u/c\mu_{022} + 2vvw/c^3k_{101} + vv/c^2k_{102} + 2vww/c^3k_{110} + 4vw/c^2k_{111} \\ +2v/ck_{112} + ww/c^2k_{120} + 2w/ck_{121}) \end{split} \tag{C.44}$$

$$\begin{split} k_{212} = \mu_{212} - (v/c\mu_{202} + 2uuw/c^3k_{011} + uu/c^2k_{012} + 2uww/c^3k_{110} + 4uw/c^2k_{111} \\ +2u/ck_{112} + ww/c^2k_{210} + 2w/ck_{211}) \end{split} \tag{C.45}$$

$$\begin{split} k_{222} = \mu_{222} - (uu/c^2\mu_{022} + 4uvvw/c^3k_{101} + 2uvv/c^3k_{102} + 4uvww/c^4k_{110} \\ +8uvw/c^3k_{111} + 4uv/c^2k_{112} + 2uww/c^3k_{120} + 4uw/c^2k_{121} + 2u/ck_{122} + vvww/c^4k_{200} \\ +2vvw/c^3k_{201} + vv/c^2k_{202} + 2vww/c^3k_{210} + 4vw/c^2k_{211} + 2v/ck_{212} \\ +ww/ck_{220} + 2w/ck_{221}) \end{split} \tag{C.46}$$

Step 2: calculating cumulants from central moments.

$$\rho c_{110} = k_{110} \tag{C.47}$$

$$\rho c_{101} = k_{101} \tag{C.48}$$

$$\rho c_{011} = k_{011} \tag{C.49}$$

$$\rho c_{200} = k_{200} \tag{C.50}$$

$$\rho c_{020} = k_{020} \tag{C.51}$$

$$\rho c_{002} = k_{002} \tag{C.52}$$

$$\rho c_{300} = k_{300} \tag{C.53}$$

$$\rho c_{030} = k_{030} \tag{C.54}$$

$$\rho c_{003} = k_{003} \tag{C.55}$$

$$\rho c_{210} = k_{210} \tag{C.56}$$

$$\rho c_{201} = k_{201} \tag{C.57}$$

$$\rho c_{120} = k_{120} \tag{C.58}$$

$$\rho c_{021} = k_{021} \tag{C.59}$$

$$\rho c_{102} = k_{102} \tag{C.60}$$

$$\rho c_{012} = k_{012} \tag{C.61}$$

$$\rho c_{111} = k_{111} \tag{C.62}$$

$$\rho c_{121} = k_{121} - k_{020}k_{101} - 2k_{011}k_{110} \tag{C.63}$$

$$\rho c_{211} = k_{211} - k_{200}k_{011} - 2k_{110}k_{101} \tag{C.64}$$

$$\rho c_{112} = k_{112} - k_{002}k_{110} - 2k_{011}k_{011} \tag{C.65}$$

$$\rho c_{220} = k_{220} - k_{200}k_{020} - 2k_{110}^2 \tag{C.66}$$

$$\rho c_{202} = k_{202} - k_{200}k_{002} - 2k_{101}^2 \tag{C.67}$$

$$\rho c_{022} = k_{022} - k_{020}k_{002} - 2k_{011}^2 \tag{C.68}$$

$$\rho c_{122} = k_{122} - k_{002}k_{120} - k_{020}k_{102} - 4k_{011}k_{111} - 2(k_{101}k_{021} + k_{110}k_{012}) \tag{C.69}$$

$$\rho c_{212} = k_{212} - k_{200}k_{012} - k_{002}k_{210} - 4k_{101}k_{111} - 2(k_{110}k_{102} + k_{011}k_{201}) \tag{C.70}$$

$$\rho c_{221} = k_{221} - k_{200}k_{021} - k_{020}k_{201} - 4k_{110}k_{111} - 2(k_{101}k_{121} + k_{011}k_{210}) \tag{C.71}$$

$$\begin{aligned}&\rho c_{222} = k_{222} - (4k_{111}^2 + k_{200}k_{022} + k_{020}k_{202} + k_{002}k_{220} +\\ &4(k_{011}k_{211} + k_{101}k_{121} + k_{110}k_{112})\\ &+2(k_{120}k_{102} + k_{210}k_{012} + k_{201}k_{021})) +\\ &(16k_{110}k_{101}k_{011} + 4(k_{101}^2k_{020} + k_{011}^2k_{200} + k_{110}^2k_{002}) + 2k_{200}k_{020}k_{002})\end{aligned} \tag{C.72}$$

Step 3: acquiring post collision cumulants from the collision operator.

$$c_{110}^* = (1-\omega_1)c_{110} \tag{C.73}$$

$$c_{101}^* = (1-\omega_1)c_{101} \tag{C.74}$$

$$c_{011}^* = (1-\omega_1)c_{011} \tag{C.75}$$

$$c_{200}^* - c_{020}^* = (1-\omega_1)(c_{200} - c_{020}) - 3(1 - \frac{\omega_1}{2})(u^2/c^2 D_x u/c - v^2/c^2 D_y v/c) \tag{C.76}$$

$$c_{200}^* - c_{002}^* = (1-\omega_1)(c_{200} - c_{002}) - 3(1 - \frac{\omega_1}{2})(u^2/c^2 D_x u/c - w^2/c^2 D_z w/c) \tag{C.77}$$

$$c^*_{200}+c^*_{020}+c^*_{002} = \omega_2+(1-\omega_2)(c_{200}+c_{020}+c_{002})-3(1-\frac{\omega_2}{2})(u^2/c^2D_xu/c+v^2/c^2D_yv/c+w^2/c^2D_zw/c) \tag{C.78}$$

$$c^*_{120} + c^*_{102} = (1 - \omega_3)(c_{120} + c_{120}) \tag{C.79}$$

$$c^*_{210} + c^*_{012} = (1 - \omega_3)(c_{210} + c_{012}) \tag{C.80}$$

$$c^*_{201} + c^*_{021} = (1 - \omega_3)(c_{201} + c_{021}) \tag{C.81}$$

$$c^*_{120} - c^*_{102} = (1 - \omega_4)(c_{120} - c_{102}) \tag{C.82}$$

$$c^*_{210} - c^*_{012} = (1 - \omega_4)(c_{210} - c_{012}) \tag{C.83}$$

$$c^*_{201} - c^*_{021} = (1 - \omega_4)(c_{201} - c_{021}) \tag{C.84}$$

$$c^*_{111} = (1 - \omega_5)c_{111} \tag{C.85}$$

$$c^*_{220} - 2c^*_{202} + c^*_{022} = (1 - \omega_6)(c_{220} - 2c_{202} + c_{022}) \tag{C.86}$$

$$c^*_{220} + c^*_{202} - 2c^*_{022} = (1 - \omega_6)(c_{220} + c_{202} - 2c_{022}) \tag{C.87}$$

$$c^*_{220} + c^*_{202} + c^*_{022} = (1 - \omega_7)(c_{220} + c_{202} + c_{022}) \tag{C.88}$$

$$c^*_{211} = (1 - \omega_8)c_{211} \tag{C.89}$$

$$c^*_{121} = (1 - \omega_8)c_{121} \tag{C.90}$$

$$c^*_{112} = (1 - \omega_8)c_{112} \tag{C.91}$$

$$c^*_{221} = (1 - \omega_9)c_{221} \tag{C.92}$$

$$c^*_{212} = (1 - \omega_9)c_{212} \tag{C.93}$$

$$c^*_{122} = (1 - \omega_9)c_{122} \tag{C.94}$$

$$c^*_{222} = (1 - \omega_{10})c_{222} \tag{C.95}$$

Step 4: extracting post collision central moments from the post collision cumulant.

$$k^*_{110} = c^*_{110}\rho \tag{C.96}$$

$$k^*_{101} = c^*_{101}\rho \tag{C.97}$$

$$k^*_{011} = c^*_{011}\rho \tag{C.98}$$

$$k^*_{200} = c^*_{200}\rho \tag{C.99}$$

$$k^*_{020} = c^*_{020}\rho \tag{C.100}$$

$$k^*_{002} = c^*_{002}\rho \tag{C.101}$$

$$k^*_{300} = c^*_{300}\rho \tag{C.102}$$

$$k^*_{030} = c^*_{030}\rho \tag{C.103}$$

$$k^*_{003} = c^*_{003}\rho \tag{C.104}$$

$$k^*_{210} = c^*_{210}\rho \tag{C.105}$$

$$k^*_{201} = c^*_{201}\rho \tag{C.106}$$

$$k^*_{120} = c^*_{120}\rho \tag{C.107}$$

$$k^*_{021} = c^*_{021}\rho \tag{C.108}$$

$$k^*_{102} = c^*_{102}\rho \tag{C.109}$$

$$k^*_{012} = c^*_{012}\rho \tag{C.110}$$

$$k^*_{111} = c^*_{111}\rho \tag{C.111}$$

$$k^*_{211} = \rho c^*_{211} + k^*_{200}k^*_{011} + 2k^*_{110}k^*_{101} \tag{C.112}$$

$$k^*_{121} = \rho c^*_{121} + k^*_{020}k^*_{101} + 2k^*_{011}k^*_{110} \tag{C.113}$$

$$k^*_{112} = \rho c^*_{112} + k^*_{002}k^*_{110} + 2k^*_{011}k^*_{011} \tag{C.114}$$

$$k^*_{220} = \rho c^*_{220} + k^*_{200}k^*_{020} + 2{k^*_{110}}^2 \tag{C.115}$$

$$k^*_{202} = \rho c^*_{202} + k^*_{200}k^*_{002} + 2{k^*_{101}}^2 \tag{C.116}$$

$$k^*_{022} = \rho c^*_{022} + k^*_{020}k^*_{002} + 2{k^*_{011}}^2 \tag{C.117}$$

$$k^*_{122} = \rho c^*_{122} + k^*_{002}k^*_{120} + k^*_{020}k^*_{102} + 4k^*_{011}k^*_{111} + 2(k^*_{101}k^*_{021} + k^*_{110}k^*_{012}) \tag{C.118}$$

$$k^*_{212} = \rho c^*_{212} + k^*_{200}k^*_{012} + k^*_{002}k^*_{210} + 4k^*_{101}k^*_{111} + 2(k^*_{110}k^*_{102} + k^*_{011}k^*_{201}) \tag{C.119}$$

$$k^*_{221} = \rho c^*_{221} + k^*_{200}k^*_{021} + k^*_{020}k^*_{201} + 4k^*_{110}k^*_{111} + 2(k^*_{101}k^*_{121} + k^*_{011}k^*_{210}) \tag{C.120}$$

$$\begin{aligned} &k^*_{222} = \rho c^*_{222} + (4{k^*_{111}}^2 + k^*_{200}k^*_{022} + k^*_{020}k^*_{202} + k^*_{002}k^*_{220} + \\ &4(k^*_{011}k^*_{211} + k^*_{101}k^*_{121} + k^*_{110}k^*_{112}) + 2(k^*_{120}k^*_{102} + k^*_{210}k^*_{012} + k^*_{201}k^*_{021})) \\ &-(16k^*_{110}k^*_{101}k^*_{011} + 4({k^*_{101}}^2k^*_{020} + {k^*_{011}}^2k^*_{200} + {k^*_{110}}^2k^*_{002}) + 2k^*_{200}k^*_{020}k^*_{002}) \end{aligned} \tag{C.121}$$

Step 5: transferring back the post collision central moments to the post collision distribution.

part a

$$\mu^*_{011} = k^*_{011} + \rho vw/c^2 \tag{C.122}$$

$$\mu^*_{110} = k^*_{110} + \rho uv/c^2 \tag{C.123}$$

$$\mu^*_{101} = k^*_{101} + \rho uw/c^2 \tag{C.124}$$

$$\mu^*_{002} = k^*_{002} + \rho ww/c^2 \tag{C.125}$$

$$\mu^*_{020} = k^*_{020} + \rho vv/c^2 \tag{C.126}$$

$$\mu^*_{200} = k^*_{200} + \rho uu/c^2 \tag{C.127}$$

$$\mu^*_{021} = \mu^*_{020} + 2v/ck^*_{011} + k^*_{021} \tag{C.128}$$

$$\mu^*_{012} = k^*_{012} + (v/c\mu^*_{002} + 2w/ck^*_{011}) \tag{C.129}$$

$$\mu^*_{102} = k^*_{102} + (u/c\mu^*_{002} + 2w/ck^*_{101}) \tag{C.130}$$

$$\mu^*_{201} = k^*_{201} + (w/c\mu^*_{200} + 2u/ck^*_{101}) \tag{C.131}$$

$$\mu^*_{210} = k^*_{210} + (v/c\mu^*_{200} + 2u/ck^*_{110}) \tag{C.132}$$

$$\mu^*_{120} = k^*_{120} + (u/c\mu^*_{020} + 2v/ck^*_{110}) \tag{C.133}$$

$$\mu^*_{111} = k^*_{111} + (uvw/c^3 + u/ck^*_{011} + v/ck^*_{101} + w/ck^*_{110}) \tag{C.134}$$

$$\mu^*_{121} = k^*_{121} + (w/c\mu^*_{120} + 2uv/c^2k^*_{011} + u/ck^*_{021} + vv/c^2k^*_{101} + 2v/ck^*_{111}) \tag{C.135}$$

$$\mu^*_{112} = k^*_{112} + (v/c\mu^*_{102} + 2uw/c^2k^*_{011} + v/ck^*_{012} + ww/c^2k^*_{110} + 2w/ck^*_{111}) \tag{C.136}$$

$$\mu^*_{211} = k^*_{211} + (w/c\mu^*_{210} + 2uv/c^2k^*_{101} + v/ck^*_{201} + uu/c^2k^*_{011} + 2u/ck^*_{111}) \tag{C.137}$$

$$\mu^*_{220} = k^*_{220} + (uu/c^2\mu^*_{020} + 4uv/c^2k^*_{110} + 2u/ck^*_{120} + vv/c^2k^*_{200} + 2v/ck^*_{210}) \tag{C.138}$$

$$\mu^*_{022} = k^*_{022} + (vv/c^2\mu^*_{002} + 4vw/c^2k^*_{011} + 2v/ck^*_{012} + ww/c^2k^*_{020} + 2w/ck^*_{021}) \tag{C.139}$$

$$\mu^*_{202} = k^*_{202} + (uu/c^2\mu^*_{002} + 4uw/c^2k^*_{101} + 2u/ck^*_{102} + ww/c^2k^*_{200} + 2w/ck^*_{201}) \tag{C.140}$$

$$\begin{aligned}\mu^*_{221} = k^*_{221} + (w/c\mu^*_{220} + 2uuv/c^3k^*_{011} + uu/c^2k^*_{021} + 2uvv/c^3k^*_{101} + 4uv/c^2k^*_{111}\\ +2u/ck^*_{121} + vv/c^2k^*_{021} + 2v/ck^*_{211})\end{aligned} \tag{C.141}$$

$$\begin{aligned}\mu^*_{122} = k^*_{122} + (u/c\mu^*_{022} + 2vvw/c^3k^*_{101} + vv/c^2k^*_{102} + 2vww/c^3k^*_{110} + 4vw/c^2k^*_{111}\\ +2v/ck^*_{112} + ww/c^2k^*_{120} + 2w/ck^*_{121})\end{aligned} \tag{C.142}$$

$$\begin{aligned}\mu^*_{212} = k^*_{212} + (v/c\mu^*_{202} + 2uuw/c^3k^*_{011} + uu/c^2k^*_{012} + 2uww/c^3k^*_{110} + 4uw/c^2k^*_{111}\\ +2u/ck^*_{112} + ww/c^2k^*_{210} + 2w/ck^*_{211})\end{aligned} \tag{C.143}$$

$$\begin{aligned}\mu^*_{222} = k^*_{222} + (uu/c^2\mu^*_{022} + 4uvvw/c^3k^*_{101} + 2uvv/c^3k^*_{102} + 4uvww/c^4k^*_{110}\\ +8uvw/c^3k^*_{111} + 4uv/c^2k^*_{112} + 2uww/c^3k^*_{120} + 4uw/c^2k^*_{121} + 2u/ck^*_{122} + vvww/c^4k^*_{200}\\ +2vvw/c^3k^*_{201} + vv/c^2k^*_{202} + 2vww/c^3k^*_{210} + 4vw/c^2k^*_{211} + 2v/ck^*_{212}\\ +ww/c^2k^*_{220} + 2w/ck^*_{221})\end{aligned} \tag{C.144}$$

part b

$$f^{*E} = 0.5(\mu^*_{200} - \mu^*_{220} + \mu^*_{222} - \mu^*_{202} - \mu^*_{120} + \mu^*_{122} - \mu^*_{102} + \mu^*_{100}) \tag{C.145}$$

$$f^{*W} = 0.5(\mu^*_{200} - \mu^*_{220} + \mu^*_{222} - \mu^*_{202} + \mu^*_{120} - \mu^*_{122} + \mu^*_{102} - \mu^*_{100}) \tag{C.146}$$

$$f^{*N} = 0.5(-\mu^*_{210} - \mu^*_{220} + \mu^*_{222} + \mu^*_{212} + \mu^*_{020} - \mu^*_{022} - \mu^*_{012} + \mu^*_{010}) \tag{C.147}$$

$$f^{*S} = 0.5(\mu^*_{210} - \mu^*_{220} + \mu^*_{222} - \mu^*_{212} + \mu^*_{020} - \mu^*_{022} + \mu^*_{012} - \mu^*_{010}) \tag{C.148}$$

$$f^{*T} = 0.5(\mu^*_{221} + \mu^*_{222} - \mu^*_{201} - \mu^*_{202} - \mu^*_{021} - \mu^*_{022} + \mu^*_{002} + \mu^*_{001}) \tag{C.149}$$

$$f^{*B} = 0.5(-\mu^*_{221} + \mu^*_{222} + \mu^*_{201} - \mu^*_{202} + \mu^*_{021} - \mu^*_{022} + \mu^*_{002} - \mu^*_{001}) \tag{C.150}$$

$$f^{*NE} = 0.25(\mu^*_{210} + \mu^*_{220} - \mu^*_{222} - \mu^*_{212} + \mu^*_{110} + \mu^*_{120} - \mu^*_{122} - \mu^*_{112}) \tag{C.151}$$

$$f^{*SW} = 0.25(-\mu^*_{210} + \mu^*_{220} - \mu^*_{222} + \mu^*_{212} + \mu^*_{110} - \mu^*_{120} + \mu^*_{122} - \mu^*_{112}) \tag{C.152}$$

$$f^{*SE} = 0.25(-\mu^*_{210} + \mu^*_{220} - \mu^*_{222} + \mu^*_{212} - \mu^*_{110} + \mu^*_{120} - \mu^*_{122} + \mu^*_{112}) \tag{C.153}$$

$$f^{*NW} = 0.25(\mu^*_{210} + \mu^*_{220} - \mu^*_{222} - \mu^*_{212} - \mu^*_{110} - \mu^*_{120} + \mu^*_{122} + \mu^*_{112}) \tag{C.154}$$

$$f^{*TE} = 0.25(-\mu^*_{221} - \mu^*_{222} + \mu^*_{201} + \mu^*_{202} - \mu^*_{121} - \mu^*_{122} + \mu^*_{101} + \mu^*_{102}) \tag{C.155}$$

$$f^{*BW} = 0.25(\mu^*_{221} - \mu^*_{222} - \mu^*_{201} + \mu^*_{202} - \mu^*_{121} + \mu^*_{122} + \mu^*_{101} - \mu^*_{102}) \tag{C.156}$$

$$f^{*BE} = 0.25(\mu^*_{21} - \mu^*_{222} - \mu^*_{201} + \mu^*_{202} + \mu^*_{121} - \mu^*_{122} - \mu^*_{101} + \mu^*_{102}) \tag{C.157}$$

$$f^{*TW} = 0.25(-\mu^*_{221} - \mu^*_{222} + \mu^*_{201} + \mu^*_{202} + \mu^*_{121} + \mu^*_{122} - \mu^*_{101} - \mu^*_{102}) \tag{C.158}$$

$$f^{*TN} = 0.25(-\mu^*_{221} - \mu^*_{222} - \mu^*_{211} - \mu^*_{212} + \mu^*_{021} + \mu^*_{022} + \mu^*_{011} + \mu^*_{012}) \tag{C.159}$$

$$f^{*BS} = 0.25(\mu^*_{221} - \mu^*_{222} - \mu^*_{211} + \mu^*_{212} - \mu^*_{021} + \mu^*_{022} + \mu^*_{011} - \mu^*_{012}) \tag{C.160}$$

$$f^{*BN} = 0.25 * (\mu^*_{221} - \mu^*_{222} + \mu^*_{211} - \mu^*_{212} - \mu^*_{021} + \mu^*_{022} - \mu^*_{011} + \mu^*_{012}) \tag{C.161}$$

$$f^{*TS} = 0.25(-\mu^*_{221} - \mu^*_{222} + \mu^*_{211} + \mu^*_{212} + \mu^*_{021} + \mu^*_{022} - \mu^*_{011} - \mu^*_{012}) \tag{C.162}$$

$$f^{*ZERO} = (-\mu^*_{200} + \mu^*_{220} - \mu^*_{222} + \mu^*_{202} - \mu^*_{020} + \mu^*_{022} - \mu^*_{002} + \mu^*_{000}) \tag{C.163}$$

$$f^{*TNE} = 0.125(\mu^*_{221} + \mu^*_{222} + \mu^*_{211} + \mu^*_{212} + \mu^*_{121} + \mu^*_{122} + \mu^*_{111} + \mu^*_{112}) \tag{C.164}$$

$$f^{*BNE} = 0.125(-\mu^*_{221} + \mu^*_{222} - \mu^*_{211} + \mu^*_{212} - \mu^*_{121} + \mu^*_{122} - \mu^*_{111} + \mu^*_{112}) \tag{C.165}$$

$$f^{*TSE} = 0.125(\mu^*_{221} + \mu^*_{222} - \mu^*_{211} - \mu^*_{212} + \mu^*_{121} + \mu^*_{122} - \mu^*_{111} - \mu^*_{112}) \tag{C.166}$$

$$f^{*BSE} = 0.125(-\mu^*_{221} + \mu^*_{222} + \mu^*_{211} - \mu^*_{212} - \mu^*_{121} + \mu^*_{122} + \mu^*_{111} - \mu^*_{112}) \tag{C.167}$$

$$f^{*TNW} = 0.125 * (\mu^*_{221} + \mu^*_{222} + \mu^*_{211} + \mu^*_{212} - \mu^*_{121} - \mu^*_{122} - \mu^*_{111} - \mu^*_{112}) \tag{C.168}$$

$$f^{*BNW} = 0.125(-\mu^*_{221} + \mu^*_{222} - \mu^*_{211} + \mu^*_{212} + \mu^*_{121} - \mu^*_{122} + \mu^*_{111} - \mu^*_{112}) \tag{C.169}$$

$$f^{*TSW} = 0.125(\mu^*_{221} + \mu^*_{222} - \mu^*_{211} - \mu^*_{212} - \mu^*_{121} - \mu^*_{122} + \mu^*_{111} + \mu^*_{112}) \tag{C.170}$$

$$f^{*BSW} = 0.125(-\mu^*_{221} + \mu^*_{222} + \mu^*_{211} - \mu^*_{212} + \mu^*_{121} - \mu^*_{122} - \mu^*_{111} + \mu^*_{112}) \tag{C.171}$$

Bibliography

[1] R. Segura and C. J. Kähler, "High pressure microPIV mesurements in dispersion system and thermo-liquid crystal (TCL) thermography combined with astigmatism particle tracking velocimetry (APTV)," *miKroPART DFG research group for 856*, Oct. 2014.

[2] N. Gregoriades, J. Clay, N. Ma, K. Koelling, and J. J. Chalmers, "Cell damage of microcarrier cultures as a function of local energy dissipation created by a rapid extensional flow.," *Biotechnology and bioengineering*, vol. 69, pp. 171–82, July 2000.

[3] J. H. Gibson, I. G. Droppo, R. Farnood, B. Mahendran, P. Seto, and S. N. Liss, "Hydrodynamic treatment of wastewater effluent flocs for improved disinfection.," *Water environment research : a research publication of the Water Environment Federation*, vol. 84, pp. 387–95, May 2012.

[4] S. Beinert, T. Gothsch, and a. Kwade, "Numerical evaluation of stresses acting on particles in high-pressure microsystems using a Reynolds stress model," *Chemical Engineering Science*, vol. 123, pp. 197–206, Feb. 2015.

[5] O. Geschke, H. Klank, and P. Tellemann, *Microsystem Engineering of Lab-on-a-chip Devices.* John Wiley & Sons, 2006.

[6] E. Goraki, M. Geier, K. Kucher, and M. Krafczyk, "Distributed cumulant lattice Boltzmann simulation of the dispersion process of ceramic agglomerates," *Chemical Engineering Research and Design*, 2014.

[7] S. Beinert, T. Gothsch, and a. Kwade, "Numerical Evaluation of Flow Fields and Stresses Acting on Agglomerates Dispersed in High-Pressure Microsystems," *Chemical Engineering & Technology*, vol. 35, pp. 1922–1930, Nov. 2012.

[8] N. Zumaeta, E. P. Byrne, and J. J. Fitzpatrick, "Breakage of protein precipitates flowing through orifices," *Chemical Engineering Research and Design*, vol. 86, pp. 107–117, Jan. 2008.

[9] M. C. Geier, *Ab initio derivation of the cascaded lattice boltzmann automaton.* PhD thesis, 2006.

[10] M. Geier, M. Schönherr, A. Pasquali, and M. Krafczyk, "The cumulant lattice equation in three dimensions: theory and validation," *Computers & Mathematics with Applications*, 2014.

[11] M. Kobayashi, "Breakup and strength of polystyrene latex flocs subjected to a converging flow," *Colloids and Surfaces A: Physicochemical and Engineering Aspects*, vol. 235, pp. 73–78, Mar. 2004.

[12] E. P. Byrne, J. J. Fitzpatrick, L. W. Pampel, and N. J. Titchener-Hooker, "Influence of shear on particle size and fractal dimension of whey protein precipitates: implications for scale-up and centrifugal clarification efficiency," *Chemical Engineering Science*, vol. 57, no. 18, pp. 3767–3779, 2002.

[13] B. Biscans, P. Guiraud, C. Laguerie, A. Massarelli, and B. Mazzarotta, "Abrasion and breakage phenomena in mechanically stirred crystallisers," *Chemical Engineering Journal*, vol. 63, pp. 85–91, 1996.

[14] G. J. Brown, "A fractal description of the progeny of double impact single particle breakage," *Minerals Engineering*, vol. 10, no. 2, pp. 229–235, 1997.

[15] S. Kumar, V. Ganvir, C. Satyanand, R. Kumar, and K. Gandhia, "Alternative mechanisms of drop breakup in stirred vessels," *Chemical Engineering Science*, vol. 46, pp. 2483–2489, Sept. 1998.

[16] C. Thornton, M. Ciomocos, and M. Adams, "Numerical simulations of agglomerate impact breakage," *Powder Technology*, vol. 105, pp. 74–82, Nov. 1999.

[17] L. G. Austin, "A treatment of impact breakage of particles," *Powder Technology*, vol. 126, pp. 85–90, June 2002.

[18] K. Shimizu, K. Minekawa, T. Hirose, and Y. Kawase, "Drop breakage in stirred tanks with Newtonian and non-Newtonian fluid systems," *Chemical Engineering Journal*, vol. 72, pp. 117–124, Feb. 1999.

[19] A. N. Sathyagal, D. Ramkrishna, W. Lafayette, and G. Narsimhan, "Droplet breakage in stirred dispersions. breakage functions from experimental drop-size distributions," *Chemical Engineering Science*, vol. 51, no. 9, 1996.

[20] P. A. Shamlou, S. Stavrinides, N. Titchener-Hooker, and M. Hoare, "Turbulent breakage of protein precipitates in mechanically stirred bioreactors," *Bioprocess Engineering*, vol. 14, no. 5, p. 237, 1996.

[21] D. J. Bell and P. Dunnill, "The influence of precipitation reactor configuration on the centrifugal recovery of isoelectric soya protein precipitate.," *Biotechnology and bioengineering*, vol. 24, pp. 2319–36, Nov. 1982.

[22] P. Ayazi Shamlou, S. Stavrinides, N. Titchener-Hooker, and M. Hoare, "Growth-independent breakage frequency of protein precipitates in turbulently agitated bioreactors," *Chemical Engineering Science*, vol. 49, pp. 2647–2656, Aug. 1994.

[23] S. Kao and S. Mason, "Dispersion of particles by shear," *Nature*, vol. 253, pp. 619–621, 1975.

[24] R. Akers, A. Rushton, and J. Stenhouse, "Floc breakage: The dynamic response of the particle size distribution in a flocculated suspension to a step change in turbulent energy dissipation," *Chemical Engineering Science*, vol. 42, pp. 787–798, Jan. 1987.

[25] S. Blaser, "Flocs in Shear and Strain Flows.," *Journal of colloid and interface science*, vol. 225, pp. 273–284, May 2000.

[26] C. Budde, D. Schaffner, and P. Walzel, "Drop breakup in liquid-liquid dispersions at an orifice plate observed in a large-scale model," *Chemical Engineering and Technology*, vol. 25, pp. 1164–1167, 2002.

[27] S. Galinat, L. Garrido Torres, O. Masbernat, P. Guiraud, F. Risso, C. Dalmazzone, and C. Noik, "Breakup of a drop in a liquidliquid pipe flow through an orifice," *AIChE Journal*, vol. 53, pp. 56–68, Jan. 2007.

[28] J. S. Percy and C. A. Sleicher, "Drop breakup in the flow of immiscible liquids through an orifice in a pipe," *AIChE Journal*, vol. 29, pp. 161–164, Jan. 1983.

[29] L. S. Scott, W. B. Hayes, and C. D. Holland, "The formation of interfacial area in immiscible liquids by orifice mixers," *AIChE Journal*, vol. 4, pp. 346–350, Sept. 1958.

[30] P. F. MacLoughlin, D. M. Malone, J. T. Murtagh, and P. M. Kieran, "The effects of turbulent jet flows on plant cell suspension cultures," *Biotechnol Bioeng*, vol. 58, pp. 595–604, 1998.

[31] D. E. Leng, R. V. Calabrese, and L. P. Edward, *Immiscible liquid liquid systems*. Hoboken, NJ, USA: John Wiley & Sons, Inc., Nov. 2003.

[32] M. Boychyn, S. S. S. Yim, P. A. Shamlou, M. Bulmer, J. More, and M. Hoare, "Characterization of ow intensity in continuous centrifuges for the development of laboratory mimics," *Chemical Engineering Science*, vol. 56, pp. 4759–4770, 2001.

[33] J. Fife, H. Ozkan, R. Derksen, and P. Grewal, "Using Computational Fluid Dynamics to predict Damage of a Biological Pesticide during Passage through a Hydraulic Nozzle," *Biosystems Engineering*, vol. 94, pp. 387–396, July 2006.

[34] N. Ma, K. W. Koelling, and J. J. Chalmers, "Fabrication and use of a transient contractional flow device to quantify the sensitivity of mammalian and insect cells to hydrodynamic forces.," *Biotechnology and bioengineering*, vol. 80, pp. 428–37, Nov. 2002.

[35] D. S. Parker, W. J. Kaufman, and D. Jenkins, "Floc Breakup in Turbulent Flocculation Processes," *Journal of the Sanitary Engineering Division*, vol. 98, no. 1, pp. 79–99, 1972.

[36] Y. Yuan and R. R. Farnood, "Strength and breakage of activated sludge flocs," *Powder Technology*, vol. 199, pp. 111–119, Apr. 2010.

[37] R. C. Sonntag and W. B. Russel, "Structure and breakup of flocs subjected to fluid stresses," *Journal of Colloid and Interface Science*, vol. 115, pp. 378–389, Feb. 1987.

[38] K. Higashitani, K. Iimura, and H. Sanda, "Simulation of deformation and breakup of large aggregates in flows of viscous fluids," *Chemical Engineering Science*, vol. 56, pp. 2927–2938, May 2001.

[39] A. K. Yeung and R. Pelton, "Micromechanics: A new approach to studying the strength and breakup of flocs," *Journal of Colloid and Interface Science*, vol. 184, pp. 579–585, Dec. 1996.

[40] J. H. Gibson, H. Hon, R. Farnood, I. G. Droppo, and P. Seto, "Effects of ultrasound on suspended particles in municipal wastewater.," *Water research*, vol. 43, pp. 2251–9, May 2009.

[41] A. X. Fernandes, *Computational fluid dynamics analysis for wastewater floc breakage in orifice flow by wastewater floc breakage in orifice flow.* PhD thesis, 2012.

[42] K. Higashitani, N. Inada, and T. Ochi, "Floc breakup along centerline of contractile flow to orifice," *Colloids and Surfaces*, vol. 56, pp. 13–23, Jan. 1991.

[43] B. R. Munson, D. F. Young, and T. Okiishi, *Fundamentals of fluid mechanics.* John Wiley and Sons, Inc, 4 ed., 2006.

[44] T. Q. Nguyen and H.-H. Kausch, "Chain scission in transient extensional flow kinetics and molecular weight dependence," *Journal of Non-Newtonian Fluid Mechanics*, vol. 30, pp. 125–140, Jan. 1988.

[45] S. Galinat, O. Masbernat, P. Guiraud, C. Dalmazzone, and C. Noïk, "Drop break-up in turbulent pipe flow downstream of a restriction," *Chemical Engineering Science*, vol. 60, pp. 6511–6528, 2005.

[46] D. F. James and J. H. Saringer, "Flow of dilute polymer solutions through converging channels," *Journal of Non-Newtonian Fluid Mechanics*, vol. 11, pp. 317–339, Jan. 1982.

[47] K. Higashitani and K. Iimura, “Two-dimensional simulation of the breakup process of aggregates in shear and elongational flows.,” *Journal of colloid and interface science*, vol. 204, pp. 320–7, Aug. 1998.

[48] J. Davies, “Drop sizes of emulsions related to turbulent energy dissipation rates,” *Chemical Engineering Science*, vol. 40, pp. 839–842, Jan. 1985.

[49] N. Zumaeta, G. M. Cartland-Glover, S. P. Heffernan, E. P. Byrne, and J. J. Fitzpatrick, “Breakage model development and application with CFD for predicting breakage of whey protein precipitate particles,” *Chemical Engineering Science*, vol. 60, pp. 3443–3452, July 2005.

[50] N. Zumaeta, E. P. Byrne, and J. J. Fitzpatrick, “Predicting precipitate breakage during turbulent flow through different flow geometries,” *Colloids and Surfaces A: Physicochemical and Engineering Aspects*, vol. 292, pp. 251–263, Jan. 2007.

[51] A. J. C. Ladd, “Numerical simulations of particulate suspensions via a discretized Boltzmann equation part I . theoretical foundation,” *Journal of Fluid Mechanics 271*, pp. 1–36, 1993.

[52] M. Krafczyk, M. Schulz, and E. Rank, “Lattice-gas simulations of two-phase flow in porous media,” *Communications in Numerical Methods in Engineering*, vol. 14, pp. 709–717, Aug. 1998.

[53] S. Geller, M. Krafczyk, J. Tölke, S. Turek, and J. Hron, “Benchmark computations based on lattice-Boltzmann, finite element and finite volume methods for laminar flows,” *Computers & fluids*, vol. 35, pp. 888–897, Sept. 2006.

[54] T. Lee and C.-L. Lin, “A stable discretization of the lattice Boltzmann equation for simulation of incompressible two-phase flows at high density ratio,” *Journal of Computational Physics*, vol. 206, pp. 16–47, June 2005.

[55] J. Tölke, S. Freudiger, and M. Krafczyk, “An adaptive scheme using hierarchical grids for lattice Boltzmann multi-phase flow simulations,” *Computers and Fluids*, vol. 35, pp. 820–830, 2006.

[56] M. Krafczyk, J. Tölke, and L.-S. Luo, “Large-Eddy simulations with a multiple-relaxtion-time LBE model,” *International Journal of Modern Physics B*, vol. 17, pp. 33–39, Jan. 2003.

[57] M. Geier, A. Greiner, and J. Korvink, “Cascaded digital lattice Boltzmann automata for high Reynolds number flow,” *Physical Review E*, vol. 73, p. 066705, June 2006.

[58] C. Richter, T. Krah, and S. Büttgenbach, "Novel 3D manufacturing method combining microelectrial discharge machining and electrochemical polishing," *Microsystem Technologies*, vol. 18, pp. 1109–1118, Feb. 2012.

[59] M. Kay, *Practical Hydraulics*. 1998.

[60] M. Geier, A. Greiner, and J. G. Korvink, "Bubble functions for the lattice Boltzmann method and their application to grid refinement," *The European Physical Journal Special Topics*, vol. 171, pp. 173–179, May 2009.

[61] S. Geller, S. Uphoff, and M. Krafczyk, "Turbulent jet computations based on MRT and Cascaded Lattice Boltzmann models," *Computers & Mathematics with Applications*, vol. 66, no. 12, pp. 1956–1966, 2012.

[62] J. A. Simpson and E. S. C. Weiner, *The Oxford English Dictionary*. 1989.

[63] P. Knight, "Chambers Science and Technology Dictionary," 1988.

[64] W. Gerstner, "Crystal form and particle size of organic pigments in printing inks and paints," *J Oil Col Chem Assoc*, vol. 49, pp. 954–973, 1966.

[65] B. 2955, "Glossary of terms relating to particle technology," 1993.

[66] B. I. 14887, "Sample preparation. Dispersing procedures for powders in liquids," 2000.

[67] A. Guinier and G. Fournet, "Small angle scattering of X-rays," *Journal of Polymer Science*, vol. 1, p. 268, 1955.

[68] S. N. Rogak and R. C. Flagan, "Stokes drag on self-similar clusters of spheres," 1990.

[69] B. B. Mandelbrot, "The Fractal Geometry of Nature," 1983.

[70] P. Meakin, "A Historical Introduction to Computer Models for Fractal Aggregates," *Journal of Sol-Gel Science and Technology*, vol. 15, no. 2, pp. 97–117, 1999.

[71] S. Velani, "Hausdorff Dimension and Diophantine Approximation," *Fractal geometry and applications a jubilee of Benoît Mandelbrot*, vol. 72, p. 43, 1993.

[72] S. R. Forrest and T. A. Witten, "Long-range correlations in smoke-particle aggregates," 2001.

[73] T. A. Witten and L. M. Sander, "Diffusion-limited aggregation, a kinetic critical phenomenon," *Physical Review Letters*, vol. 47, pp. 1400–1403, 1981.

[74] T. Witten and L. Sander, "Diffusion-limited aggregation," *Physical Review B*, vol. 27, pp. 5686–5697, 1983.

[75] P. Meakin, “Diffusion-controlled cluster formation in 2-6 dimensional space,” *Physical Review A*, vol. 27, pp. 1495–1507, 1983.

[76] R. Jullien and R. Botet, *Aggregation and Fractal Aggregates [Hardcover].* World Scientific Pub Co Inc, 1987.

[77] P. Meakin and F. Family, “Structure and kinetics of reaction-limited aggregation,” *Physical Review A*, vol. 38, pp. 2110–2123, 1988.

[78] L. Gmachowski, “Calculation of the fractal dimension of aggregates,” *Colloids and Surfaces A: Physicochemical and Engineering Aspects*, vol. 211, pp. 197–203, Dec. 2002.

[79] R. Benzi, S. Succi, and M. Vergassola, “The lattice Boltzmann equation: theory and applications,” *Physics Reports*, vol. 222, pp. 145–197, Dec. 1992.

[80] S. Chen and G. D. Doolen, “Lattice Boltzmann method for fluid flows,” *Annual Review of Fluid Mechanics*, vol. 30, pp. 329–364, Jan. 1998.

[81] G. McNamara and G. Zanetti, “Use of the Boltzmann equation to simulate lattice-gas automata,” *Physical Review Letters*, vol. 61, pp. 2332–2335, Nov. 1988.

[82] T. Inamuro, T. Ogata, S. Tajima, and N. Konishi, “A lattice Boltzmann method for incompressible two-phase flows with large density differences,” *Journal of Computational Physics*, vol. 198, pp. 628–644, Aug. 2004.

[83] Y. H. Qian, D. D’Humières, and P. Lallemand, “Lattice BGK Models for Navier-Stokes Equation,” *EPL (Europhysics Letters)*, vol. 17, p. 479, 1992.

[84] S. Succi, *The lattice Boltzmann equation for fluid dynamic and beyond.* Oxford University Press, 2001.

[85] A. T. White and C. K. Chong, “Rotational invariance in the three-dimensional lattice Boltzmann method is dependent on the choice of lattice,” *Journal of Computational Physics*, vol. 230, pp. 6367–6378, July 2011.

[86] S. K. Kang and Y. A. Hassan, “The effect of lattice models within the lattice Boltzmann method in the simulation of wall-bounded turbulent flows,” *Journal of Computational Physics*, vol. 232, pp. 100–117, Jan. 2013.

[87] P. Bhatnagar, E. Gross, and M. Krook, “A model for collision processes in gases. I. Small amplitude processes in charged and neutral one-component systems,” *Physical Review*, vol. 94, pp. 511–525, May 1954.

[88] D. D'Humières, I. Ginzburg, M. Krafczyk, P. Lallemand, and L.-S. Luo, "Multiple-relaxation-time lattice Boltzmann models in three dimensions.," *Philosophical transactions. Series A, Mathematical, physical, and engineering sciences*, vol. 360, pp. 437–51, Mar. 2002.

[89] S. Uphoff, *Development and Validation of turbulence models for Lattice Boltzmann schemes.* PhD thesis, TU Braunschweig, 2012.

[90] M. Geier, A. Greiner, and J. G. Korvink, "A factorized central moment lattice Boltzmann method," in *European Physical Journal: Special Topics*, vol. 171, pp. 55–61, 2009.

[91] M. Geier, A. Greiner, and J. G. Korvink, "Reference frame independent partitioning of the momentum distribution function in lattice Boltzmann methods with multiple relaxation rates," 2008.

[92] S. Seeger and H. Hoffmann, "The cumulant method for computational kinetic theory," *Continuum Mechanics and Thermodynamics*, vol. 12, pp. 403–421, Dec. 2000.

[93] S. Seeger and K. H. Hoffmann, "The cumulant method for the space-homogeneous Boltzmann equation," *Continuum Mechanics and Thermodynamics*, vol. 17, pp. 51–60, Apr. 2005.

[94] P. Bailey, J. Myre, S. Walsh, D. Lilja, and M. Saar, "Accelerating Lattice Boltzmann Fluid Flow Simulations Using Graphics Processors," *2009 International Conference on Parallel Processing*, 2009.

[95] M. Schönherr, K. Kucher, M. Geier, M. Stiebler, S. Freudiger, and M. Krafczyk, "Multi-thread implementations of the lattice Boltzmann method on non-uniform grids for CPUs and GPUs," *Computers & Mathematics with Applications*, vol. 61, pp. 3730–3743, June 2011.

[96] J. Linxweiler, *Ein integrierter Softwareansatz zur interaktiven Exploration und Steuerung von Strömungssimulationen auf Many-Core-Architekturen.* PhD thesis, TU Braunschweig, 2011.

[97] O. Filippova and D. Hänel, "Boundary-Fitting and Local Grid Refinement for Lattice-BGK Models," 1998.

[98] A. Dupuis and B. Chopard, "Theory and applications of an alternative lattice Boltzmann grid refinement algorithm," *Physical Review E*, vol. 67, p. 066707, June 2003.

[99] M. Geier, "How to grid refine (3D)," tech. rep., 2012.

[100] K. N. Premnath, "On the three-dimensional central moment lattice Boltzmann method," no. February 2012.

[101] K. Iglberger, *Lattice Boltzmann Simulation of Flow around moving Particles.* PhD thesis, TU Erlangen, 2005.

[102] M. Dietzel, M. Sommerfeld, L. Guo, D. D. Joseph, Y. Matsumoto, Y. Sommerfeld, and Y. Wang, "LBM simulations on agglomerate transport and deposition," in *The 6th international symposium on multiphase flow, heat mass transfer and energy conversion*, vol. 796, pp. 796–801, 2010.

[103] S. Hou, J. Sterling, S. Chen, and G. D. Doolen, "A Lattice Boltzmann Subgrid Model for High Reynolds Number Flows," *Pattern formation and lattice gas automata*, vol. 6, pp. 1–18, 1996.

[104] H. Yu, L. S. Luo, and S. S. Girimaji, "LES of turbulent square jet flow using an MRT lattice Boltzmann model," *Computers and Fluids*, vol. 35, pp. 957–965, 2006.

[105] J. Smagorinsky, "General circulation experiments with the primutive equations," *Monthly Weather Review*, vol. 91, pp. 99–164, Mar. 1963.

[106] V. Yakhot, S. A. Orszag, S. Thangam, T. B. Gatski, and C. G. Speziale, "Development of turbulence models for shear flows by a double expansion technique," *Physics of Fluids A: Fluid Dynamics*, vol. 4, p. 1510, July 1992.

[107] J. W. Deardorff, "A numerical study of three-dimensional turbulent channel flow at large Reynolds numbers," *Journal of Fluid Mechanics*, vol. 41, p. 453, Mar. 2006.

[108] M. Geier, "De-aliasing and stabilization formalism of the cascaded lattice Boltzmann automaton for under-resolved high Reynolds number flow," in *International Journal for Numerical Methods in Fluids*, vol. 56, pp. 1249–1254, 2008.

[109] U. M. Ascher and L. R. Petzold, *Computer Methods for Ordinary Differential Equations and Differential-Algebraic Equations.* Philadelphia: Society for Industrial and Applied Mathematics, 1998.

[110] G. I. Taylor and A. E. Green, "Mechanism of the Production of Small Eddies from Large Ones," *Proceedings of the Royal Society A: Mathematical, Physical and Engineering Sciences*, vol. 158, pp. 499–521, Feb. 1937.

[111] G. K. Batchelor, *An Introduction to Fluid Dynamics.* 2000.

[112] G. G. Stokes, "On the Effect of the Internal Friction of Fluids on the Motion of Pendulums," *Transactions of the Cambridge Philosophical Society*, vol. 9, 1851.

[113] H. Lamb, *Hydrodynamics.* Cambridge, University Press, 6 ed., 1932.

[114] J. Happel and H. Brenner, *Low Reynolds number hydrodynamics: with special applications to particulate media.* 1983.

[115] R. COX, “The motion motion of long slender bodies in a viscous fluid Part 1. General theory,” *Journal of Fluid Mechanics*, vol. 44, 1970.

[116] B. G. K. Batchelor, “Slender-body theory for particles of arbitrary cross-section in Stokes flow,” *Journal of Fluid Mechanics*, vol. 44, 1970.

[117] B. M. E. O. Neill and S. R. Majumdar, “Asymmetrical slow viscous fluid motions caused by the translation or rotation of two spheres . Part I : the determination of exact solutions for any values of the ratio of radii and separation parameters,” *Journal of Applied Mathematics and Physics ZAMP*, vol. 21, no. 2, pp. 180–187, 1970.

[118] P. Ganatos, *A Numerical Solution Technique for Three-dimensional Multiparticle Stokes Flows.* 1978.

[119] P. Mazur and W. van Saarloos, “Many-sphere hydrodynamic interactions and mobilities in a suspension,” *Physica A: Statistical Mechanics and its Applications*, vol. 115, pp. 21–57, Sept. 1982.

[120] A. J. C. Ladd, “Hydrodynamic interactions in a suspension of spherical particles,” *The Journal of Chemical Physics*, vol. 88, p. 5051, Apr. 1988.

[121] H. Hasimoto, “On the periodic fundamental solutions of the Stokes equations and their application to viscous flow past a cubic array of spheres,” *Journal of Fluid Mechanics*, vol. 5, no. 1933, pp. 317–328, 1958.

[122] C. J. van Oss, “A Review of: Colloidal Hydrodynamics. T. G. M. van de Ven. Academic Press, London and New York, 1989. pp. 582. $77.50.,” *Journal of Dispersion Science and Technology*, vol. 11, pp. 548–549, Oct. 1990.

[123] M. Elimelech, J. Gregory, X. Jia, R. Williams, J. Gregory, X. Jia, and R. A. Williams, *Particle Deposition & Aggregation.* Elsevier, 1995.

[124] C. P. Johnson, X. Li, and B. E. Logan, “Settling Velocities of Fractal Aggregates,” *Environmental Science & Technology*, vol. 30, pp. 1911–1918, Jan. 1996.

[125] P. Wiltzius, “Hydrodynamic behavior of fractal aggregates.,” *Physical review letters*, vol. 58, pp. 710–713, Feb. 1987.

[126] D. Heyes, M. Nuevo, J. Morales, and A. Branka, “Translational and rotational diffusion of model nanocolloidal dispersions studied by molecular dynamics simulations,” *Journal of Physics: Condensed Matter*, vol. 10, pp. 10159–10178, 1998.

[127] R. G. Larson, “The Structure and Rheology of Complex Fluids,” in *New York Oxford*, p. 688, 1999.

[128] A. Gastaldi and M. Vanni, “The distribution of stresses in rigid fractal-like aggregates in a uniform flow field.,” *Journal of colloid and interface science*, vol. 357, pp. 18–30, May 2011.

[129] W. Van Saarloos, “On the hydrodynamic radius of fractal aggregates,” 1987.

[130] P. Vainshtein and M. Shapiro, “Porous agglomerates in the general linear flow field,” *Journal of Colloid and Interface Science*, vol. 298, pp. 183–191, 2006.

[131] M. Vanni, “Creeping flow over spherical permeable aggregates,” *Chemical Engineering Science*, vol. 55, 2000.

[132] J. G. Kirkwood and J. Riseman, “The Intrinsic Viscosities and Diffusion Constants of Flexible Macromolecules in Solution,” *The Journal of Chemical Physics*, vol. 16, p. 565, 1948.

[133] J. G. D. L. Torre and V. A. Bloomfield, “Hydrodynamic properties of macromolecular complexes. I. Translation,” *Biopolymers*, vol. 16, pp. 1747–1763, 1977.

[134] P. Meakin, Z.-Y. Chen, and J. M. Deutch, “The translational friction coefficient and time dependent cluster size distribution of three dimensional clustercluster aggregationa),b),” *The Journal of Chemical Physics*, vol. 82, p. 3786, 1985.

[135] M. Lattuada, H. Wu, and M. Morbidelli, “A simple model for the structure of fractal aggregates,” *Journal of Colloid and Interface Science*, vol. 268, pp. 106–120, 2003.

[136] V. Becker, E. Schlauch, M. Behr, and H. Briesen, “Restructuring of colloidal aggregates in shear flows and limitations of the free-draining approximation,” *Journal of Colloid and Interface Science*, vol. 339, pp. 362–372, 2009.

[137] V. Becker and H. Briesen, “A master curve for the onset of shear induced restructuring of fractal colloidal aggregates,” *Journal of Colloid and Interface Science*, vol. 346, pp. 32–36, 2010.

[138] M. Doi and D. Chen, “Simulation of aggregating colloids in shear flow,” *Journal Of Chemical Physics*, vol. 90, pp. 5271–5279, 1989.

[139] M. Fanelli, D. L. Feke, and I. Manas-Zloczower, “Prediction of the dispersion of particle clusters in the nano-scalePart I: Steady shearing responses,” *Chemical Engineering Science*, vol. 61, pp. 473–488, Jan. 2006.

[140] L. J. Durlofsky and J. F. Brady, “Dynamic simulation of bounded suspensions of hydrodynamically interacting particles,” 1989.

[141] J. Brady, “Stokesian Dynamics,” *Annual Review of Fluid Mechanics*, vol. 20, pp. 111–157, 1988.

[142] A. S. Kim and K. D. Stolzenbach, “The permeability of synthetic fractal aggregates with realistic three-dimensional structure.,” *Journal of colloid and interface science*, vol. 253, pp. 315–328, 2002.

[143] C. Binder, C. Feichtinger, H.-j. Schmid, N. Thürey, W. Peukert, and U. Rüde, “Simulation of the hydrodynamic drag of aggregated particles.,” *Journal of colloid and interface science*, vol. 301, pp. 155–67, Sept. 2006.

[144] S. Harada, R. Tanaka, H. Nogami, and M. Sawada, “Dependence of fragmentation behavior of colloidal aggregates on their fractal structure,” *Journal of Colloid and Interface Science*, vol. 301, pp. 123–129, 2006.

[145] Y. M. Harshe, M. Lattuada, and M. Soos, “Experimental and modeling study of breakage and restructuring of open and dense colloidal aggregates,” *Langmuir*, vol. 27, pp. 5739–5752, 2011.

[146] L. S. Fellay and M. Vanni, “The effect of flow configuration on hydrodynamic stresses and dispersion of low density rigid aggregates.,” *Journal of colloid and interface science*, vol. 388, pp. 47–55, Dec. 2012.

[147] B. Maury, “Direct Simulations of 2D Fluid-Particle Flows in Biperiodic Domains,” *Journal of Computational Physics*, vol. 156, pp. 325–351, 1999.

[148] M. Uhlmann, “An immersed boundary method with direct forcing for the simulation of particulate flows,” *Journal of Computational Physics*, vol. 209, pp. 448–476, 2005.

[149] F. Lucci, A. Ferrante, and S. Elghobahsi, “Modulation of isotropic turbulence by particles of Taylor length-scale size,” *Journal of Fluid Mechanics*, vol. 650, p. 5, 2010.

[150] A. T. Cate, J. J. Derksen, L. M. Portela, and H. E. A. Van Den Akker, “Fully resolved simulations of colliding monodisperse spheres in forced isotropic turbulence,” *Journal of Fluid Mechanics*, vol. 519, pp. 233–271, 2004.

[151] H. Gao, H. Li, and L.-P. Wang, “Lattice Boltzmann simulation of turbulent flow laden with finite-size particles,” *Computers & Mathematics with Applications*, vol. 65, pp. 194–210, 2013.

[152] C. Feichtinger, K. Iglberger, and S. Donath, “Large scale simulation of fluid structure interaction using Lattice Boltzmann methods and the physics engine ,” in *Proceedings Computational Techniques and Applications Conference*, vol. 50, 2008.

[153] T. M. Buzug, *Advances in Medical Engineering.* Springer Science & Business Media, 2007.

[154] Faxen and H., "Die Geschwindigkeit zweier Kugeln, die unter Einwirkung der Schwere in einer zähen Flüssigkeit fallen.," *Zeitschrift für angewandte Mathematik und Mechanik*, vol. 7, pp. 79–80, 1927.

[155] C. Binder, *Settling of Fractal Aggregates in Viscous Media Sedimentation fraktaler Aggregate in viskosen Medien.* PhD thesis, 2012.

[156] A. S. Kim and R. Yuan, "Hydrodynamics of an ideal aggregate with quadratically increasing permeability.," *Journal of colloid and interface science*, vol. 285, pp. 627–33, May 2005.

[157] Y. Gong and F. X. Tanner, "Comparison of RANS and LES Models in the Laminar Limit for a Flow Over a Backward-Facing Step Using OpenFOAM," in *Nineteenth International Multidimensional Engine Modeling Meeting at the SAE Congress April*, (Detroit, Michigan Comparison), 2009.

[158] V. L. Streeter, *Handbook of Fluid Dynamics.* 1961.

[159] A. Fluent, "ANSYS Fluent 12.0 user's guide," *Ansys Inc*, vol. 15317, pp. 1–2498, 2009.

[160] M. L. Shur, M. K. Strelets, A. K. Travin, and P. R. Spalart, "Turbulence modeling in rotating and curved channels - Assessing the Spalart-Shur correction," 2000.

[161] U. Schumann, "Realizability of Reynolds-stress turbulence models," *Physics of Fluids*, vol. 20, p. 721, Aug. 1977.

[162] G. Haller, "An objective definition of a vortex," 2005.

[163] M. A. Green, C. W. Rowley, and G. Haller, "Detection of Lagrangian coherent structures in three-dimensional turbulence," 2007.

[164] Y. Dubief and F. Delcayre , "On coherent-vortex identification in turbulence," 2000.

[165] P. Chakraborty, S. Balachandar, and R. J. Adrian, "On the relationships between local vortex identification schemes," 2005.

[166] J. Hunt, A. Wray, and P. Moin, "Eddies, streams, and convergence zones in turbulent flows," *In its Studying Turbulence Using Numerical Simulation Databases*, 1988.

[167] K. K. Kuo and R. Acharya, *Fundamentals of Turbulent and Multiphase Combustion.* Hoboken, New Jersey: John Wiley & Sons, Inc., 2012.

[168] M. T. Landahl and E. Mollo-Christensen, *Turbulence and Random Processes in Fluid Mechanics.* 1992.

[169] H. Tennekes and J. L. Lumley, *A First Course in Turbulence.* MIT Press, 1972.

[170] J. Fröhlich and D. von Terzi, "Hybrid LES/RANS methods for the simulation of turbulent flows," *Progress in Aerospace Sciences*, vol. 44, pp. 349–377, July 2008.

[171] J. Blazek, *Computational Fluid Dynamics: Principles and Applications.* Elsevier, 2005.

[172] D. H. Bache, "Floc rupture and turbulence: A framework for analysis," *Chemical Engineering Science*, vol. 59, pp. 2521–2534, 2004.

[173] F. A. Morrison, *An Introduction to Fluid Mechanics.* Cambridge University Press, 2013.

Curriculum Vitae

General Information

PLACE AND DATE OF BIRTH: Iran — 16 September 1984
OFFICE ADDRESS: Universitt Braunschweig
Institute of Computational Modeling in Civil Engineering
Pockelsstr. 3, 38106 Braunschweig, Germany
PHONE: +49 (0531) 391 94512
EMAIL: ehsan@irmb.tu-bs.de

Education

2011-PRESENT	PhD-Student at the Institute of Computational Modeling in Civil Engineering, **TU Universität Braunschweig**, Germany
2007-2011	M.Sc. in Mechanical Engineering **Isfahan University of Technology**, Iran
2003-2007	B.Sc. in Mechanical Engineering **Persian Gulf University**, Iran
1999-2003	High School Diploma in Physics and Mathematics **National Organization for Development of Exceptional Talents**, Iran

Eidesstattliche Erklärung

Name: Ehsan Goraki Fard
Geburtsdatum/-ort: 16. September 1984, Boushehr im Iran
Straße: Hans-sommer Str. 25
Ort: Braunschweig

Hiermit erkläre ich an Eides statt, dass ich die vorgelegte Dissertation mit dem Titel

A Cumulant LBM approach for Large Eddy Simulation of Dispersion Reactors

selbstständig verfasst, nicht schon als Diplom- oder Prüfungsarbeit verwendet und alle in Anspruch genommenen Hilfen in der Dissertation angegeben habe.

Ich versichere an Eides statt, dass ich diesen Promotionsantrag erstmalig einreiche und keine früheren Versuche einer Promotion unternommen habe.

____
(Ort, Datum, Unterschrift)